

# Analysis Note of the Experiment

## Supplementary note on diffractive analyses of 2015 proton-proton data:

- [1] Measurement of Central Exclusive Production of  $h\bar{h}$  pairs ( $h = \pi, K, p$ ) with Roman Pot detectors in diffractive proton-proton interactions at  $\sqrt{s} = 200$  GeV
- [2] Measurement of particle production with Roman Pot detectors in diffractive proton-proton interactions at  $\sqrt{s} = 200$  GeV

Leszek Adamczyk , Łukasz Fulek , and Rafał Sikora

*AGH University of Science and Technology, FPACS, Kraków, Poland*

November 15, 2018

### Abstract

In this note we present supplementary material related to analyses of diffractive processes based on 2015 data from proton-proton collisions at  $\sqrt{s} = 200$  GeV. This dataset was collected with newly installed Roman Pot detectors in Phase II\* configuration which ensured efficient triggering and measuring diffractively scattered protons.

We focus on issues which are common in aforementioned analyses: calculation of efficiencies, corrections to Monte Carlo simulations and derivation of systematic uncertainties of our measurements.

# Contents

<b>1</b>	<b>Bad run list</b>	<b>4</b>
<b>2</b>	<b>TPC vertex and track selection</b>	<b>5</b>
2.1	TPC vertex . . . . .	5
2.2	TPC tracks . . . . .	5
2.2.1	Quality cuts . . . . .	5
2.2.2	Vertex matching quality . . . . .	5
2.2.3	TOF hit matching . . . . .	5
2.2.4	Kinematic range . . . . .	5
<b>3</b>	<b>Efficiencies</b>	<b>6</b>
3.1	TPC track acceptance and reconstruction efficiency . . . . .	6
3.2	TOF acceptance, hit reconstruction and track matching efficiency . . . . .	6
<b>4</b>	<b>Energy Loss Correction</b>	<b>8</b>
<b>5</b>	<b>Forward protons</b>	<b>10</b>
5.1	Detector layout . . . . .	10
5.2	Roman Pot data reconstruction . . . . .	10
5.2.1	Roman Pot track points and tracks . . . . .	10
5.2.2	Alignment . . . . .	11
5.3	Roman Pot simulation . . . . .	12
5.3.1	General description . . . . .	12
5.3.2	Detector model . . . . .	13
5.3.3	Aperture tuning . . . . .	13
5.3.4	Embedding technique . . . . .	15
<b>6</b>	<b>dE/dx adjustment</b>	<b>16</b>
<b>7</b>	<b>TPC track pointing resolution adjustment</b>	<b>20</b>
<b>8</b>	<b>Dead material in front of TPC</b>	<b>23</b>
<b>9</b>	<b>Systematic errors</b>	<b>28</b>
9.1	TPC track reconstruction efficiency . . . . .	28
9.1.1	Embedding (pile-up) effect . . . . .	28
9.1.2	Dead material effect on TPC track reconstruction efficiency . . . . .	29
9.2	TOF matching efficiency . . . . .	33
9.2.1	Embedding (pile-up) effect . . . . .	33
9.2.2	Simulation accuracy (absolute error on TOF efficiency) . . . . .	34
<b>Appendix A</b>	<b>TPC track reconstruction efficiency</b>	<b>38</b>
<b>Appendix B</b>	<b>TOF hit reconstruction and matching efficiency</b>	<b>51</b>
<b>Appendix C</b>	<b>Energy Loss Correction</b>	<b>64</b>
<b>Appendix D</b>	<b>Apertures tuning in Geant4 simulation</b>	<b>76</b>
<b>Appendix E</b>	<b>Dead material effect on TPC track reconstruction efficiency</b>	<b>78</b>
<b>Appendix F</b>	<b>Fits to dE/dx spectra, comparison of dE/dx and <math>n_X^\sigma</math> between data and MC</b>	<b>95</b>
<b>Appendix G</b>	<b>Tag&amp;Probe fits for TOF hit reconstruction and matching efficiency</b>	<b>116</b>
<b>List of Figures</b>		<b>123</b>
<b>List of Tables</b>		<b>123</b>



# 1. Bad run list

Diffractive analyses [1, 2] were performed with the use of data from runs with completion status “Successful” in the STAR run log [3]. During analysis of these runs no problems with the reconstructed data were found. The distributions of the TPC track-related quantities and performance of remaining subsystems used in analyses did not indicate issues preventing this data from inclusion to physics analyses.

On top of above we omitted from analyses data taken with Roman Pot detectors far from their nominal positions. By the nominal position we understand the vertical distance between the nominal beam trajectory and the closest edge of the Silicon Strip Detector housed inside Roman Pot. This positions were first measured during dedicated survey [4] and later precisely calculated for all runs and for all detectors using elastic proton-proton scattering events [5, 6].

Below we show histogram (Fig. 1.1a) and graph (Fig. 1.1b) of the beam-detector positions of all Roman Pots during runs with active RP triggers<sup>1</sup>. Based on these plots we set the limit of the nominal position of the detector with respect to the beam to  $y_{\text{thr}} = 34$  mm. If any of 8 detectors was further from the beam than the threshold ( $|y| > y_{\text{thr}}$ ) the run was omitted from analysis. The benefit of that selection was reduction of the systematic effects related to low/asymmetric acceptance of detectors when they are at far/significantly differing distances from the nominal beam trajectory.

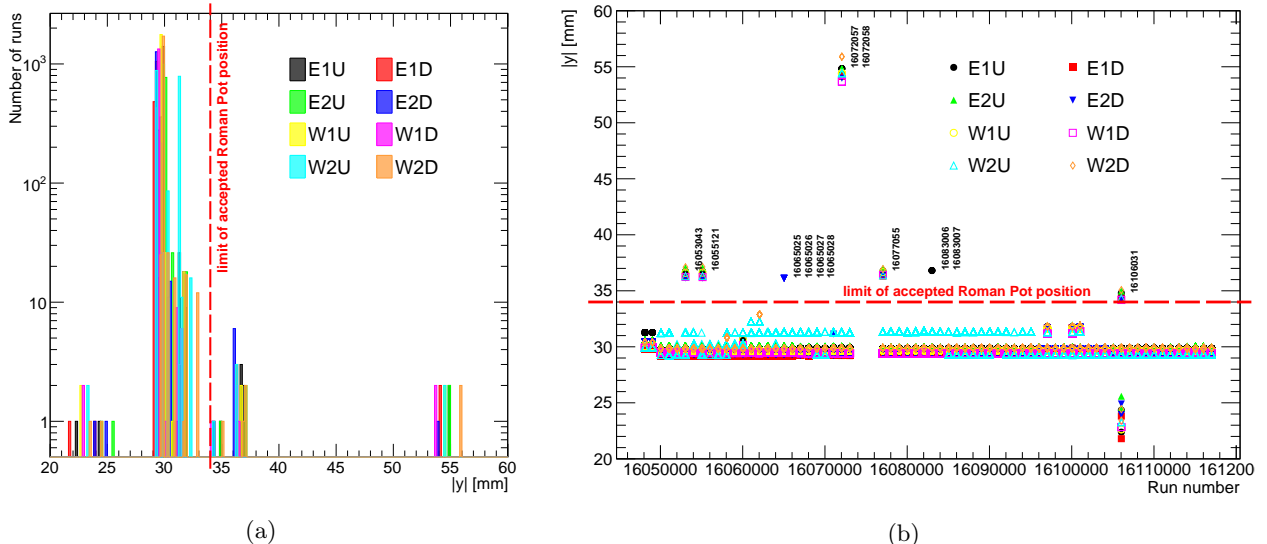


Figure 1.1: Histogram of beam-detector distance  $|y|$  (1.1a) and graph showing run-dependence of  $|y|$  (1.1b) for all Roman Pots.

Runs in which detector positions did not fulfill beam-detector distance limits are listed below:

16053043	16055121	16065025	16065026	16065027	16065028
16072057	16072058	16077055	16083006	16083007	16106031

Full list of runs with diffractive triggers (“RP\\_xxxx”) and the list of runs for each trigger can be found at the web address given in Ref. [7].

<sup>1</sup>Roman Pots were not moved during the run. They were only moved between the runs.

# 2. TPC vertex and track selection

Charged particle tracks and primary vertices reconstructed with the TPC were selected in our analyses with the set of cuts listed below. These cuts were used in all sub-analyses described in this note and our physics analyses described in Ref. [1] and [2], unless stated differently. The goal of these criteria was to reject overlapping pile-up events, off-time pile-up tracks and ensure satisfactory resolution of the track momentum and specific energy loss.

Limit values of quantities in all selection cuts were chosen to balance the selection efficiency, background rejection power and related systematic uncertainties. Cuts in Sec. 2.2.1 and 2.2.2 were established based on histograms like the ones presented in Fig. 7.5. Cuts on  $z_{\text{vtx}}$  and track  $p_T$  and  $\eta$  were set based on the  $z_{\text{vtx}}$  distribution ( $\sigma(z_{\text{vtx}}) \approx 50$  cm) and joint acceptance and efficiency of the TPC and TOF (see Appendix A and B).

## 2.1 TPC vertex

- **Single primary vertex** (exactly one that contains at least one track matched with hit in TOF),
- $|z_{\text{vtx}}| < 80$  cm.

## 2.2 TPC tracks

### 2.2.1 Quality cuts

All TPC tracks had to satisfy quality criteria:

- $N_{\text{hits}}^{\text{fit}} \geq 25$  - at least 25 hits used in the helix fit (for good momentum resolution),
- $N_{\text{hits}}^{\text{dE/dx}} \geq 15$  - at least 15 hits used in  $dE/dx$  calculation (for good  $dE/dx$  resolution),
- $N_{\text{hits}}^{\text{fit}}/N_{\text{hits}}^{\text{poss}} \geq 0.52$  - number of hits used in the fit not less than 52% of the number of hits potentially left by the particle,
- $|d_0| < 1.5$  cm - transverse impact parameter w.r.t. the beamline (see Fig. 7.1) not larger than 1.5 cm (for selection of tracks of real primary particles which by definition have origin in the interaction point which lies on the beamline).

### 2.2.2 Vertex matching quality

Primary TPC tracks had to match well to the primary vertex:

- $\text{DCA}(R) < 1.5$  cm - radial component of the DCA vector between the global helix and the vertex not larger than 1.5 cm (value consistent with  $|d_0|$  limit),
- $|\text{DCA}(z)| < 1$  cm - absolute magnitude of longitudinal component of the DCA vector between the global helix and the vertex not larger than 1 cm.

### 2.2.3 TOF hit matching

TPC tracks had to be matched with hits reconstructed in TOF:

- **TOF match flag**  $\neq 0$ .

### 2.2.4 Kinematic range

TPC tracks had to be contained within the kinematic range:

- $|\eta| < 0.7$ ,
- pions:  $p_T > 0.2$  GeV,  
kaons:  $p_T > 0.3$  GeV,  
protons:  $p_T > 0.4$  GeV.

# 3. Efficiencies

## 3.1 TPC track acceptance and reconstruction efficiency

We defined joint acceptance and efficiency of reconstruction of a track in the TPC,  $\epsilon_{\text{TPC}}$ , as the probability that particle from the primary interaction generates signal in the detector which is reconstructed as a global track that satisfies all quality criteria (cuts 2.2.1).

Thechnically this quantity was derived from single particle STARsim MC embedded into zero-bias triggers in the following procedure:

1. True-level primary particles of given ID and charge were selected (*set A*).
2. Each particle from *set A* was checked if global TPC track with more than half of hit points generated by this particle was reconstructed (definition of true level particle-track matching). All global tracks which were associated with true-level primary particles and satisfied quality criteria (cut 2.2.1) formed *set B*.
3. The joint TPC acceptance and efficiency was calculated as the ratio of the histograms of true-level quantities (such as  $p_T$ ,  $\eta$ ,  $z_{\text{vtx}}$ ) for particles from *set B* and particles from *set A*:

$$\epsilon_{\text{TPC}}(p_T, \eta, z_{\text{vtx}}; \text{sign, PID}) = \frac{(p_T, \eta, z_{\text{vtx}}) \text{ histogram for particles of given sign and ID from } \textit{set } B}{(p_T, \eta, z_{\text{vtx}}) \text{ histogram for particles of given sign and ID from } \textit{set } A}. \quad (3.1)$$

The sample TPC efficiency plot is shown in Fig. 3.1. All remaining TPC efficiency plots are contained in Appendix A.

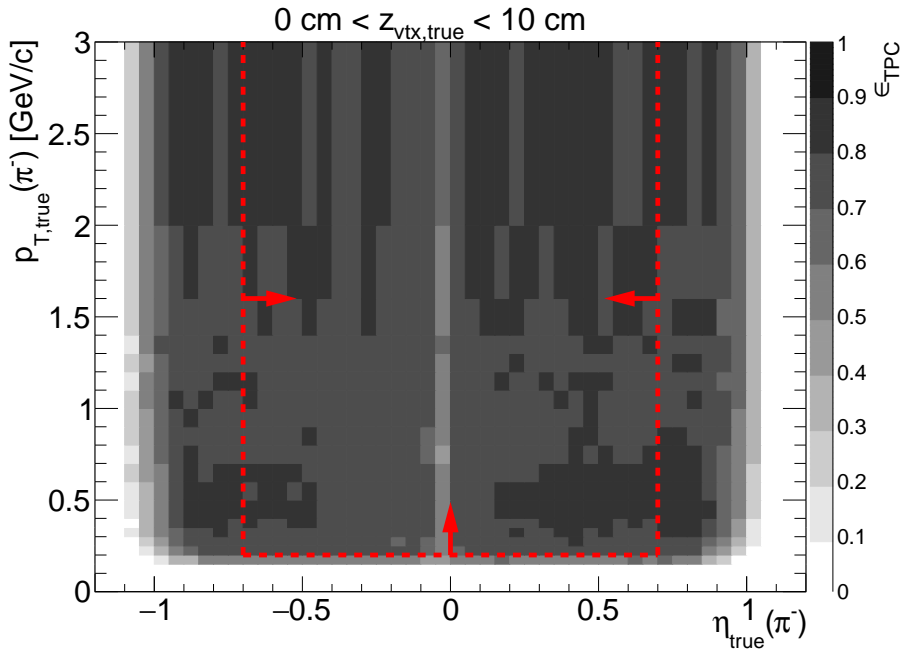


Figure 3.1: Sample TPC acceptance and reconstruction efficiency of  $\pi^-$ . Plot represents the TPC efficiency  $\epsilon_{\text{TPC}}$  (z-axis) as a function of true particle pseudorapidity  $\eta$  (x-axis) and transverse momentum  $p_T$  (y-axis) in single  $z$ -vertex bin whose range is given at the top. Red lines and arrows indicate region accepted in analyses.

## 3.2 TOF acceptance, hit reconstruction and track matching efficiency

Combined TOF acceptance, hit reconstruction efficiency and matching efficiency with TPC tracks,  $\epsilon_{\text{TOF}}$ , was defined as the probability that the global TPC track that satisfy quality criteria (cuts 2.2.1) is matched with hit in TOF (2.2.3). This quantity is generally referred as “TOF efficiency”.

It was calculated in the very similar way to TPC efficiency - single particle STARsim MC embedded into zero-bias triggers was used. Tracks belonging to *set B* from Sec. 3.1 were utilized. From these tracks a sub-sample of tracks with non-zero TOF matching flag was extracted (*set C*). The TOF efficiency was calculated as

$$\epsilon_{\text{TOF}}(p_T, \eta, z_{vtx}; \text{sign, PID}) = \frac{(p_T, \eta, z_{vtx}) \text{ histogram for particles of given sign and ID from set } C}{(p_T, \eta, z_{vtx}) \text{ histogram for particles of given sign and ID from set } B}. \quad (3.2)$$

An additional note has to be made here about the correction which is applied to TOF matching flag in MC analysis. It was found that in embedded simulation the dead TOF elements were not masked. To correct for this effect (hence obtain more reliable TOF efficiency) a data-based map of TOF modules was created, separately for each RHIC fill. Map was filled with modules which were matched with TPC tracks in the data. In all MC sample analyses (including efficiency determination) each TPC track with non-zero TOF match flag was additionally checked if TOF module that it was matched with had any entries in the data-based map. If not - the TOF match flag was considered 0.

The sample TOF efficiency plot is shown in Fig. 3.2. All remaining TOF efficiency plots are contained in Appendix B.

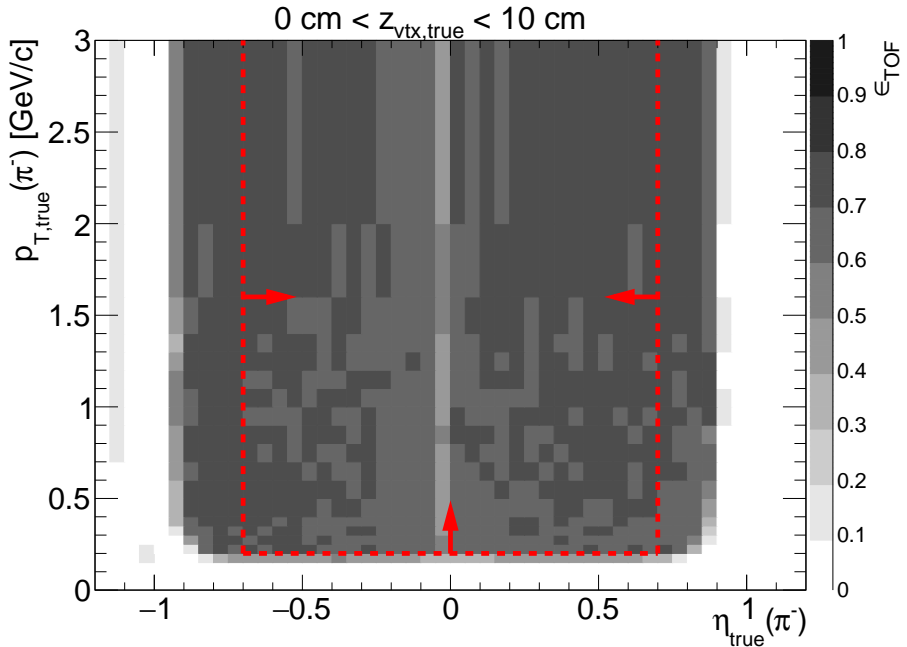


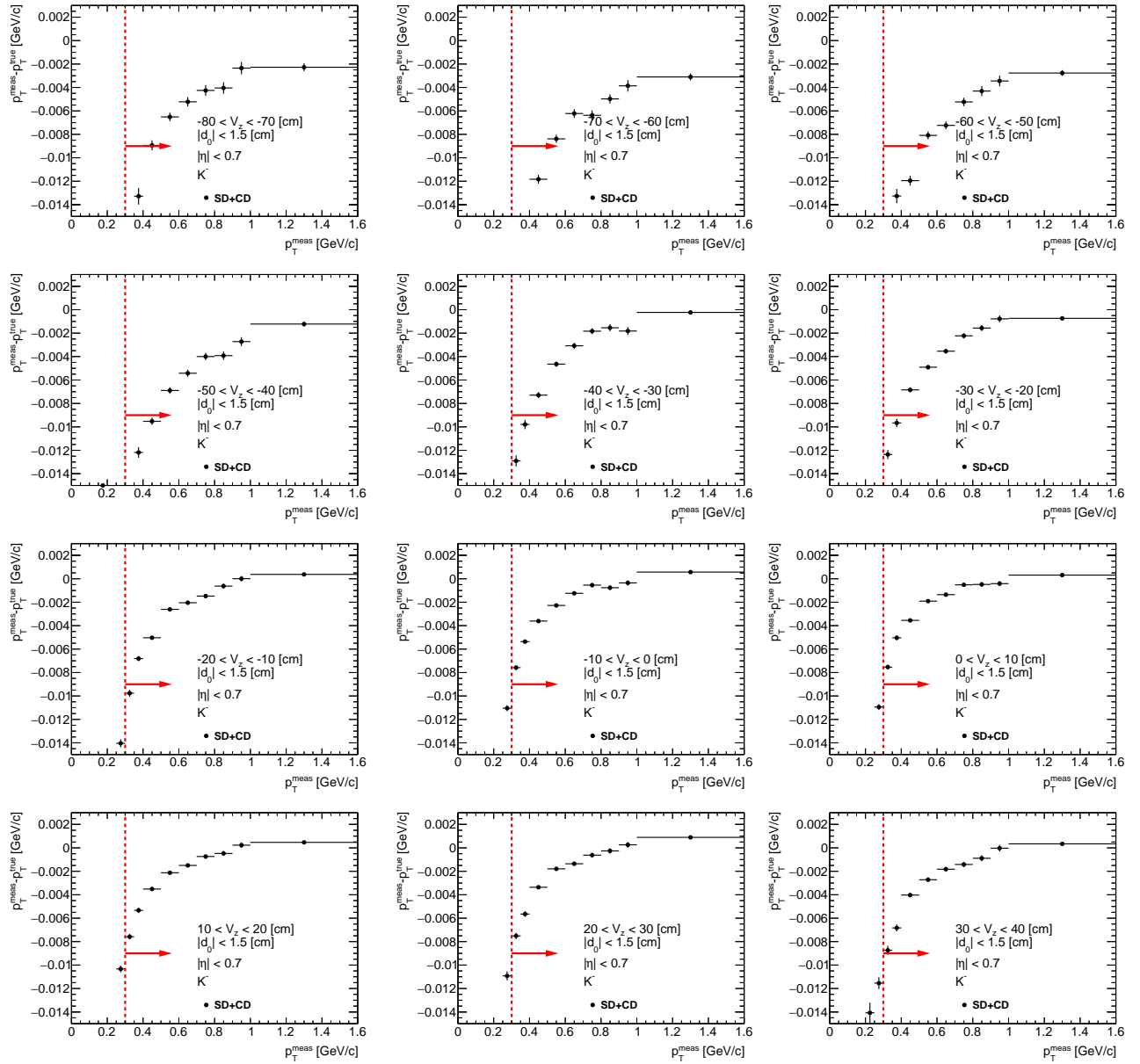
Figure 3.2: Sample plot of TOF acceptance, reconstruction and matching efficiency of  $\pi^-$ . Plot represents the TOF efficiency  $\epsilon_{\text{TOF}}$  (z-axis) as a function of true particle pseudorapidity  $\eta$  (x-axis) and transverse momentum  $p_T$  (y-axis) in single  $z$ -vertex bin whose range is given at the top. Red lines and arrows indicate region accepted in analyses.

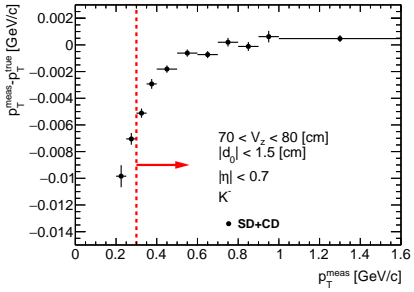
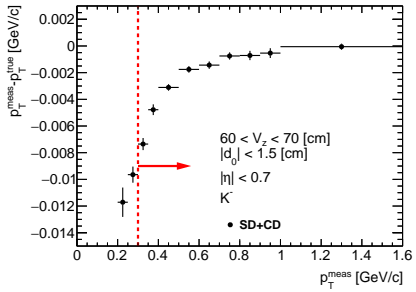
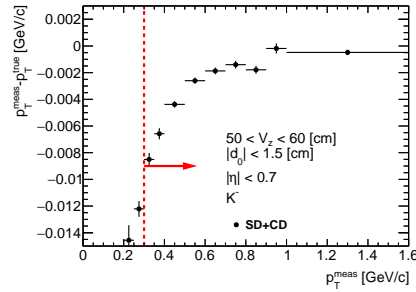
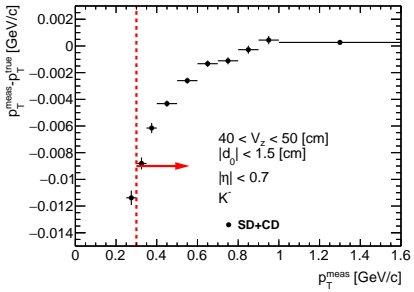
As shown in Sec. 9.2.2, it was found during estimation of the systematic uncertainty of the TOF efficiency that the data-driven efficiency and MC efficiency (obtained with a method described in this section) differ significantly. Therefore the final TOF efficiency which is used to correct the data is a modified MC efficiency. Form of MC efficiency modification is given in ... .

# 4. Energy Loss Correction

Particles passing through the detector material loose energy as they travel. The track momentum  $p_T^{true}$  is reconstructed by fitting a helical path to the track points left in the detector. Fitting the track points to an ideal helical track tends to underestimate the momentum due to these energy loss effects. To minimize biases due to this effect, correction procedure is applied during standard track momentum reconstruction procedure for both data and MC simulation. For this procedure all particles are assumed to be pions and the reconstructed momentum  $p_T^{meas}$  is corrected by the amount of energy loss for a pion. For anything that is not a pion some rest bias is still present since on average energy loss is specific for each particle type. These biases can be determined from simulated tracks run through GEANT. The correction  $p_T^{meas} - p_T^{true}$  was calculated for each particle species as a function of  $p_T^{meas}$ ,  $\eta$  and  $z$ -vertex. The energy loss correction averaged over  $|\eta| < 0.7$  for  $K^-$  is shown in Fig. 4.1. The energy loss corrections for other particle species are shown in Figs. C.1 to C.9 in Appendix C.

Figure 4.1: Energy loss correction  $p_T^{meas} - p_T^{true}$  for  $K^-$  as a function of reconstructed transverse momentum  $p_T^{meas}$  ( $|\eta| < 0.7$ ) in single  $z$ -vertex bin whose range is given on each plot. Red lines and arrows indicate region accepted in analyses.





# 5. Forward protons

The main detector system used in our analyses is the Roman Pot setup in Phase II\* configuration (Roman Pots in Phase I took data with STAR during special runs in last days of  $p + p$  collisions in 2009, see e.g. Ref. [8–10]). It allowed to trigger on forward protons and reconstruct their momentum with high efficiency and precision.

## 5.1 Detector layout

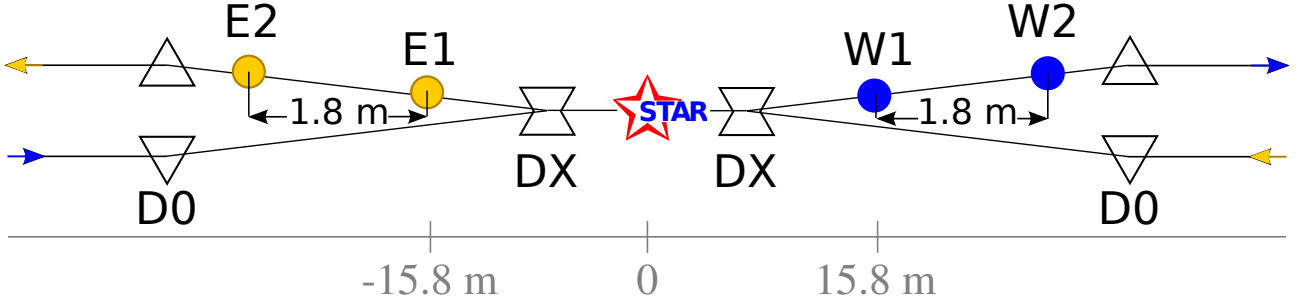


Figure 5.1: Schematic representation (top view) of the Roman Pot Phase II\* at STAR (not to scale).

As presented in Figure 5.1 the Roman Pot Phase II\* setup consists of detectors located in two stations on each side of the interaction point (IP) in a distance of 15.8 m and 17.6 m from the IP. Each station has two Roman Pots positioned vertically, one above and the other below the beamline (Fig. 5.2). Detectors are situated downstream the DX dipole magnets responsible for head-on targeting of the incoming beams and bending outgoing beams back into the accelerator pipeline. The constant and uniform magnetic field of the DX magnet works as a spectrometer and thus knowledge on the track angle and position in the detector allows complete reconstruction of the proton momentum, including the fractional momentum loss  $\xi$  (as described in [11]). The naming convention of elements of RP setup is described in Ref. [12].

Single Roman Pot (the vessel, Fig. 5.5) houses a package of 4 silicon strip detector planes (Fig. 5.6) - one pair of SSDs with vertical and one with horizontal orientation of the strips, and hence measurement of the position of a proton hit is possible in both transverse spatial coordinates,  $x$  and  $y$ . The pitch (distance between neighbouring strips) in a single detector is 100  $\mu\text{m}$ , therefore intrinsic spatial resolution is at the level of 30  $\mu\text{m}$ . In addition to the silicon detectors, the package contains plastic scintillator that covers whole active area of the silicon, attached at the back. Two lightguides are glued at the top edge of scintillator which direct the light generated when ionizing particle passes through it to the photomultiplier tubes (PMTs) connected at the very end of each. This counter is used to trigger on forward protons and also provides the timing information.

## 5.2 Roman Pot data reconstruction

### 5.2.1 Roman Pot track points and tracks

Roman Pot data is stored in MuDST in StMuRpsCollection. This class contains objects reconstructed with St\_pp2pp\_Maker. The basic (low-level) data objects are the clusters characterized by their length (number of adjacent strips with signal above the threshold), energy (sum of ADC counts in each constituent strip) and

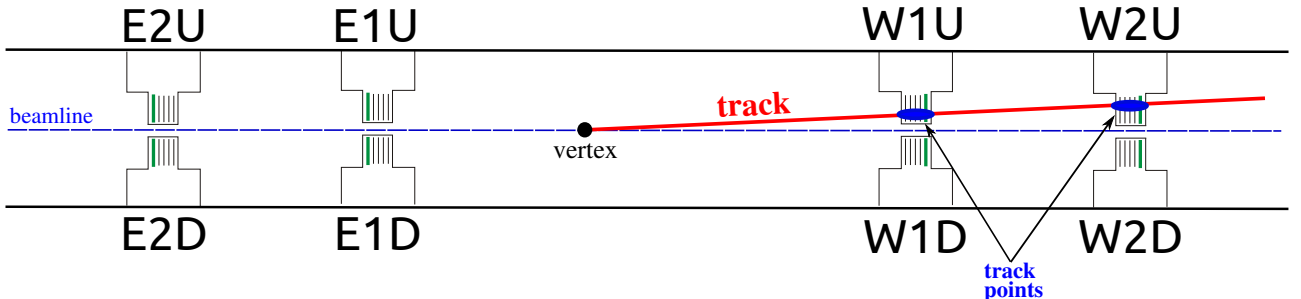


Figure 5.2: Side view of the Roman Pot Phase II\* setup (not to scale) with an illustration of Roman Pot track point and track.

position. Vectors of clusters are provided independently for each silicon plane. Another low-level data are informations about time (TAC) and signal strength (ADC) for each PMT.

Our physics analyses utilized mainly the high-level objects which are the track points (StMuRpsTrackPoint) and tracks (StMuRpsTrack) stored in vector members of StMuRpsCollection. In short, these objects represent real particles (e.g. their momentum vector) in the same way as the TPC tracks represent particles traversing TPC. Concept of track point and track is depicted in Fig. 5.2 and described in some more details in Ref. [13].

The algorithm for RP track reconstruction is implemented in St\_pp2pp\_Maker. It is a multi-track algorithm which first forms track points from clusters (there may be many track points in single RP), and then form tracks from all possible combinations of track points in Roman Pots in the same branch [13, 14]. The track points and tracks are additionally tuned with Roman Pot “afterburner” package (StMuRpsUtil, [15]) which recalculates positions of hits and momenta of tracks according to the final alignment corrections and known vertex position.

### 5.2.2 Alignment

Precise knowledge of positioning of detectors in space is crucial for correct reconstruction of proton momentum. Therefore a process of detector alignment was done, which involved a few steps. At first, dedicated detector survey [4] was performed before the start of run 15, which provided initial calibration of the LVDTs installed

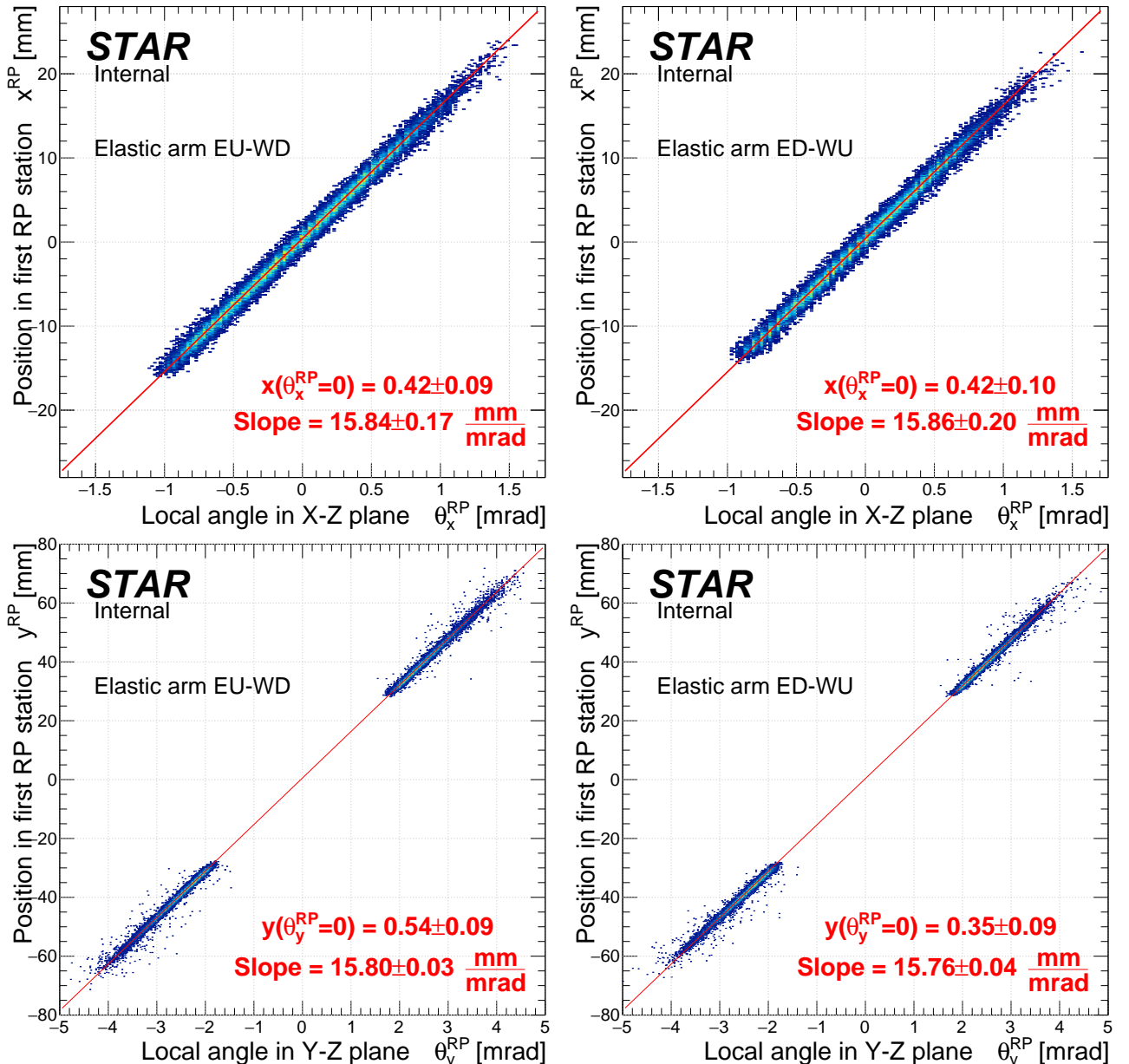


Figure 5.3: Correlation between the hit position of constituent track point in the first RP station ( $y$ -axis) and the local angle of track ( $x$ -axis) in elastic scattering events. The  $y$ -intercept has interpretation of the average position of the interaction vertex in given coordinate.

in Roman Pot movement system. This was sufficient to know the positioning of detectors at a  $\gtrsim 1$  mm level. Next, the alignment analysis using elastic scattering events was done, as described in the analysis note of elastic proton-proton scattering [16]. This analysis provided detectors alignment at a level of single pitch ( $\sim 100\mu\text{m}$ ). In the last step determination of the average vertex position was done, as described below.

Vertex position is not necessary to correctly reconstruct forward proton observables in elastic scattering events e.g. squared four-momentum transfer  $|t|$  - this is because one can use momentum balance constraint of elastically scattered protons (collinearity constraint) and calculate scattering angle from the straight line fit to all track points of east and west proton tracks, without knowledge where the interaction vertex was. The same approach cannot be used in other processes like Single or Central Diffraction, since there is only single forward proton (SD) or two forward protons are independent in terms of scattering angles and momentum loss (CD, CEP).

This fact led to development of the method of extraction of the average vertex position using the elastic scattering data, as presented in Ref. [17]. For this purpose RP\\_ET triggers from randomly chosen runs (16085056 and 16085057) were used with single (exactly one) global RP track reconstructed on each side of the IP. Tracks were required to be collinear at  $2\sigma$  level. Selected clean sample of elastic scattering events was used to prepare the plots of the position of the track point in near RP station vs. the local angle of the RP track with respect to the global  $z$ -axis (Fig. 5.3). The least squares fit of a line (with perpendicular offsets) to all data points in the scatterplot was performed. As a result four lines were obtained, one per arm per transverse coordinate. The slope of the line has interpretation of the distance from the nominal IP ( $z = 0$ ) to the 1<sup>st</sup> RP station at 15.8 m. One can see that the slopes are well consistent with this value. The intercept of the line equals to the average position of the vertex in given coordinate. One finds that  $\langle x \rangle_{\text{IP}}$  obtained from the fits to data points in two independent elastic arms are perfectly consistent, while in  $\langle y \rangle_{\text{IP}}$  parameters differ by 1.5 standard deviations. We conclude that extracted values of average positions of the vertex are trustworthy and we can average the numbers obtained from two independent arms. As a result we use in our analyses numbers  $\langle x \rangle_{\text{IP}} = 0.42$  mm,  $\langle y \rangle_{\text{IP}} = 0.45$  mm, both in the reconstruction/recalculation of proton tracks with StMuRpsUtil package, and generation of MC events.

In Ref. [17] the method of  $\langle z \rangle_{\text{IP}}$  extraction is also presented, however the result  $\langle z \rangle_{\text{IP}} = 3$  cm is much smaller than event-by-event variation of the vertex position along  $z$ -axis (vertex spread is  $\sigma(z_{\text{vtx}}) = 50$  cm), and more importantly it is much less than the distance between nominal IP and the Roman Pots (3 cm compared to 15.8 m). Such small offset has effectively no influence on the error on proton momentum reconstruction, therefore we neglect it.

Due to time dependence of the beam conditions, automatic beam orbit corrections etc., the average position of the vertex may change from run to run. The measure of this variation is a by-product of Roman Pot alignment procedure which was done for every run. In Ref. [18] the middle points of the track (MPTs, position of the track at  $z = 0$ ) are plotted as a function of run number. One can see that MPTs in  $x$  and  $y$  are roughly constant along the entire data taking period in 2015 and consistent with numbers derived in Fig. 5.3. Another cross-check for the correctness of extracted  $\langle x \rangle_{\text{IP}}$  and  $\langle y \rangle_{\text{IP}}$  was done with the use of elastic scattering MC simulation in Geant4. Several MC samples were generated with differently positioned vertex. The same procedure was performed as the one described in this section and the output values of  $\langle x \rangle_{\text{IP}}$  and  $\langle y \rangle_{\text{IP}}$  were always consistent with the true values. Also the comparisons of the hit maps of elastic scattering protons were done between the data and MC, and the best matching was found for vertex generated at  $\langle x \rangle_{\text{IP}} = 0.42$  mm and  $\langle y \rangle_{\text{IP}} = 0.45$  mm (e.g. [19]).

## 5.3 Roman Pot simulation

### 5.3.1 General description

Simulation of the STAR detector (STARsim) implemented in Geant3 does not contain a model of the Roman Pot detectors. Because of this, a dedicated simulation program "pp2pp" was prepared to enable precise measurements with the Roman Pot data. The development of this software started in 2012 as two independent projects for "Geant4 simulation tool kit" subject at AGH UST, which were later included in B.Sc. theses of the authors. One project was devoted to modeling of the Roman Pot and Silicon Strip Detector package [20], the other was aimed to implement simulation of the collider elements with full magnet lattice (including  $B$  field) [21] between the IP and Roman Pot location in Phase I configuration (at  $z = \pm 55$  m) based on the MAD-X twiss files. At that stage the two programs were used in analyses of 2009  $p + p$  data [10, 22] taken with Roman Pots during special high- $\beta^*$  runs. Both projects were merged in 2013 and since then are continuously developed by the Krakow group.

Currently the simulation program is a standalone Geant4 application that allows to simulate any type of particle, track it from the IP to the Roman Pots location (either in Phase I/run 2009 or Phase II\*/run 2015&17 configuration) and obtain the true level and reconstructed information in the standard STAR data format - MuDST classes stored the ROOT tree. In the reconstruction the original STAR St\\_pp2pp\\_Maker class is used. The program has multiple generation options: the input can be directly from STARsim, Pythia, HepMC format

or a simple text file. There are also built-in modes, such as elastic scattering event generation. One can customize the beam conditions, magnet settings (beam energy), Roman Pot positions, and many others. The application is installed at RCF and free to use by any STAR collaborator. Implementation of extensions desired by analyzers is possible after contact with authors. Some more information about the Roman Pot simulation (geometry, usage) can be found in the presentation from the LFS-UPC PWG weekly meeting (Ref. [23]).

### 5.3.2 Detector model

The geometry of the collider elements (beampipe, magnets) and Roman Pot detectors (vessel, SSD packages) is implemented in Geant4 according to the best available sources of information. The dimensions, positioning and material of the beam pipe and magnets were taken from the technical drawings available at RHIC C-AD and were discussed with the designers of these elements. In case of Roman Pot vessels and detector packages not only technical drawings were used to find the appropriate dimensions, but also dedicated survey was made in which some elements were measured with caliper.

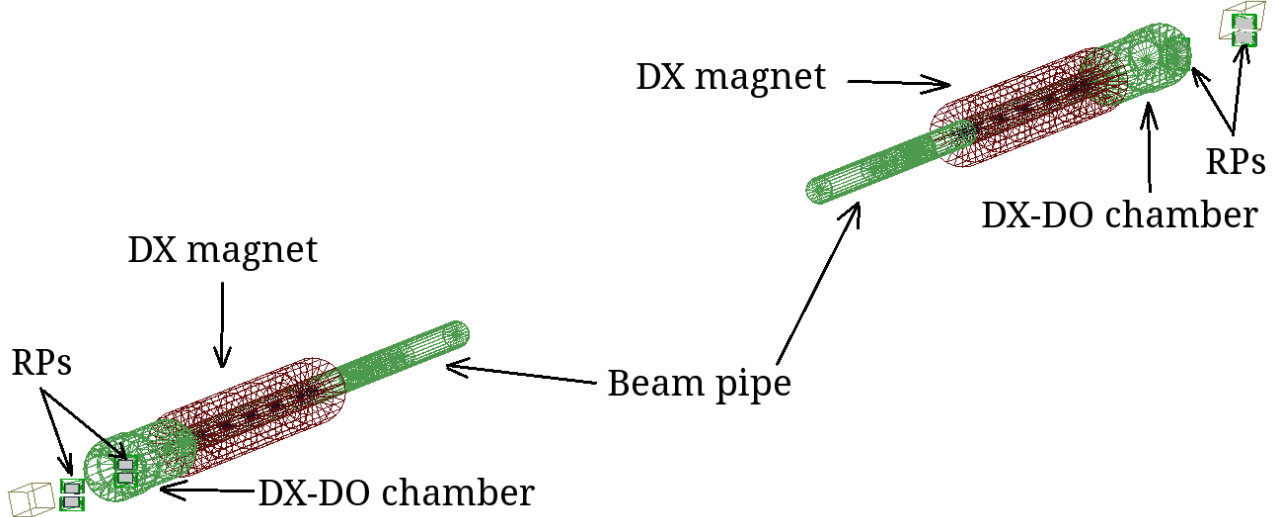


Figure 5.4: View of the Geant4 implementation od the Roman Pot Phase II\* detector setup.

In Fig. 5.4 we show the general view of the "world" volume in Geant4 pp2pp simulation with labeled the most significant elements of the geometry. In Fig. 5.7 we show a few shots of the Roman Pot housing and the SSD package implemented in Geant4, together with the real photographs of the Roman Pot and SSD package in Figs. 5.1 and 5.6.

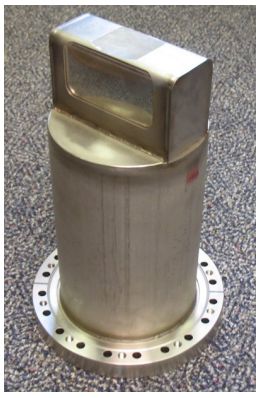


Figure 5.5: Roman Pot vessel (photo).

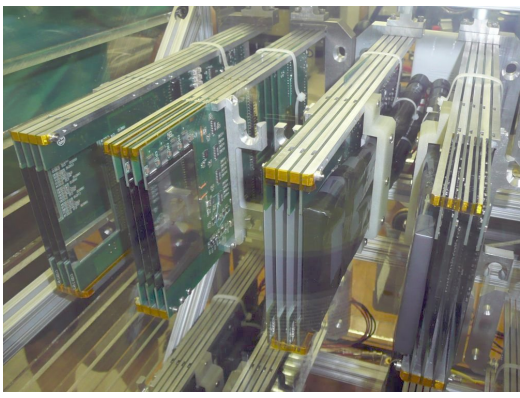


Figure 5.6: Silicon Strip Detector packages stored in the protective atmosphere (photo).

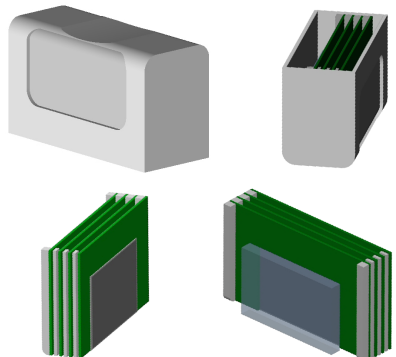


Figure 5.7: Geant4 implementations of the Roman Pot vessel and SSD package with trigger counter.

### 5.3.3 Aperture tuning

It turned out during initial validations of the Geant4 simulation for run 15 with elastic proton-proton scattering events that the distribution of the  $(x, y)$  position of the proton in Roman Pots does not agree between the data

and MC at a satisfactory level. It was understood that the perfect positioning of the elements of the collider assumed in the geometry model may need some tuning, especially the positioning DX magnet which particularly limits acceptance of the RP detectors. The DX magnets are moved each time the switch between symmetric (e.g.  $p + p$ ) and asymmetric (e.g.  $p + Au$ ) collisions takes place to accommodate for the non-zero tilt of the beams in asymmetric collisions required to close beam orbits and provide collisions in the STAR IR. Therefore lateral offset of this element was expected to be the most significant ingredient needed to correctly describe forward proton acceptance in the RP location.

In order to quantitatively determine the agreement between the true DX position and position implemented in Geant4 a dedicated analysis of the DX “shadow” in the proton hit maps was performed. This algorithm looked for the sharp drop of event counts along the  $x$  coordinate in the histogram of  $y$ - vs.  $x$ -position of the track points in collinear elastic scattering events with single proton tracks on both sides of the IP. The result (for a single RP station) is presented in Fig. 5.8a and 5.8b for the data and MC, respectively. The envelope of the DX shadow found by the algorithm is marked with black circles. The points were transformed by swapping  $x$  and  $y$  axis and fitted with a circle, as shown in Fig. 5.8c. The parameters of the circle (radius  $R$  and center

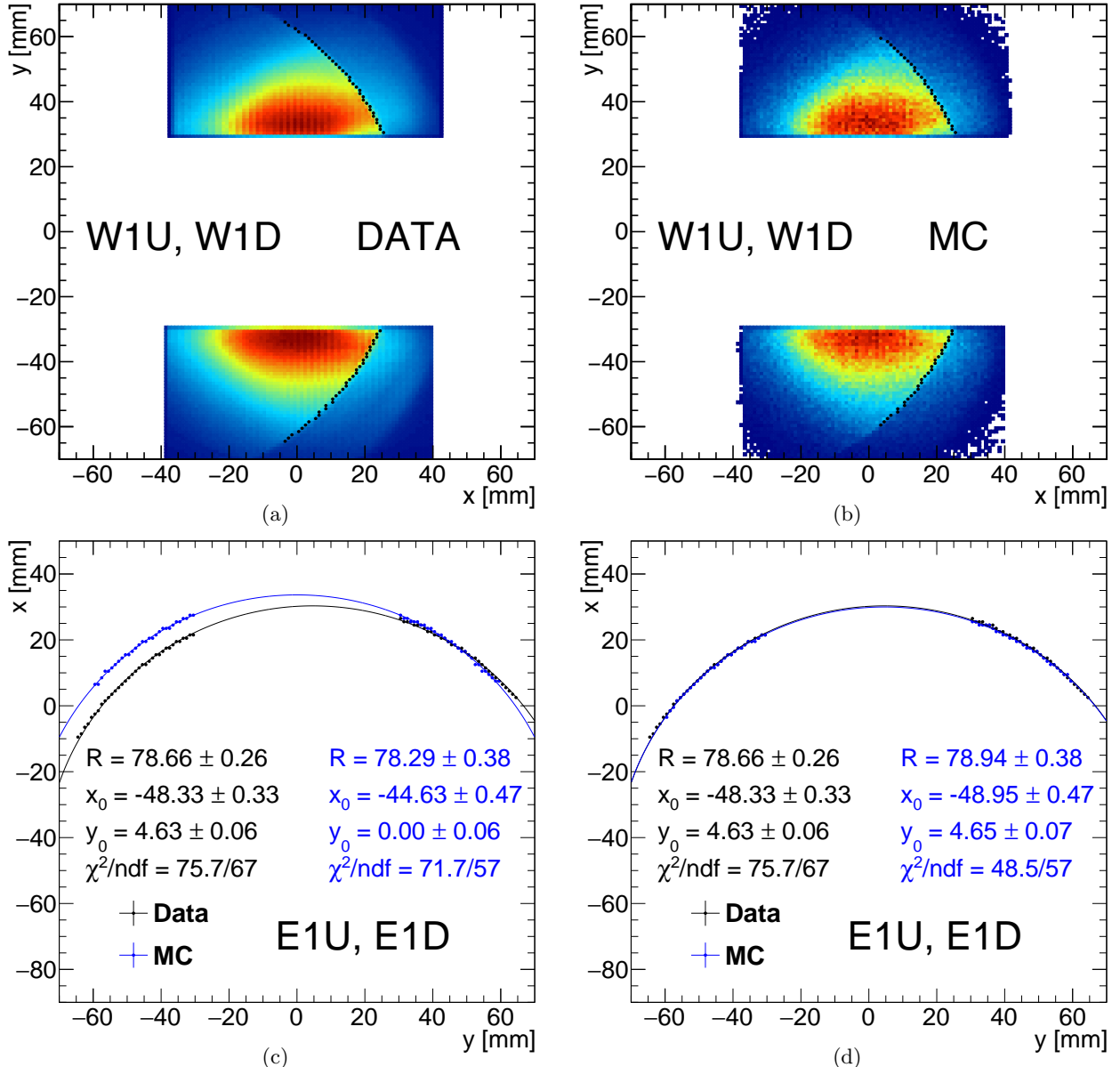


Figure 5.8: Sample hit map of track points of proton tracks in events selected as elastic scattering in the data (5.8a) and MC (5.8b) with the DX aperture “shadow” marked with black points. The DX aperture envelopes were fitted with circles (5.8c) which helped to establish the offsets of DX magnet positions in  $x$  and  $y$  with respect to the ideal (nominal) geometry, leading to nearly perfect agreement between the data and MC after introducing the offsets in Geant4 geometry (5.8d).

point  $(x_0, y_0)$  do not reflect directly the position of the DX, but they were used to find the best shift of the DX on the east and west side in the iterative method. The satisfactory agreement of the DX aperture envelopes between the data and MC was finally found when the shifts of the DX magnets with respect to their nominal positions were equal to  $\Delta x_{\text{DX}}^{\text{East}} = -3.1$  mm,  $\Delta y_{\text{DX}}^{\text{East}} = 4.0$  mm,  $\Delta x_{\text{DX}}^{\text{West}} = -2.4$  mm,  $\Delta y_{\text{DX}}^{\text{West}} = 0.4$  mm. The comparison of the DX shadow envelope after the tune is shown in Fig. 5.8d. All comparisons are presented in Appendix D.

### 5.3.4 Embedding technique

# 6. $dE/dx$ adjustment

Particle identification in our analyses is done using merged information from the TPC (specific energy loss of tracks  $dE/dx$ ) and from the TOF (time of hit matched to TPC track). As can be seen in Fig. F.5,  $dE/dx$  information from the MC events simulated in STARsim (in red) poorly matches the data points (black). This results e.g. in large systematic error of estimate of particle identification efficiency.

This problem was discussed under ticket #3272 (Ref. [24]). There were trials to improve the TPC calibration in simulation, but the problem remained. It was finally concluded that the origin of the problem lies in the model of energy loss used in the STARsim, therefore any further action was postponed.

In order to tune simulated response of the TPC in terms of  $dE/dx$ , hence also reduce the systematic uncertainty related to particle identification, a correction method was developed based on proper transformation (recalculation) of simulated  $dE/dx$  to obtain new  $dE/dx$  whose distribution matches the data. We know that  $n_X^\sigma$  (where  $X = \pi, K, p, \dots$ ) variable for particle  $X$  follows a gaussian distribution

$$n_X^\sigma = \left( \ln \frac{dE/dx}{\langle dE/dx \rangle_X} \right) / \sigma_{dE/dx}, \quad f(n_X^\sigma) = \mathcal{N}(n_X^\sigma; \mu = 0, \sigma = 1), \quad (6.1)$$

therefore  $dE/dx$  itself by definition follows log-normal distribution:

$$f(dE/dx) = \mathcal{LogN}(dE/dx; \mu = \langle dE/dx \rangle, \sigma = \sigma_{dE/dx}) = \frac{1}{\sqrt{2\pi} \cdot \sigma \cdot dE/dx} e^{-\frac{\ln^2 \frac{dE/dx}{\langle dE/dx \rangle}}{2\sigma^2}}. \quad (6.2)$$

The desired transformation should preserve the shape of  $dE/dx$  distribution so that it is still described by  $\mathcal{LogN}$ , however it should change  $\mu$  and  $\sigma$  so that these values are equal to ones in the data. The transformation that satisfies above postulate is

$$dE/dx' = c \cdot (dE/dx)^a. \quad (6.3)$$

Parameters of the distribution  $\mathcal{LogN}(dE/dx')$  are then

$$\mu' = c \cdot \mu^a, \quad \sigma' = a \cdot \sigma. \quad (6.4)$$

From above we get formulae for parameters of the transformation:

$$a = \sigma'/\sigma, \quad c = \frac{\mu'}{\mu^a}. \quad (6.5)$$

To sum up, one has to find the MPV and width parameter of the  $dE/dx$  spectrum of each particle in the data and MC, and use relations (6.5) in order to find parameters of the transformation introduced in Eq. (6.3).

The most challenging part of the task was extraction of the  $\langle dE/dx \rangle$  and  $\sigma_{dE/dx}$  from the data. In case of MC one can select tracks matched to true-level particles of given ID and thus separate  $dE/dx$  of different particles, which makes extraction of the distribution shape straightforward. Unfortunately, it is not possible to apply the same method to the data - here one has to deal with overlapping of the reconstructed  $dE/dx$  from different particles. Therefore fits of sum of  $f(dE/dx)$  corresponding to different particles were performed to reconstructed track  $dE/dx$  in narrow momentum bins. The width of momentum bins was chosen to compromise statistics and validity of assumption of constant parameters of  $dE/dx$  distribution over bin range.

It was found during the fitting that log-normal distribution is not a perfect model of the reconstructed  $dE/dx$ . The problems with description of the data were mainly in the tail-part of the distribution from single particle. Precise model was necessary to obtain satisfactory quality of fits and trustworthy values of parameters. After some research the best model of  $dE/dx$  distribution from single particle was found to be

$$f(dE/dx) = \begin{cases} \frac{A}{\sqrt{2\pi} \cdot \sigma \cdot dE/dx} \exp \left( -\frac{1}{2} \left( \frac{\ln \frac{dE/dx}{\langle dE/dx \rangle}}{\sigma} \right)^2 \right) & \text{for } \frac{\ln \frac{dE/dx}{\langle dE/dx \rangle}}{\sigma} \leq k \\ \frac{A}{\sqrt{2\pi} \cdot \sigma \cdot dE/dx} \exp \left( -k \cdot \frac{\ln \frac{dE/dx}{\langle dE/dx \rangle}}{\sigma} + \frac{1}{2} k^2 \right) & \text{for } \frac{\ln \frac{dE/dx}{\langle dE/dx \rangle}}{\sigma} > k. \end{cases} \quad (6.6)$$

Such form was motivated by the function presented in Ref. [25], here adopted for the log-normal instead of normal distribution. Because the modification of the log-normal distribution is introduced only at high-end tail, the validity of the transformation discussed above still holds. To reduce fit complexity the  $k$  parameter was set the same for all particle species and fixed to value equal 2.2, which worked well for both data and embedded MC. Particles and their anti-particles were assumed to have the same  $dE/dx$  distributions for a given momentum and were analyzed together. The same track selection was used both for data and MC, with the quality criteria

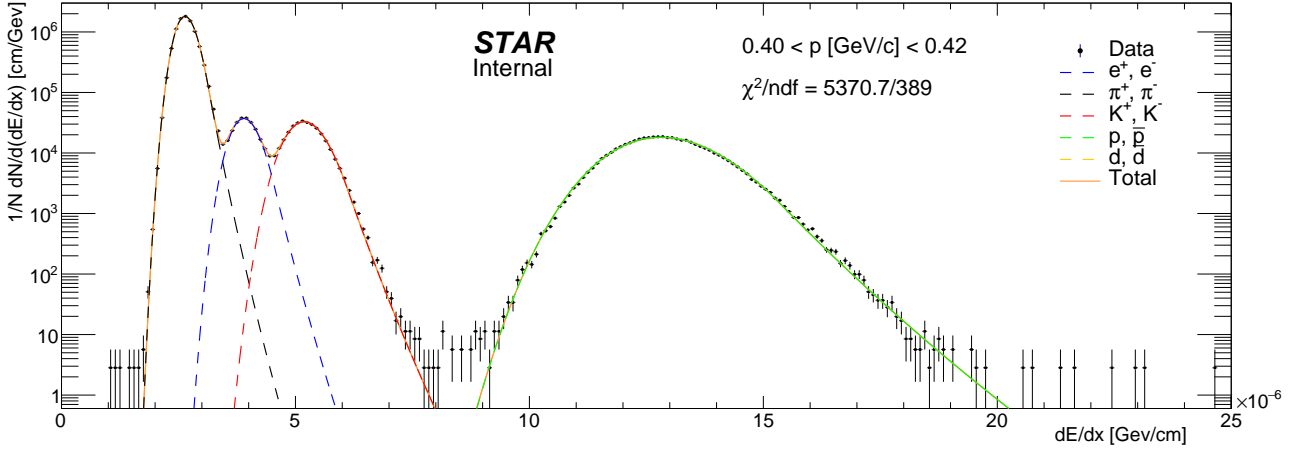


Figure 6.1: Sample fit of sum of functions from Eq. (6.6) corresponding to different particle species to  $dE/dx$  spectra in the data in a single momentum bin.

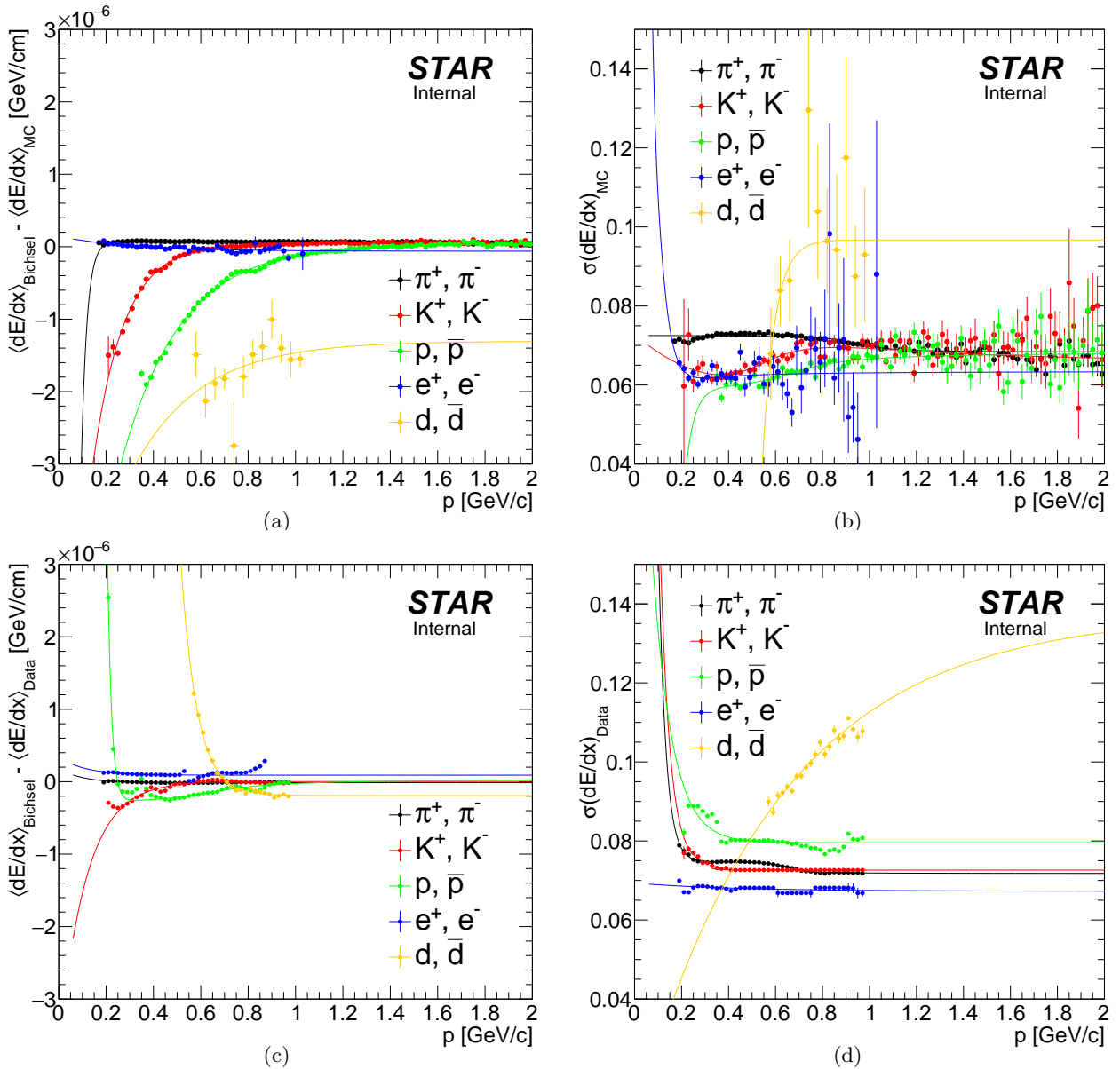


Figure 6.2: Difference between MPV of  $dE/dx$  predicted by Bichsel parametrization and obtained from the fit of Eq. (6.6) to  $dE/dx$  distribution in the data (6.2c) and MC sample (6.2a) and  $dE/dx$  width parameter in data (6.2d) and MC (6.2b) as a function of reconstructed particle momentum for a few particle species. Solid lines represent fits to points of corresponding color. Only statistical errors are shown.

described in Sec. 2. The sample fit in a single momentum bin can be found in Fig. 6.1. Fits in all momentum bins can be found in Appendix F.

Results of the fits for all considered particle species (pions, kaons, protons, electrons and deuterons) are commonly presented in Fig. 6.2 with color markers. Figures 6.2c and 6.2a show the offset of the MPV of reconstructed  $dE/dx$  relative to the Bichsel parametrization in the data and embedded MC, respectively, and Fig. 6.2d and 6.2b show the width of reconstructed  $dE/dx$  (in the same order). Function able to qualitatively describe dependence of the parameters as a function of track momentum was empirically found to be given by Eq. (6.7):

$$g(p) = P_1 + P_2 \cdot \exp(-P_3 \cdot p) + P_4 \cdot \arctan(P_5 \cdot (p - P_6)) \quad (6.7)$$

This function was fitted to points corresponding to each particle type and fit result is shown in Fig. 6.2 with lines colored in accordance to markers. Values of parameters of above function are tabulated in Tab. 6.1.

PID	$\langle dE/dx \rangle_{\text{Bichsel}} - \langle dE/dx \rangle_{\text{MC}}$						$\sigma(dE/dx)_{\text{MC}}$					
	$P_1$	$P_2$	$P_3$	$P_4$	$P_5$	$P_6$	$P_1$	$P_2$	$P_3$	$P_4$	$P_5$	$P_6$
$\pi^\pm$	7.183e-8	-1.647e-4	41.68				0.0705			-1.42e-3	9.860	0.951
$K^\pm$	4.359e-8	-9.285e-6	7.697				0.0511	0.034	1.675	1.01e-2	4.934	0.528
$p, \bar{p}$	3.556e-8	-8.621e-6	3.980				0.0630	-7.725	27.17	3.37e-3	5.245	0.670
$e^\pm$	-6.219e-8	2.065e-7	3.241				0.0354	0.982	26.58	1.79e-2	41.515	0.095
$d, \bar{d}$	-1.305e-6	-5.268e-6	3.486				0.0967	-1526	18.75			

PID	$\langle dE/dx \rangle_{\text{Bichsel}} - \langle dE/dx \rangle_{\text{Data}}$						$\sigma(dE/dx)_{\text{Data}}$					
	$P_1$	$P_2$	$P_3$	$P_4$	$P_5$	$P_6$	$P_1$	$P_2$	$P_3$	$P_4$	$P_5$	$P_6$
$\pi^\pm$	-1.399e-8	2.012e-7	10.39				0.0734	1.907	31.86	-8.20e-4	22.788	0.653
$K^\pm$	2.325e-9	-3.690e-6	8.712				0.0808	-0.040	7.951	5.62e-3	-17.08	0.269
$p, \bar{p}$	-1.458e-7	0.6655	59.06	1.171e-7	4.660	0.644	0.0795	0.181	12.12			
$e^\pm$	9.005e-8	2.494e-7	8.834				0.0680	8.8e-4	1.549			
$d, \bar{d}$	-1.910e-7	5.637e-3	14.48				0.1161	-0.147	2.890			

(a)

(b)

Table 6.1: Parameters of functions from Fig. 6.2 describing reconstructed track  $dE/dx$  as a function of reconstructed momentum for a few particle species in the data (6.1b) and embedded MC (6.1a). Blank cells denote parameters equal 0. Units of parameters  $P_i$  are such that if one provides momentum in Eq. (6.7) in  $\text{GeV}/c$  the resultant offset of  $dE/dx$  MPV with respect to Bichsel parametrization is in  $\text{GeV}/\text{cm}$ , and the resultant  $\sigma$  parameter is unitless.

The correctness of the entire procedure described in this section was verified by comparing the reconstructed track  $dE/dx$  between the data and embedded MC without and with the  $dE/dx$  transformed using Eq. (6.3) and parameters from Tab. 6.1. Some difficulty arised in this comparison due to inconsistent relative content of different particle species in the data and embedded MC sample. Problem was ressolved by separating  $dE/dx$  histograms of different particle species in MC (in the same way as it was done for extraction of  $dE/dx$  MPV and  $\sigma$  for each particle ID) and fitting the sum of histograms from different particle types to the data histogram (in momentum bins). The only free parameters in the fit were relative contents of histogram from singe particle type in the data histogram. A sample comparison between the  $dE/dx$  in data and embedded MC is presented in Fig. 6.3. Comparison in all other momentum bins is contained in Appendix F (Fig. F.5). Fits were done for adjusted  $dE/dx$  (filled green). Histograms for unadjusted  $dE/dx$  (hashed red) were composed using the same relative content of particles as obtained from the fit of adjusted  $dE/dx$ . The ratio of the MC to the data shown in the lower pad of Fig. 6.3 and Fig. F.5 clearly demonstrates better agreement of the MC and the data in terms of position and width of peaks in  $dE/dx$  spectrum after the adjustment.

Exactly the same cross-check was done for  $n_X^\sigma$  variables, which are directly used to identify particles in our analyses. They carry information about the distance (in width units) of reconstructed  $dE/dx$  from the MPV of  $dE/dx$  according to Bichsel parametrization - they are kind of a pull variables. For every track  $n_X^\sigma$  was recalculated using its definition as shown in Eq. (6.8):

$$n_X^\sigma = \ln \left( \frac{dE/dx'}{\langle dE/dx \rangle_{\text{Bichsel}}^X} \right) / \delta(dE/dx), \quad (6.8)$$

where instead of original  $dE/dx$  the adjusted one ( $dE/dx'$ ) was used. Uncertainty of reconstructed  $dE/dx$ ,  $\delta(dE/dx)$ , was left unchanged. The sample comparison of  $n_{\text{pion}}^\sigma$ ,  $n_{\text{kaon}}^\sigma$  and  $n_{\text{proton}}^\sigma$  variables can be found in Fig. 6.4. Comparison in full set of momentum bins is placed in Appendix F. As in case of  $dE/dx$  comparison,

in the lower pads of Fig. 6.4 the ratio of the MC to the data also demonstrates better agreement of the MC and the data, which was the goal of the adjustment.

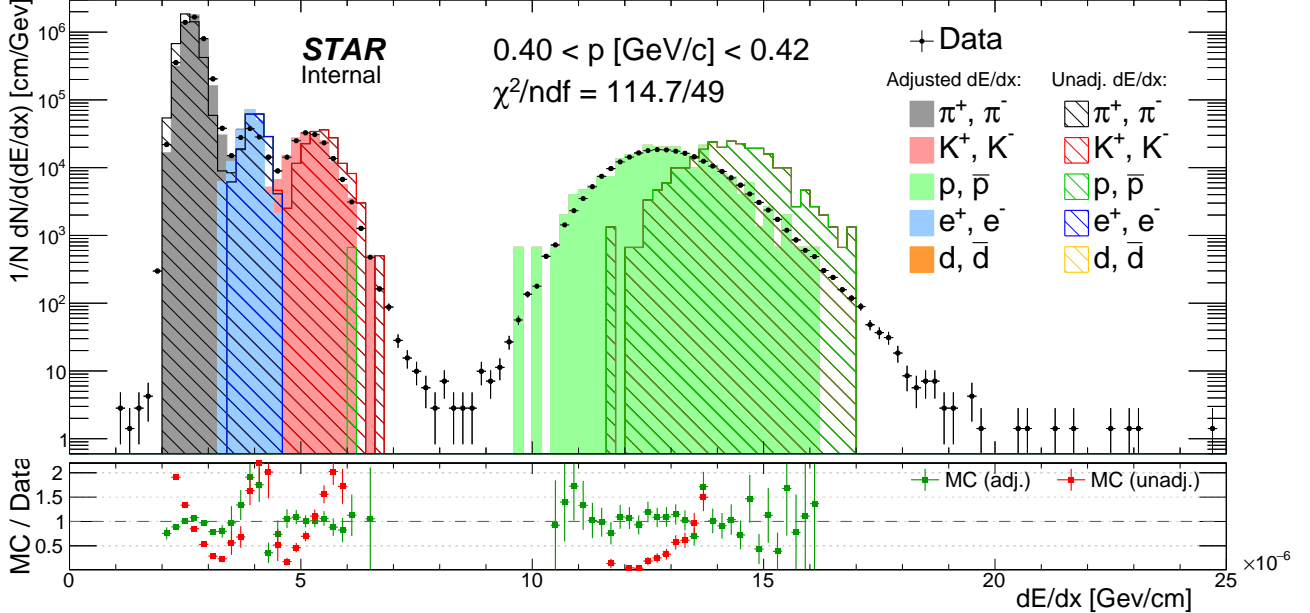


Figure 6.3: Sample comparison of  $dE/dx$  spectrum between data and embedded MC (before and after  $dE/dx$  adjustment) in a single momentum bin. Lower pad shows the ratio between embedded MC and data before and after  $dE/dx$  adjustment. In both upper and lower pads the same color code is used. Only statistical errors are shown. Due to limited statistics of embedded MC some data points do not have corresponding entries in MC.

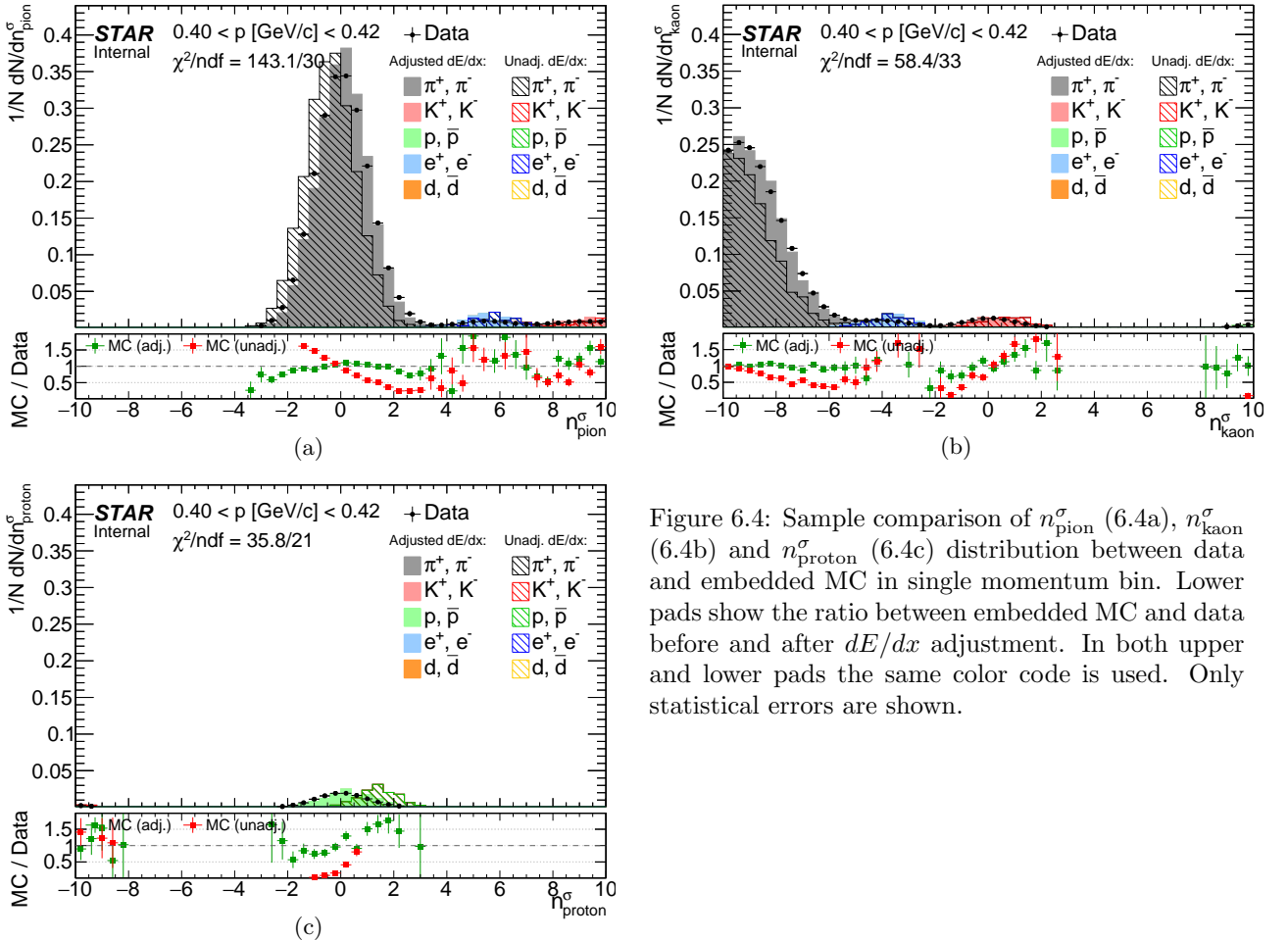


Figure 6.4: Sample comparison of  $n_{\text{pion}}^\sigma$  (6.4a),  $n_{\text{kaon}}^\sigma$  (6.4b) and  $n_{\text{proton}}^\sigma$  (6.4c) distribution between data and embedded MC in single momentum bin. Lower pads show the ratio between embedded MC and data before and after  $dE/dx$  adjustment. In both upper and lower pads the same color code is used. Only statistical errors are shown.

# 7. TPC track pointing resolution adjustment

It was found during the analysis that distributions of quantities which describe the pointing resolution of the TPC tracks do not agree well between the data and embedded MC. Namely, the resolutions of the global helices associated with the tracks were found to be significantly better in the STAR simulation than in the data, what manifests as narrower DCA and  $d_0$  distribution in the embedded MC, comparing to corresponding distribution in the data (Fig. 7.5). This issue was discussed under ticket #3332 (Ref. [26]).

This problem could affect the momentum resolution and thus all other resolutions and response matrices used in data unfolding. Therefore the resolution adjustment procedure was performed to find appropriate parameters of the “artificial” helix deterioration and finally obtain agreement between DCA and  $d_0$  distributions (and all related resolutions) in the data and embedded MC.

In order to reduce pointing resolution in the MC an additional smearing of the helix radius  $\sigma(R)$  was introduced. Based on  $d_0$  comparison in Fig. 7.5a it was decided to account also for the systematic bias of the helix radius  $\Delta\mu(R)$ <sup>1</sup>, which may be present e.g. due to differences in the material budget used the simulation and reconstruction. Both smearing and bias of the helix radius were introduced only for MC tracks which were matched with the true-level particles since only simulated tracks require adjustment (tracks from zero-bias event used in embedding already contain all detector effects).

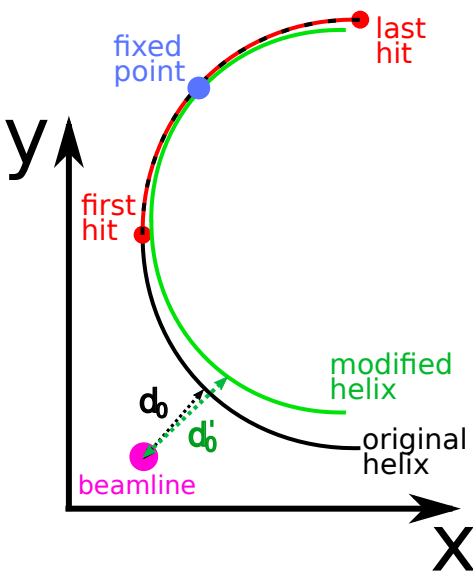


Figure 7.1: Sketch of helix modification procedure and  $d_0$  calculation.

Extraction of  $\Delta\mu(R)$  and  $\sigma(R)$  parameter required to achieve agreement of pointing resolution between embedded MC and the data involved a few steps, as listed below:

1. Series of  $d_0$  histograms in bins of  $p_T$  (100 MeV/c wide) was prepared, each for different size of distortion (different  $\Delta\mu(R)$  and  $\sigma(R)$ ) of global helix of the TPC tracks matched with true-level particles (example plot in single  $p_T$  bin is shown in Fig. 7.2):

- (a) for each set of parameters  $\Delta\mu(R)$  and  $\sigma(R)$  the helix radius  $R$  was recalculated independently for each track following the Eq. (7.1):

$$R' = R \times \mathcal{N}(1 + \Delta\mu(R), \sigma(R)), \quad (7.1)$$

- (b) new helix of a radius  $R'$  was assigned to a track and used to calculate  $d_0$ . The modified helix was obtained by changing the radius of original helix from  $R$  to  $R'$  with a fixed middle point between the first and last TPC hit of a global track represented by the helix (Fig. 7.1). The momentum of the track was also recalculated:

$$p'_T = p_T \times \frac{R'}{R}, \quad \eta' = \eta \times \frac{R'}{R}. \quad (7.2)$$

2. In each  $p_T$  bin the  $\chi^2/\text{NDF}$  was calculated between the data and MC  $d_0$  histogram in a range  $-1.5 \text{ cm} < d_0 < 1.5 \text{ cm}$  (corresponding to  $d_0$  cut used in analyses), for every point in parameter space of radius distortion (for every set of  $\Delta\mu(R)$  and  $\sigma(R)$ ). An example (single  $p_T$  bin) of map of  $-\chi^2/\text{NDF}$  in a parameter space is presented in Fig 7.3.
3. In each bin of recalculated  $p_T$  the 2-dim parabola  $z(x, y; a, b, x_0, y_0, z_0)$  given in Eq. (7.3) ( $z = \chi^2/\text{NDF}$ ,  $x = \Delta\mu(R)$ ,  $y = \sigma(R)$ ) was fitted to  $-\chi^2/\text{NDF}$  in the global minimum region to obtain the best-fit distortion parameters.

$$z = z_0 - a(x - x_0)^2 - b(y - y_0)^2. \quad (7.3)$$

4. The best-fit smearing  $\sigma(R)$  (equal to parabola parameter  $y_0$ ) and best-fit bias  $\Delta\mu(R)$  ( $x_0$ ) from individual  $p_T$  bins was plotted as a function of global track  $p_T$  (Fig. 7.4). Each point was assigned with an error being a quadratic sum of two components: the error on  $x_0$  ( $y_0$ ) resulting from the parabola fit to  $-\chi^2/\text{NDF}$ , and length of corresponding semi-axis of ellipsis formed by the intersection of fitted parabola with the  $xy$ -plane at  $z = z_0 - 1/\text{NDF}$  (from definition of the parameter uncertainty given by the change of overall  $\chi^2$  by 1 unit). Resultant formulae for the error of each individual point in Fig. 7.4 are

<sup>1</sup>Transverse impact parameter  $d_0$  takes positive value if the beamline is contained inside the helix (in the  $yz$ -plane projection), otherwise it is negative. Any asymmetry in the  $d_0$  distribution in the MC with respect to the data indicates presence of systematic difference in reconstructed  $d_0$ , hence also in reconstructed  $R$ .

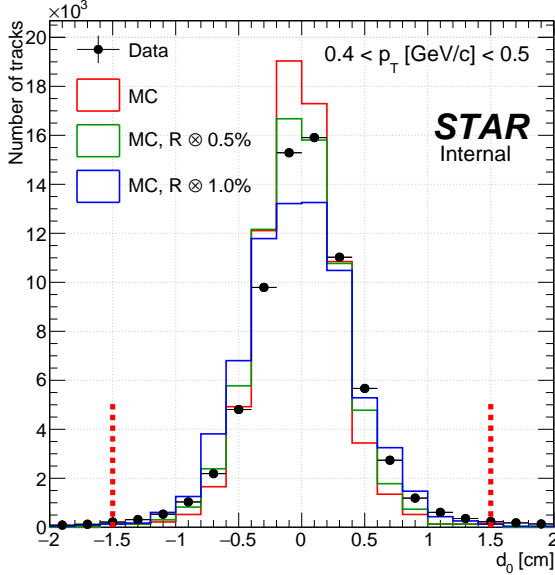


Figure 7.2: Example of comparison of  $d_0$  histograms in single  $p_T$  bin in the data (black points) and embedded MC (colored lines) in the procedure of TPC pointing resolution adjustment. Only MC histograms for  $\Delta\mu(R) = 0$  and  $\sigma(R) = 0, 5 \times 10^{-3}$  and  $10^{-2}$  were shown for explanatory purposes.

$$\delta(\Delta\mu(R)) = \sqrt{\delta_{\text{fit}}^2(x_0) + \frac{1}{2a\text{NDF}}}, \quad (7.4)$$

From Fig. 7.2 one can read that  $\text{NDF} = 14$ . In calculation of uncertainties correlation of  $\Delta\mu(R)$  and  $\sigma(R)$  have not been accounted.

5. The empirically determined functions were fitted to points representing  $\Delta\mu(R)$  and  $\sigma(R)$  dependence on the global track  $p_T$ . Their form and values of parameters are given in Fig. 7.4.

Helices of global TPC tracks were deteriorated according to Eq. (7.1) and the parametrizations of global track  $p_T$ -dependence of  $\Delta\mu(R)$  and  $\sigma(R)$  from Fig. 7.4, to verify if better agreement between the data and embedded MC is found after the adjustment. Filled histograms in Fig. 7.5 show  $d_0$  and DCA distributions after the described adjustment, and filled circles in the bottom pad show their ratio to the data points. Clearly, there is much better agreement between embedded MC and the data after the pointing resolution adjustment. Remaining differences may arise from incomplete theoretical model of the CEP process implemented in GenEx leading to different  $p_T$  spectra of the data and the model (e.g. model does not contain resonant  $\pi^+\pi^-$  production).

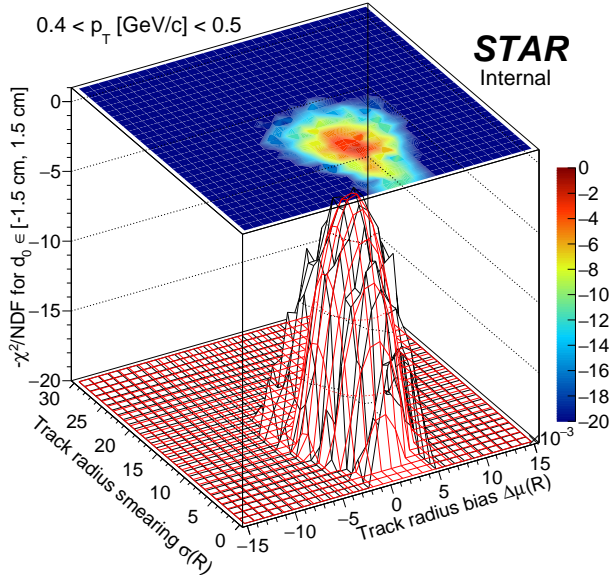


Figure 7.3: Example of  $-\chi^2/\text{NDF}$  map in a parameter space in the procedure of TPC pointing resolution adjustment. The red surface represents parabola fitted in the vicinity of the global minimum.

$$\delta(\sigma(R)) = \sqrt{\delta_{\text{fit}}^2(y_0) + \frac{1}{2b\text{NDF}}}. \quad (7.5)$$

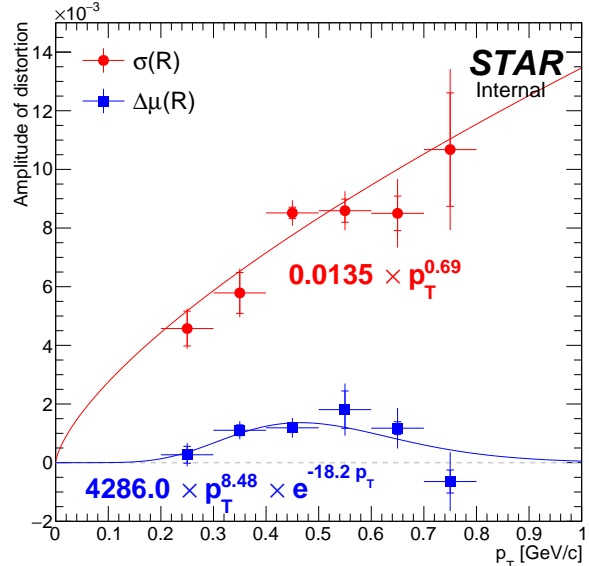
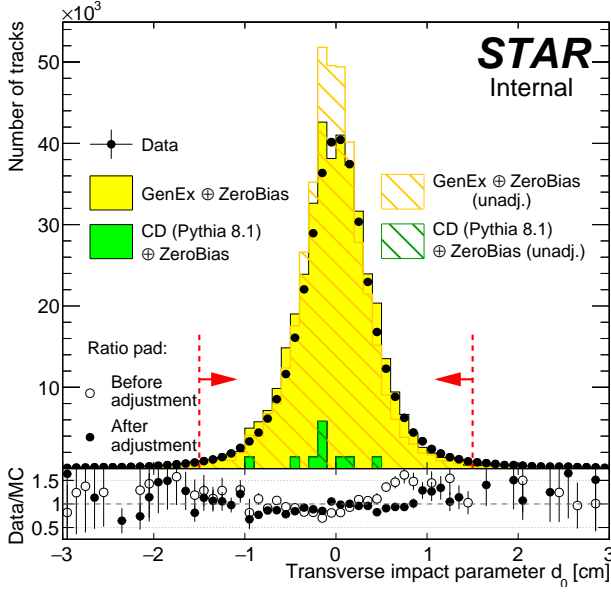
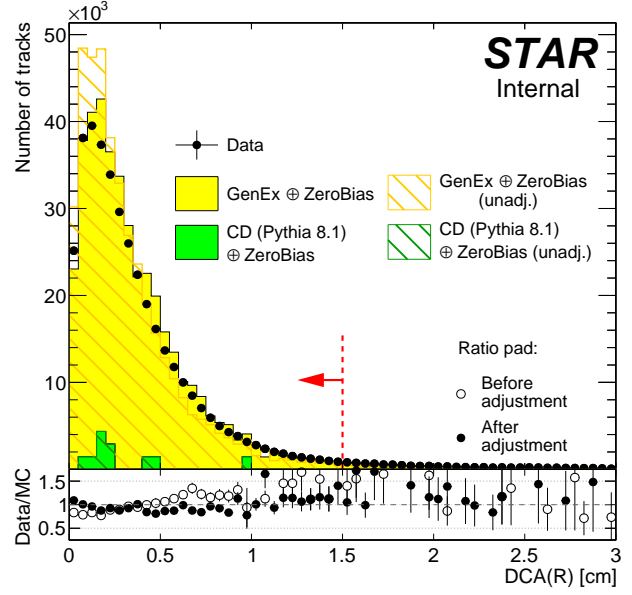


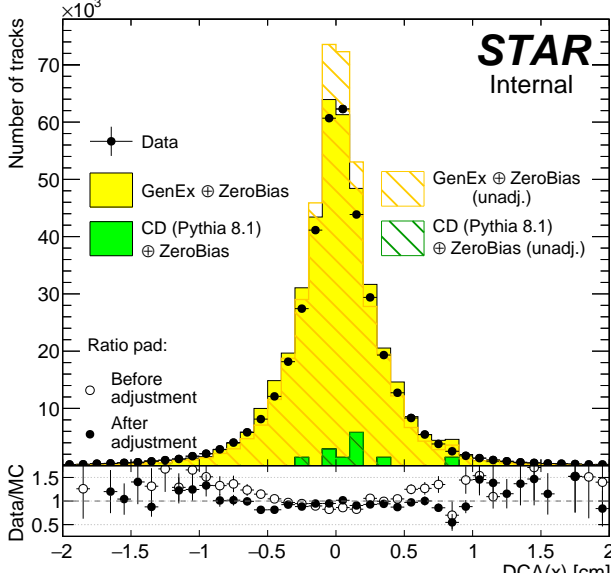
Figure 7.4: Best-fit parameters obtained in the procedure of the TPC track pointing resolution adjustment. Uncertainties on parameters resulting solely from the fit of Eq. (7.3) to  $-\chi^2/\text{NDF}$  are represented by the lines with perpendicular endings. Total uncertainties (Eqs. (7.4), (7.5)) extend beyond. The empirical functions fitted to points are drawn with corresponding colors, and formula of each is written aside.



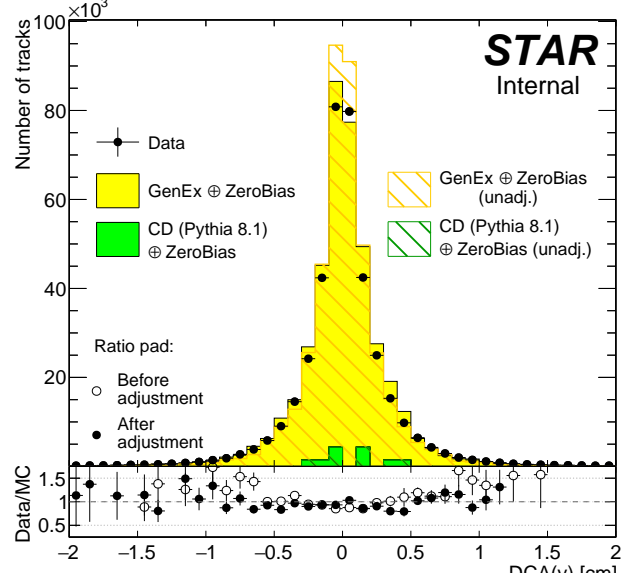
(a)



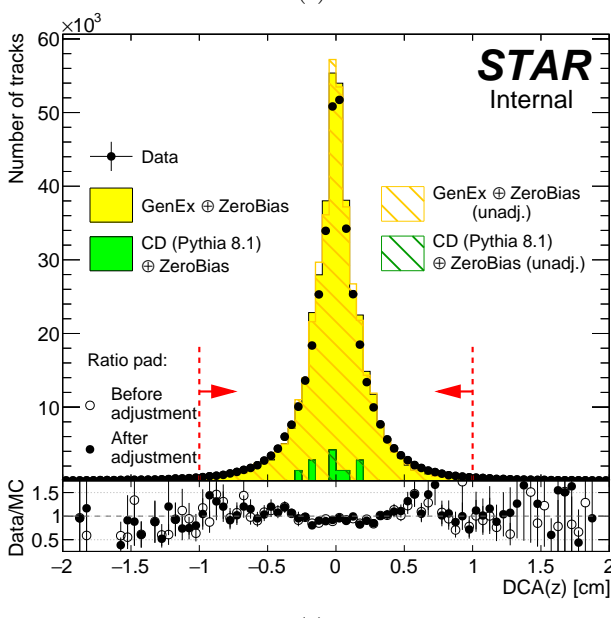
(b)



(c)



(d)



(e)

Figure 7.5: Comparison of distribution of pion transverse impact parameter  $d_0$  (7.5a) and transverse (7.5b),  $x$ - (7.5c),  $y$ - (7.5d) and  $z$ -component (7.5e) of the DCA vector between the global helix and primary vertex in the data (CEP) and embedded MC (GenEx). Distributions for unadjusted helices are drawn as hashed histograms, while filled histograms are for adjusted helices. Normalizations of the signal and backgrounds were established from the comparison of  $p_T^{\text{miss}}$  and  $\Delta\theta$  distributions after full selection (without cut on the presented quantity and without exclusivity cut), as described in Sec. XXX of Ref. [1]. Red dashed lines and red arrows indicate the range of each quantity which is accepted in analyses.

# 8. Dead material in front of TPC

Particle detected and reconstructed in the TPC must first pass through the detector material standing in between the accelerator vacuum and TPC gas. This affects track reconstruction efficiency, as the particle may interact with that material - in worst case inelastically, and induce secondary particles thus lower reconstruction efficiency. Accuracy of modeling of the detector material in the STAR simulation, especially in run 15 with the HFT installed, influences systematic error e.g. on the TPC track reconstruction efficiency. In this section the density of secondary vertices is compared between the data and embedded MC. The density of secondary vertices is directly proportional to the amount of the material in given volume, hence any discrepancy between secondary vertex distribution in the data and MC can be a hint for inaccuracies of the STAR simulation which should be accordingly covered by the systematic uncertainties. It should be stressed that this analysis is not aimed to tune the material budget in the STAR simulation, as there are much better data for this than high-luminosity proton-proton collisions from run 15. The aim of presented study is to obtain reasonable estimate of the component of systematic uncertainty of the TPC track reconstruction efficiency related to the error on the amount and distribution of simulated material.

Analysis of the distribution of secondary vertices was performed using both zero-bias (ZB) data and minimum-bias MC (Pythia) embedded into zero-bias triggers. Because of insufficient statistics of the ZB data, for the purpose of analysis presented in this section both standard ZB data sample (from ZB triggers in st\_rp stream) and the subsample of RP\_CP triggers (see Ref. [7] for trigger details) with identified elastic proton-proton scat-

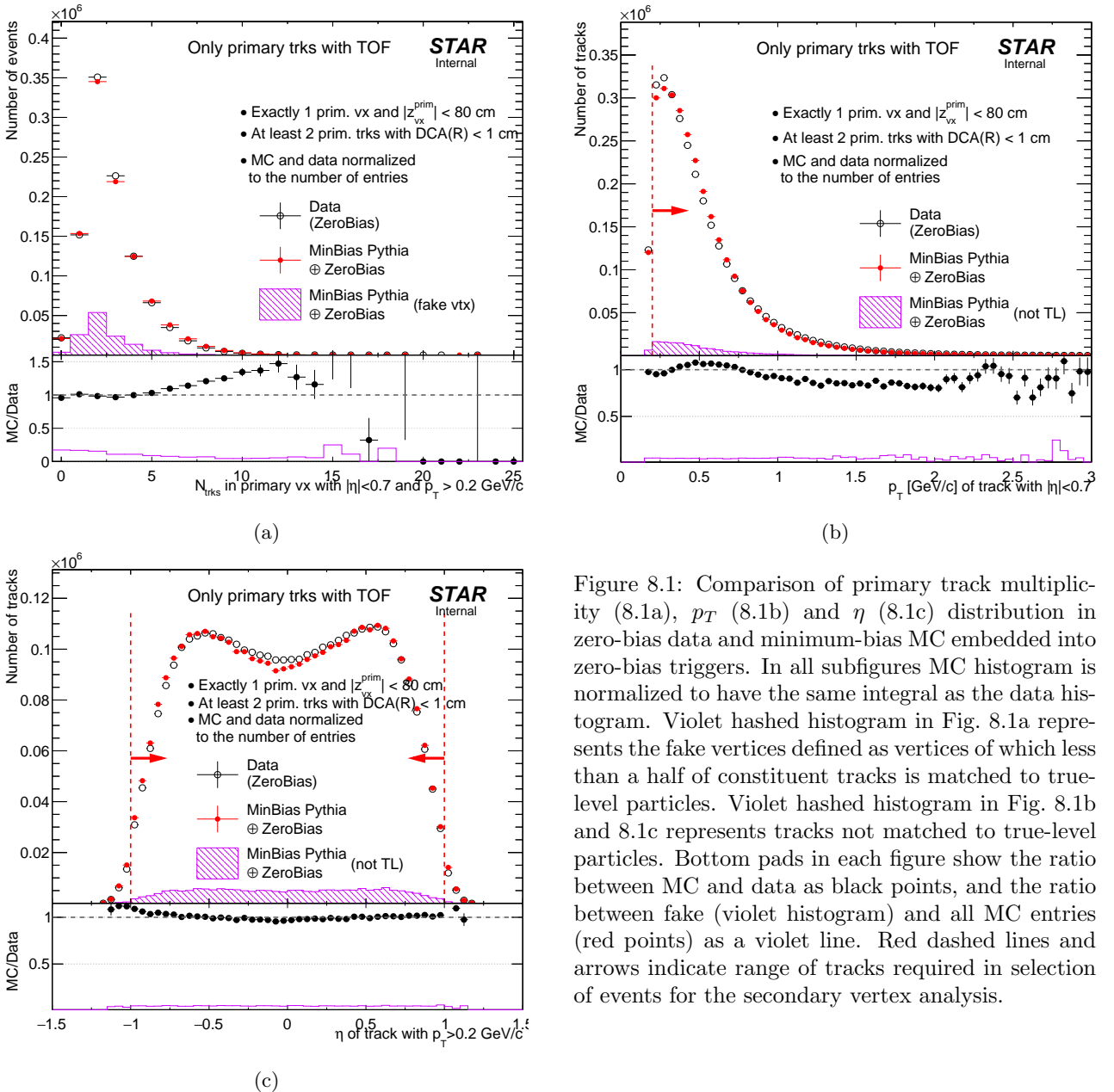


Figure 8.1: Comparison of primary track multiplicity (8.1a),  $p_T$  (8.1b) and  $\eta$  (8.1c) distribution in zero-bias data and minimum-bias MC embedded into zero-bias triggers. In all subfigures MC histogram is normalized to have the same integral as the data histogram. Violet hashed histogram in Fig. 8.1a represents the fake vertices defined as vertices of which less than a half of constituent tracks is matched to true-level particles. Violet hashed histogram in Fig. 8.1b and 8.1c represents tracks not matched to true-level particles. Bottom pads in each figure show the ratio between MC and data as black points, and the ratio between fake (violet histogram) and all MC entries (red points) as a violet line. Red dashed lines and arrows indicate range of tracks required in selection of events for the secondary vertex analysis.

tering events using loose RP track selection were used. The latter subsample is in good approximation a ZB sample in terms of central detector, as it was triggered only by the east and west coincidence of Roman Pots - any particles present in the TPC and TOF must be product of pile-up interaction. In all plots and later in the text we refer to this merged sample as ZB data sample.

Analysis started with the following selection of events:

1. Exactly 1 reconstructed primary vertex (with tracks matched to hits in TOF),
2.  $|z_{vx}| < 80$  cm,
3.  $\geq 2$  prim. TOF tracks with:  $DCA(R) < 1$  cm,  $|\eta| < 1$ ,  $p_T > 0.2$  GeV/c,  $N_{\text{hits}}^{\text{fit}} \geq 25$ ,  $N_{\text{hits}}^{\text{dE/dx}} \geq 15$ ,  $N_{\text{hits}}^{\text{fit}}/N_{\text{hits}}^{\text{poss}} \geq 0.52$ .

The aim of above criteria was to select pile-up-free events with well defined vertex. Cut on  $z$ -vertex is identical to one used in physics analyses. Figure 8.1 shows comparison of quantities characterizing an event. In general a moderate agreement between MC and data can be observed, considered sufficient for trustworthy result of described analysis.

As a next step the TPC tracks were selected for the search and reconstruction of secondary vertices. The requirements were as follows:

1. Global TPC tracks matched with TOF not associated with any primary TPC track,
2.  $|\eta| < 0.7$ ,  $p_T > 0.2$  GeV/c,  $N_{\text{hits}}^{\text{fit}} \geq 25$ ,  $N_{\text{hits}}^{\text{dE/dx}} \geq 15$ ,  $N_{\text{hits}}^{\text{fit}}/N_{\text{hits}}^{\text{poss}} \geq 0.52$ ,
3. Distance of closest approach to the STAR  $z$ -axis ( $x, y = (0, 0)$ ,  $d_0^{(0,0)}$ , larger than inner radius of the beampipe:  $d_0^{(0,0)} > 2$  cm.

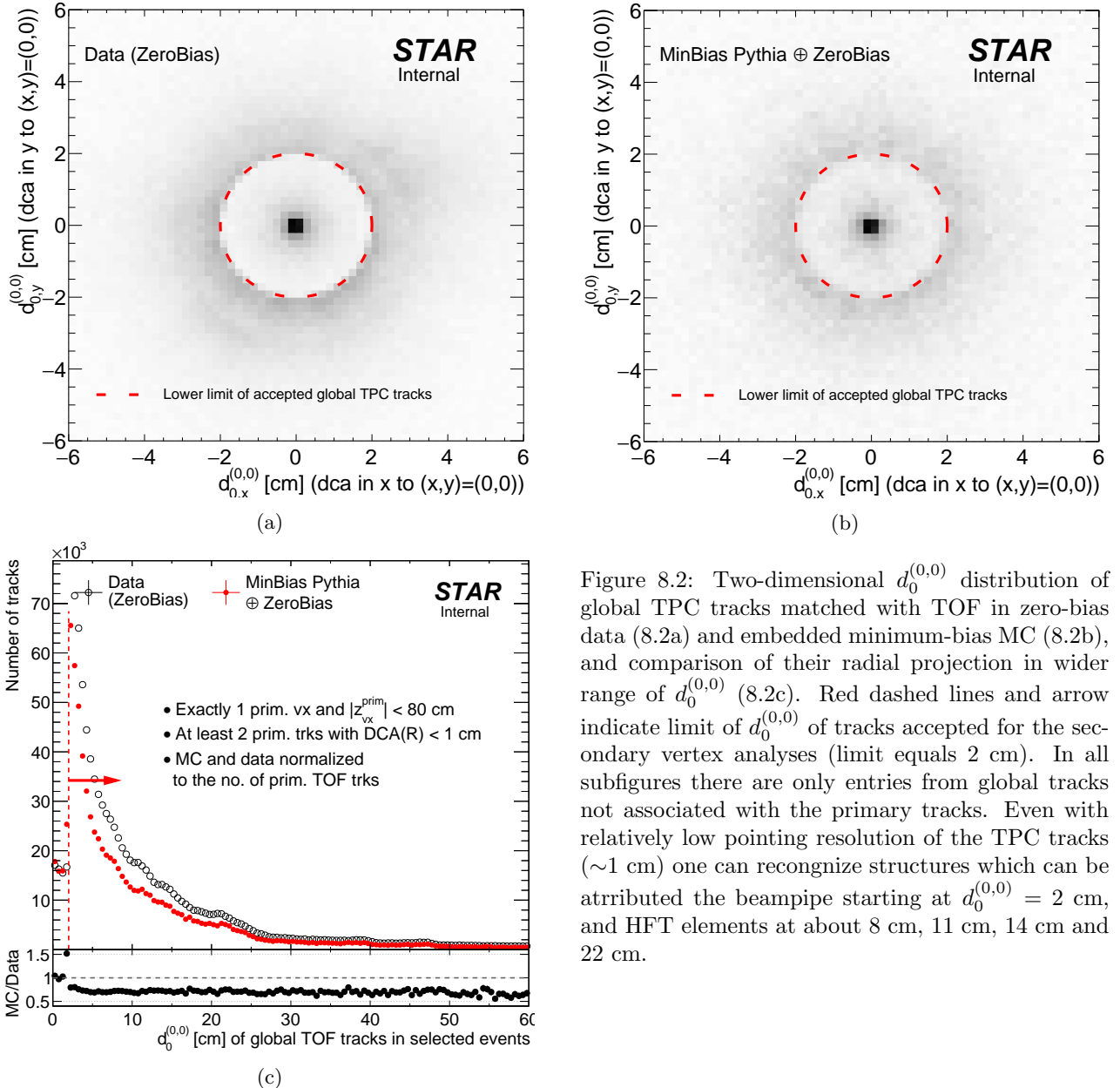


Figure 8.2: Two-dimensional  $d_0^{(0,0)}$  distribution of global TPC tracks matched with TOF in zero-bias data (8.2a) and embedded minimum-bias MC (8.2b), and comparison of their radial projection in wider range of  $d_0^{(0,0)}$  (8.2c). Red dashed lines and arrow indicate limit of  $d_0^{(0,0)}$  of tracks accepted for the secondary vertex analyses (limit equals 2 cm). In all subfigures there are only entries from global tracks not associated with the primary tracks. Even with relatively low pointing resolution of the TPC tracks ( $\sim 1$  cm) one can recognize structures which can be attributed the beampipe starting at  $d_0^{(0,0)} = 2$  cm, and HFT elements at about 8 cm, 11 cm, 14 cm and 22 cm.

These cuts were intended to select in-time TPC tracks with high chance of being a product of secondary interaction of primary particle with the detector material. The higher limit of accepted  $d_0^{(0,0)}$  was set in analysis, the less background was found in the secondary vertex distribution for a price of limited access to secondary vertices of low radial distance from STAR  $z$ -axis. Cut of 2 cm was found a good compromise. In Fig. 8.2 we present comparison of  $d_0^{(0,0)}$  distribution of selected global TOF-matched TPC tracks in the data and embedded MC (without cut on  $d_0^{(0,0)}$ ). To some extent this distribution reflects the material density (secondary vertex density) in the radial direction, therefore we present it with the MC distribution normalized to the same total number of primary tracks as in the data. Number of secondary vertices is proportional to the number of primary particles, so we use such normalization to allow direct comparison of the distributions:

$$\text{MC normalization factor} = \frac{\langle N_{\text{trks/evt}}^{\text{DATA}} \rangle \times N_{\text{evts}}^{\text{DATA}}}{\langle N_{\text{trks/evt}}^{\text{MC}} \rangle \times N_{\text{evts}}^{\text{MC}}} = \frac{N_{\text{trks}}^{\text{DATA}}}{N_{\text{trks}}^{\text{MC}}} \quad (8.1)$$

Especially in Fig. 8.2c one can find structures/peaks that might be attributed to subdetectors (PXL, IST, SST) of the HFT. Notable is different yield of histograms which could indicate different amount of simulated dead material with respect to real conditions. The reason of this inconsistency was found in imperfect simulation of the pointing resolution of the TPC tracks - because the resolution is higher in the simulation, more true primary tracks are reconstructed as primary tracks hence less such tracks are accepted in the global track selection (comparing to data). This effect is accounted later in the background subtraction procedure.

After secondary track candidates were selected, the described algorithm for secondary vertex reconstruction was used:

1. Loop over all pairs of secondary track candidates, store pairs whose DCA is less than 0.5 cm (nearby tracks passing a proximity cut),
2. Link pairs of nearby tracks into sets of tracks connected by the common nearby tracks,
3. Loop over all sets defined in 2., in each set loop over all pairs from given set, reject worst-matching tracks (these with largest DCA to others) until all pairs of tracks have DCA less than 0.5 cm,
4. Based on number of tracks in secondary vertex, total charge, specific energy loss,  $dE/dx$ , cosine of the opening angle of two tracks  $\cos(\theta)$  and invariant mass of two tracks  $m_{\text{inv}}$  determine if the vertex is from resonance decay or photoconversion (see Ref. [27]); if none of the two then assume hadronic vertex,
5. Calculate the vertex position as the average DCA point of all track pairs in the vertex.

As a result secondary vertices were reconstructed, whose multiplicity distribution is depicted in Fig. 8.3. Analysis was continued only with vertices of multiplicity equal 2. The first reason was that most of vertices consist of just a pair of tracks. Another reason was the background subtraction method developed only for vertices made of two tracks. In addition to this, only vertices representing primary particles in the pseudorapidity range  $-0.7 < \eta < 0.7$  were analyzed. To enable such selection a variable  $\eta_{\text{vtx}}$  was defined, as shown in Fig. 8.4.

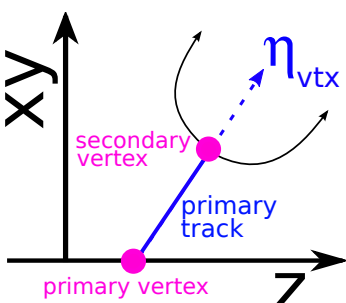


Figure 8.4:  $\eta_{\text{vtx}}$  definition (sketch).

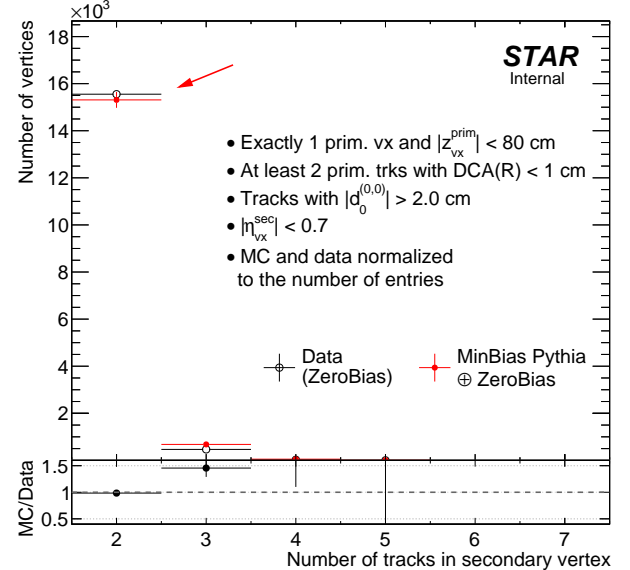


Figure 8.3: Multiplicity of tracks in reconstructed secondary vertices. Red arrow points to bin with vertices used in final analyses of vertex distribution.

Raw distributions of  $R_{\text{vtx}}^{\text{secondary}}$  and  $z_{\text{vtx}}^{\text{secondary}}$  are shown in Fig. 8.5a and Fig. 8.5b, respectively. In  $R_{\text{vtx}}^{\text{secondary}}$  spectrum one can find peaks in the regions where the HFT subdetectors are placed. Peaks seem to lie on top of a tail whose origin has been identified with the secondary vertices made of pairs containing true primary tracks which were not associated with any primary vertex and unfortunately passed selection of global tracks for the secondary vertex reconstruction. Without this background subtracted, the ratio of MC to data varies mostly between 0.5 and 0.7. For this reason a method of estimation of the background was invented, as described in the next paragraph.

Background estimation makes use of different content of fake secondary vertices depending on the proximity cut used in the secondary vertex reconstruction. Figure 8.6 shows the percentage of background (fake pairs) distributed over the distance of closest approach between two tracks. A comment needs to be

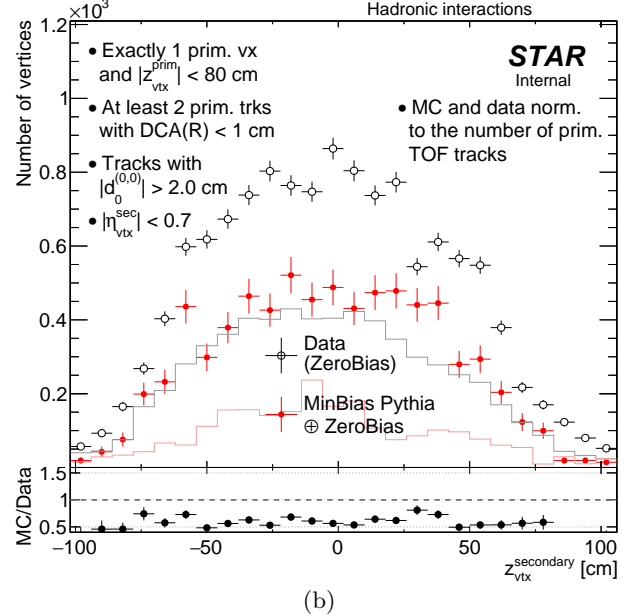
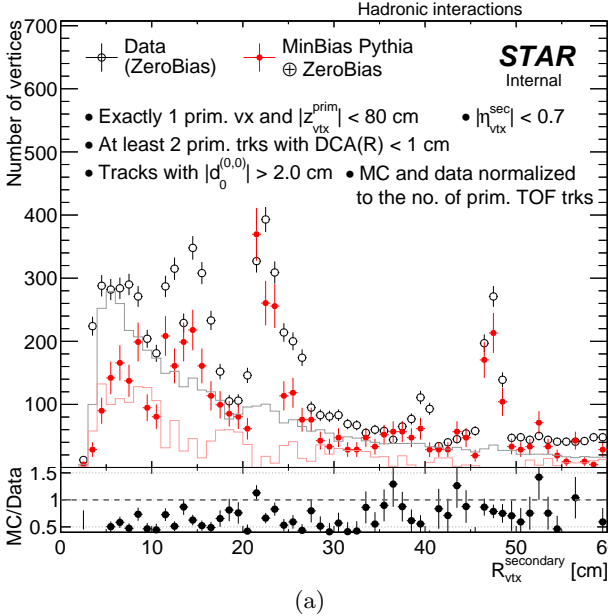


Figure 8.5: Comparison of raw  $R_{vtx}^{\text{secondary}}$  (8.5a) and  $z_{vtx}^{\text{secondary}}$  (8.5b) distribution in the data (opened black circles) and embedded MC (filled red circles). Only vertices recognized as products of hadronic interactions are shown in the figure. Solid lines denote estimated background content in the distribution of corresponding color.

made that the agreement of the shape of the tails in data and MC distributions was achieved only after the adjustment of the TPC resolution in MC, as described in Sec. 7. This agreement allows to believe in proper description of the data by MC in terms of background distribution over DCA of two global tracks, which is used in the background estimation.

It agrees with intuition that the most optimal cut to select pairs from the secondary vertices is as low as about 0.5 cm, however one can select sample with slightly different ratio of signal to background if the proximity cut is changed to accept tracks of DCA within some higher limits. In Fig. 8.6 the nominal proximity cut is

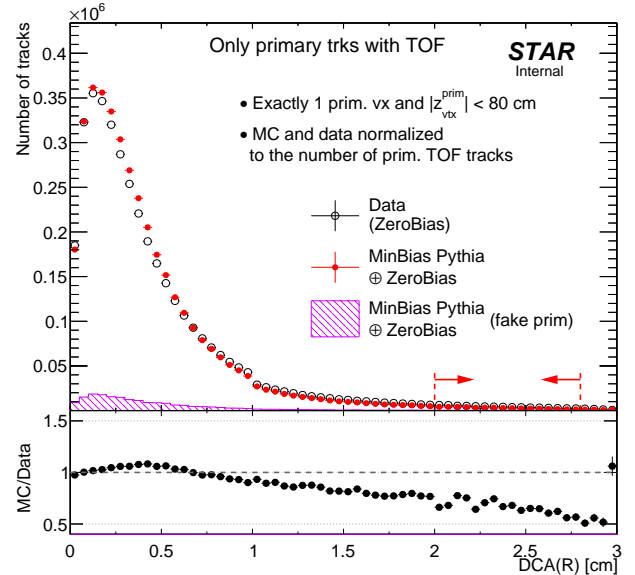
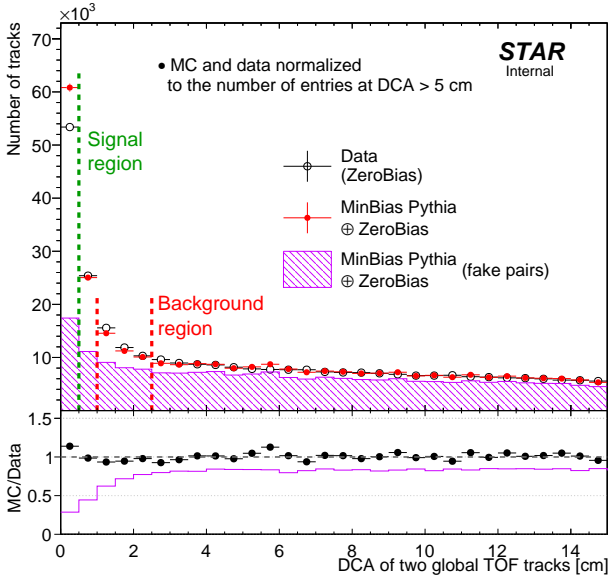


Figure 8.6: Comparison of DCA between all pairs of secondary track candidates selected for the secondary vertex reconstruction in the data and embedded MC. MC histogram is normalized to the data at  $\text{DCA} > 5 \text{ cm}$ . Violet hashed histogram depicts pairs contained in MC histogram and not originating from the same vertex. Solid violet line in the lower pad denotes ratio of violet and red histogram.

Figure 8.7: Comparison of radial DCA of all primary tracks matched with TOF and passing quality criteria in events selected for secondary vertex analysis, between the data and embedded MC. Violet hashed histogram represents tracks not matched to true-level particles. Red dashed lines and arrows limit region used to find normalization that compensates different background yield in reconstructed secondary vertex distributions in data and embedded MC.

marked with the green line (signal region), while the modified proximity cut is marked with red lines (background region). With such two versions of cuts used in vertexing the two independent distributions of secondary vertices can be obtained: one with the standard proximity cut -  $\mathcal{H}_1$ , the other with modified proximity cut, in our case  $1.0 \text{ cm} < \text{DCA} < 2.5 \text{ cm}$  -  $\mathcal{H}_2$ . Limits in modified proximity cut were set to such values in order to ensure enough statistics as well as provide satisfactory resolution of secondary vertex position calculated as a middle point between DCA points on helices associated with the tracks. One can note that the content of histograms can be described by the set of equations given below:

$$\left\{ \begin{array}{l} \mathcal{H}_1 = (1 - B) \times \text{signal} + B \times \text{background}, \\ \mathcal{H}_2 = (1 - B') \times \text{signal} + B' \times \text{background}, \end{array} \right. \quad (8.2)$$

$$\left\{ \begin{array}{l} \text{signal} = \frac{B' \times \mathcal{H}_1 - B \times \mathcal{H}_2}{B' - B} \\ \text{background} = \frac{(1 - B) \times \mathcal{H}_2 - (1 - B') \times \mathcal{H}_1}{B' - B} \end{array} \right. \quad (8.4)$$

in which parameters  $B$  and  $B'$  denote the background fraction in the distribution resultant from analysis utilizing nominal and modified proximity cut, respectively. The solution to set of Eqs. (8.2), (8.3) is the following:

$$\left\{ \begin{array}{l} \text{signal} = \frac{B' \times \mathcal{H}_1 - B \times \mathcal{H}_2}{B' - B} \\ \text{background} = \frac{(1 - B) \times \mathcal{H}_2 - (1 - B') \times \mathcal{H}_1}{B' - B} \end{array} \right. \quad (8.5)$$

An important remark here is that the background fraction extracted from the ratio of violet and red histograms in Fig. 8.6 can be used directly in Eqs. (8.2)-(8.5) only for background estimation in MC. In case of background estimation in data parameters  $B$  and  $B'$  have to be corrected for the leakage of true primary tracks to set of selected secondary track candidates, as it was described in one of preceding paragraphs. The correction factor  $\kappa$  is extracted from the ratio of the radial DCA of the primary TPC tracks in events selected for the secondary vertex study (Fig. 8.7). Histogram range selected for calculation of the ratio was set to  $2.0 \text{ cm} < \text{DCA}(R) < 2.6 \text{ cm}$ , as this range coincides with the  $d_0^{(0,0)}$  of global tracks accepted for the analysis.  $\kappa$  calculated in this range equals 1.48. Variation of value of  $\kappa$  with changed limits of  $\text{DCA}(R)$  selected for the ratio calculation do not influence significantly the final result. The correction is done by multiplying fraction  $B$  and  $B'$  by  $\kappa$  only when estimating the background in the data.

Background determined with the described method is shown in Fig. 8.1 with the solid lines colored according to corresponding markers. This background was subtracted and final, background-free distributions of the secondary vertex positions in the transverse and longitudinal direction are presented in Fig. 8.8. Most relevant region - the HFT detector extending between  $\sim 2 \text{ cm}$  and  $\sim 30 \text{ cm}$  is satisfactorily well described by MC. Also, the inner wall of the TPC at  $\sim 48 \text{ cm}$  well matches between data and MC.

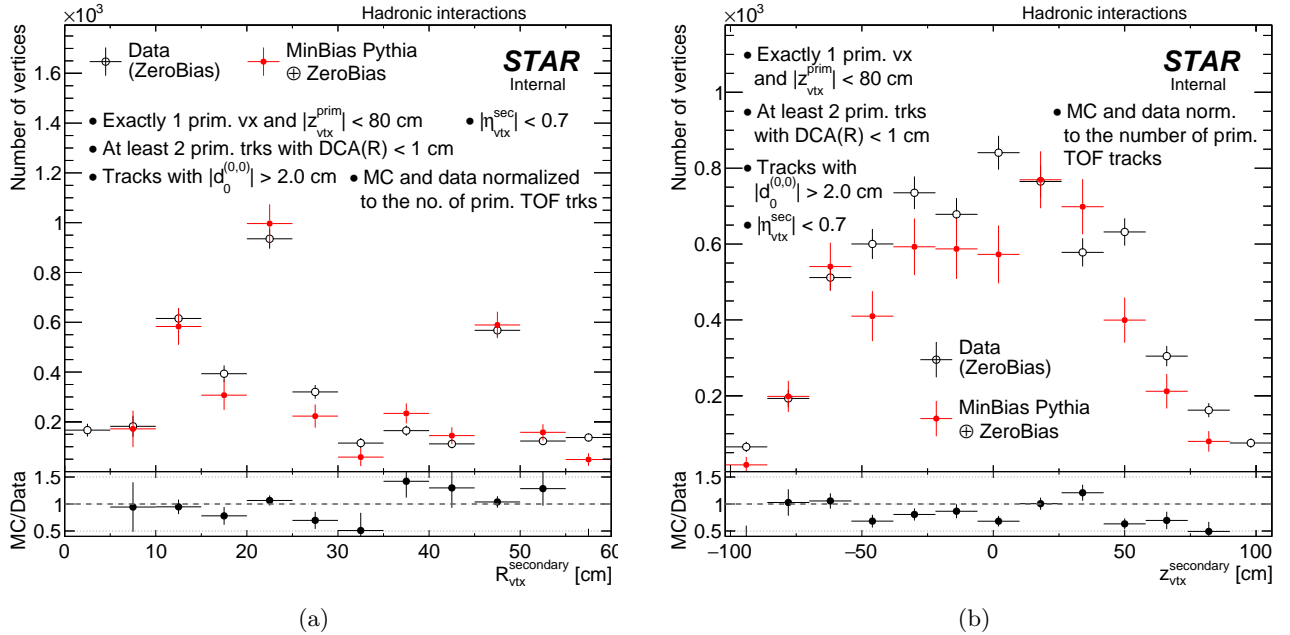


Figure 8.8: Comparison of background-subtracted  $R_{\text{vtx}}^{\text{secondary}}$  (8.8a) and  $z_{\text{vtx}}^{\text{secondary}}$  (8.8b) distribution in the data (open black circles) and embedded MC (filled red circles). Only vertices recognized as products of hadronic interactions are shown in the figure.

# 9. Systematic errors

## 9.1 TPC track reconstruction efficiency

### 9.1.1 Embedding (pile-up) effect

One major difference between simulation and real data is the presence of pile-up events. The average number of pile-up tracks in a triggering event is proportional to the BBC coincidence rate. It is expected that the difference between simulation and real data drops at lower BBC rates, and the effects of pile-up tracks could be much reduced by fitting the tracking efficiency as a function of BBC rate and using the extrapolated value at zero luminosity to compare with simulation.

The embedded MC was divided into two samples due to mean BBC\_AND rate:  $\langle \text{BBC\_AND} \rangle = 700 \text{ kHz}$  and  $\langle \text{BBC\_AND} \rangle = 1400 \text{ kHz}$ . Next, the track reconstruction efficiency was calculated for those two samples and no-pile-up MC corresponding to them. The difference between TPC track reconstruction efficiencies for pile-up and no-pile-up MCs was calculated as:

$$\Delta\epsilon_{TPC}^{1400/700 \text{ kHz}} = \frac{N_{reco}^{\text{no-pile-up}} - N_{reco}^{\text{pile-up}}}{N_{gen}} \quad (9.1)$$

where:

$N_{gen}$ -number of MC tracks,

$N_{reco}^{\text{no-pile-up}}$  - number of reconstructed tracks, matched with MC tracks in no-pile-up MC,

$N_{reco}^{\text{pile-up}}$  - number of reconstructed tracks, matched with MC tracks in pile-up MC.

The difference between high and low pile-up runs is given by:

$$\Delta\epsilon_{TPC} = \Delta\epsilon_{TPC}^{1400 \text{ kHz}} - 2 \cdot \Delta\epsilon_{TPC}^{700 \text{ kHz}} \quad (9.2)$$

Finally, above difference, shown in Figs. 9.2 and 9.3 for  $\pi^\pm$ , varies between 2 – 3% and was taken as systematic uncertainty related to TPC track reconstruction efficiency.

Figure 9.2:  $\pi^\pm$  TPC track reconstruction efficiency as a function of  $p_T$  ( $|\eta| < 0.7$ ,  $|V_z| < 80 \text{ cm}$ ) for embedded MC samples with  $\langle \text{BBC\_AND} \rangle = 700 \text{ kHz}$  and  $\langle \text{BBC\_AND} \rangle = 1400 \text{ kHz}$ . The efficiencies from corresponding no-pile-up MC samples were also shown. Additionally, the differences from Eq. 9.2 were drawn in the bottom of each plot.

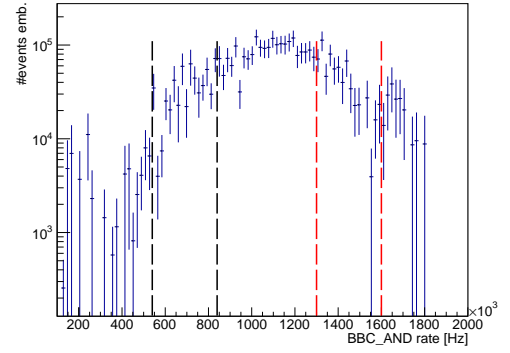
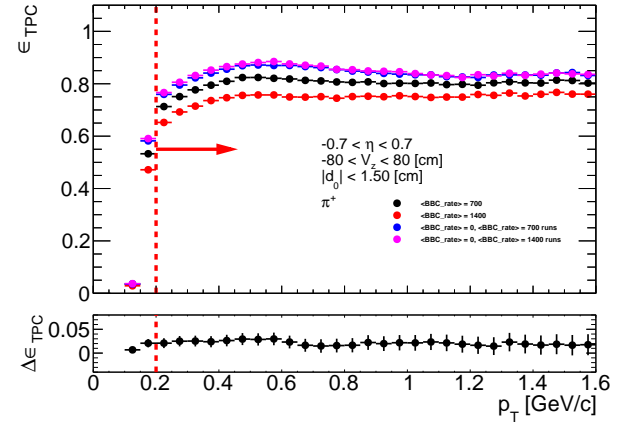
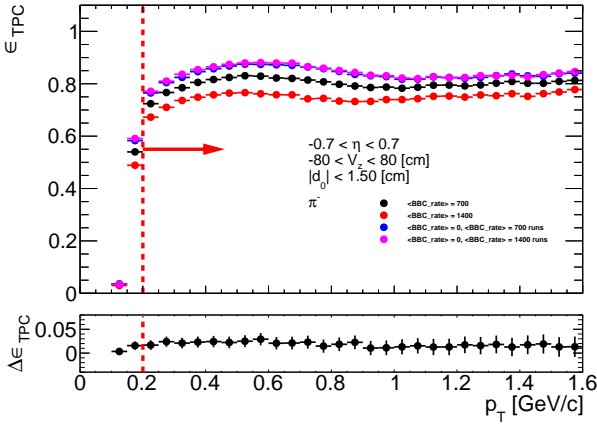
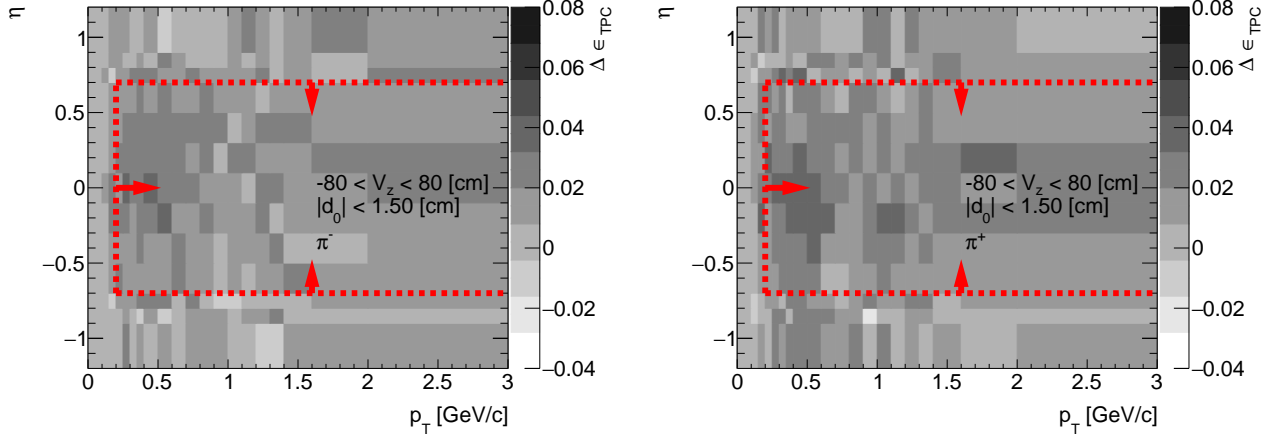


Figure 9.1: Number of events in embedded MC as a function of BBC\_AND rate. The black and red lines represent the events with  $\langle \text{BBC\_AND} \rangle = 700 \text{ kHz}$  and  $\langle \text{BBC\_AND} \rangle = 1400 \text{ kHz}$ , respectively.

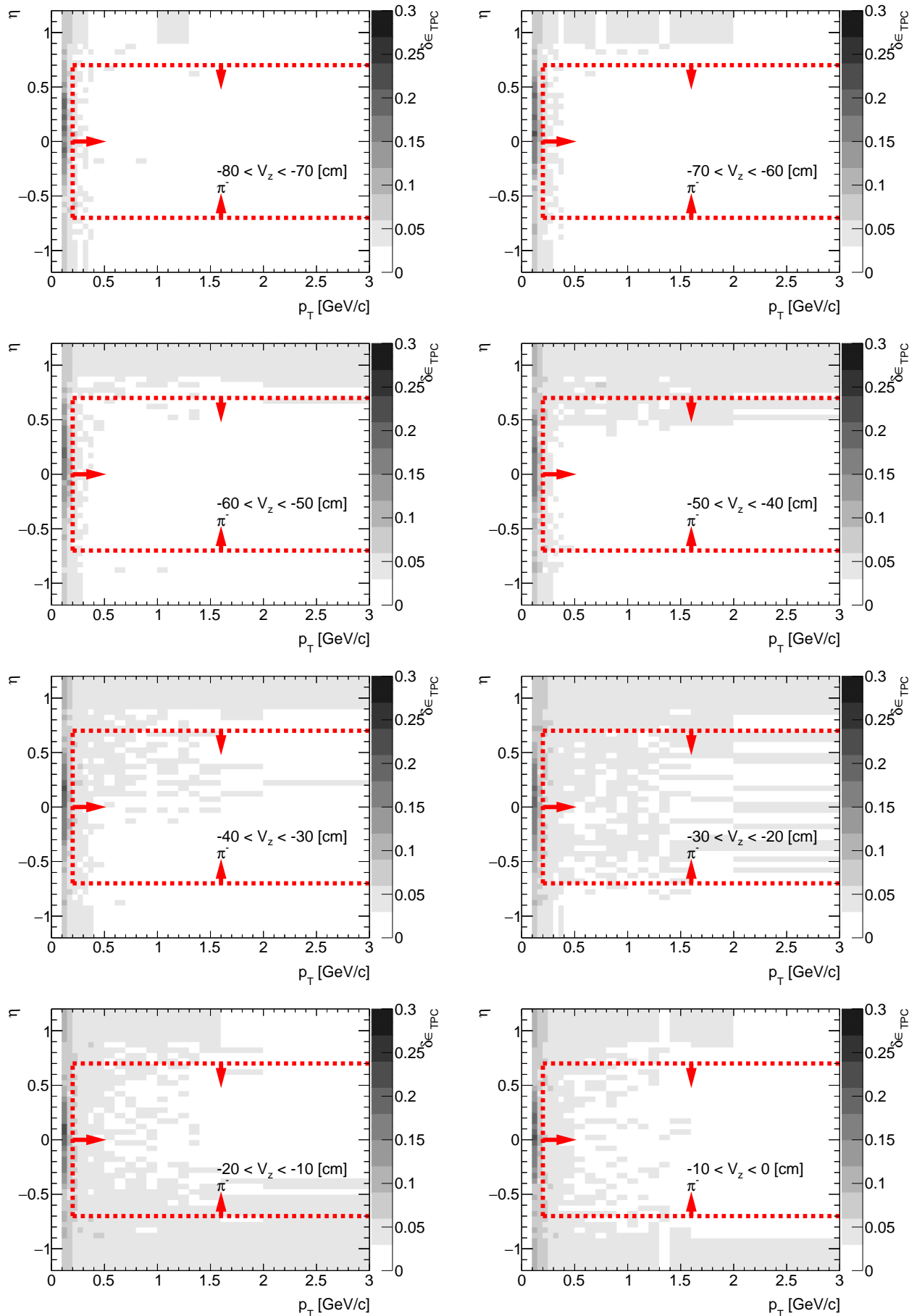
Figure 9.3: The difference  $\Delta\epsilon_{TPC} = \Delta\epsilon_{TPC}^{1400 \text{ kHz}} - 2 \cdot \Delta\epsilon_{TPC}^{700 \text{ kHz}}$  for  $\pi^\pm$  as a function of  $p_T$  and  $\eta$  ( $|V_z| < 80 \text{ cm}$ ).



### 9.1.2 Dead material effect on TPC track reconstruction efficiency

The amount of dead material in front of TPC differs up to 20% between data and simulation (see Sec. 8). First, the amount of lost particles,  $\delta\epsilon_{TPC}$ , due to the interaction with dead material in front of TPC was estimated using no-pile-up MC samples. The results for  $\pi^-$  in CD are shown in Fig. 9.4. Then the symmetric systematic uncertainty to the TPC track reconstruction efficiency due to dead material was introduced as  $\pm 0.2 \cdot \delta\epsilon_{TPC}$ . In Fig. 9.5 the systematic uncertainty is shown for each particle species in CD as a function of  $p_T$  ( $|\eta| < 0.7, |V_z| < 80 \text{ cm}$ ). The results for other particles and SD are shown in Figs. in Appendix E.

Figure 9.4: The amount of lost  $\pi^-$  due to the interaction with dead material in front of TPC. Each plot represents the fraction of lost  $\pi^-$ ,  $\delta\epsilon_{TPC}$  (z-axis), as a function of true particle pseudorapidity  $\eta$  (y-axis) and transverse momentum  $p_T$  (x-axis) in single  $z$ -vertex bin.



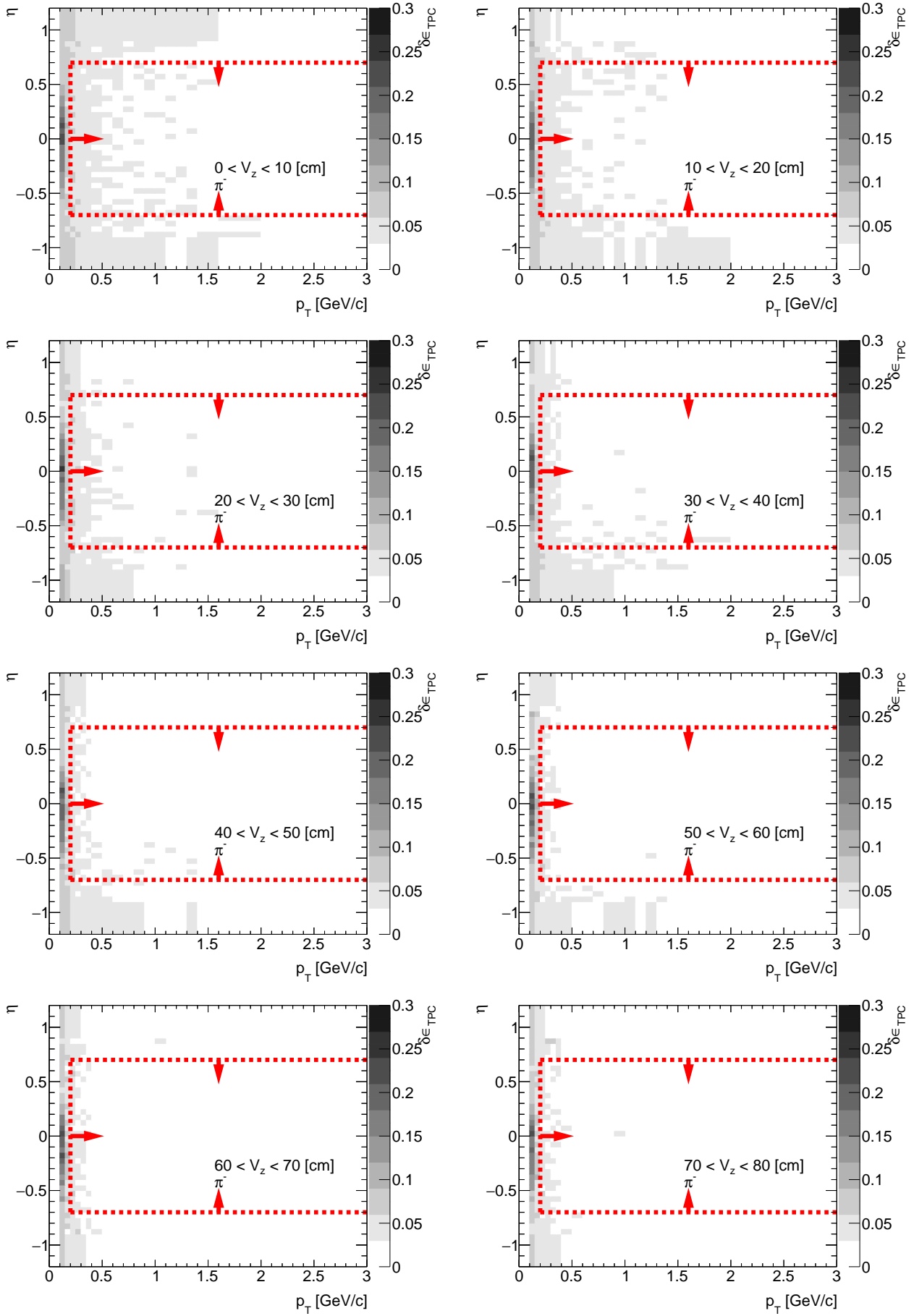
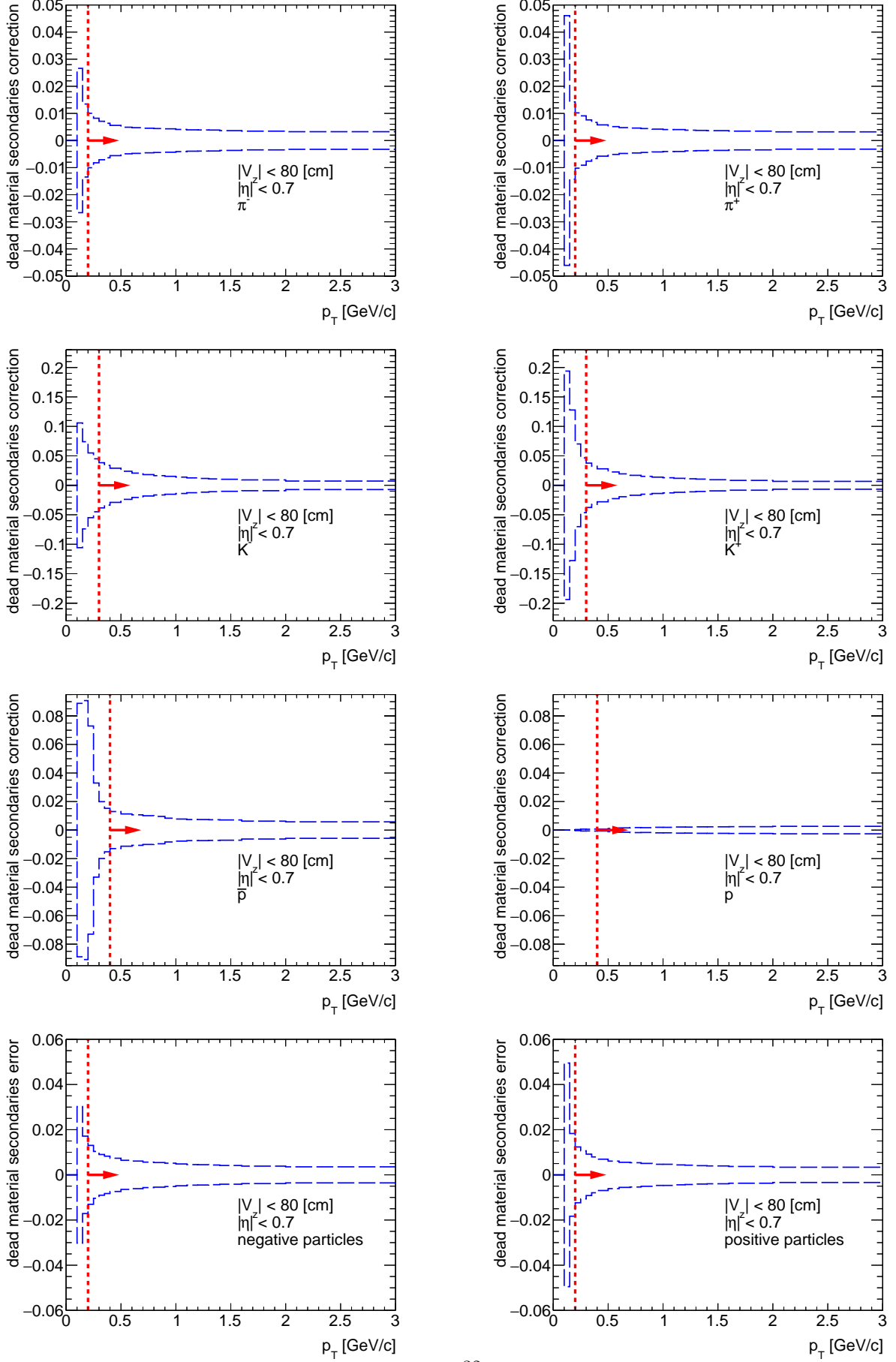


Figure 9.5: The systematic uncertainty to the TPC track reconstruction efficiency due to amount of dead material in front of TPC using MC samples for CD. Each plot represents the systematic uncertainty as a function of true particle  $p_T$  ( $|\eta| < 0.7, |V_z| < 80 \text{ cm}$ ) for given particle species:  $\pi^-, \pi^+, K^-, K^+, \bar{p}$  and  $p$ . It was also calculated for negative and positive particles without identification.



## 9.2 TOF matching efficiency

### 9.2.1 Embedding (pile-up) effect

The approach to calculate the systematic uncertainty on TOF matching efficiency related to pile-up was quite similar to the one used for TPC track reconstruction efficiency (Sec. 9.1.1). However, the TOF matching efficiency is conditional and depends on TPC track reconstruction efficiency. Since that, the difference between high and low pile-up runs is given by:

$$\Delta\epsilon_{TOF}^{1400/700 \text{ kHz}} = \frac{N_{TPC-TOF}^{no-pile-up}}{N_{TPC}^{no-pile-up}} - \frac{N_{TPC-TOF}^{pile-up}}{N_{TPC}^{pile-up}} \quad (9.3)$$

where:

$N_{TPC-TOF}^{pile-up}$  - number of reconstructed tracks, matched with MC tracks and TOF hit in pile-up MC,

$N_{TPC-TOF}^{no-pile-up}$  - number of reconstructed tracks, matched with MC tracks and TOF hit in no-pile-up MC,

$N_{TPC}^{pile-up}$  - number of reconstructed tracks, matched with MC tracks in pile-up MC,

$N_{TPC}^{no-pile-up}$  - number of reconstructed tracks, matched with MC tracks in no-pile-up MC.

Next the difference between high and low pile-up events was calculated with the formula similar to the one given by Eq. 9.2 and is shown in Figs. 9.6 and 9.7. The origin of  $N_{TPC-TOF}$  increase is not known (it may be due to lack of pile-up in TPC or TOF). Since that, it is impossible to correctly calculate the statistical error for  $\Delta\epsilon_{TOF}$ . Nevertheless,  $\Delta\epsilon_{TOF}$  is smaller than 0.5% and can be neglected in comparison with other systematic uncertainties.

Figure 9.6:  $\pi^\pm$  TOF matching efficiency as a function of  $p_T$  ( $|\eta| < 0.7$ ,  $|V_z| < 80$  cm) for embedded MC samples with  $\langle BBC\_AND \rangle \geq 700$  kHz and  $\langle BBC\_AND \rangle \geq 1400$  kHz. The efficiencies from corresponding no-pile-up MC samples were also shown. Additionally, the differences from Eq. 9.2 were drawn in the bottom of each plot.

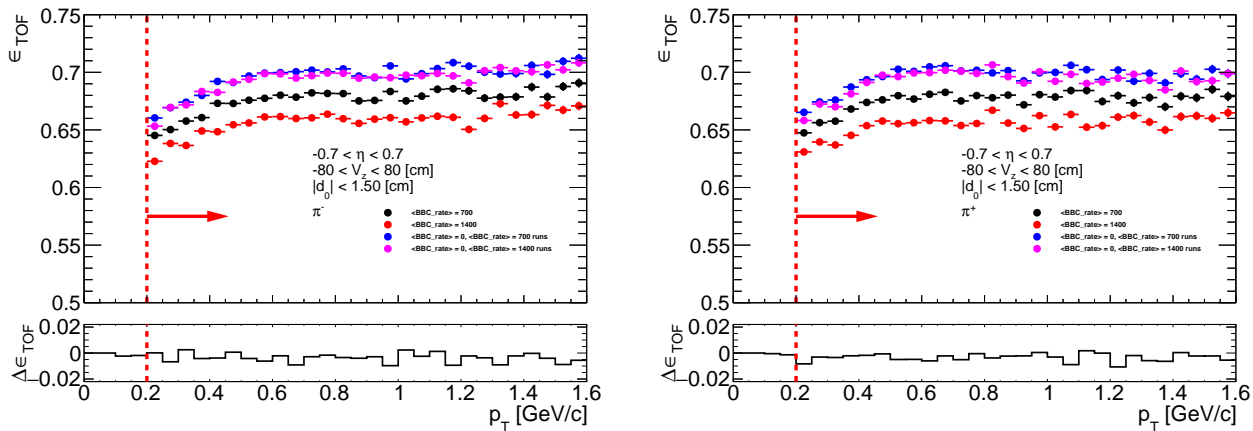
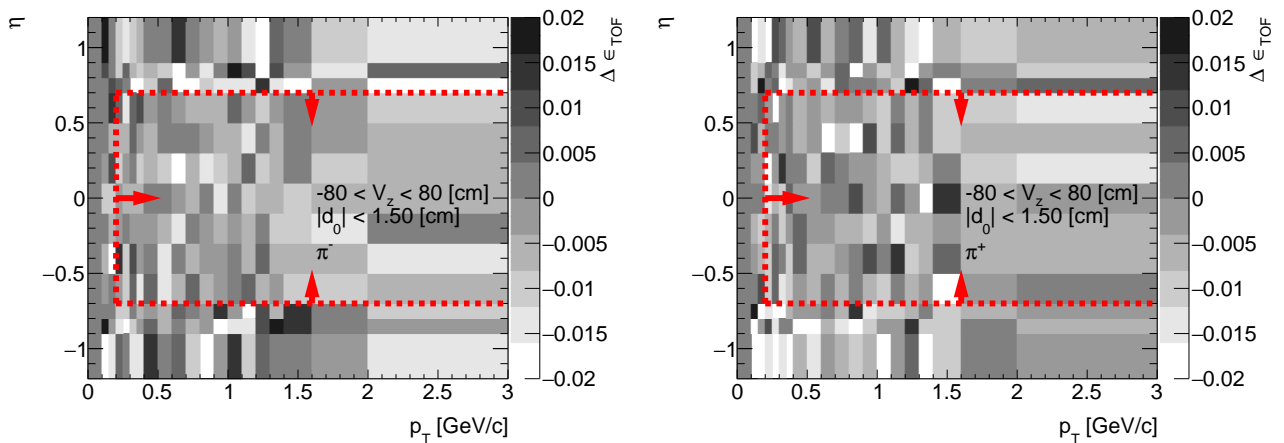


Figure 9.7: The difference  $\Delta\epsilon_{TOF} = \Delta\epsilon_{TOF}^{1400 \text{ kHz}} - 2 \cdot \Delta\epsilon_{TOF}^{700 \text{ kHz}}$  for  $\pi^\pm$  as a function of  $p_T$  and  $\eta$  ( $|V_z| < 80$  cm).



### 9.2.2 Simulation accuracy (absolute error on TOF efficiency)

The efficiency of TOF hit reconstruction and matching with the TPC tracks that was used in our analyses was taken directly from the STAR simulation. This makes the inaccuracies in the description of real detector geometry and its response propagating to physics results and introducing a bias. We decided to estimate the systematic uncertainty connected with the accuracy of description of the TOF system in (data-embedded) STAR simulation by extracting the TOF efficiency in the very same way from the data and embedded MC and comparing the results.

Unfortunately, in 2015 there were no low-luminosity (heavy-ion) runs that would imply lack of off-time pile-up tracks in TPC and thus would allow calculating the TOF efficiency in straightforward way, namely by dividing number of selected TPC tracks that were matched with TOF hits by number of all selected TPC tracks (matched or unmatched). For this reason a variation of the “tag and probe” method was developed and used.

The mentioned tag&probe method made use of the CEP of  $\pi^+\pi^-$  events. In short, events with forward proton track on each side of STAR and with a TOF-matched primary TPC track (tag) were selected. Among the remaining primary TPC tracks in the same vertex the opposite-sign TPC track (probe) was chosen as the one which provides the minimum total transverse momentum of all four tracks. The probe was checked whether it has been matched with the TOF hit or not. The ratio of the matched TPC tracks to all (matched or unmatched) TPC tracks defined the TOF efficiency. The method is illustrated in the sketch in Fig. 9.8. The detailed description of the procedure of the TOF efficiency extraction is provided below:

1. Data from two triggers were used (independently): RP\_CPT and RP\_CPT2 (trigger details in Tab. 2.1 of Ref. [1]). Embedded  $\pi^+\pi^-$  GenEx MC sample was subjected to the same trigger conditions (depending on the data to be compared with). Since there is no simulation of the TOF trigger we used in MC analysis L0 TOF multiplicity reconstructed from the offline hits according to TOF trigger system description (see Ref. [28]). In Fig. 9.9 we show performance of implemented method of L0 TOF multiplicity reconstruction. One can find satisfactory correlation of the true multiplicity and the reconstructed one.
2. Events were selected with the following set of cuts from nominal CEP analysis (Ref. [1]): **C1**, **C2** (TPC vertex), **C4** (RP tracks), **C5** (TPC-RP vertex matching), **C6** (veto signal in large BBC), providing significant reduction of background events.
- 3.

$$\varepsilon^{\text{TOF}}(p_T) = A \cdot \exp \left\{ - (B/p_T)^C \right\} \quad (9.4)$$

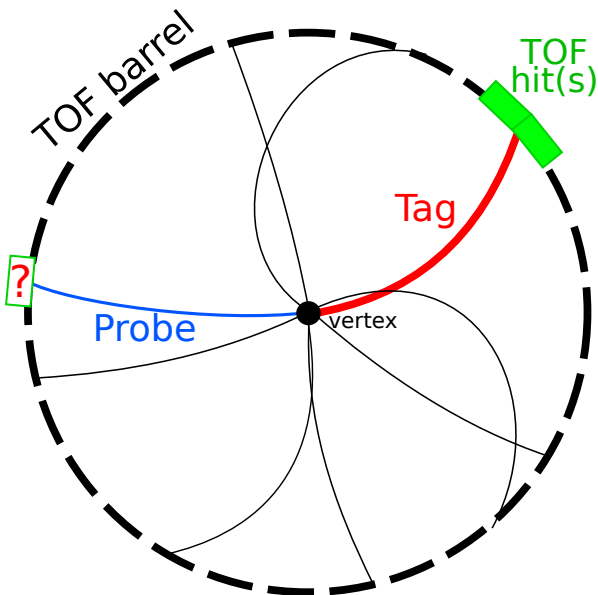


Figure 9.8: Sketch of the cross section of the central detector and CEP event with off-time pile-up tracks with drafted tag&probe method used to determine the TOF hit reconstruction and matching efficiency.

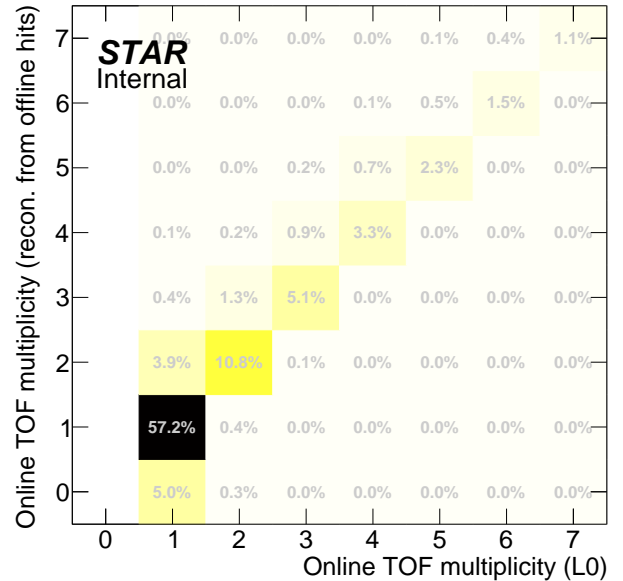


Figure 9.9: Comparison of original online TOF multiplicity at L0 (horizontal axis) and TOF multiplicity reconstructed from the offline hits (vertical axis) for RP\_CPT triggers.

$$n_{\text{probe}}^{\text{TOF}} = \underbrace{N \times \varepsilon^{\text{TOF}} \varepsilon''_{\text{vtx}} \times \varepsilon^{\text{TOF}}}_{\pi^+ \text{ is tag, } \pi^- \text{ is probe}} + \underbrace{N \times \varepsilon^{\text{TOF}} \times \varepsilon^{\text{TOF}} \varepsilon''_{\text{vtx}}}_{\pi^+ \text{ is probe, } \pi^- \text{ is tag}} = 2N (\varepsilon^{\text{TOF}})^2 \varepsilon''_{\text{vtx}} \quad (9.5)$$

$$n_{\text{probe}}^{\text{!TOF}} = \underbrace{N \times \varepsilon^{\text{TOF}} \varepsilon'_{\text{vtx}} \times (1 - \varepsilon^{\text{TOF}})}_{\pi^+ \text{ is tag, } \pi^- \text{ is probe}} + \underbrace{N \times (1 - \varepsilon^{\text{TOF}}) \times \varepsilon^{\text{TOF}} \varepsilon'_{\text{vtx}}}_{\pi^+ \text{ is probe, } \pi^- \text{ is tag}} = 2N (1 - \varepsilon^{\text{TOF}}) \varepsilon^{\text{TOF}} \varepsilon'_{\text{vtx}} \quad (9.6)$$

$$\tilde{n}_{\text{probe}}^{\text{TOF}} = \frac{n_{\text{probe}}^{\text{TOF}}}{\varepsilon''_{\text{vtx}}} \quad (9.7) \qquad \tilde{n}_{\text{probe}}^{\text{!TOF}} = \frac{n_{\text{probe}}^{\text{!TOF}}}{\varepsilon'_{\text{vtx}}} \quad (9.8) \qquad \varepsilon^{\text{TOF}} = \frac{\tilde{n}_{\text{probe}}^{\text{TOF}}}{\tilde{n}_{\text{probe}}^{\text{TOF}} + \tilde{n}_{\text{probe}}^{\text{!TOF}}} \quad (9.9)$$

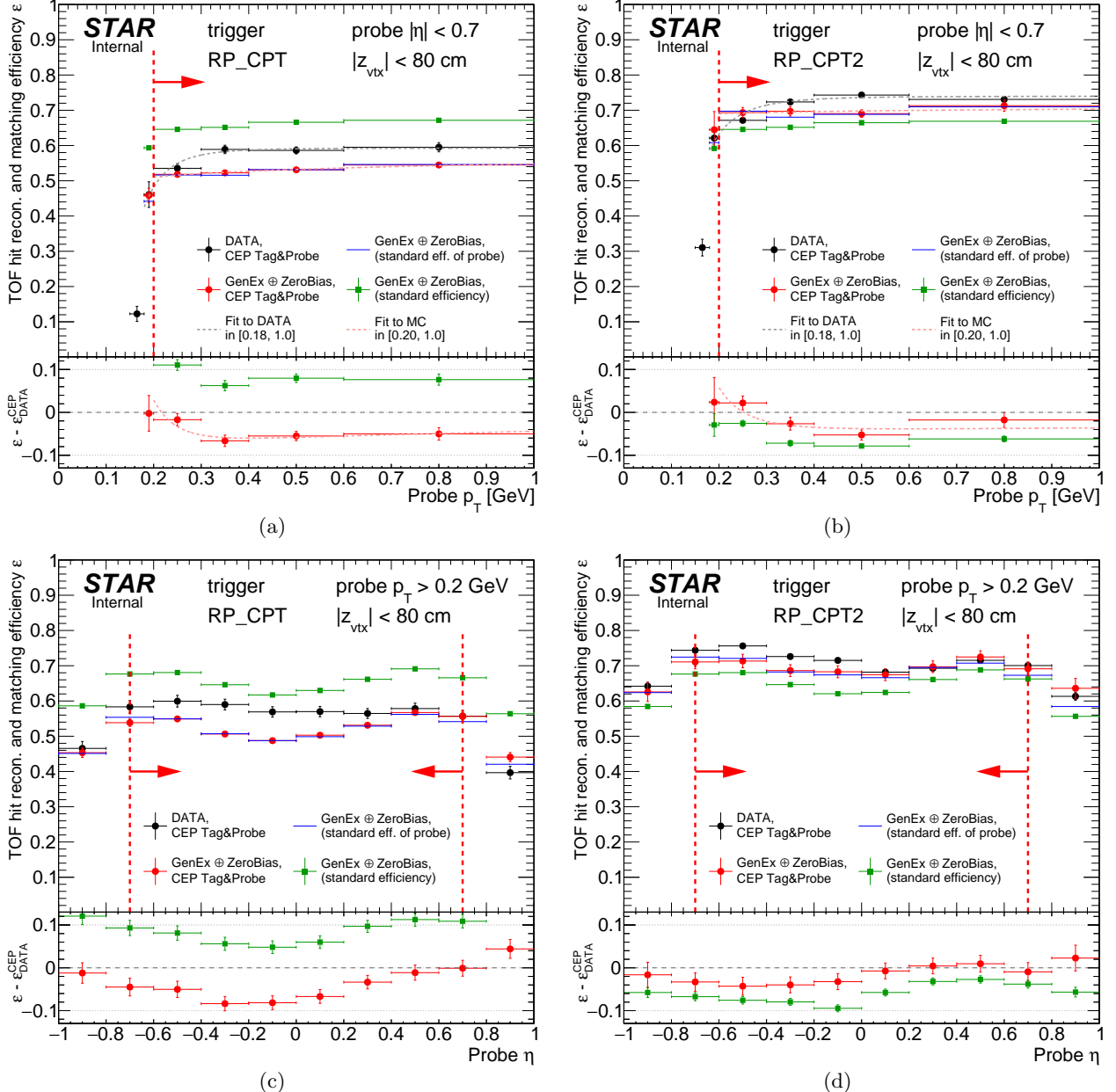


Figure 9.10: Tag&Probe TOF efficiency from CEP data (black points) compared with the result from embedded CEP MC (red points) as a function of TPC track  $p_T$  (top row) and  $\eta$  (bottom row). The left and right hand side column represents results obtained from RP\_CPT and RP\_CPT2 triggers, respectively. Green points represent the TOF efficiency calculated in the standard way from embedded CEP MC sample. Blue lines denote the TOF efficiency calculated in the standard way solely from the selected probe tracks that were matched to primary pions at the true level. Difference between red points and blue lines show the potential bias of tag and probe method. Dashed lines are fits of function given by Eq. (9.4) to points of corresponding color. Dashed vertical lines with arrows indicate region of  $p_T$  and  $\eta$  accepted in analyses.

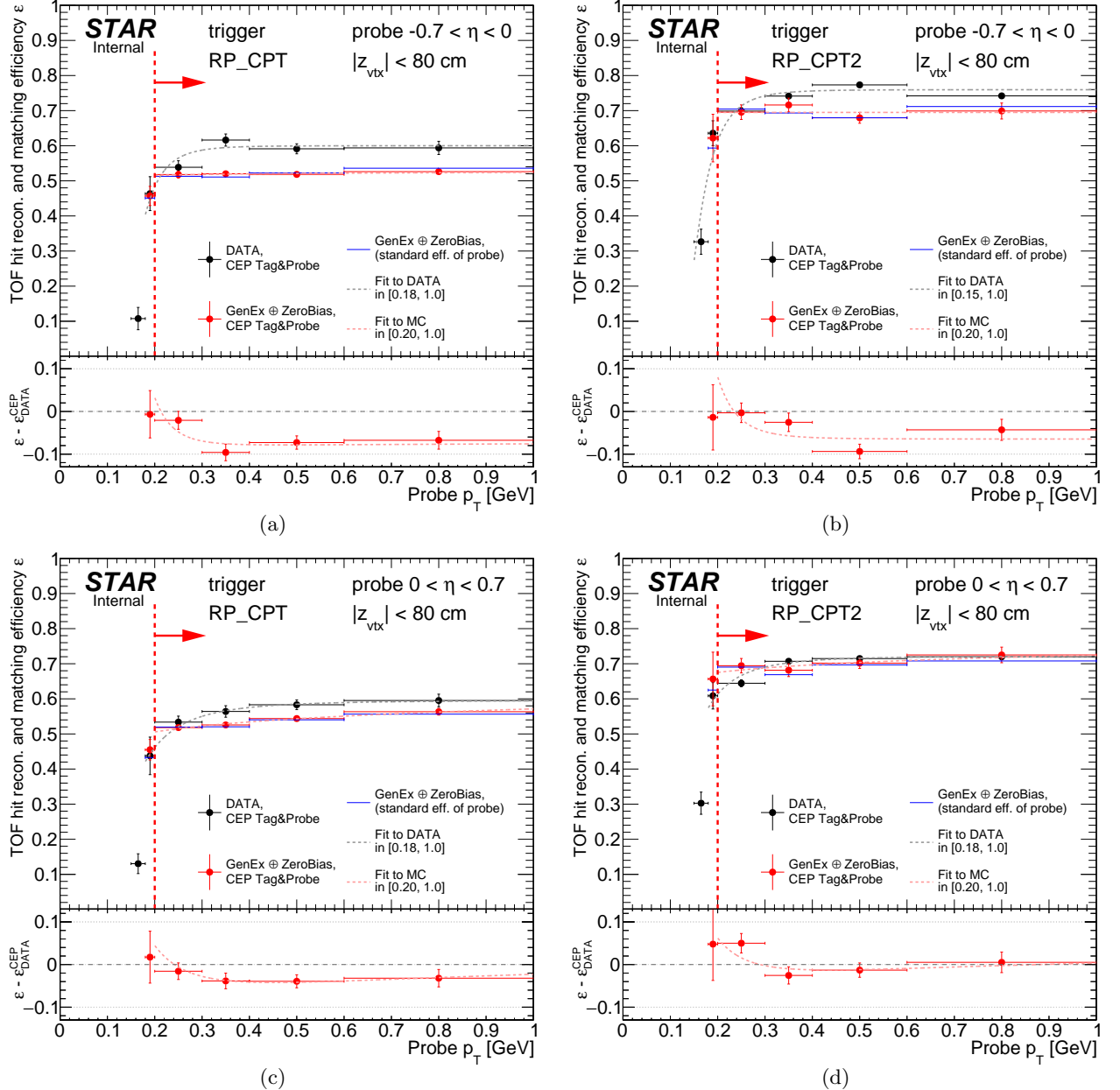
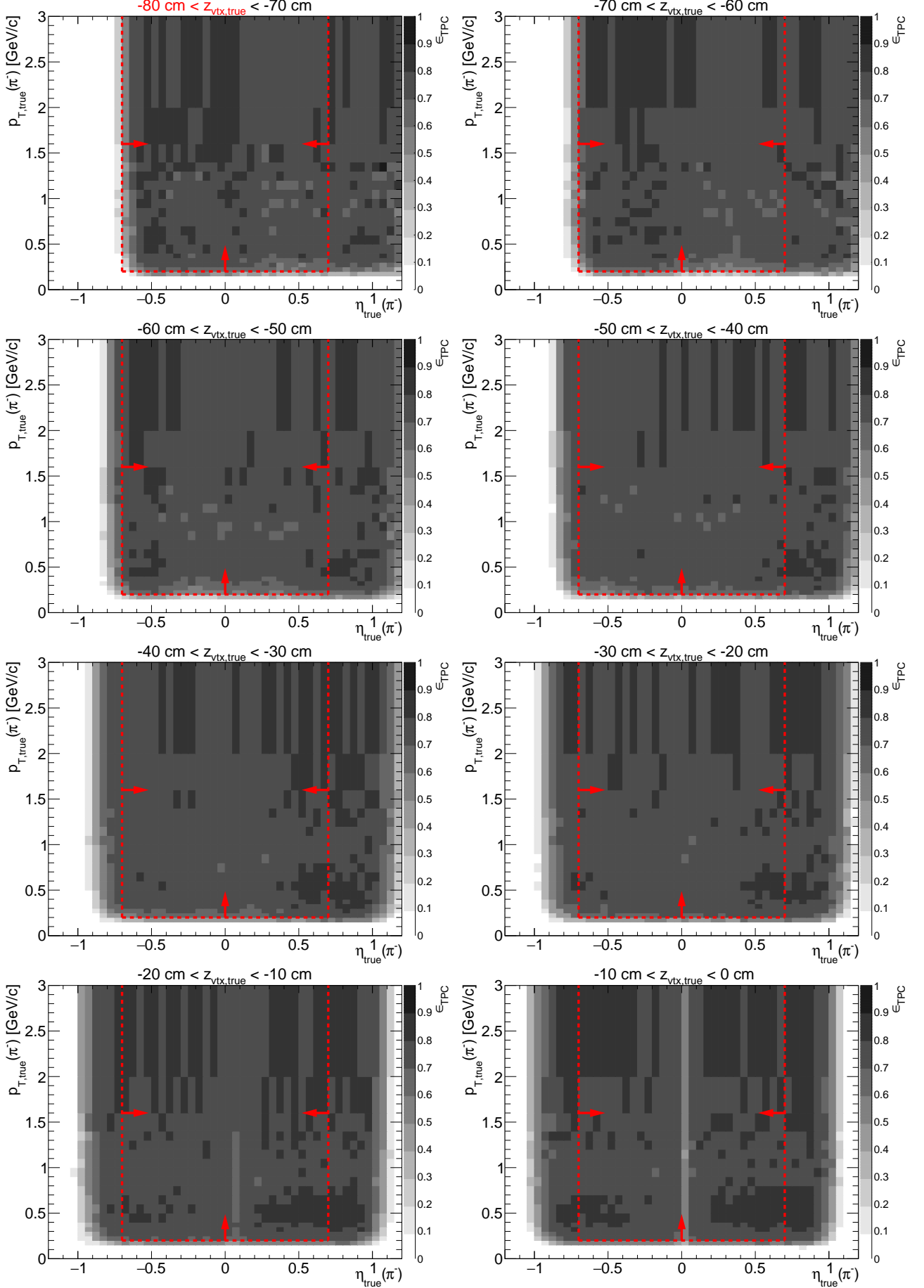


Figure 9.11: Tag&Probe TOF efficiency from CEP data (black points) compared with the result from embedded CEP MC (red points) as a function of TPC track  $p_T$  for negative (top row) and positive (bottom row)  $\eta$  of the probe. The left and right hand side column represents results obtained from RP\_CPT and RP\_CPT2 triggers, respectively. Blue lines denote the TOF efficiency calculated in the standard way solely from the selected probe tracks that were matched to primary pions at the true level. Difference between red points and blue lines show the potential bias of tag and probe method. Dashed lines are fits of function given by Eq. (9.4) to points of corresponding color. Dashed vertical lines with arrows indicate region of  $p_T$  and  $\eta$  accepted in analyses.

# Appendix A

## TPC track reconstruction efficiency

Figure A.1: TPC acceptance and reconstruction efficiency of  $\pi^-$ . Each plot represents the TPC efficiency  $\epsilon_{\text{TPC}}$  ( $z$ -axis) as a function of true particle pseudorapidity  $\eta$  ( $x$ -axis) and transverse momentum  $p_T$  ( $y$ -axis) in single  $z$ -vertex bin whose range is given at the top. Red lines and arrows indicate region accepted in analyses.



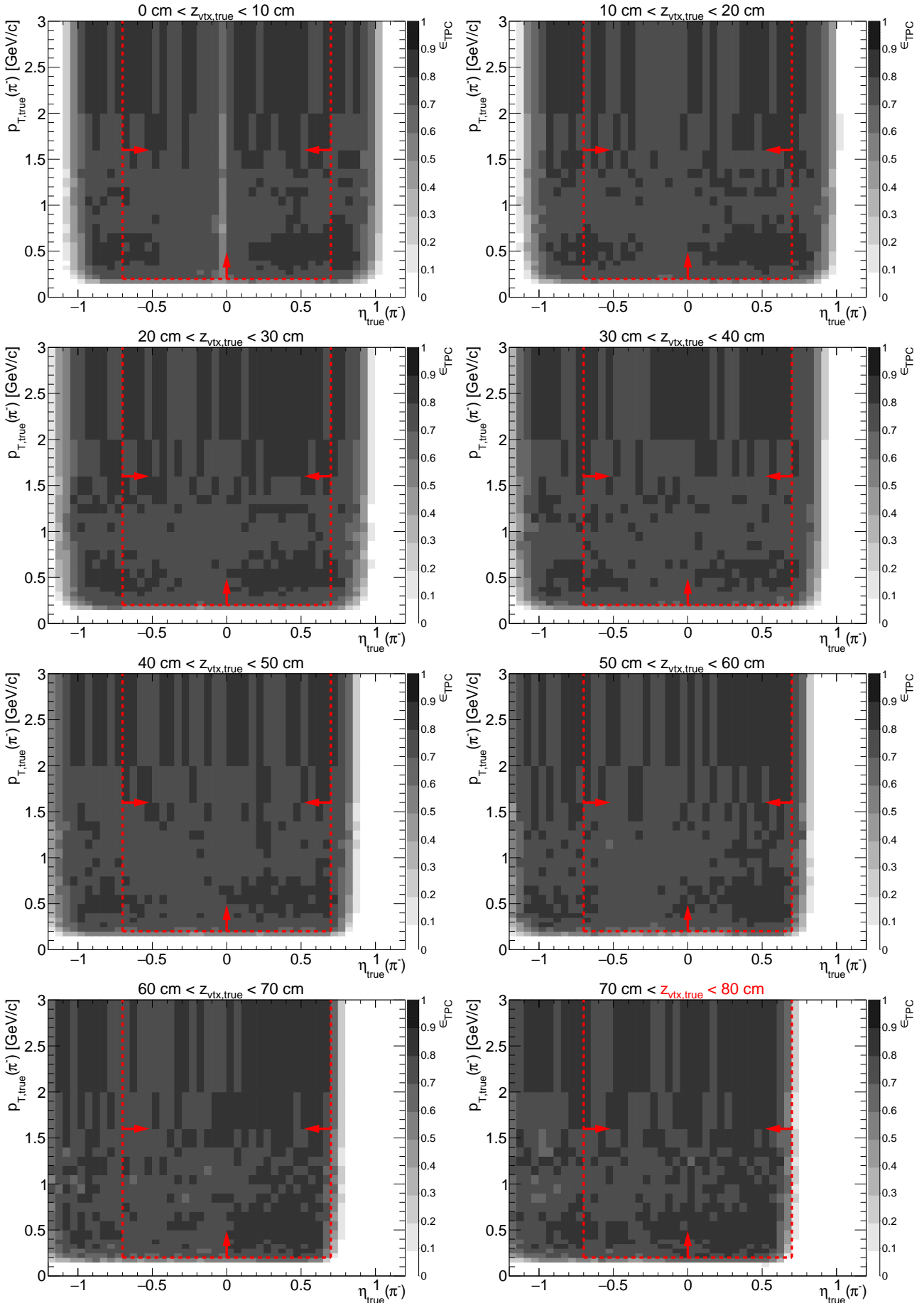
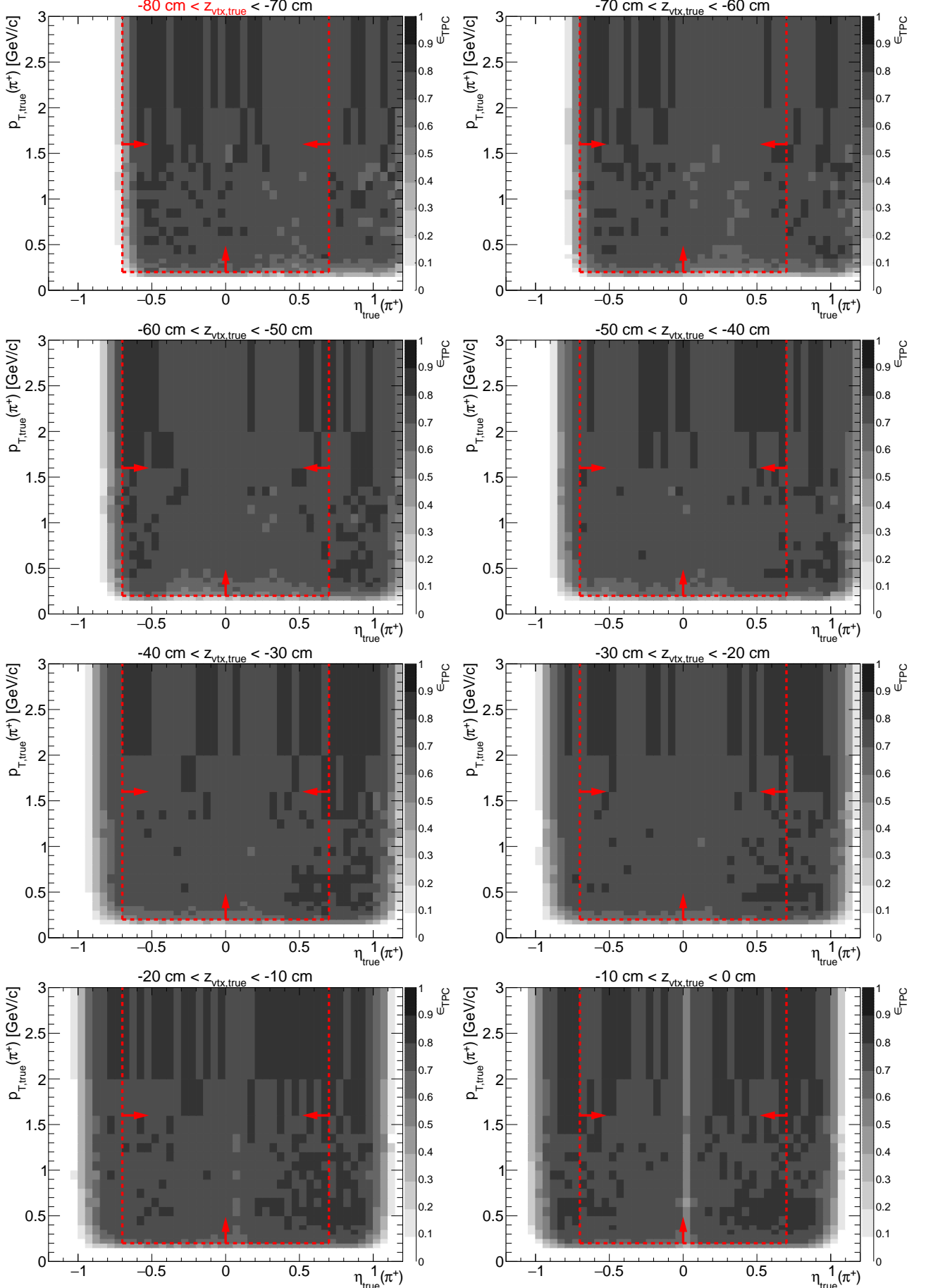


Figure A.2: TPC acceptance and reconstruction efficiency of  $\pi^+$ . Each plot represents the TPC efficiency  $\epsilon_{\text{TPC}}$  ( $z$ -axis) as a function of true particle pseudorapidity  $\eta$  ( $x$ -axis) and transverse momentum  $p_T$  ( $y$ -axis) in single  $z$ -vertex bin whose range is given at the top. Red lines and arrows indicate region accepted in analyses.



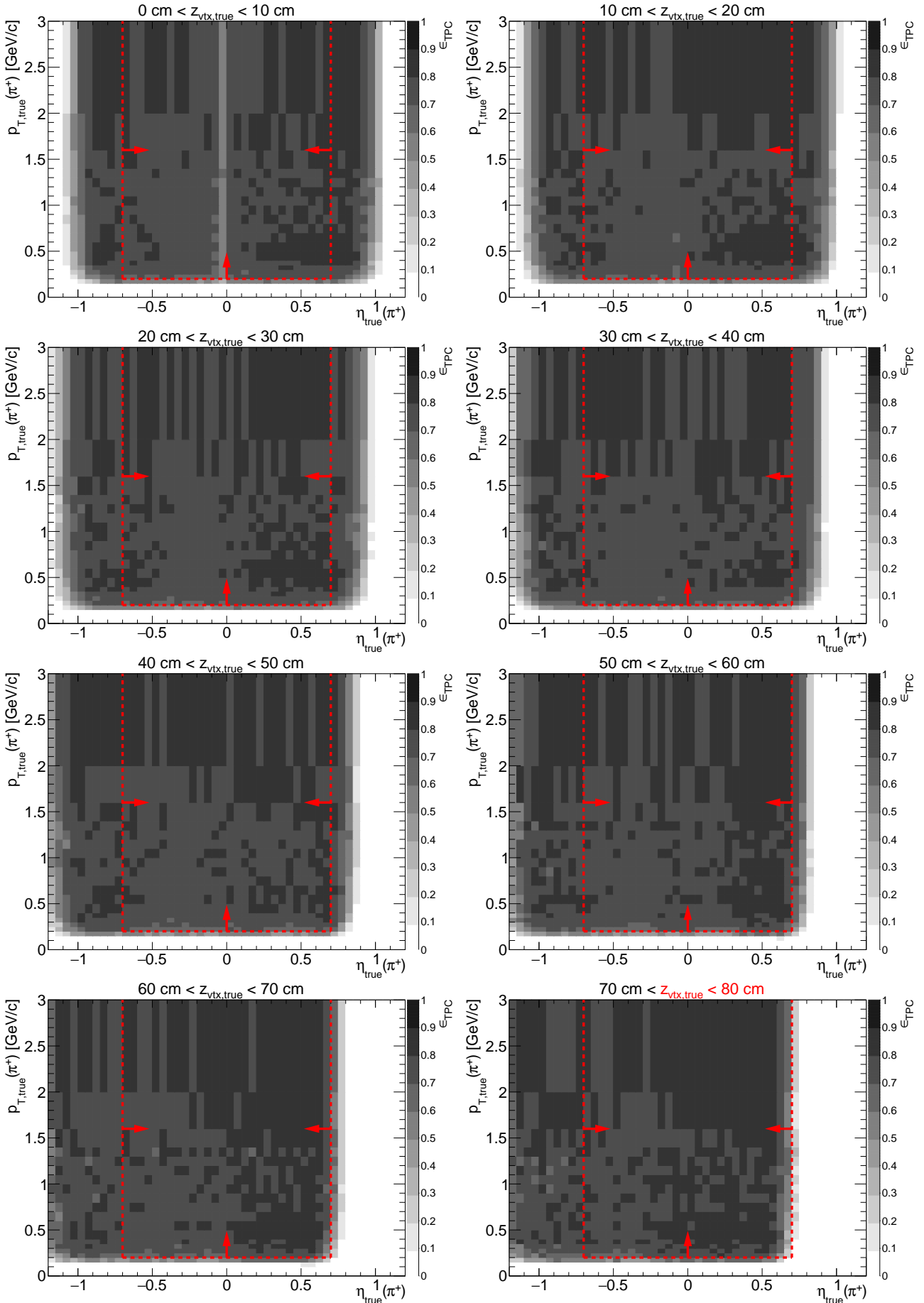
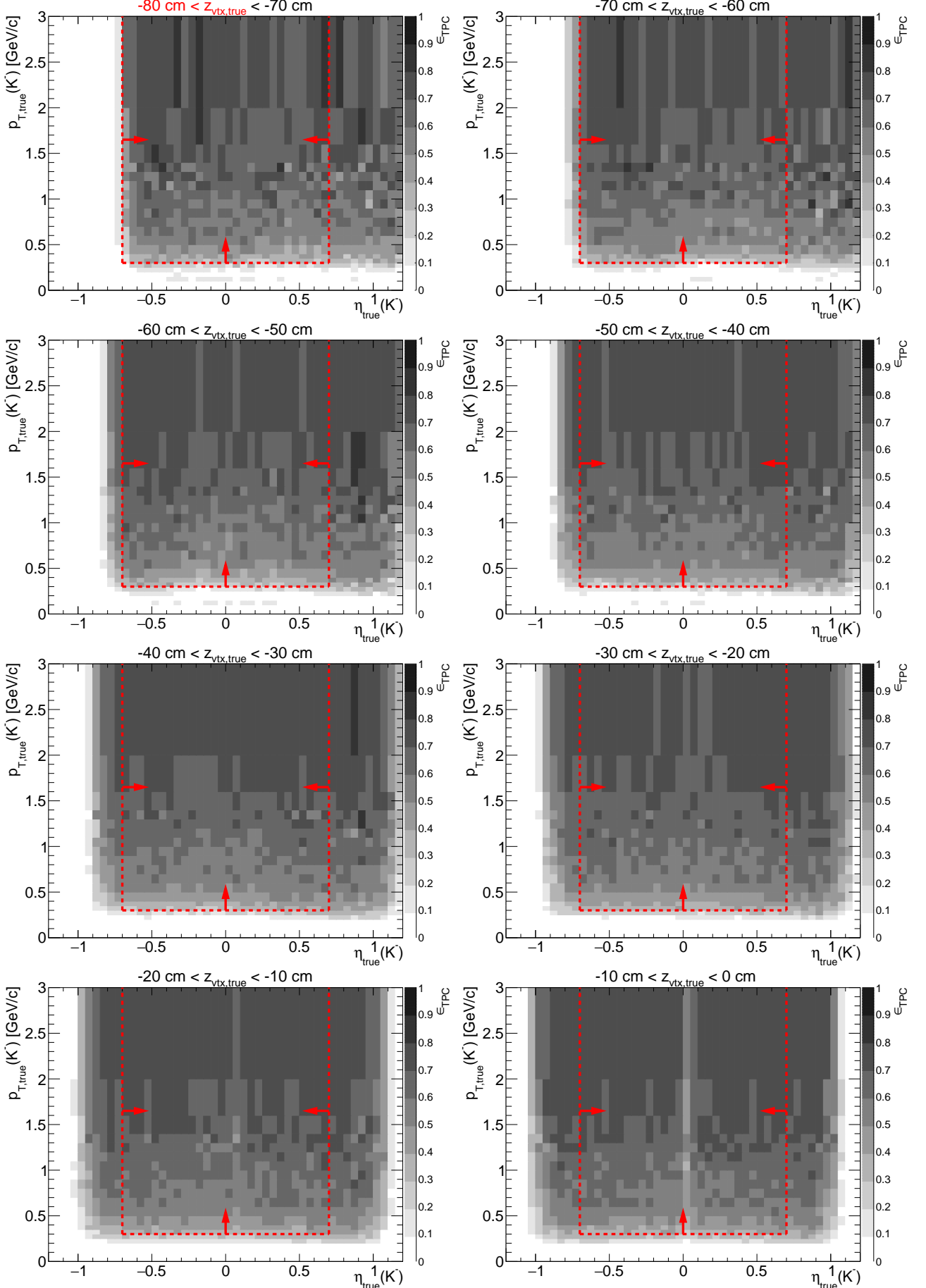


Figure A.3: TPC acceptance and reconstruction efficiency of  $K^-$ . Each plot represents the TPC efficiency  $\epsilon_{\text{TPC}}$  ( $z$ -axis) as a function of true particle pseudorapidity  $\eta$  ( $x$ -axis) and transverse momentum  $p_T$  ( $y$ -axis) in single  $z$ -vertex bin whose range is given at the top. Red lines and arrows indicate region accepted in analyses.



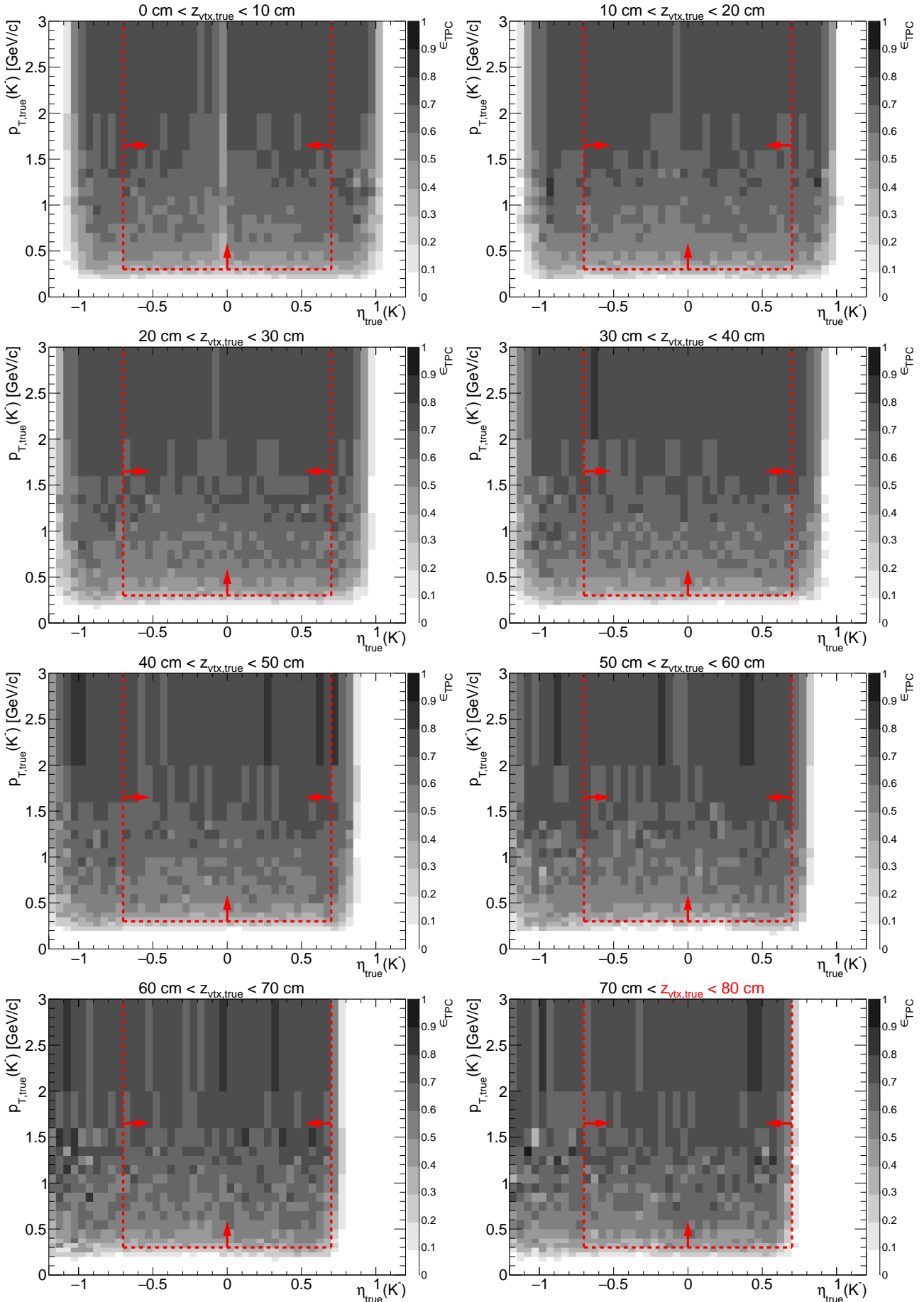
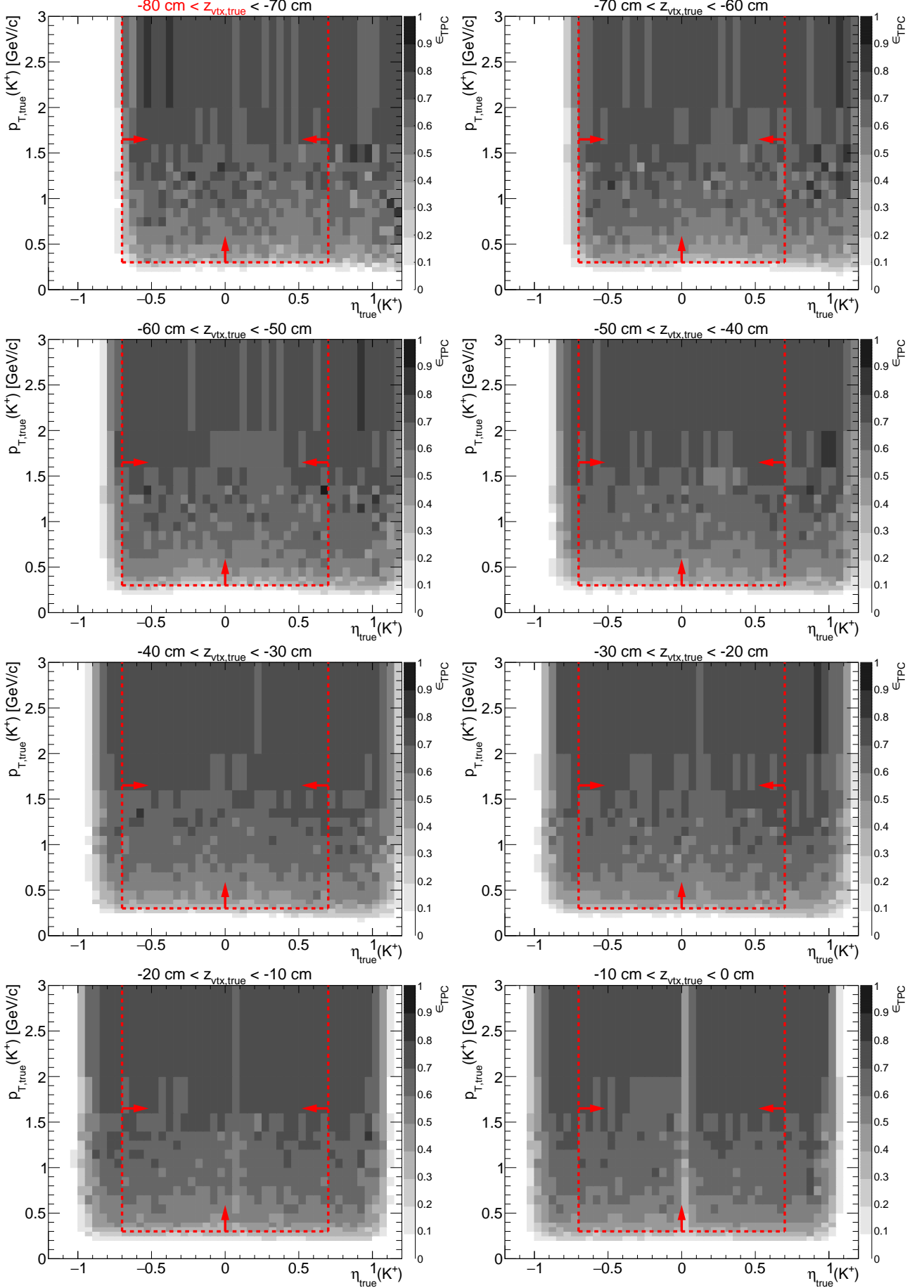


Figure A.4: TPC acceptance and reconstruction efficiency of  $K^+$ . Each plot represents the TPC efficiency  $\epsilon_{\text{TPC}}$  ( $z$ -axis) as a function of true particle pseudorapidity  $\eta$  ( $x$ -axis) and transverse momentum  $p_T$  ( $y$ -axis) in single  $z$ -vertex bin whose range is given at the top. Red lines and arrows indicate region accepted in analyses.



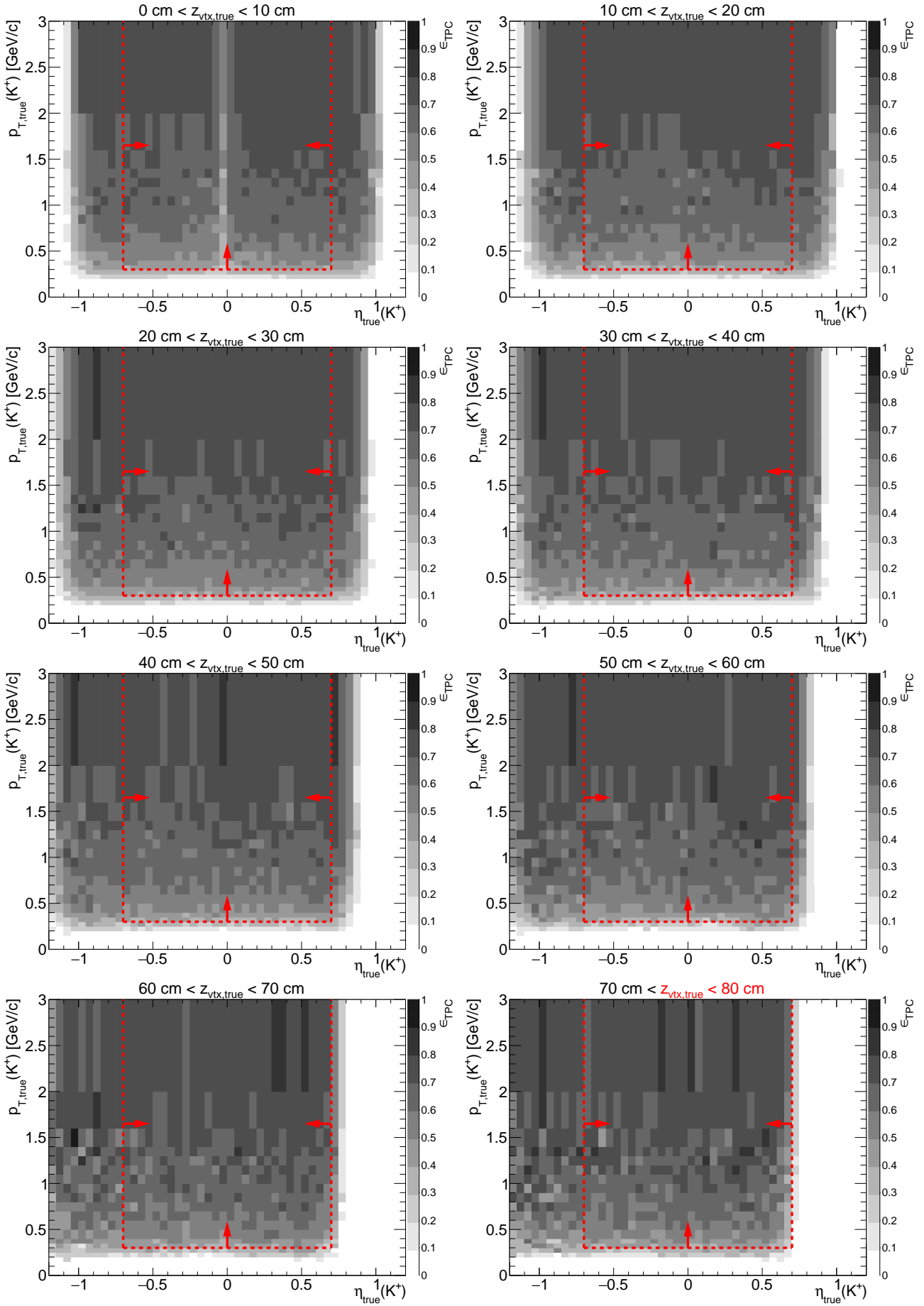
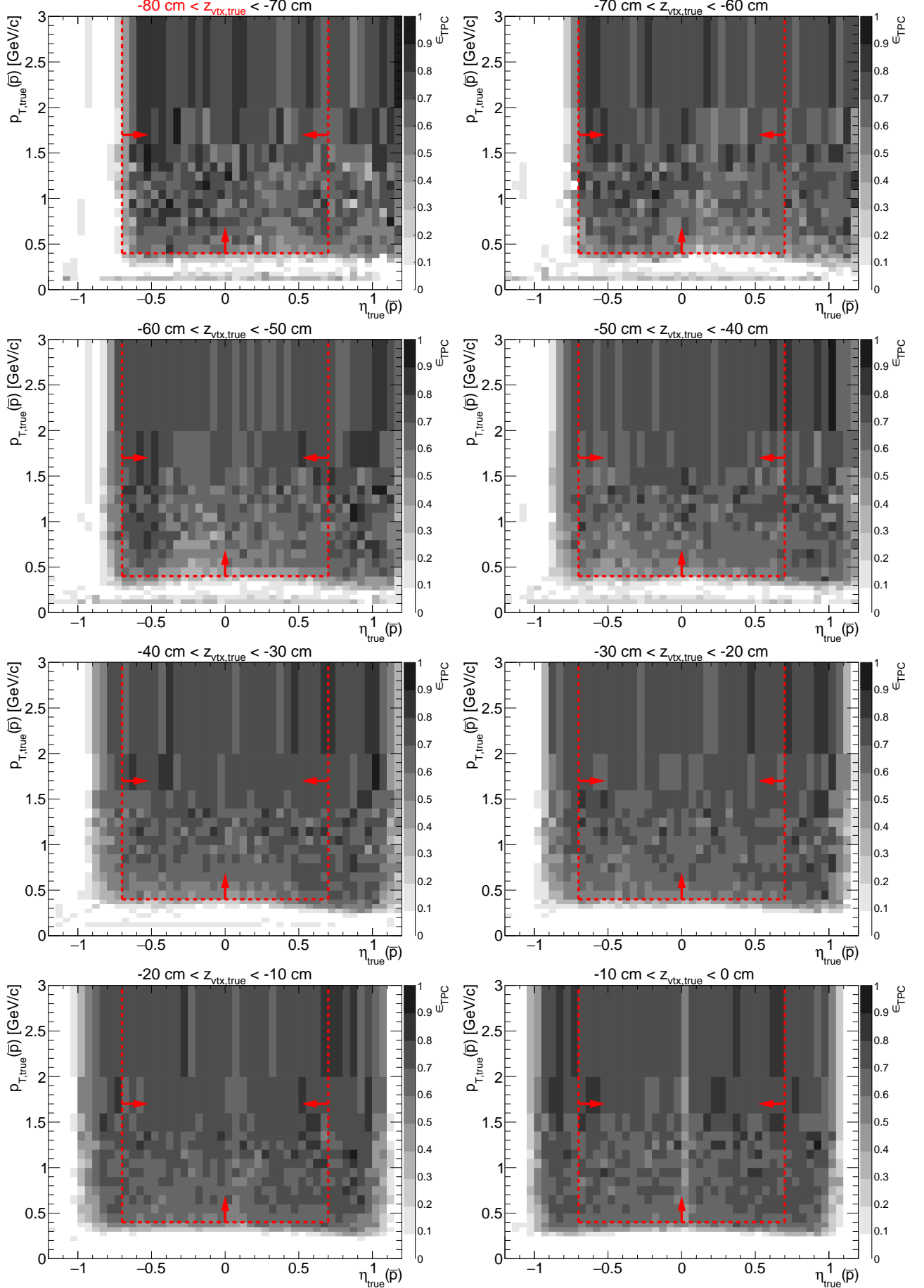


Figure A.5: TPC acceptance and reconstruction efficiency of  $\bar{p}$ . Each plot represents the TPC efficiency  $\epsilon_{\text{TPC}}$  ( $z$ -axis) as a function of true particle pseudorapidity  $\eta$  ( $x$ -axis) and transverse momentum  $p_T$  ( $y$ -axis) in single  $z$ -vertex bin whose range is given at the top. Red lines and arrows indicate region accepted in analyses.



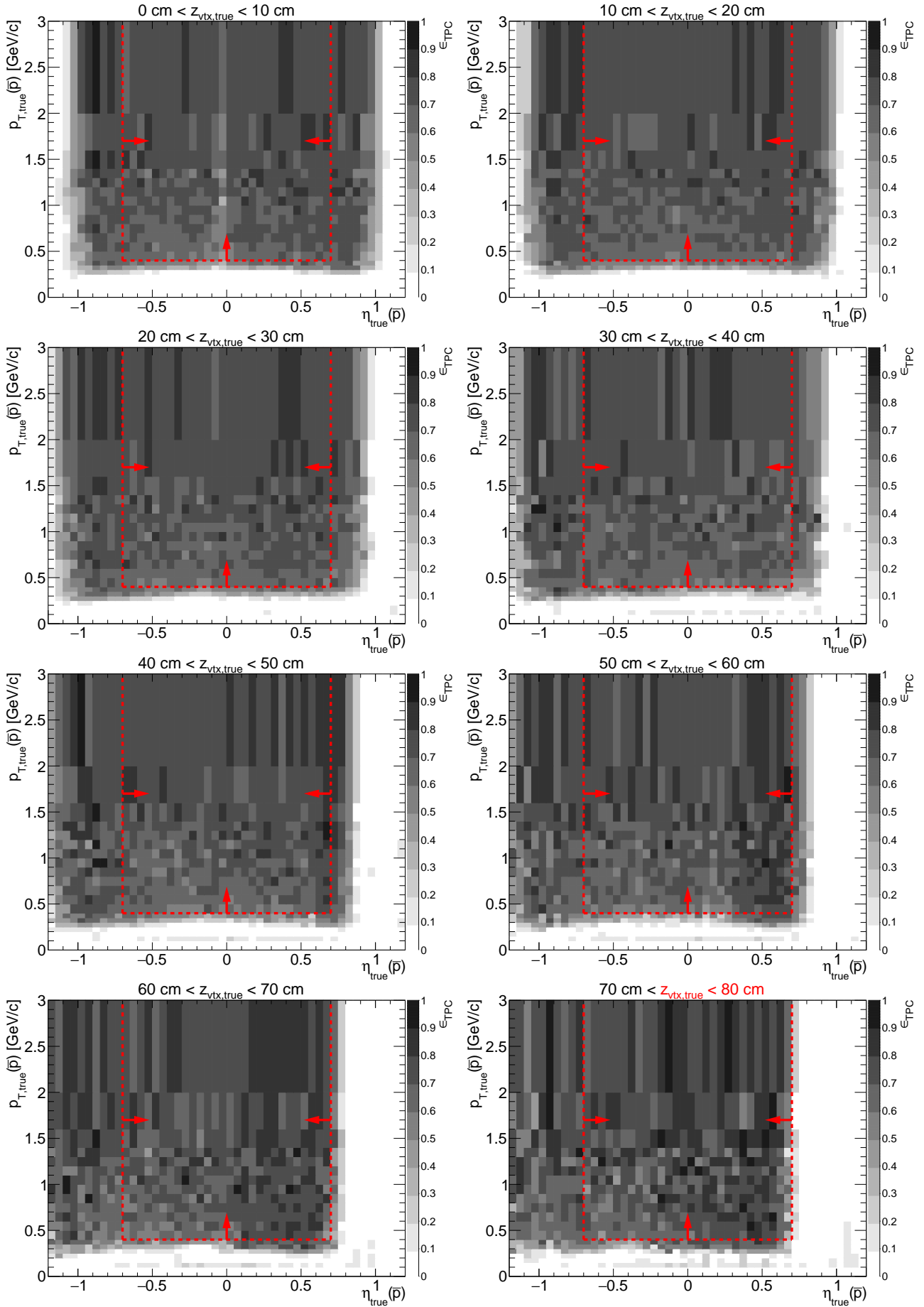
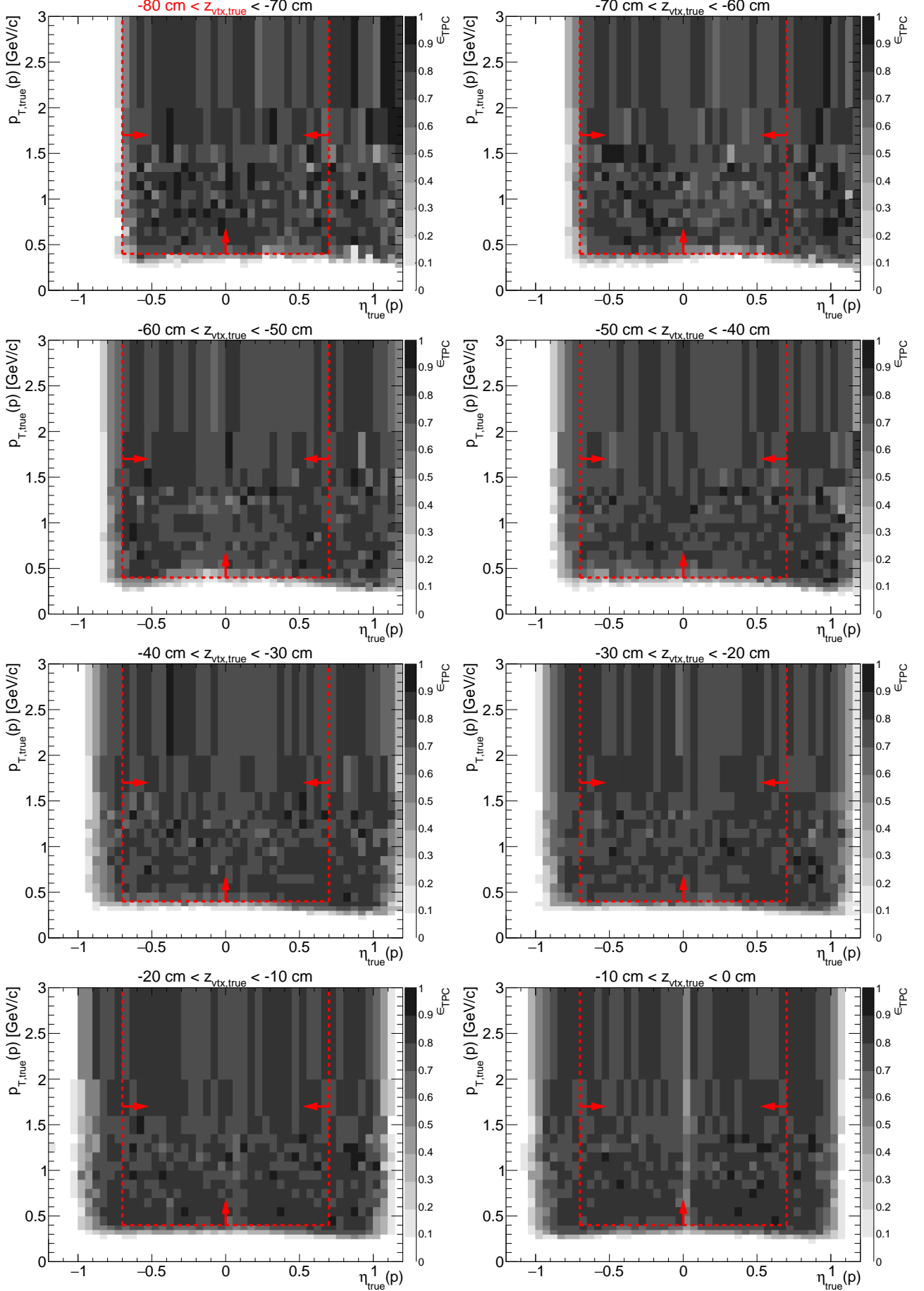
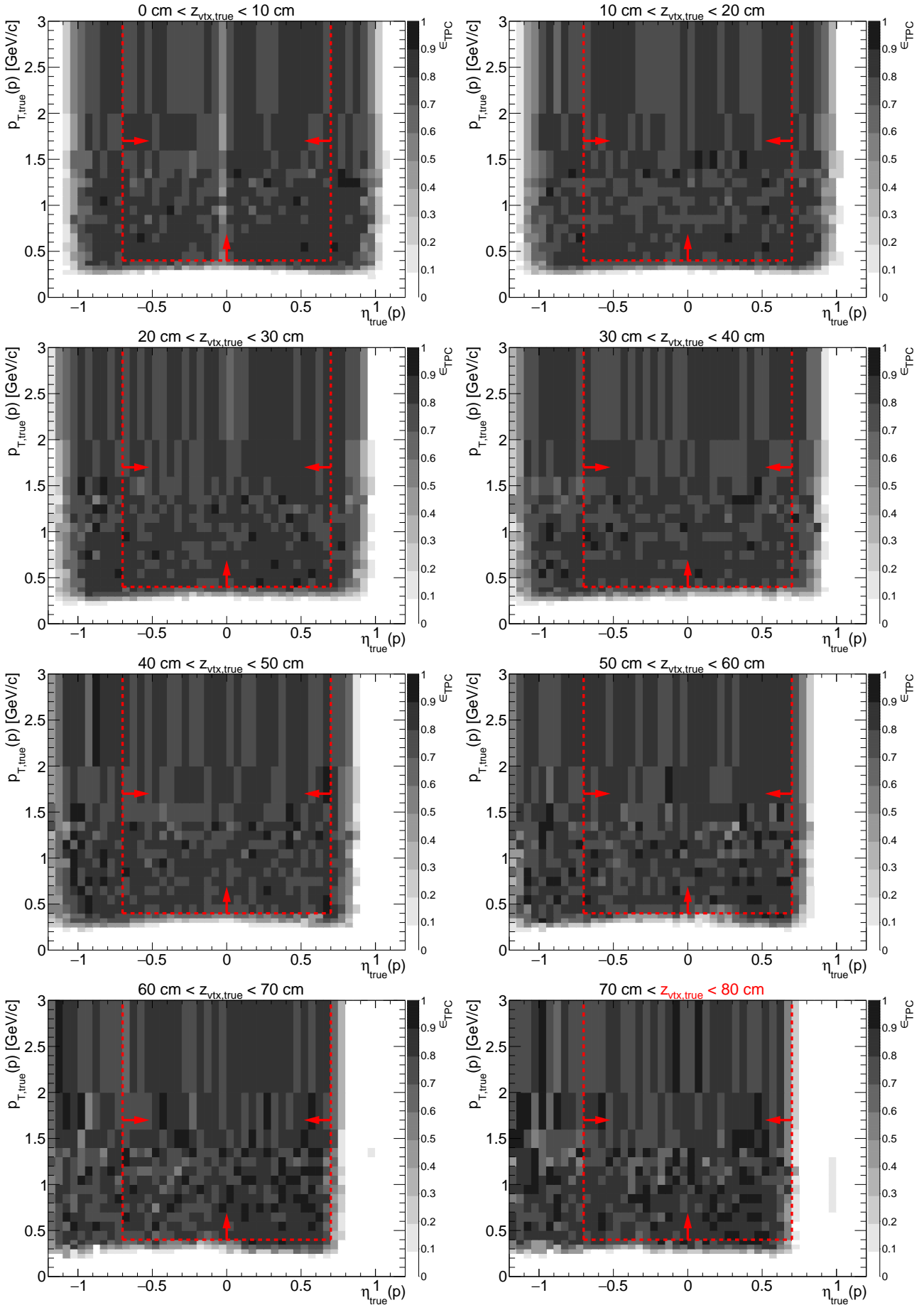


Figure A.6: TPC acceptance and reconstruction efficiency of  $p$ . Each plot represents the TPC efficiency  $\epsilon_{\text{TPC}}$  ( $z$ -axis) as a function of true particle pseudorapidity  $\eta$  ( $x$ -axis) and transverse momentum  $p_T$  ( $y$ -axis) in single  $z$ -vertex bin whose range is given at the top. Red lines and arrows indicate region accepted in analyses.

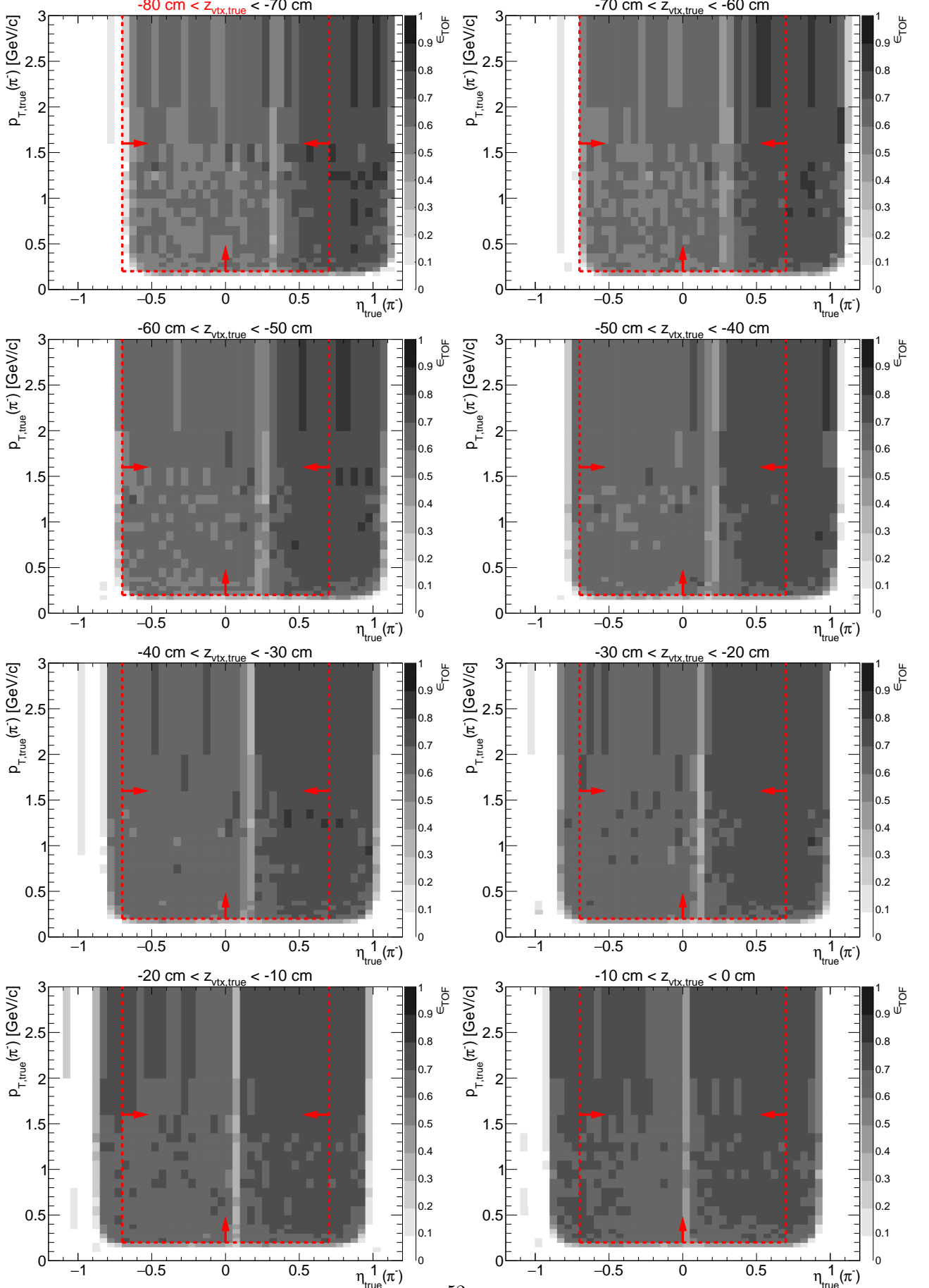




# **Appendix B**

## **TOF hit reconstruction and matching efficiency**

Figure B.1: TOF acceptance, reconstruction and matching efficiency of  $\pi^-$ . Each plot represents the TOF efficiency  $\epsilon_{\text{TOF}}$  ( $z$ -axis) as a function of true particle pseudorapidity  $\eta$  ( $x$ -axis) and transverse momentum  $p_T$  ( $y$ -axis) in single  $z$ -vertex bin whose range is given at the top. Red lines and arrows indicate region accepted in analyses.



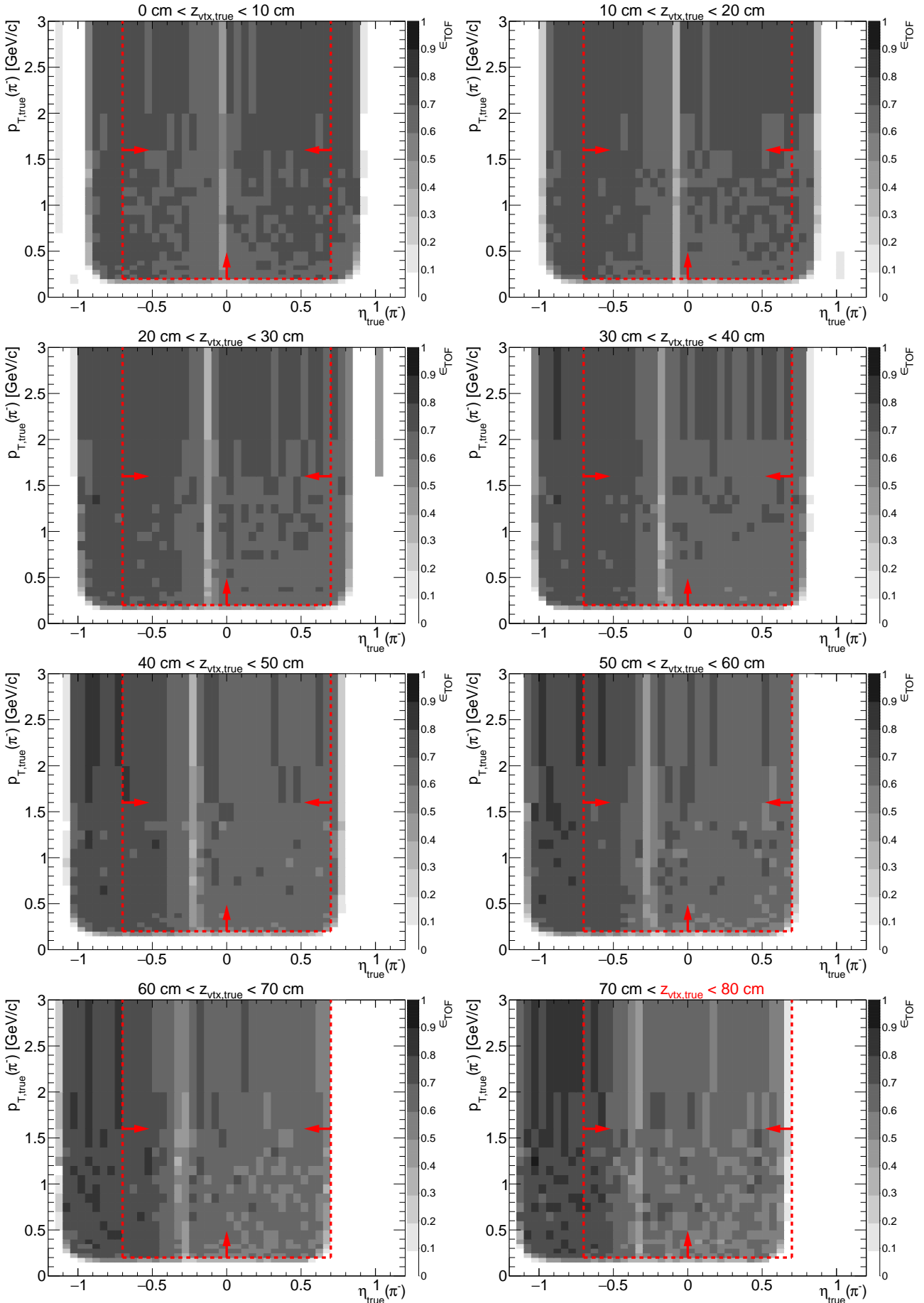
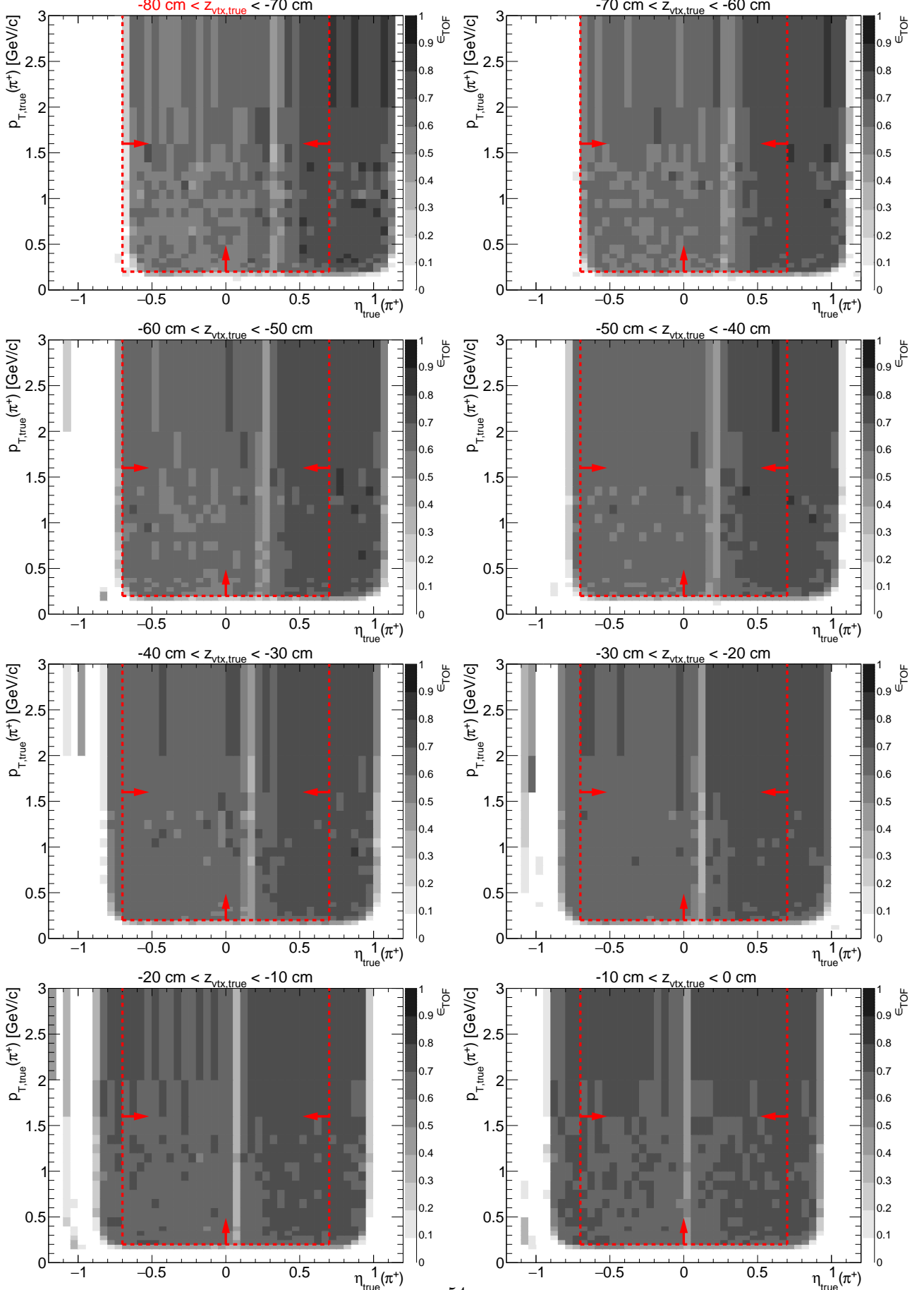


Figure B.2: TOF acceptance, reconstruction and matching efficiency of  $\pi^+$ . Each plot represents the TOF efficiency  $\epsilon_{\text{TOF}}$  ( $z$ -axis) as a function of true particle pseudorapidity  $\eta$  ( $x$ -axis) and transverse momentum  $p_T$  ( $y$ -axis) in single  $z$ -vertex bin whose range is given at the top. Red lines and arrows indicate region accepted in analyses.



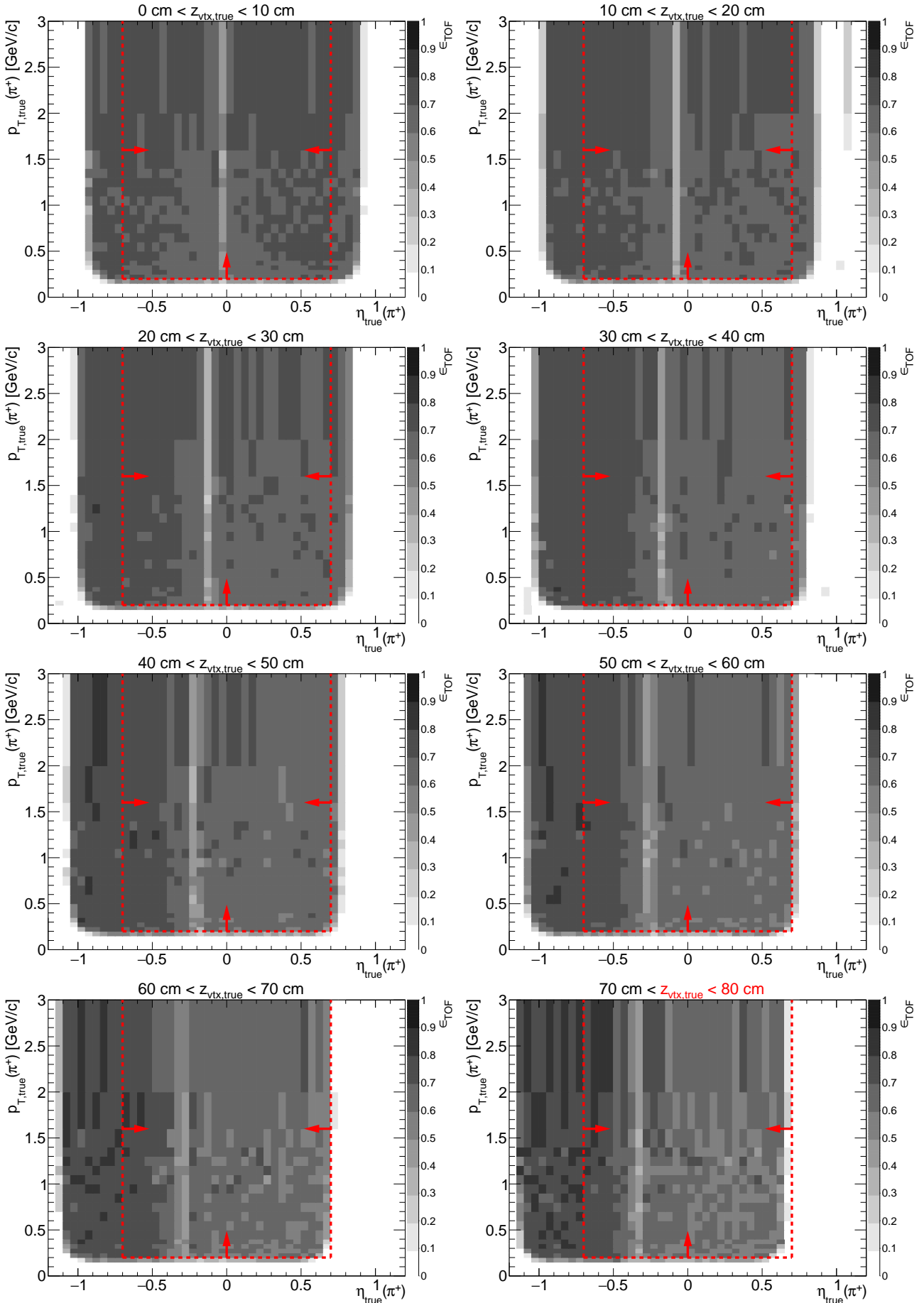
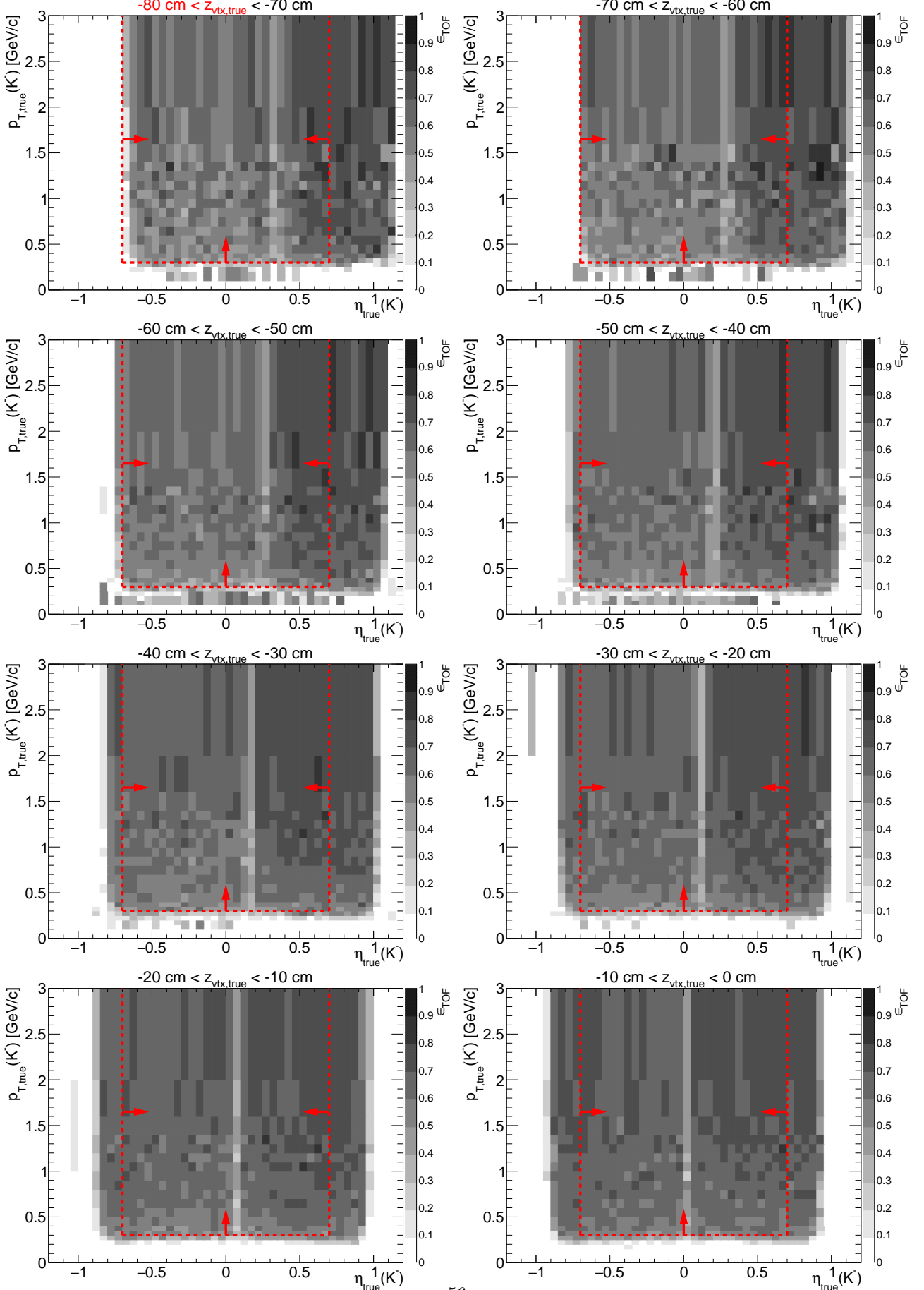


Figure B.3: TOF acceptance, reconstruction and matching efficiency of  $K^-$ . Each plot represents the TOF efficiency  $\epsilon_{\text{TOF}}$  ( $z$ -axis) as a function of true particle pseudorapidity  $\eta$  ( $x$ -axis) and transverse momentum  $p_T$  ( $y$ -axis) in single  $z$ -vertex bin whose range is given at the top. Red lines and arrows indicate region accepted in analyses.



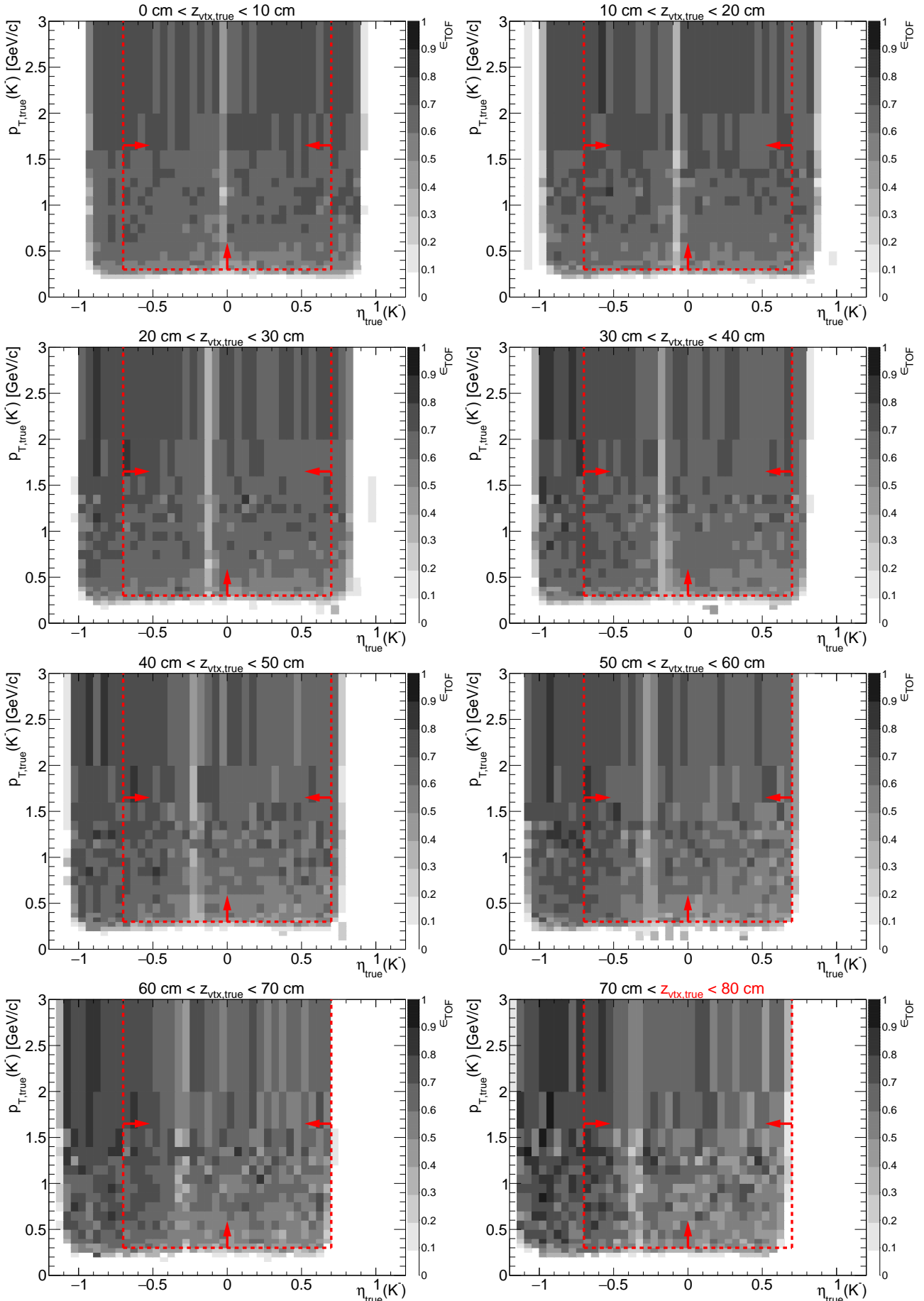
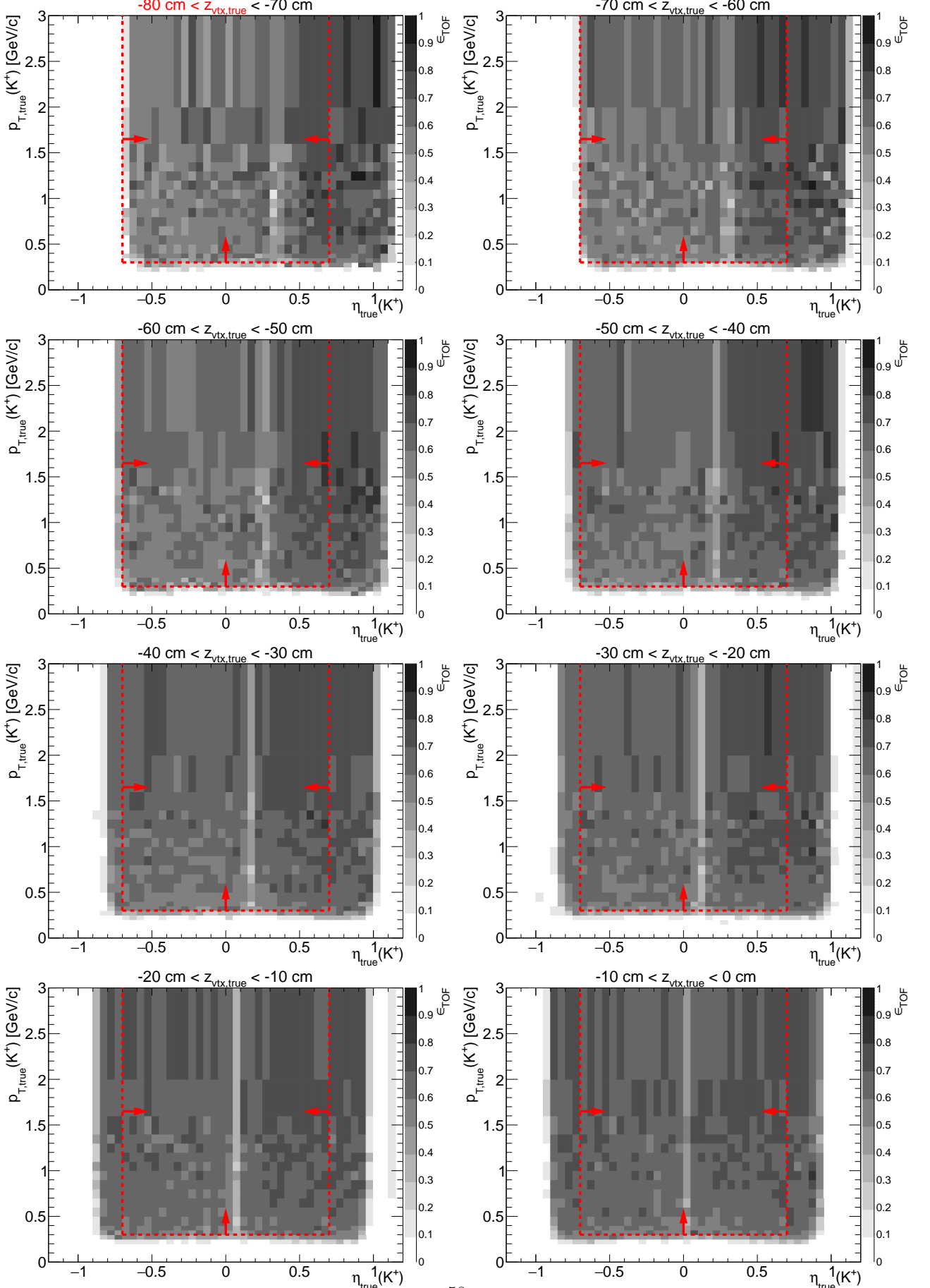


Figure B.4: TOF acceptance, reconstruction and matching efficiency of  $K^+$ . Each plot represents the TOF efficiency  $\epsilon_{\text{TOF}}$  ( $z$ -axis) as a function of true particle pseudorapidity  $\eta$  ( $x$ -axis) and transverse momentum  $p_T$  ( $y$ -axis) in single  $z$ -vertex bin whose range is given at the top. Red lines and arrows indicate region accepted in analyses.



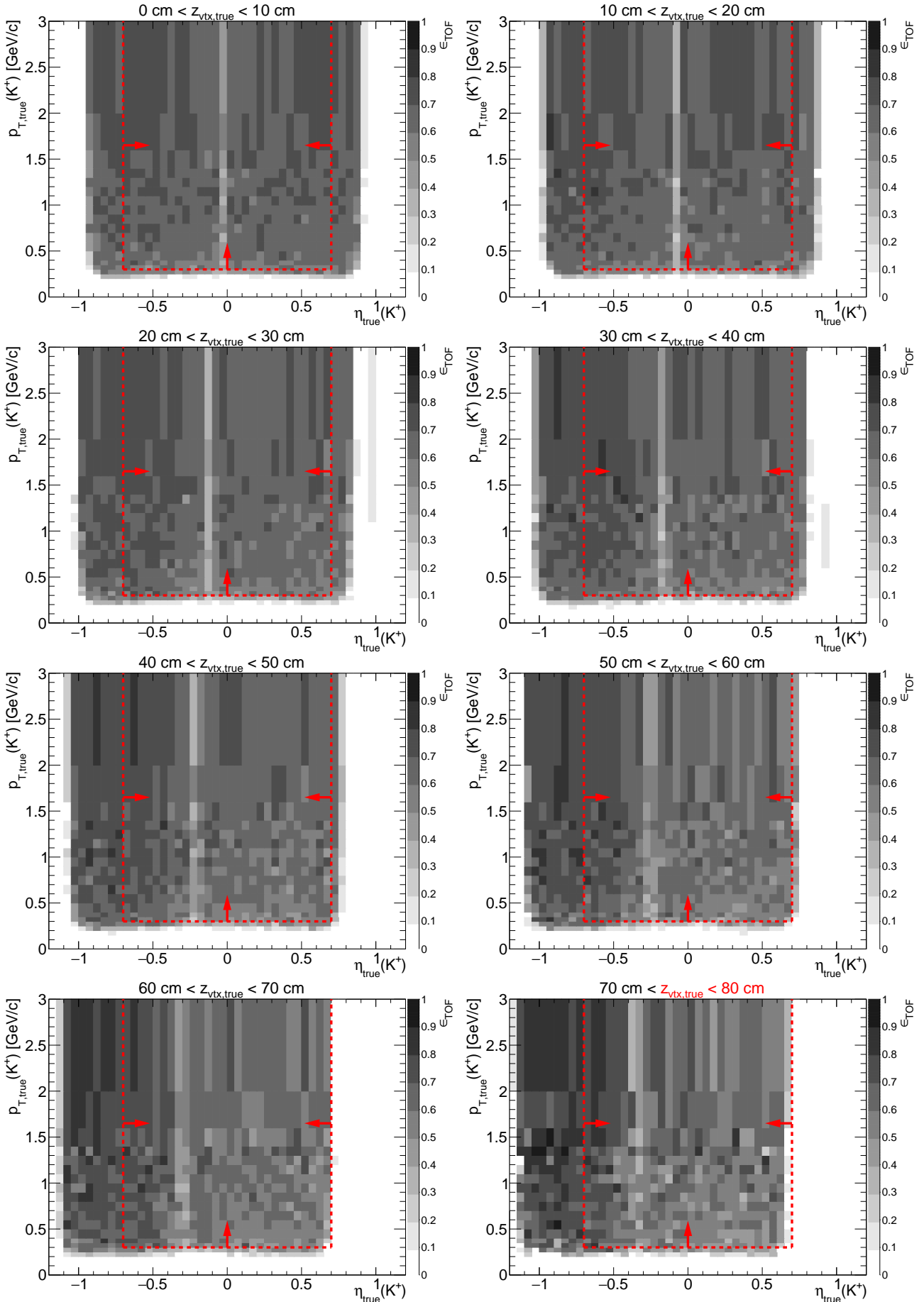
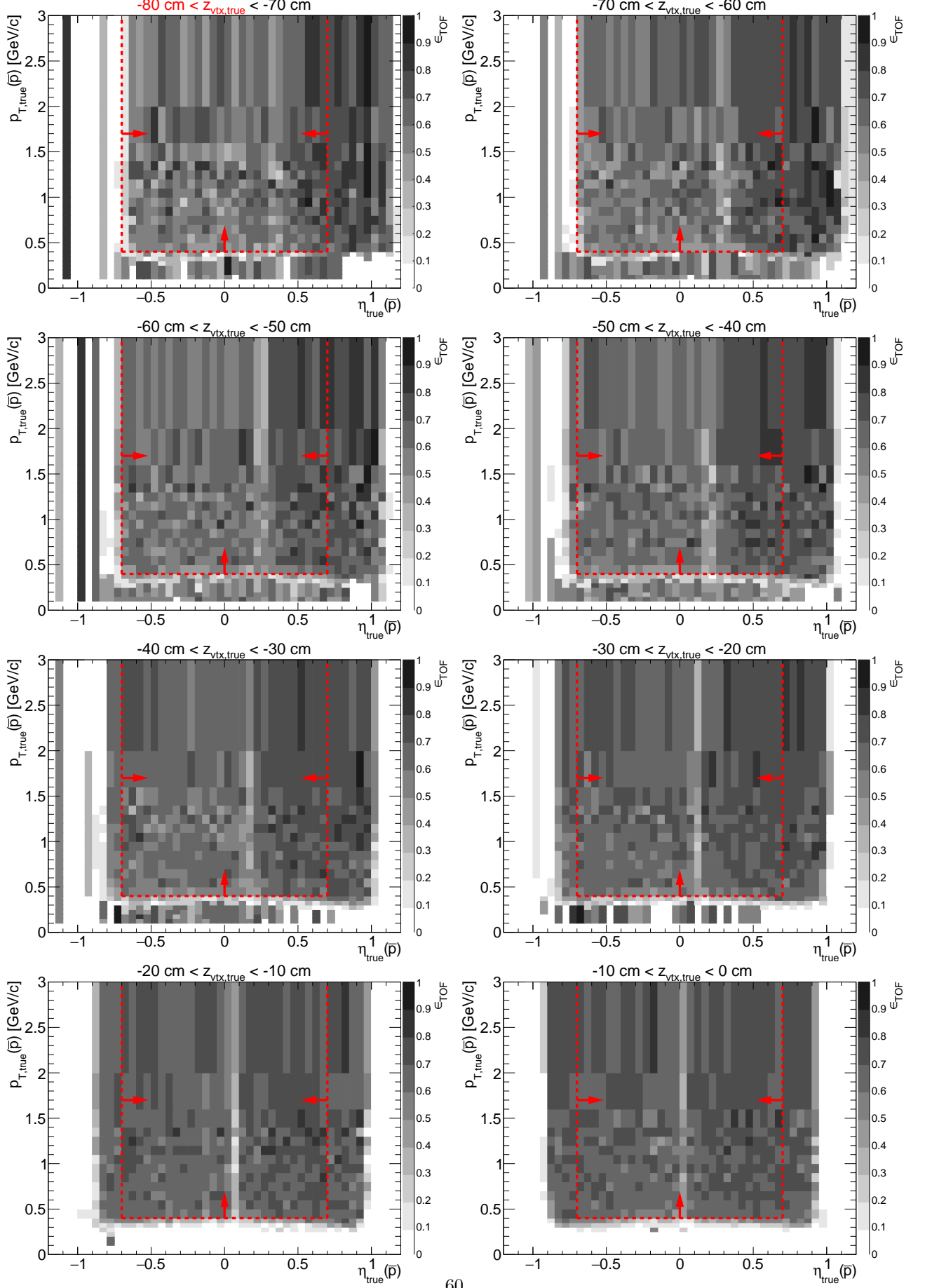


Figure B.5: TOF acceptance, reconstruction and matching efficiency of  $\bar{p}$ . Each plot represents the TOF efficiency  $\epsilon_{\text{TOF}}$  ( $z$ -axis) as a function of true particle pseudorapidity  $\eta$  ( $x$ -axis) and transverse momentum  $p_T$  ( $y$ -axis) in single  $z$ -vertex bin whose range is given at the top. Red lines and arrows indicate region accepted in analyses.



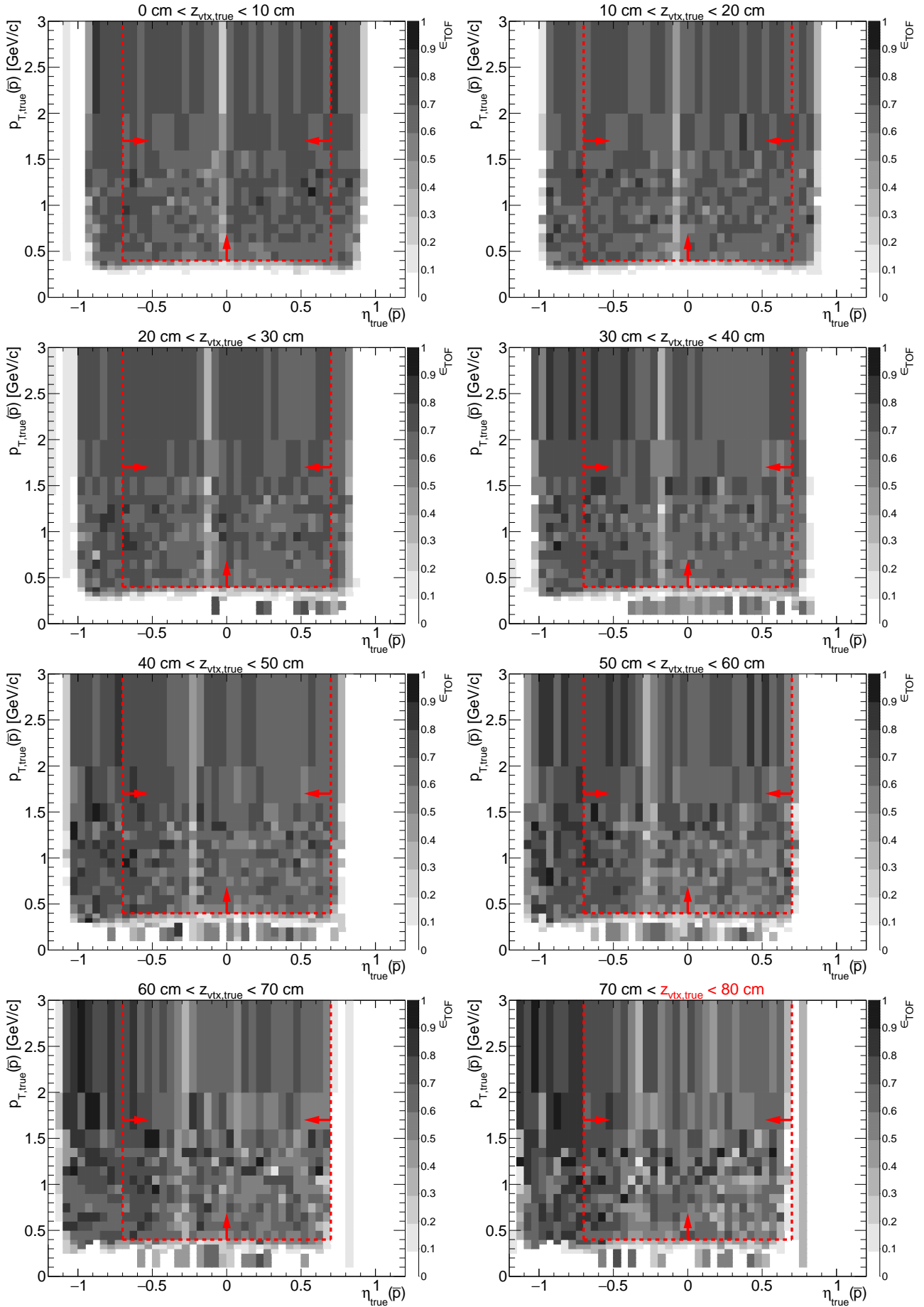
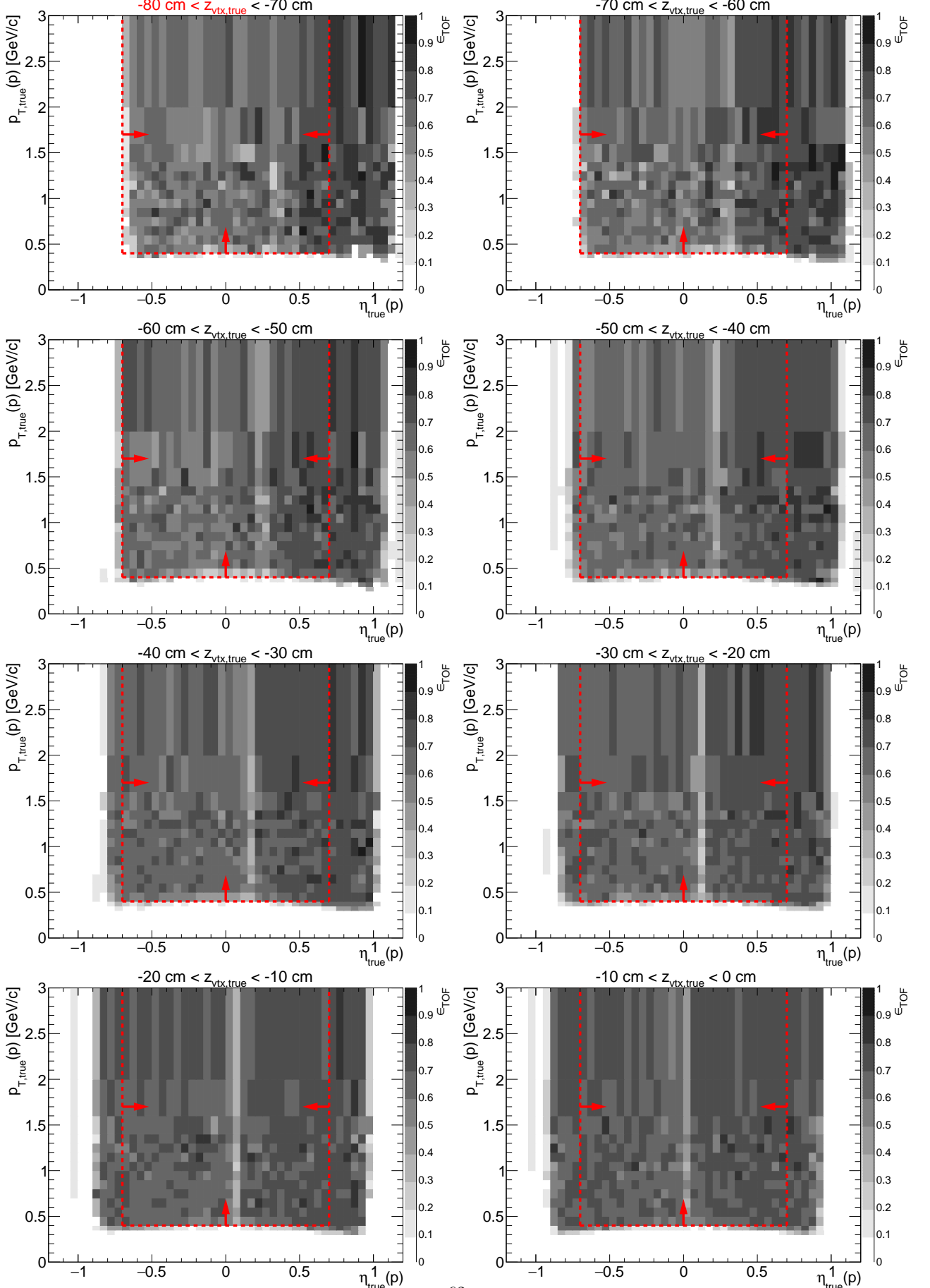
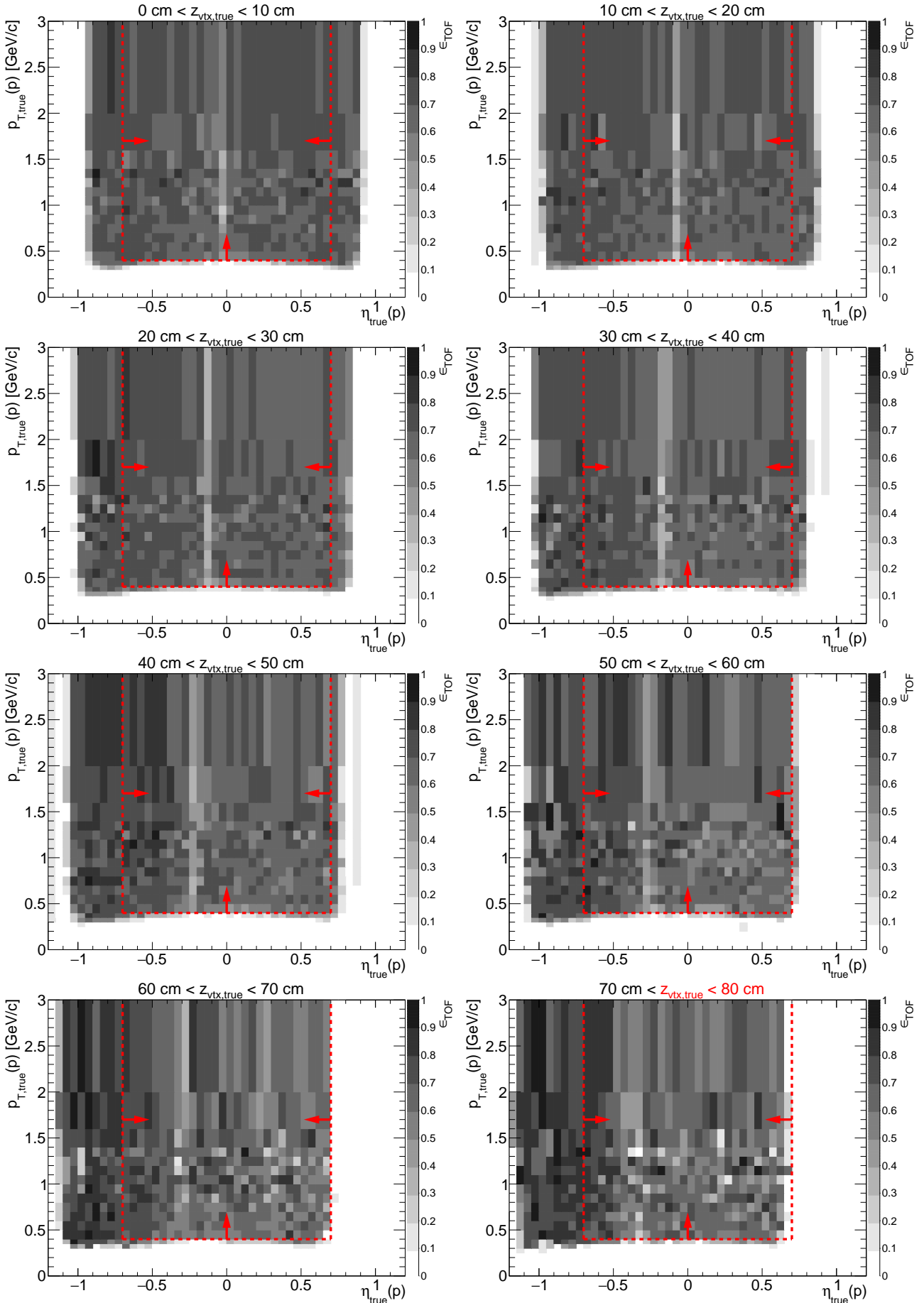


Figure B.6: TOF acceptance, reconstruction and matching efficiency of  $p$ . Each plot represents the TOF efficiency  $\epsilon_{\text{TOF}}$  ( $z$ -axis) as a function of true particle pseudorapidity  $\eta$  ( $x$ -axis) and transverse momentum  $p_T$  ( $y$ -axis) in single  $z$ -vertex bin whose range is given at the top. Red lines and arrows indicate region accepted in analyses.

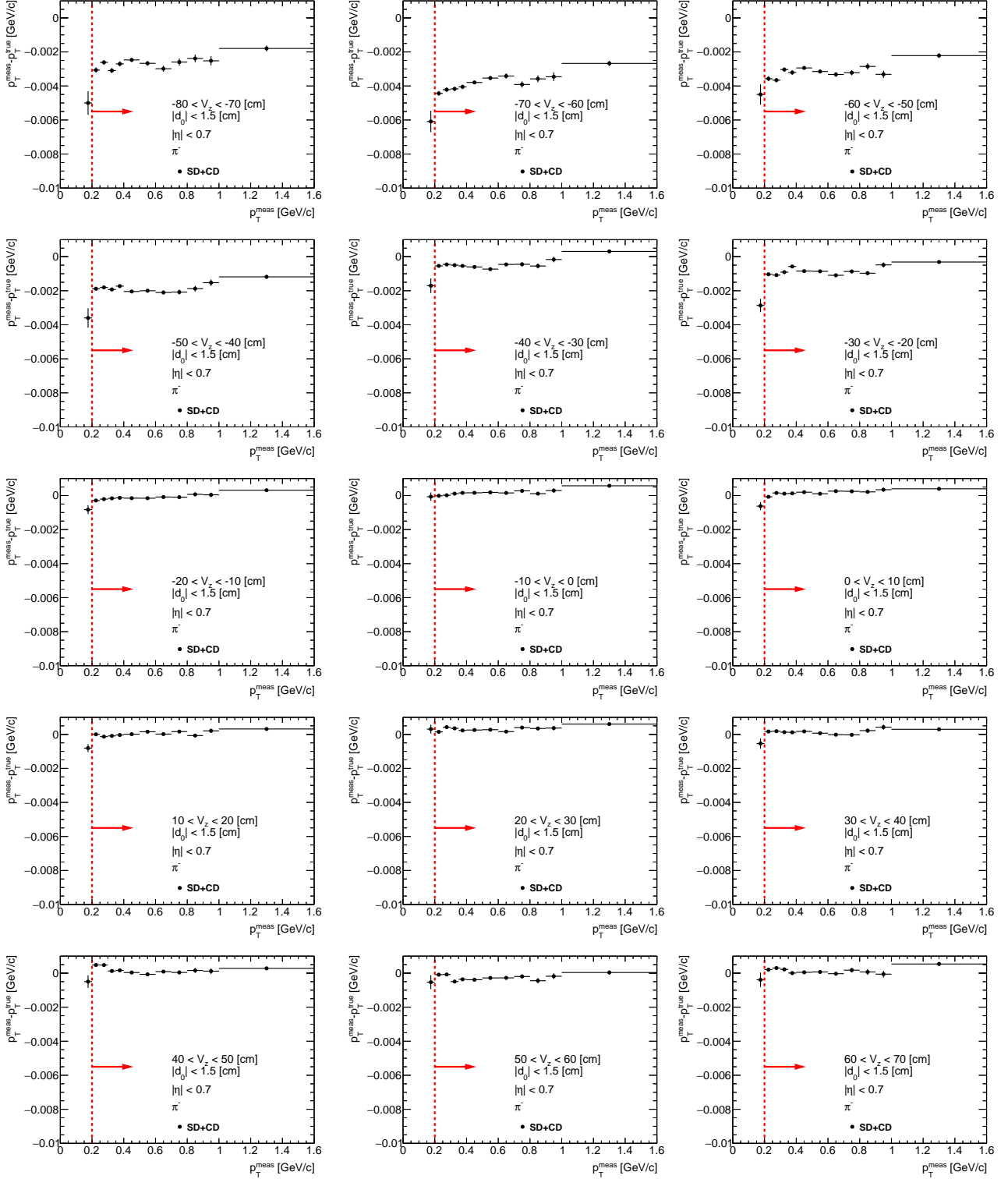




# Appendix C

## Energy Loss Correction

Figure C.1: Energy loss correction  $p_T^{meas} - p_T^{true}$  for  $\pi^-$  as a function of reconstructed transverse momentum  $p_T^{meas}$  ( $|\eta| < 0.7$ ) in single  $z$ -vertex bin whose range is given on each plot. Red lines and arrows indicate region accepted in analyses. One can notice an offset of about 3 – 4 MeV for negative  $z$ -vertex. It is a known issue with STAR simulation where HFT support material is badly described for negative  $z < -30$  cm.



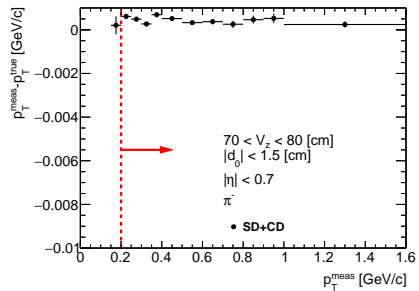


Figure C.2: Energy loss correction  $p_T^{meas} - p_T^{true}$  for  $\pi^+$  as a function of reconstructed transverse momentum  $p_T^{meas}$  ( $|\eta| < 0.7$ ) in single  $z$ -vertex bin whose range is given on each plot. Red lines and arrows indicate region accepted in analyses. One can notice an offset of about 3 – 4 MeV for negative  $z$ -vertex. It is a known issue with STAR simulation where HFT support material is badly described for negative  $z < -30$  cm.

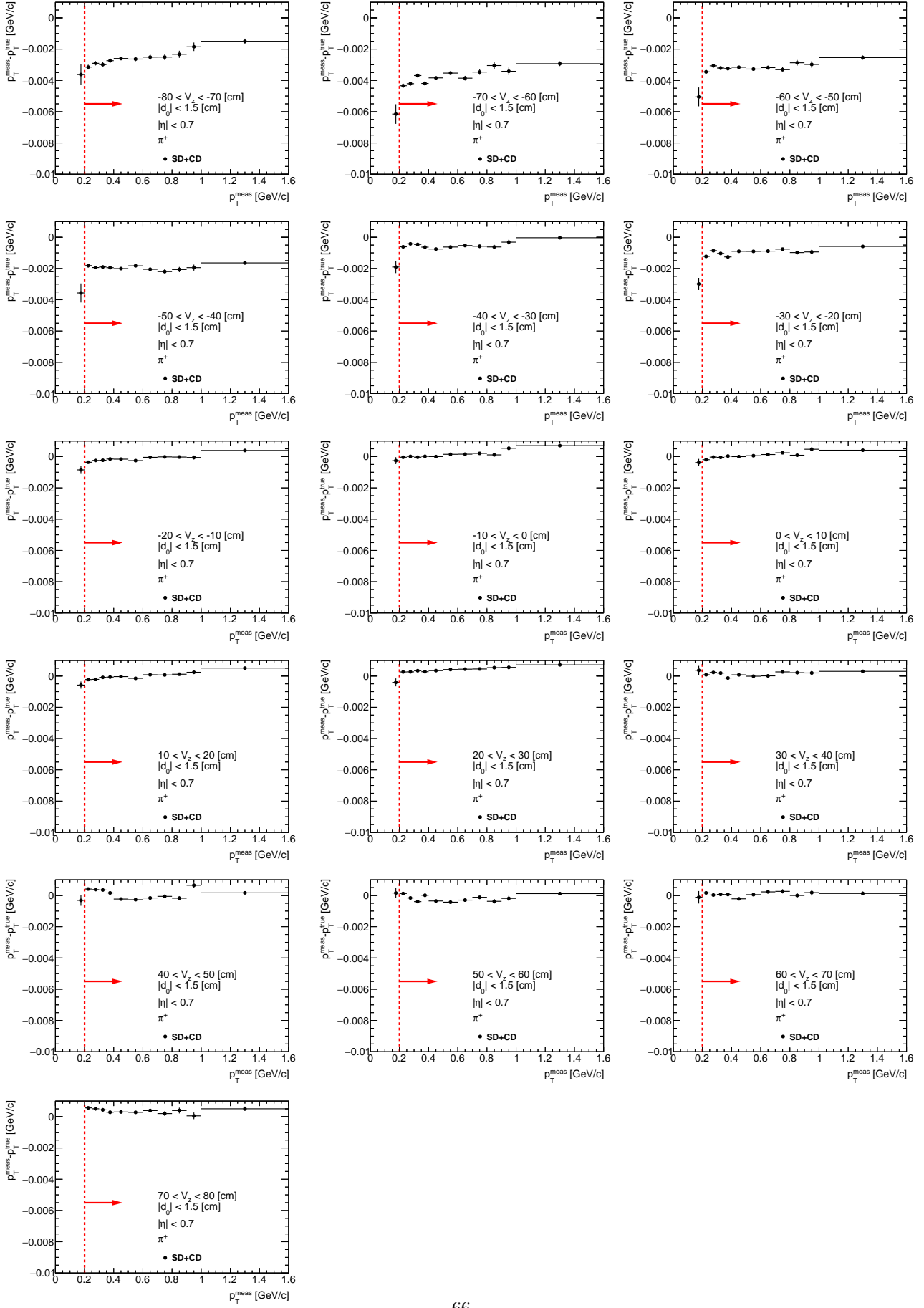


Figure C.3: Energy loss correction  $p_T^{meas} - p_T^{true}$  for  $K^+$  as a function of reconstructed transverse momentum  $p_T^{meas}$  ( $|\eta| < 0.7$ ) in single  $z$ -vertex bin whose range is given on each plot. Red lines and arrows indicate region accepted in analyses.

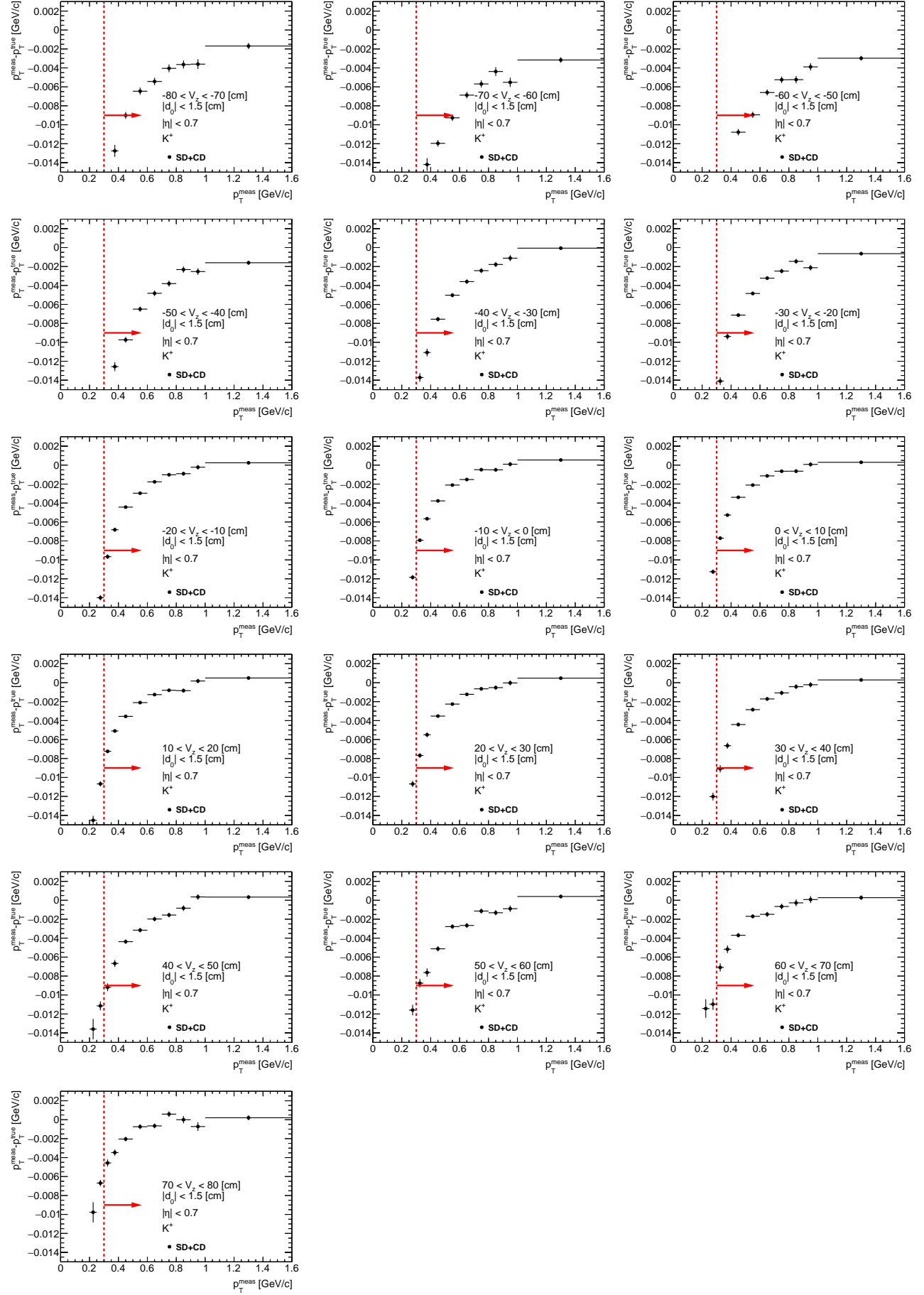


Figure C.4: Energy loss correction  $p_T^{meas} - p_T^{true}$  for  $\bar{p}$  as a function of reconstructed transverse momentum  $p_T^{meas}$  ( $|\eta| < 0.7$ ) in single  $z$ -vertex bin whose range is given on each plot. Red lines and arrows indicate region accepted in analyses.

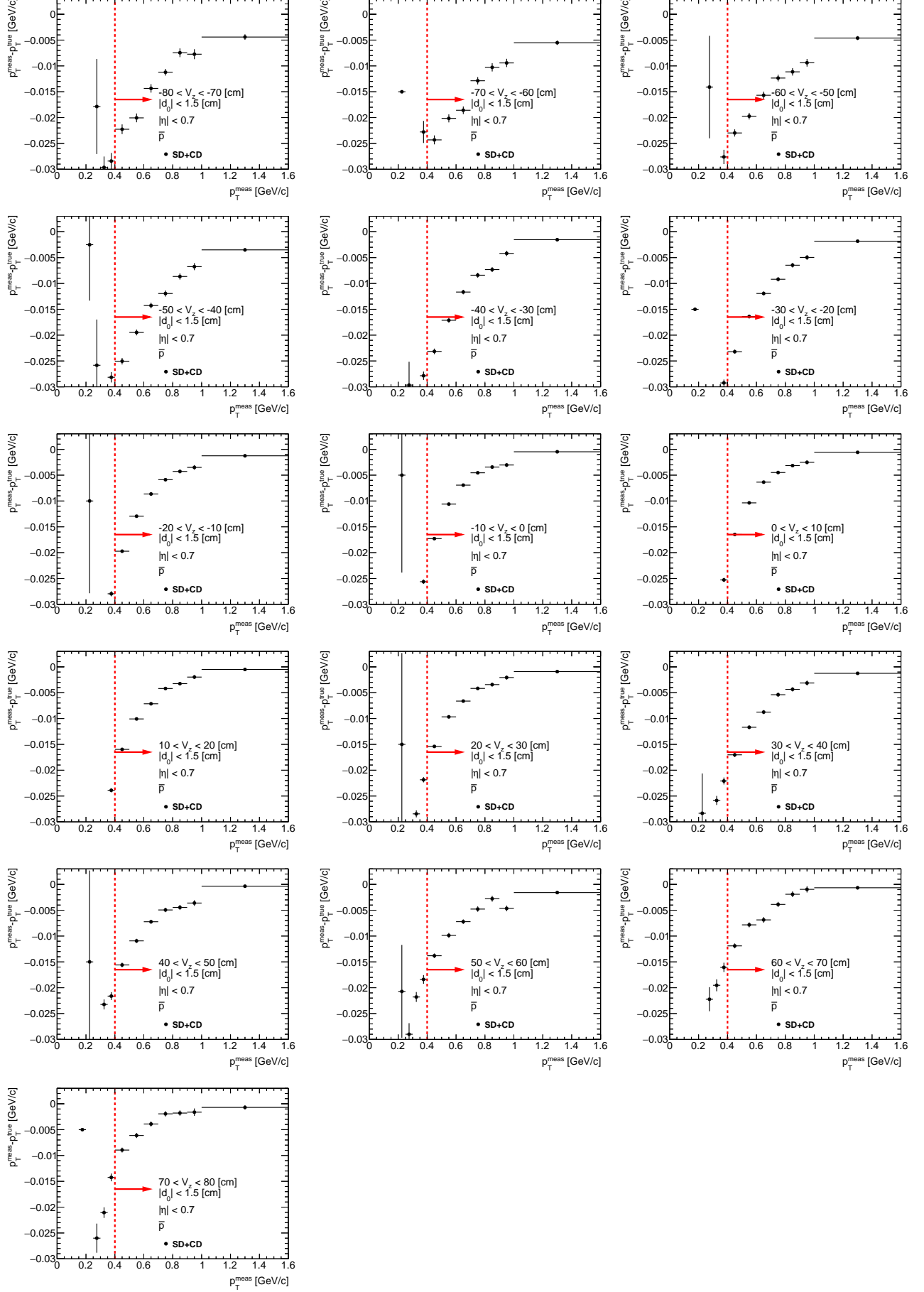


Figure C.5: Energy loss correction  $p_T^{meas} - p_T^{true}$  for  $p$  as a function of reconstructed transverse momentum  $p_T^{meas}$  ( $|\eta| < 0.7$ ) in single  $z$ -vertex bin whose range is given on each plot. Red lines and arrows indicate region accepted in analyses.

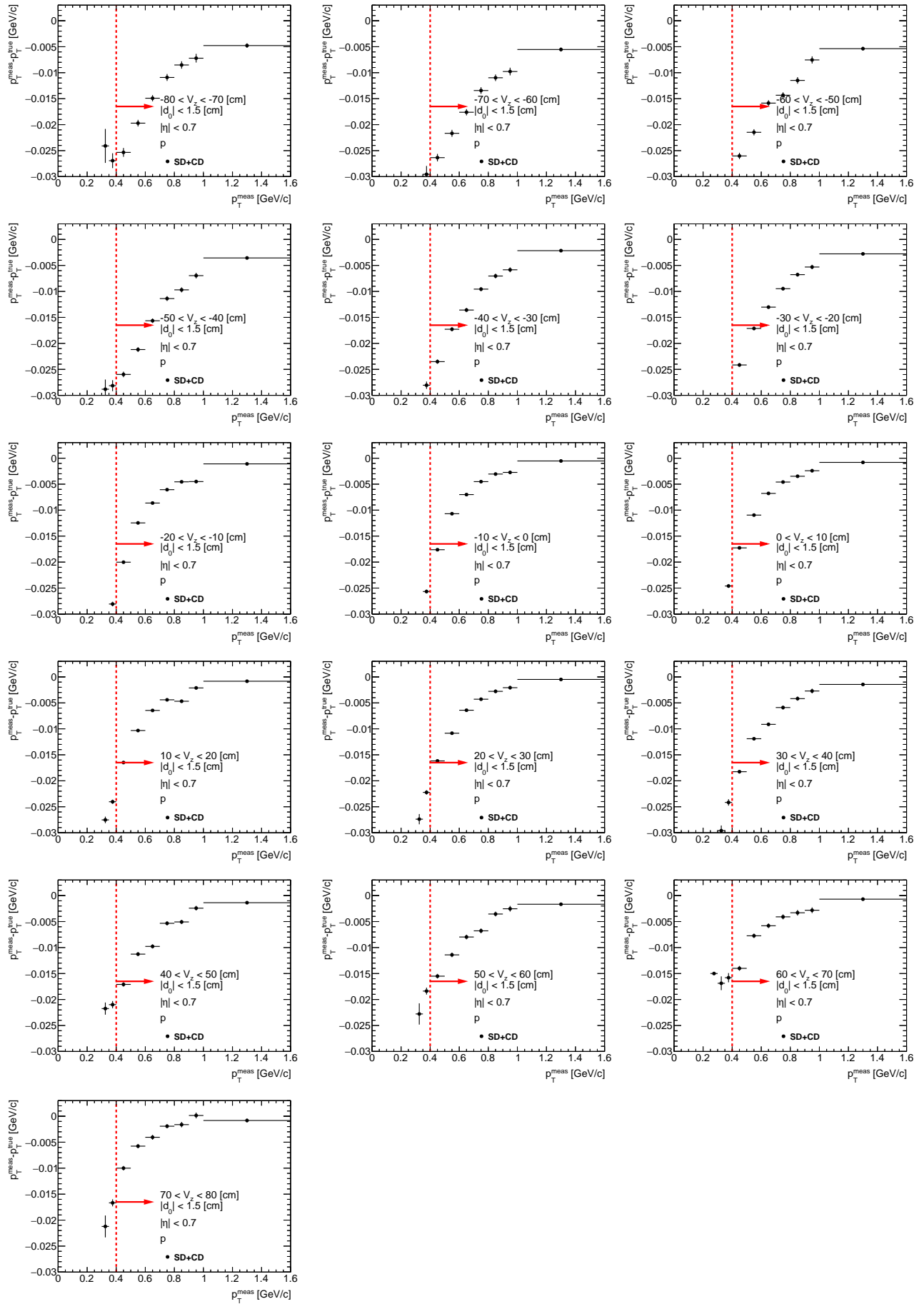


Figure C.6: Energy loss correction  $p_T^{meas} - p_T^{true}$  for negative particles as a function of reconstructed transverse momentum  $p_T^{meas}$  ( $|\eta| < 0.7$ ) in single  $z$ -vertex bin whose range is given on each plot. Red lines and arrows indicate region accepted in analyses.

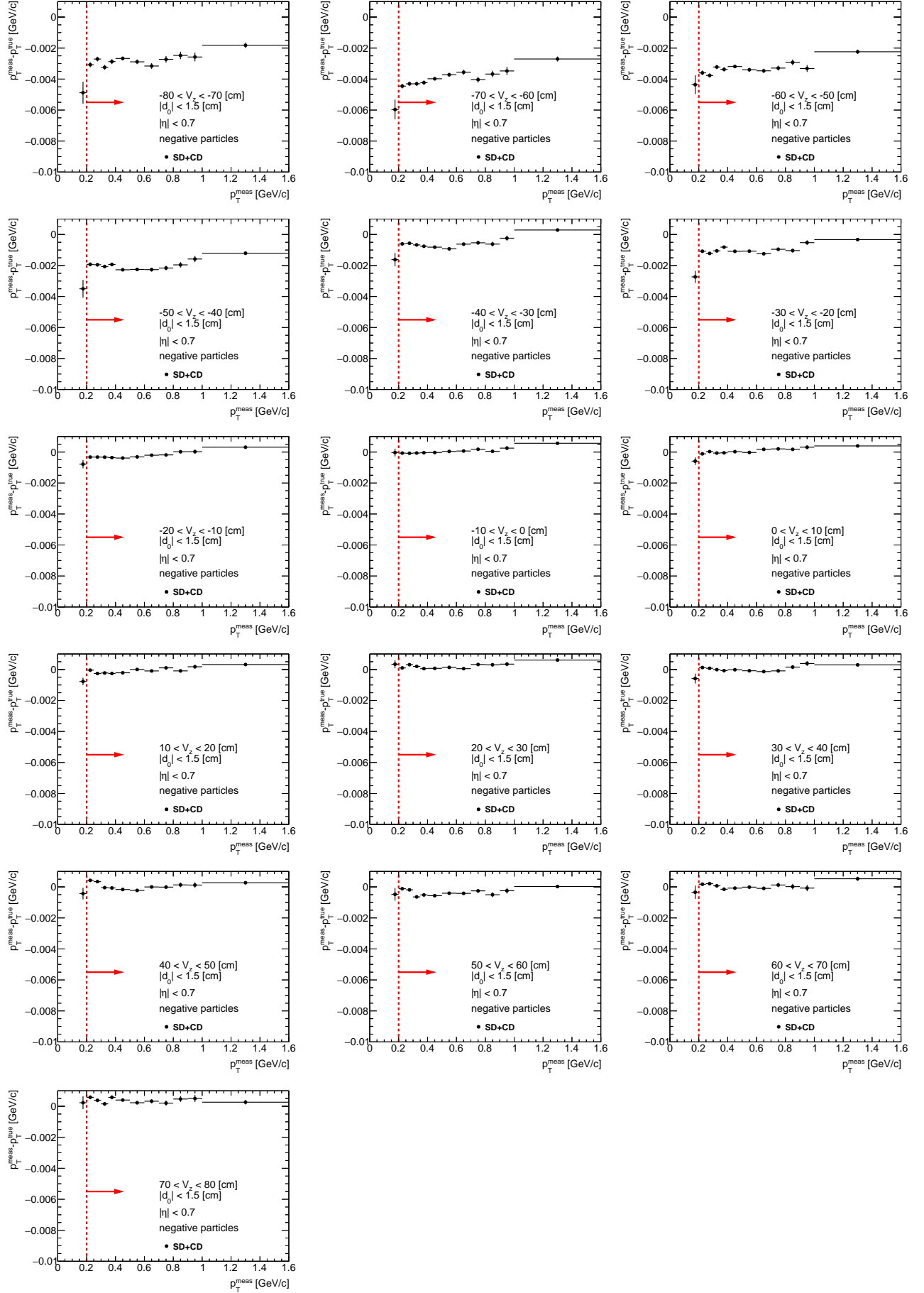


Figure C.7: Energy loss correction  $p_T^{meas} - p_T^{true}$  for positive particles as a function of reconstructed transverse momentum  $p_T^{meas}$  ( $|\eta| < 0.7$ ) in single  $z$ -vertex bin whose range is given on each plot. Red lines and arrows indicate region accepted in analyses.

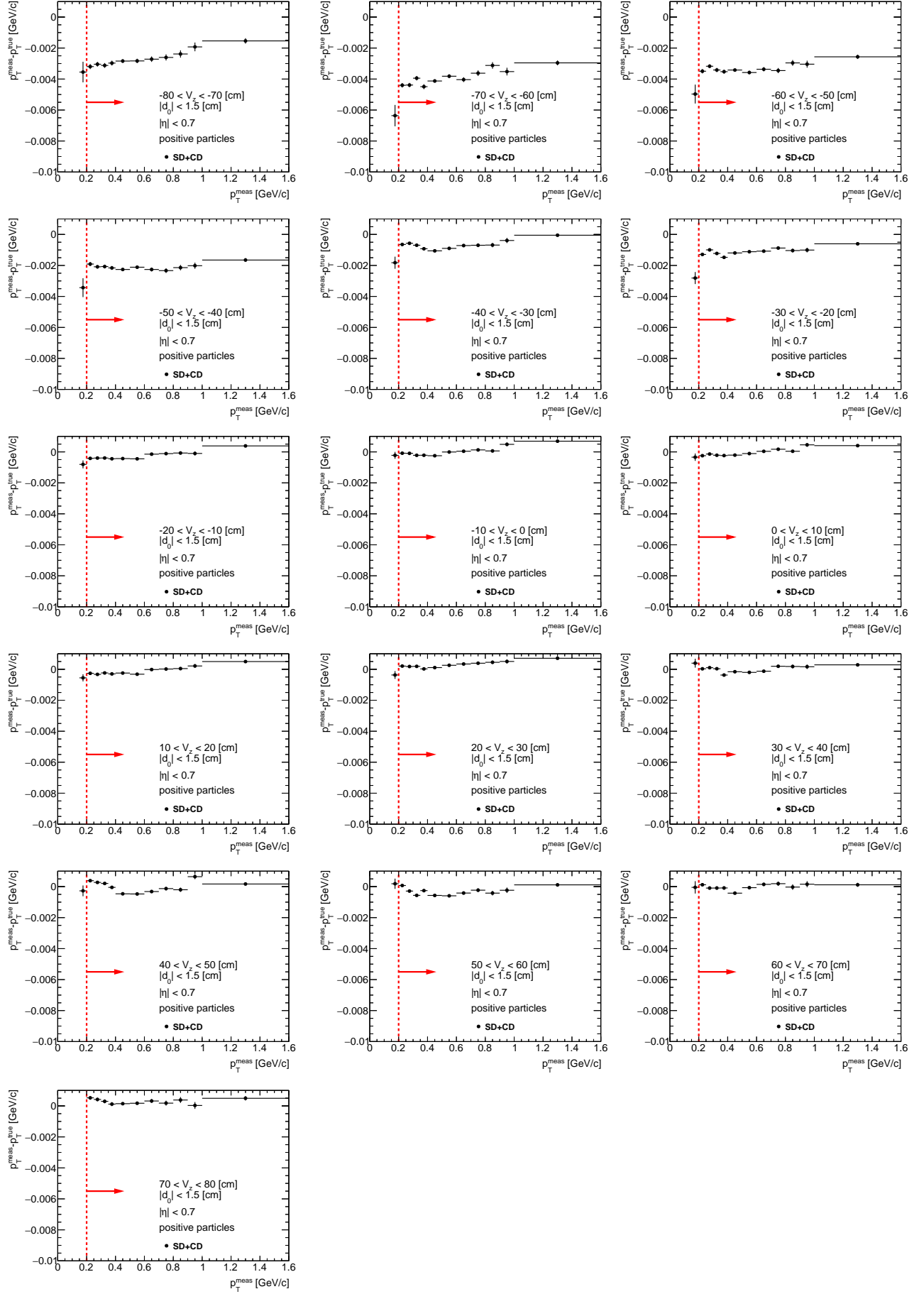
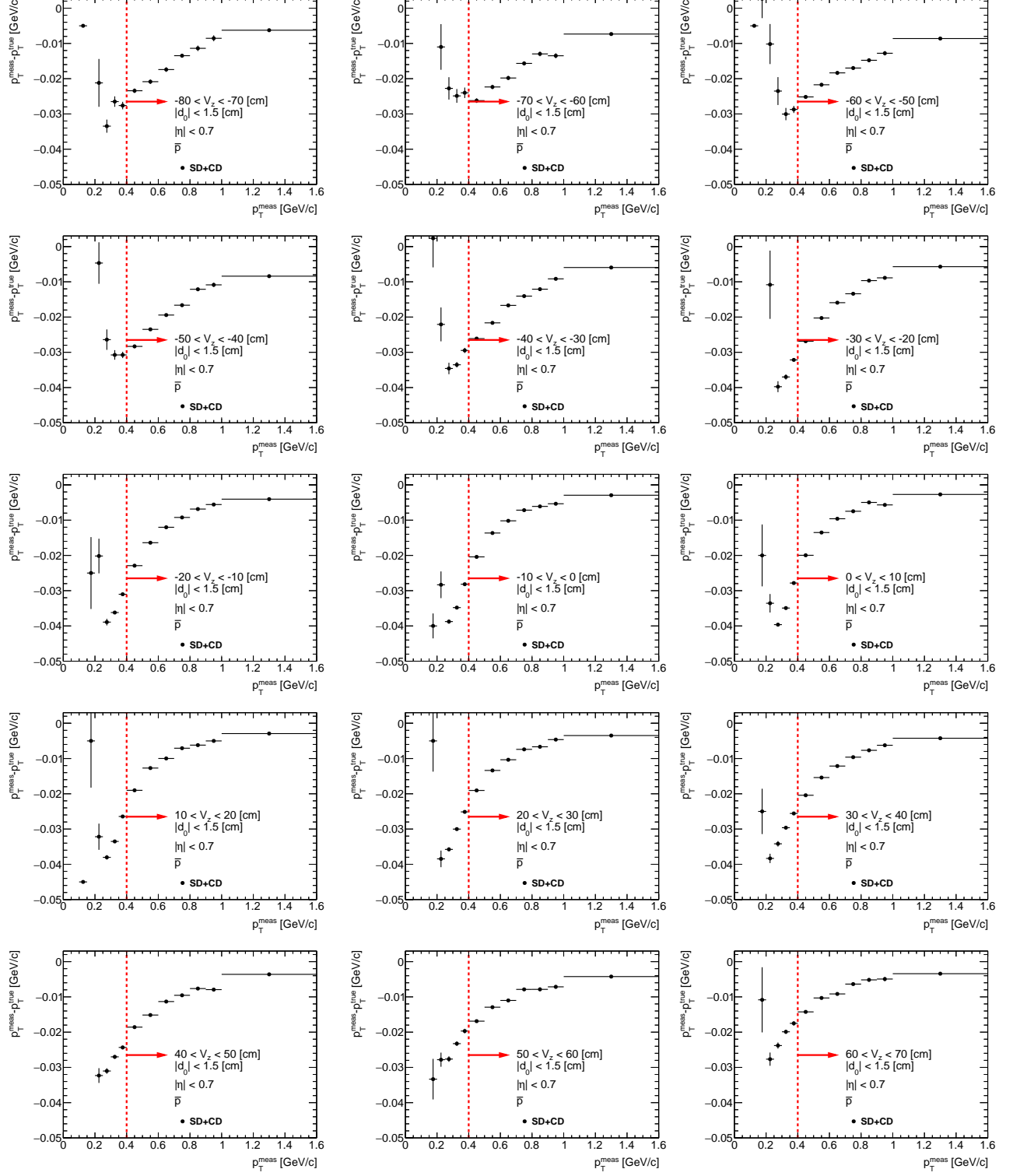


Figure C.8: Energy loss correction  $p_T^{meas} - p_T^{true}$  for  $\bar{p}$  as a function of reconstructed global track transverse momentum  $p_T^{meas}$  ( $|\eta| < 0.7$ ) in single  $z$ -vertex bin whose range is given on each plot. Red lines and arrows indicate region accepted in analyses. One may need the energy loss correction for reconstructed global proton and antiproton tracks to estimate the knock-out proton background. During the reconstruction, global tracks are corrected only for energy losses in TPC, whereas primary tracks have the information of dead material inside and in front of TPC. Since that, there is an offset of about 4 MeV for global tracks.



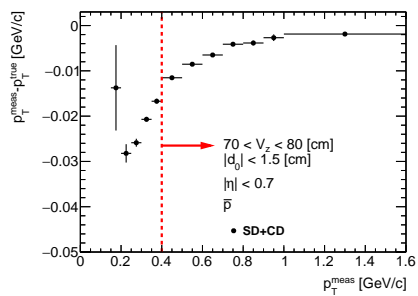
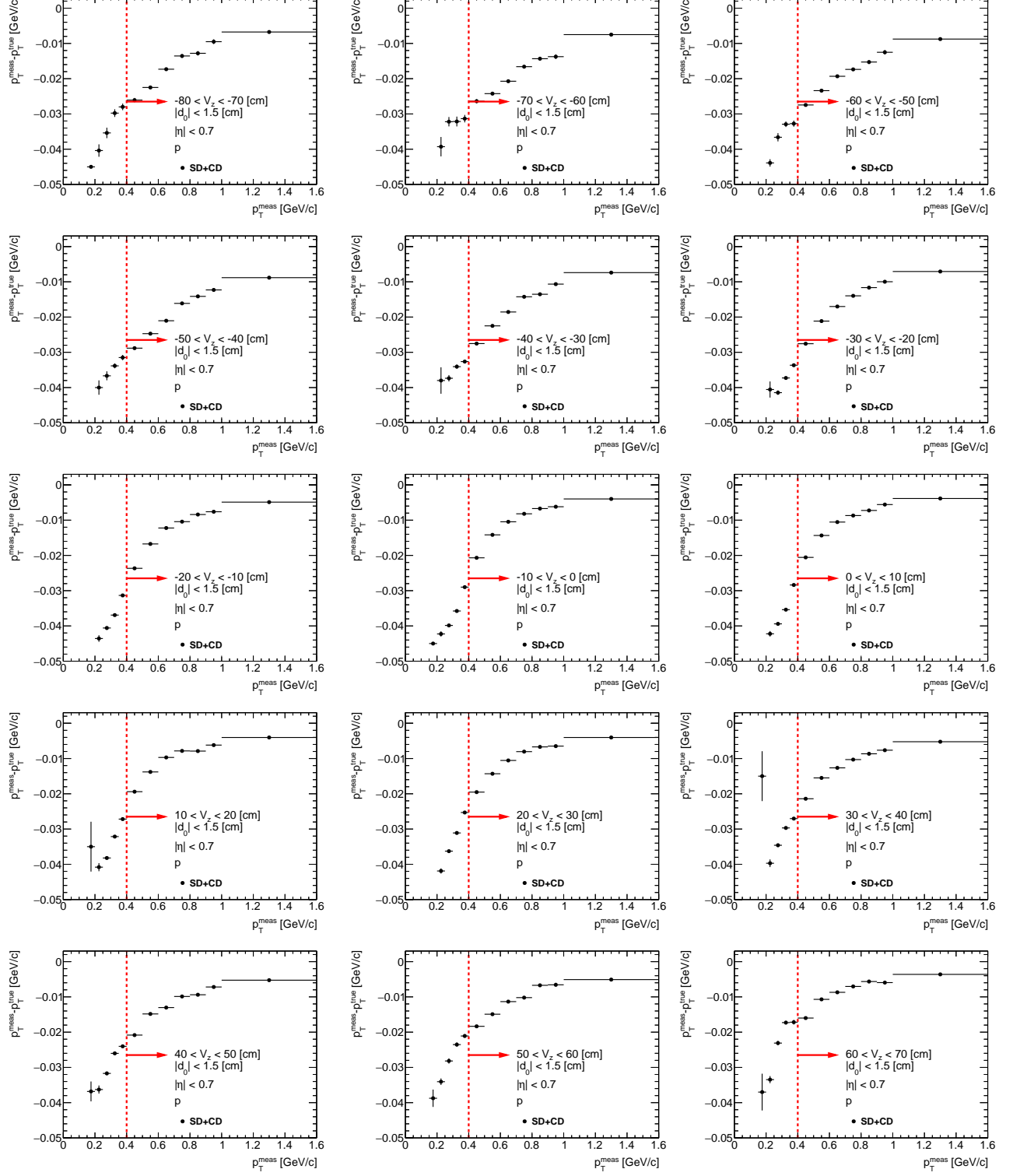
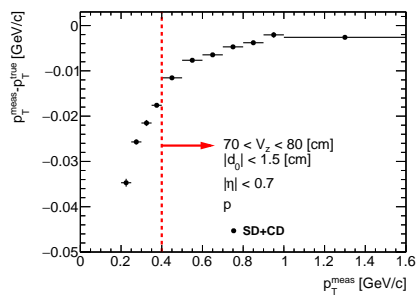


Figure C.9: Energy loss correction  $p_T^{meas} - p_T^{true}$  for  $p$  as a function of reconstructed global track transverse momentum  $p_T^{meas}$  ( $|\eta| < 0.7$ ) in single  $z$ -vertex bin whose range is given on each plot. Red lines and arrows indicate region accepted in analyses. One may need the energy loss correction for reconstructed global proton and antiproton tracks to estimate the knock-out proton background. During the reconstruction, global tracks are corrected only for energy losses in TPC, whereas primary tracks have the information of dead material inside and in front of TPC. Since that, there is an offset of about 4 MeV for global tracks.

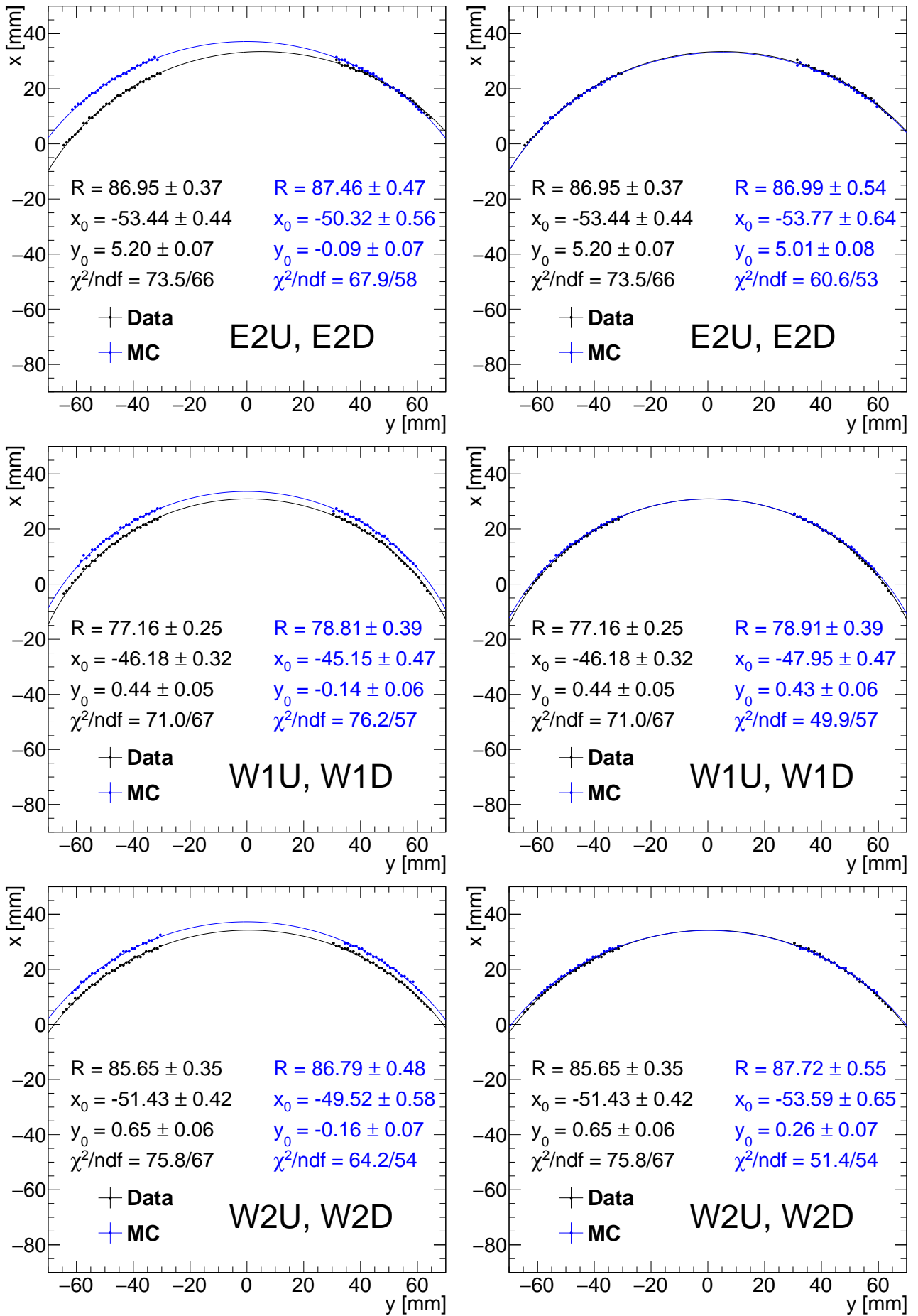




# **Appendix D**

## **Apertures tuning in Geant4 simulation**

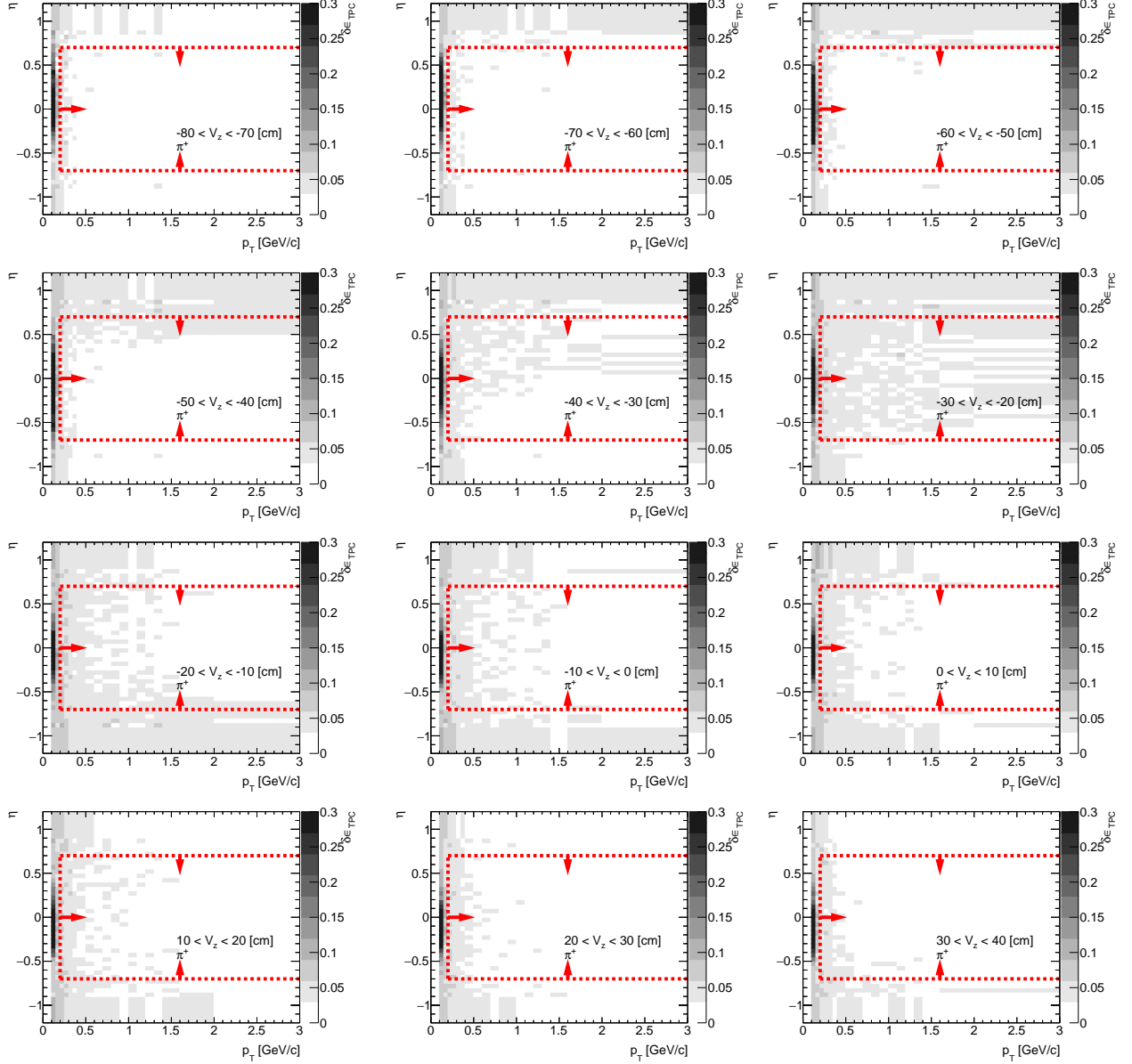
Figure D.1: Apertures.



# Appendix E

## Dead material effect on TPC track reconstruction efficiency

Figure E.1: The amount of lost  $\pi^-$  due to the interaction with dead material in front of TPC in CD MC sample. Each plot represents the fraction of lost  $\pi^+$ ,  $\delta\epsilon_{TPC}$  ( $z$ -axis), as a function of true particle pseudorapidity  $\eta$  ( $y$ -axis) and transverse momentum  $p_T$  ( $x$ -axis) in single  $z$ -vertex bin.



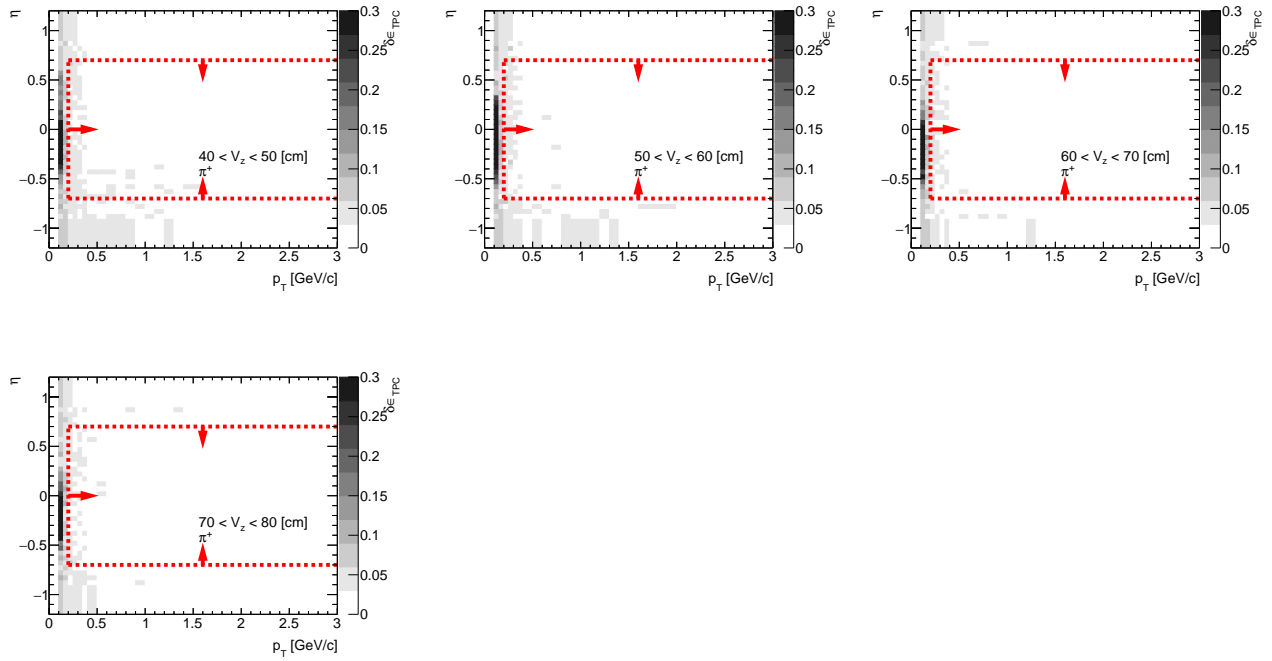


Figure E.2: The amount of lost  $K^-$  due to the interaction with dead material in front of TPC in CD MC sample. Each plot represents the fraction of lost  $K^-$ ,  $\delta\epsilon_{TPC}$  ( $z$ -axis), as a function of true particle pseudorapidity  $\eta$  ( $y$ -axis) and transverse momentum  $p_T$  ( $x$ -axis) in single  $z$ -vertex bin.

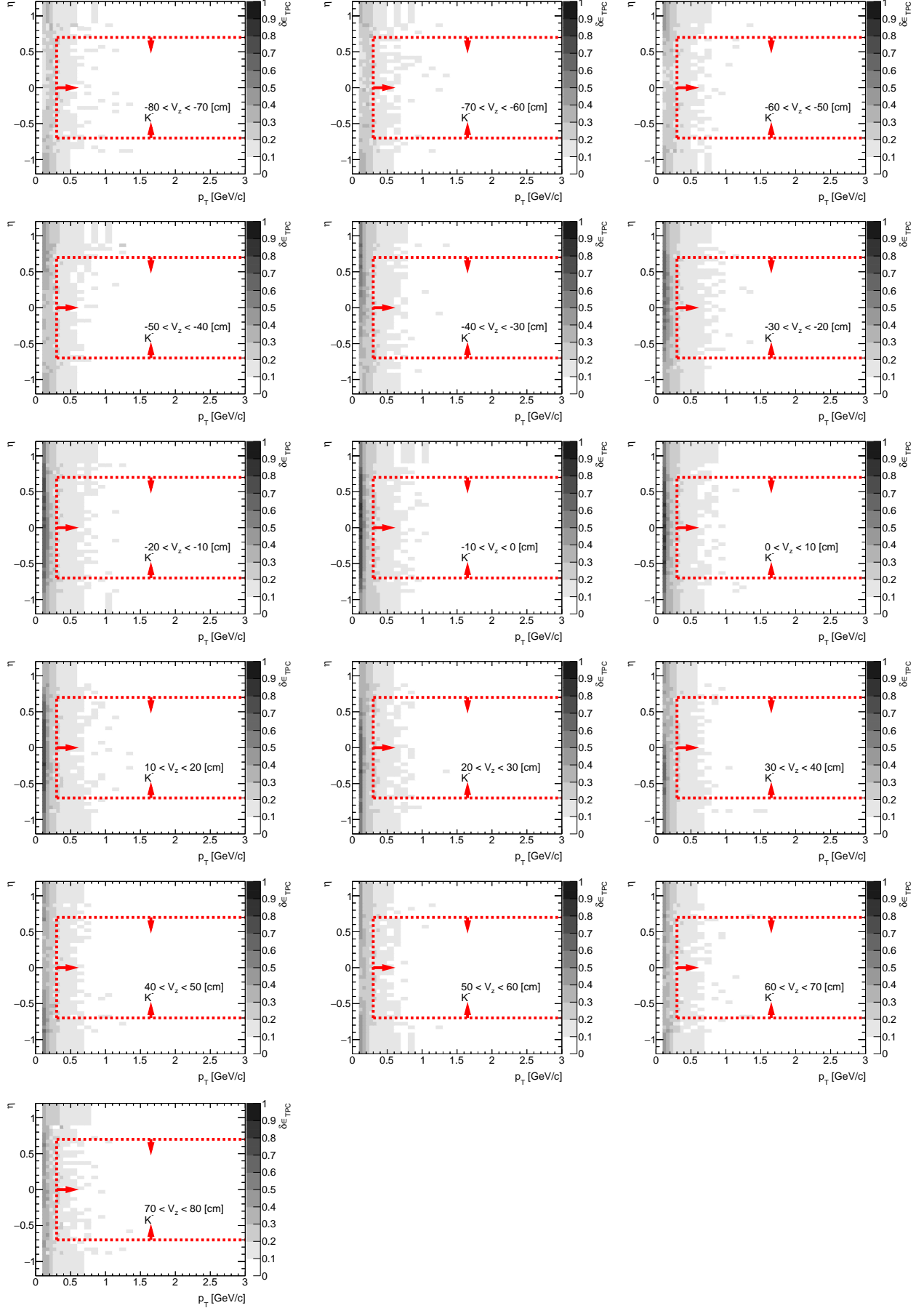


Figure E.3: The amount of lost  $K^+$  due to the interaction with dead material in front of TPC in CD MC sample. Each plot represents the fraction of lost  $K^+$ ,  $\delta\epsilon_{TPC}$  ( $z$ -axis), as a function of true particle pseudorapidity  $\eta$  ( $y$ -axis) and transverse momentum  $p_T$  ( $x$ -axis) in single  $z$ -vertex bin.

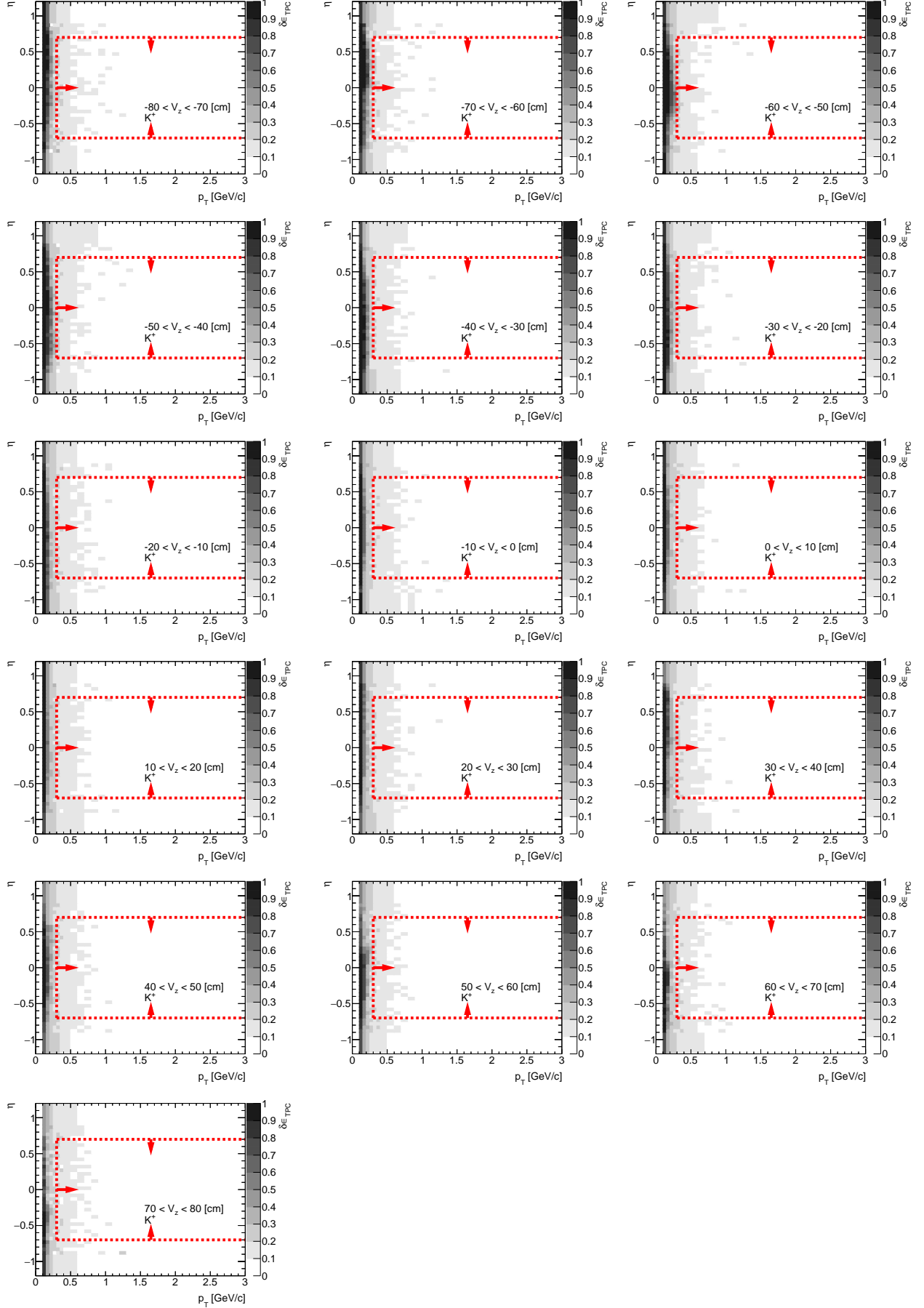


Figure E.4: The amount of lost  $\bar{p}$  due to the interaction with dead material in front of TPC in CD MC sample. Each plot represents the fraction of lost  $\bar{p}$ ,  $\delta\epsilon_{TPC}$  ( $z$ -axis), as a function of true particle pseudorapidity  $\eta$  ( $y$ -axis) and transverse momentum  $p_T$  ( $x$ -axis) in single  $z$ -vertex bin.

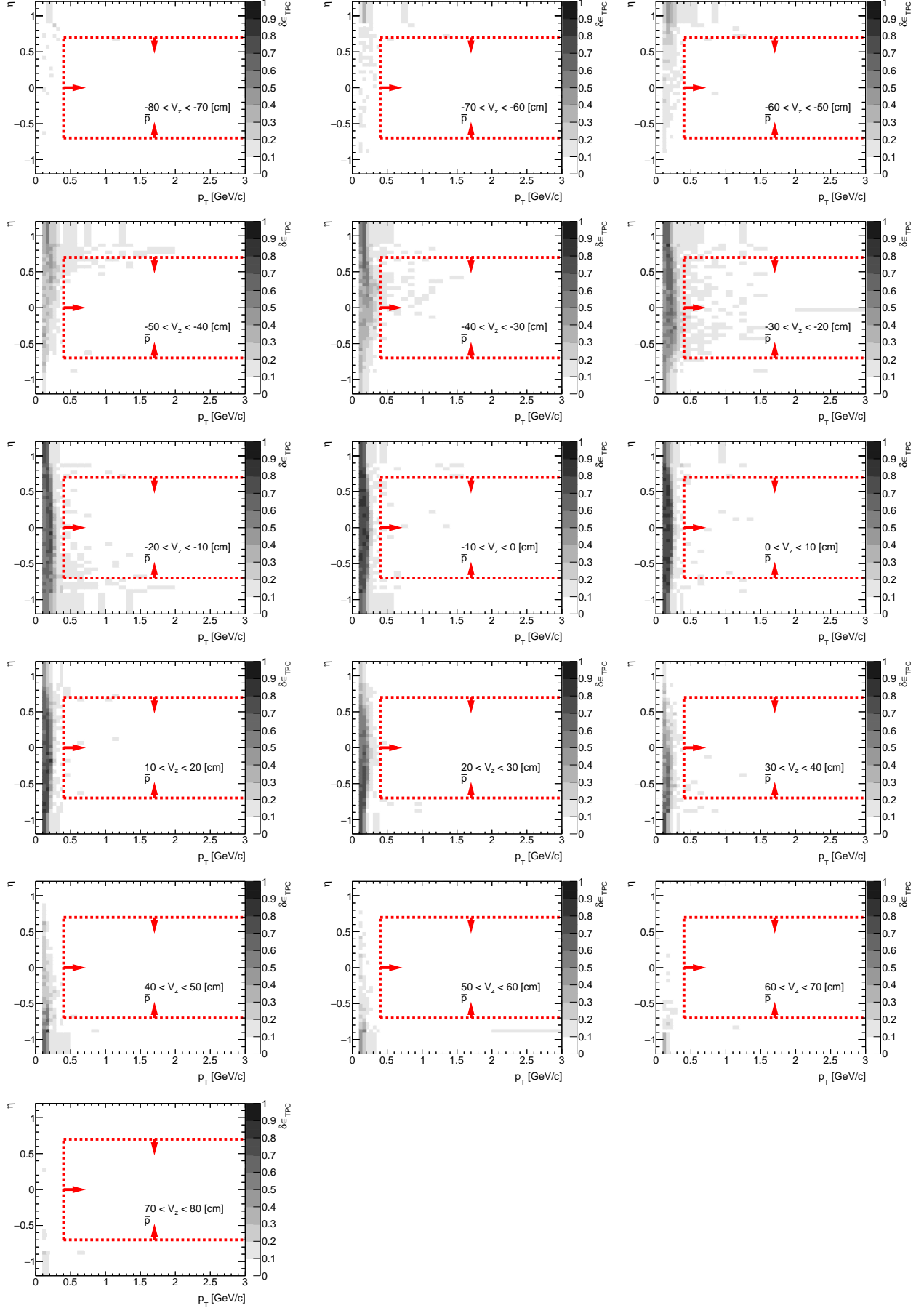


Figure E.5: The amount of lost  $p$  due to the interaction with dead material in front of TPC in CD MC sample. Each plot represents the fraction of lost  $p$ ,  $\delta\epsilon_{TPC}$  ( $z$ -axis), as a function of true particle pseudorapidity  $\eta$  ( $y$ -axis) and transverse momentum  $p_T$  ( $x$ -axis) in single  $z$ -vertex bin.

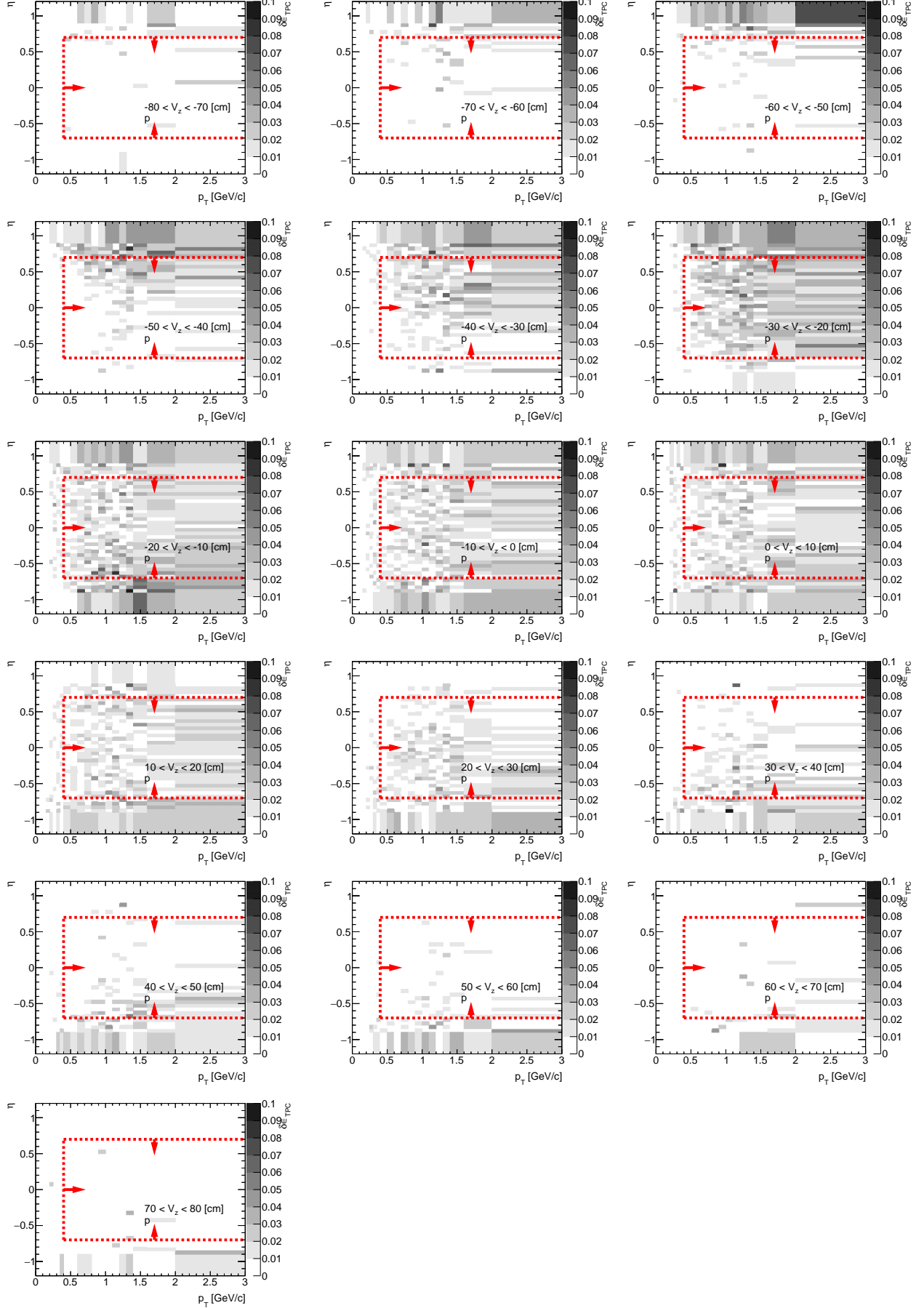


Figure E.6: The amount of lost negative particles due to the interaction with dead material in front of TPC in CD MC sample. Each plot represents the fraction of lost negative particles,  $\delta\epsilon_{TPC}$  (z-axis), as a function of true particle pseudorapidity  $\eta$  (y-axis) and transverse momentum  $p_T$  (x-axis) in single  $z$ -vertex bin.

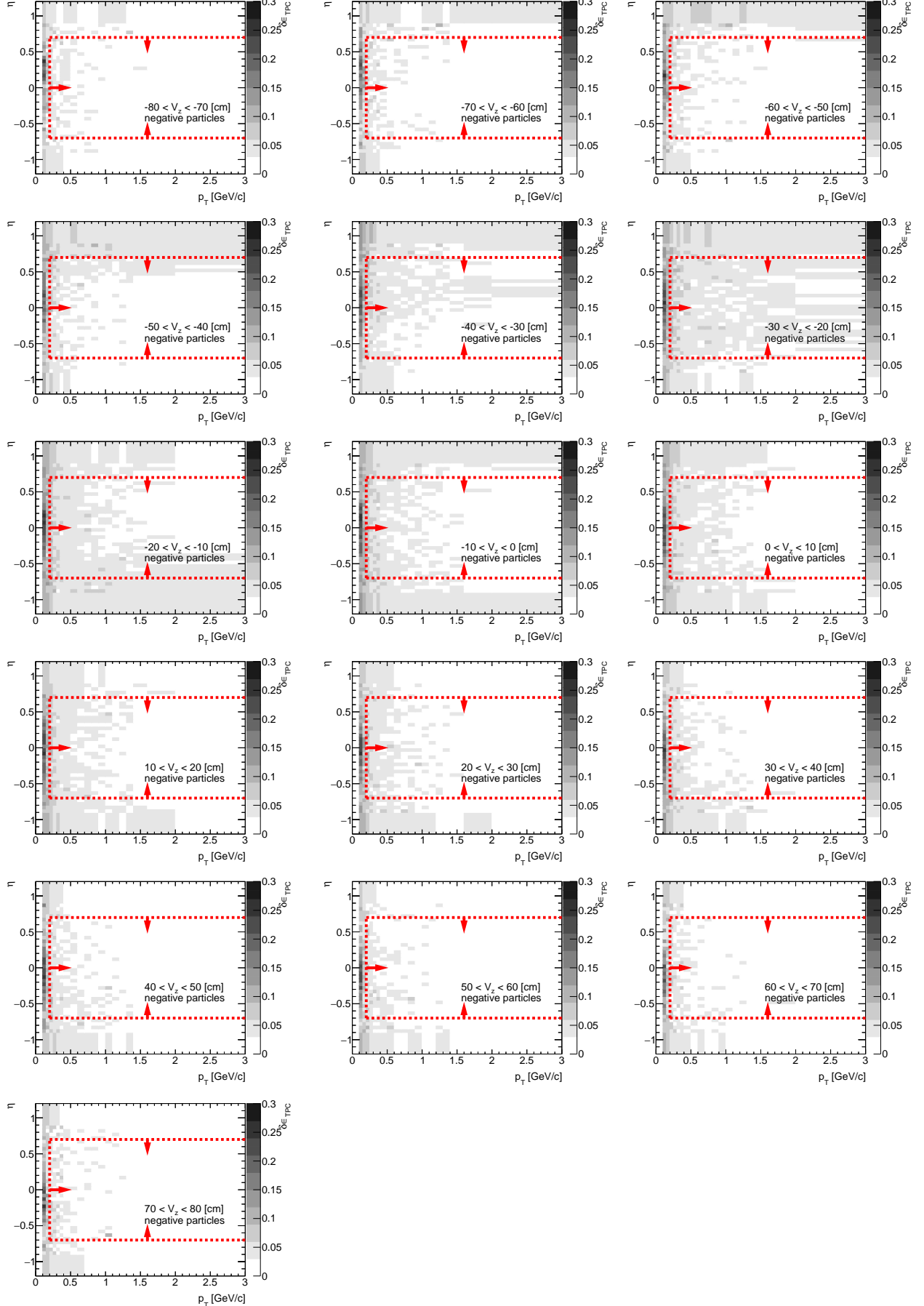


Figure E.7: The amount of lost positive particles due to the interaction with dead material in front of TPC in CD MC sample. Each plot represents the fraction of lost positive particles,  $\delta\epsilon_{TPC}$  (z-axis), as a function of true particle pseudorapidity  $\eta$  (y-axis) and transverse momentum  $p_T$  (x-axis) in single  $z$ -vertex bin.

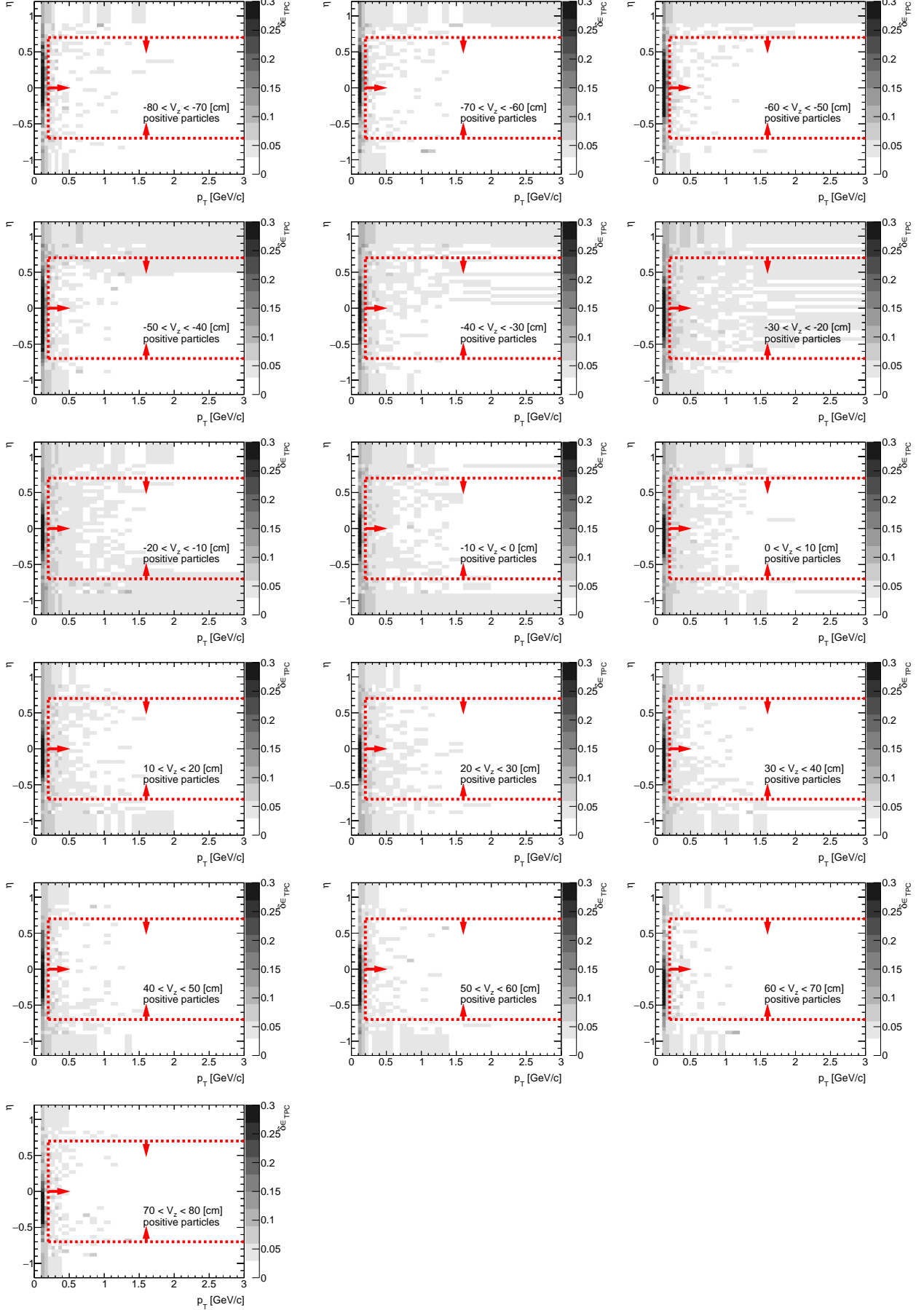


Figure E.8: The amount of lost  $\pi^-$  due to the interaction with dead material in front of TPC in SD MC sample. Each plot represents the fraction of lost  $\pi^-$ ,  $\delta\epsilon_{TPC}$  ( $z$ -axis), as a function of true particle pseudorapidity  $\eta$  ( $y$ -axis) and transverse momentum  $p_T$  ( $x$ -axis) in single  $z$ -vertex bin.

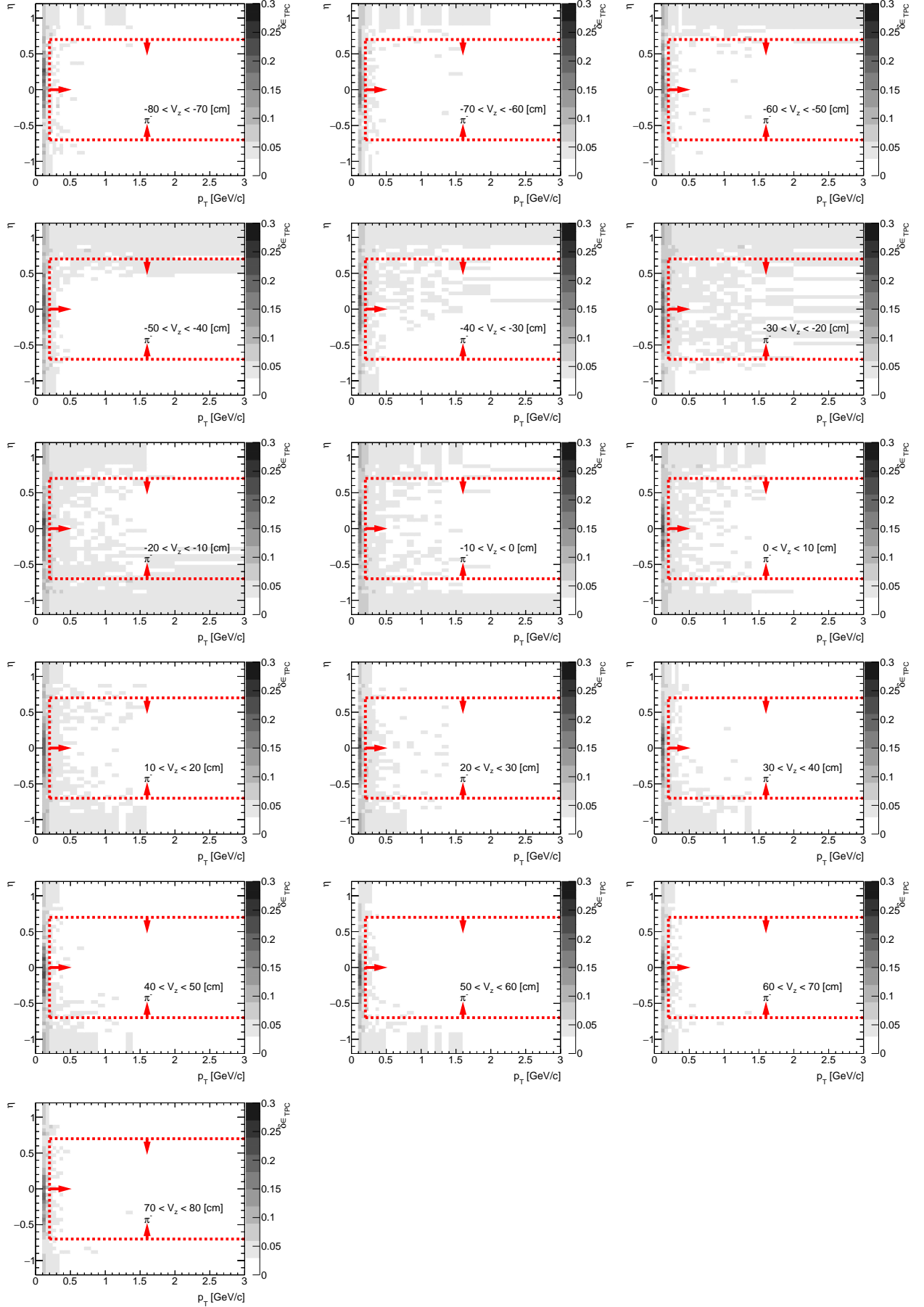


Figure E.9: The amount of lost  $\pi^+$  due to the interaction with dead material in front of TPC in SD MC sample. Each plot represents the fraction of lost  $\pi^+$ ,  $\delta\epsilon_{TPC}$  ( $z$ -axis), as a function of true particle pseudorapidity  $\eta$  ( $y$ -axis) and transverse momentum  $p_T$  ( $x$ -axis) in single  $z$ -vertex bin.

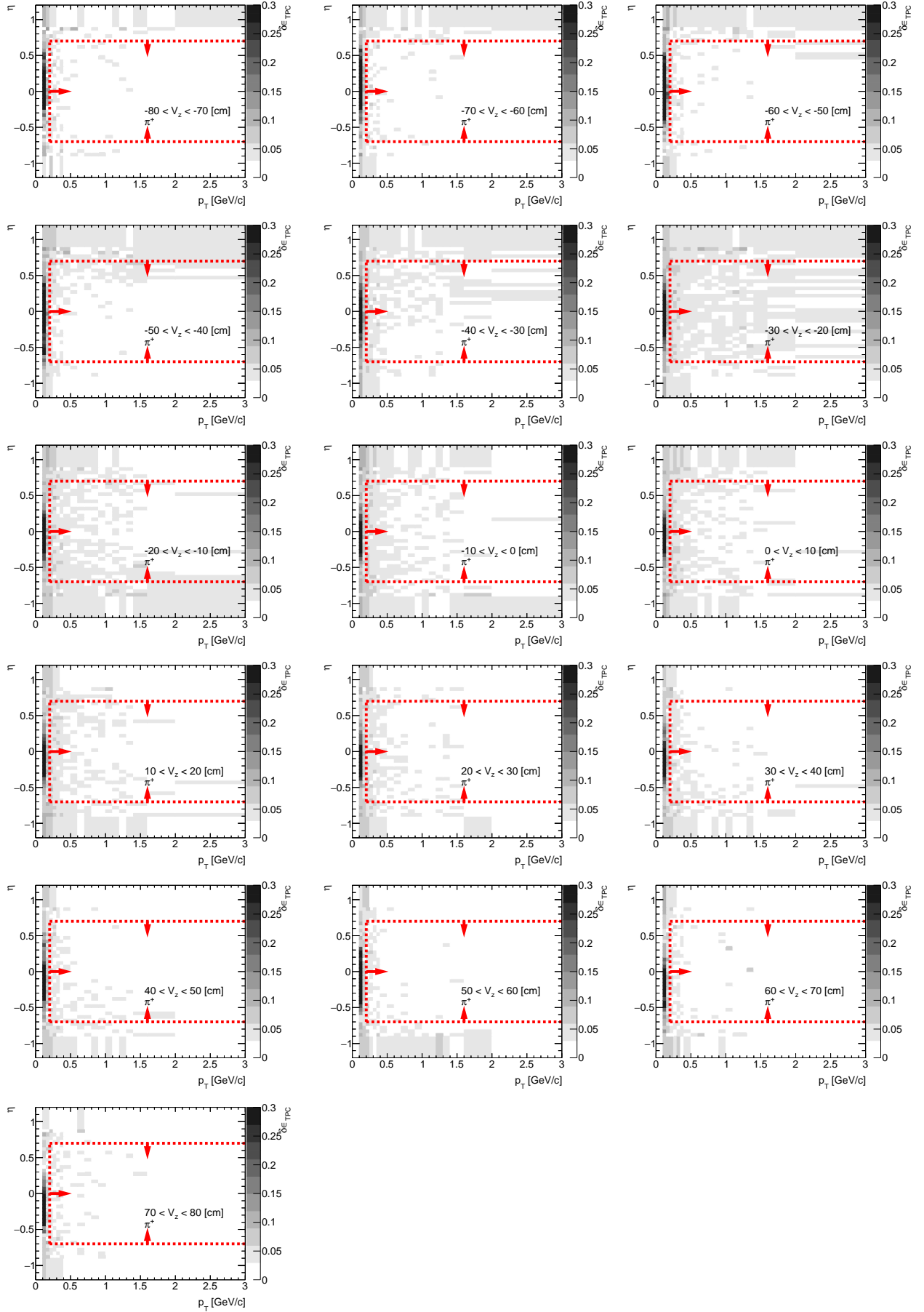


Figure E.10: The amount of lost  $K^-$  due to the interaction with dead material in front of TPC in SD MC sample. Each plot represents the fraction of lost  $K^-$ ,  $\delta\epsilon_{TPC}$  ( $z$ -axis), as a function of true particle pseudorapidity  $\eta$  ( $y$ -axis) and transverse momentum  $p_T$  ( $x$ -axis) in single  $z$ -vertex bin.

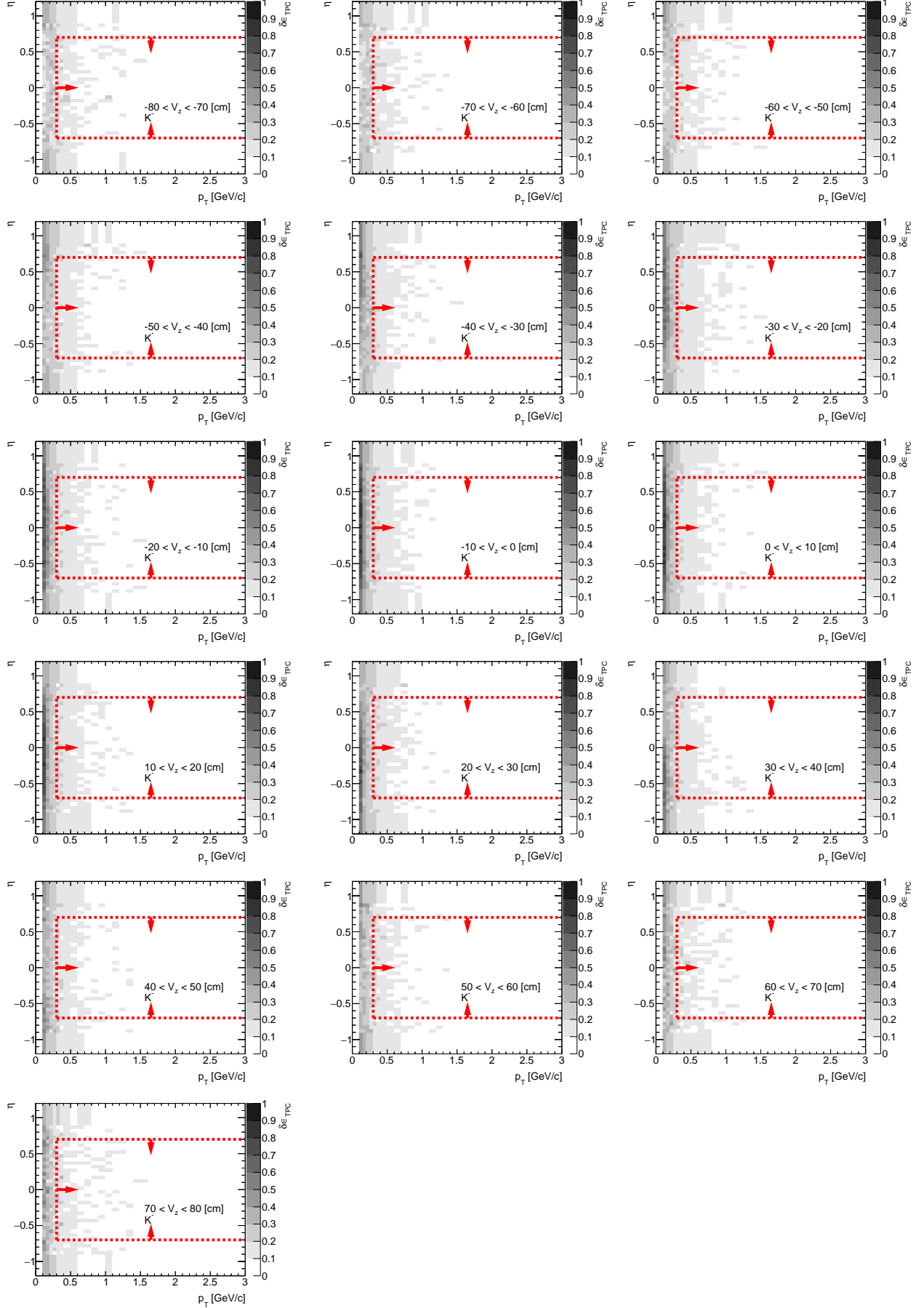


Figure E.11: The amount of lost  $K^+$  due to the interaction with dead material in front of TPC in SD MC sample. Each plot represents the fraction of lost  $K^+$ ,  $\delta\epsilon_{TPC}$  ( $z$ -axis), as a function of true particle pseudorapidity  $\eta$  ( $y$ -axis) and transverse momentum  $p_T$  ( $x$ -axis) in single  $z$ -vertex bin.

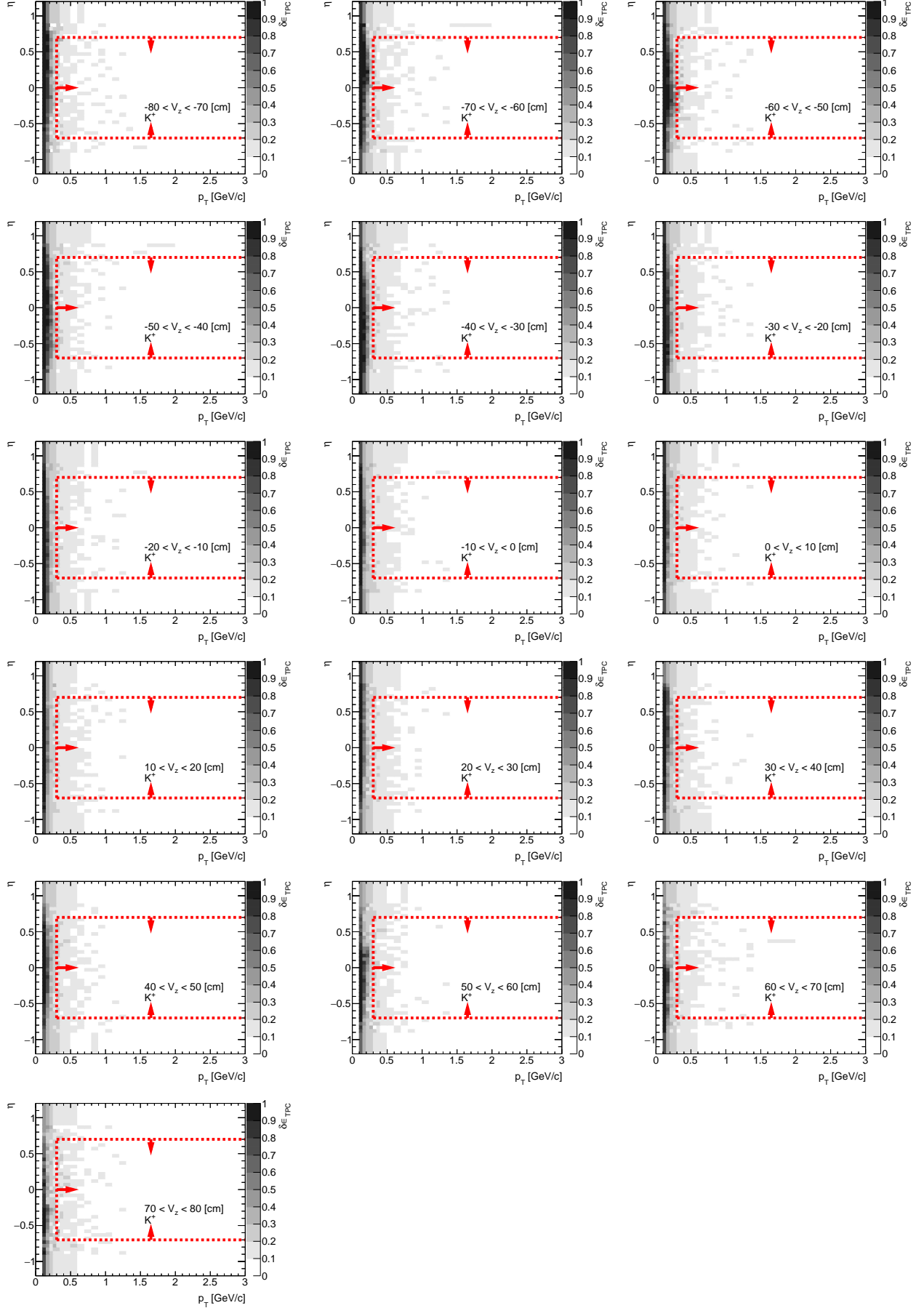


Figure E.12: The amount of lost  $\bar{p}$  due to the interaction with dead material in front of TPC in SD MC sample. Each plot represents the fraction of lost  $\bar{p}$ ,  $\delta\epsilon_{TPC}$  ( $z$ -axis), as a function of true particle pseudorapidity  $\eta$  ( $y$ -axis) and transverse momentum  $p_T$  ( $x$ -axis) in single  $z$ -vertex bin.

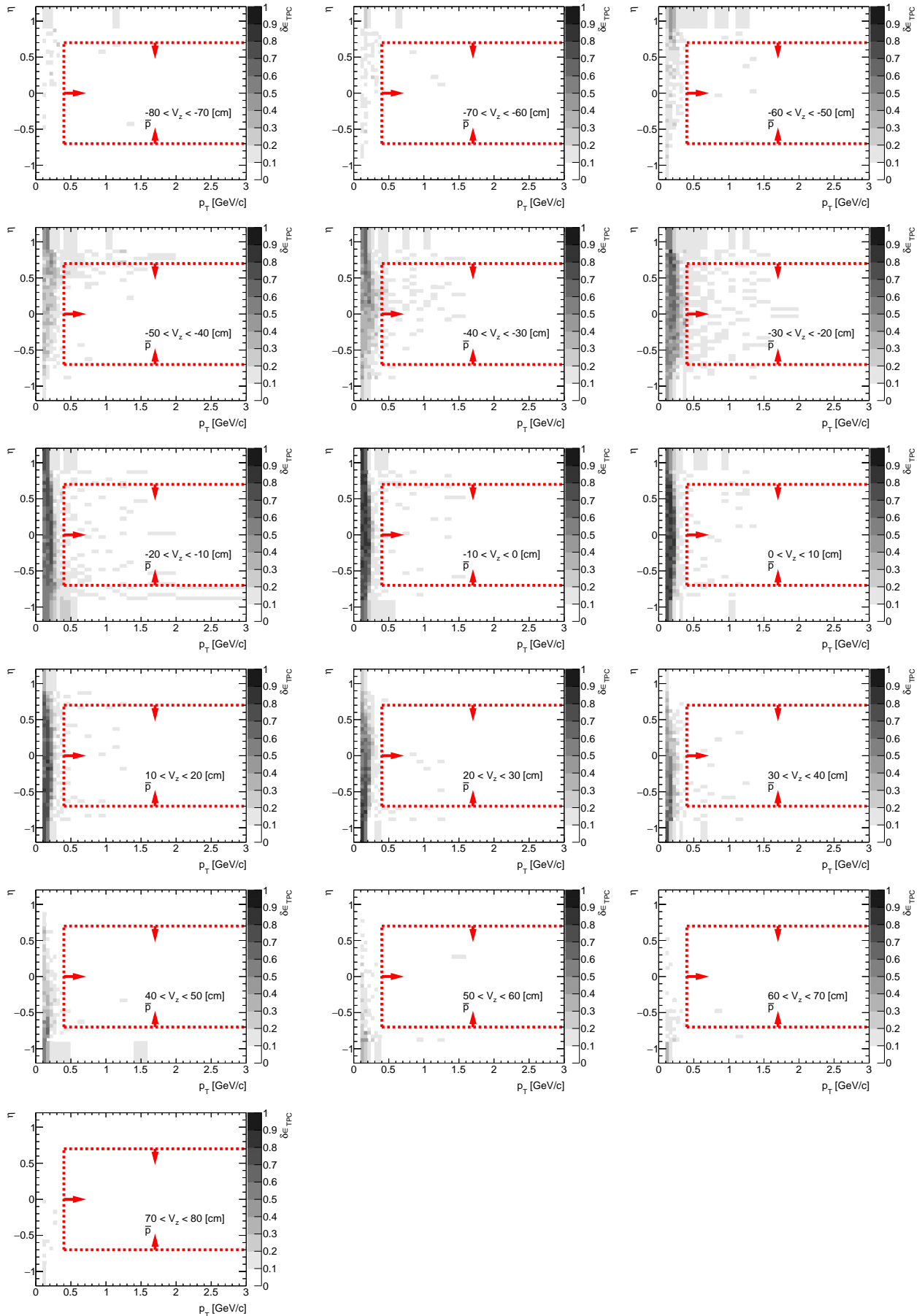


Figure E.13: The amount of lost  $p$  due to the interaction with dead material in front of TPC in SD MC sample. Each plot represents the fraction of lost  $p$ ,  $\delta\epsilon_{TPC}$  ( $z$ -axis), as a function of true particle pseudorapidity  $\eta$  ( $y$ -axis) and transverse momentum  $p_T$  ( $x$ -axis) in single  $z$ -vertex bin.

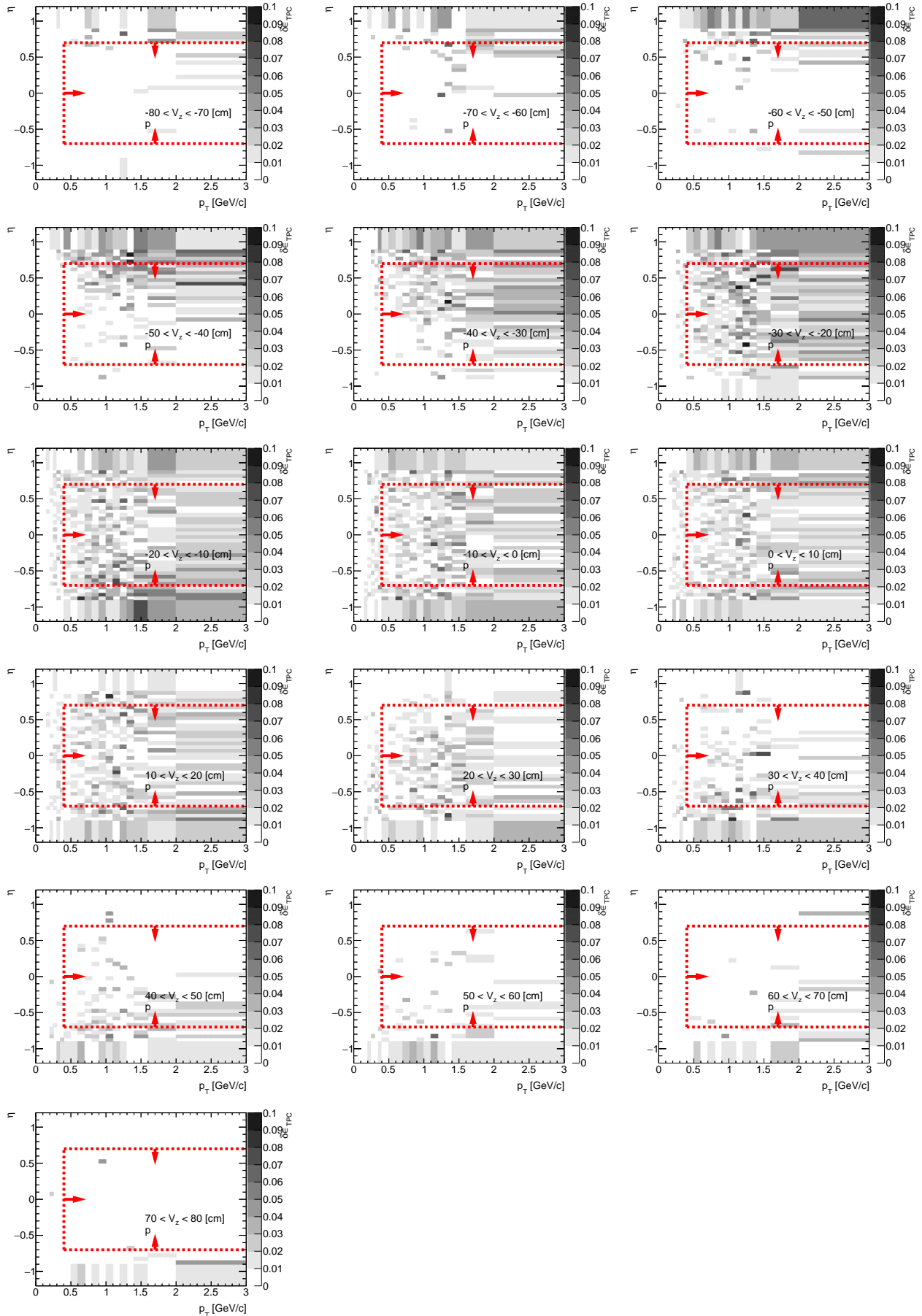


Figure E.14: The amount of lost negative particles due to the interaction with dead material in front of TPC in SD MC sample. Each plot represents the fraction of lost negative particles,  $\delta\epsilon_{TPC}$  (z-axis), as a function of true particle pseudorapidity  $\eta$  (y-axis) and transverse momentum  $p_T$  (x-axis) in single  $z$ -vertex bin.

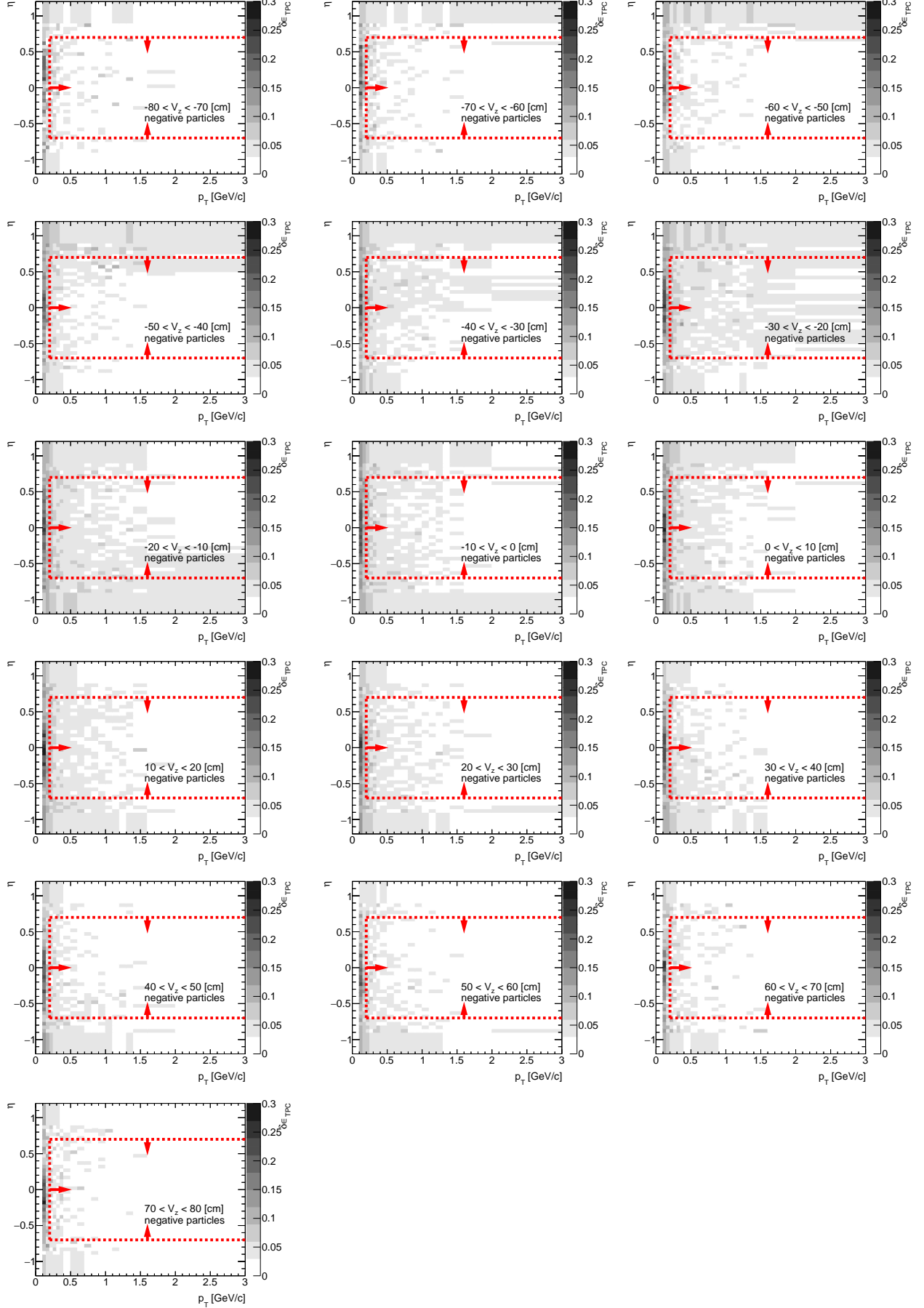


Figure E.15: The amount of lost positive particles due to the interaction with dead material in front of TPC in SD MC sample. Each plot represents the fraction of lost positive particles,  $\delta\epsilon_{TPC}$  (z-axis), as a function of true particle pseudorapidity  $\eta$  (y-axis) and transverse momentum  $p_T$  (x-axis) in single  $z$ -vertex bin.

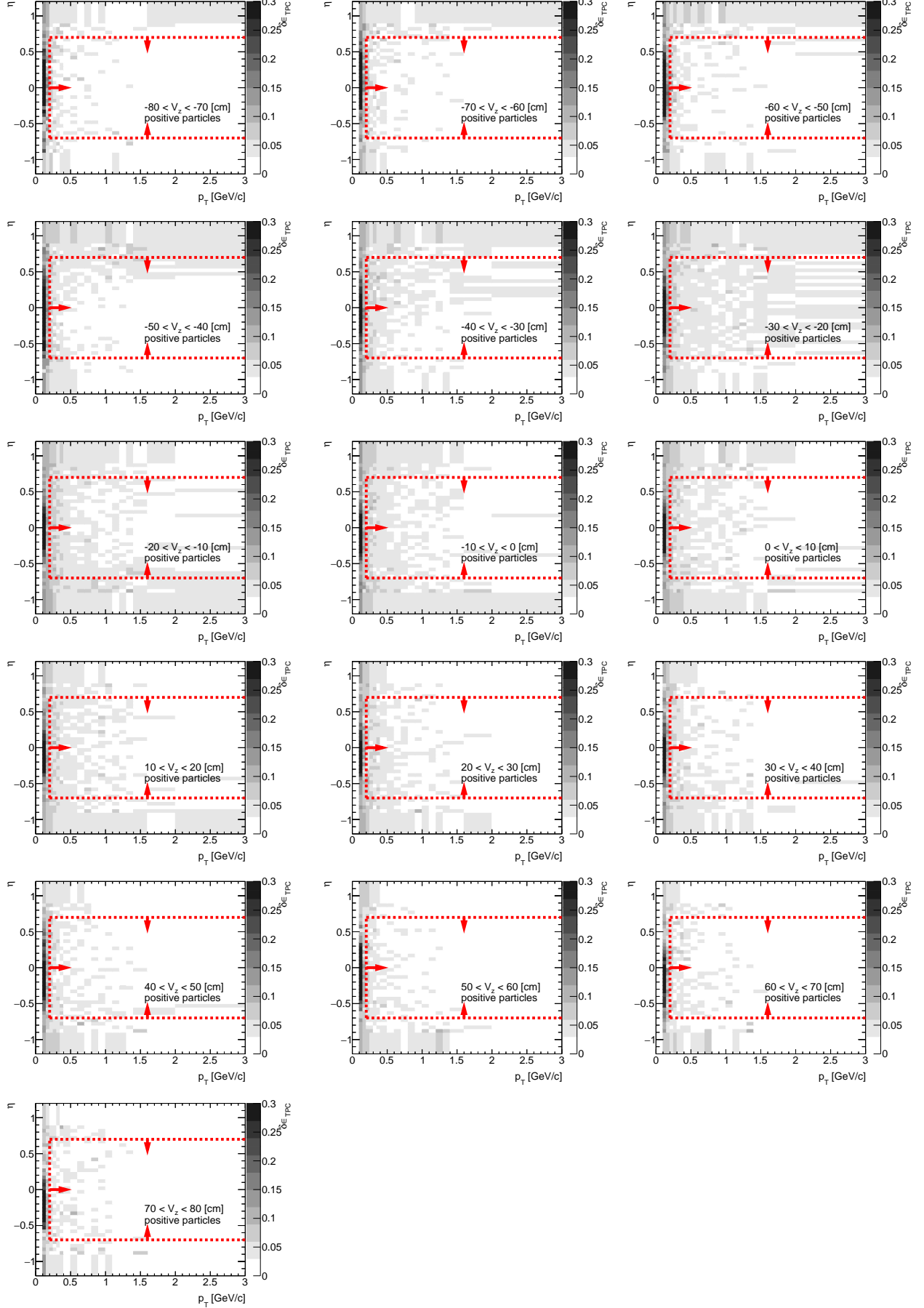
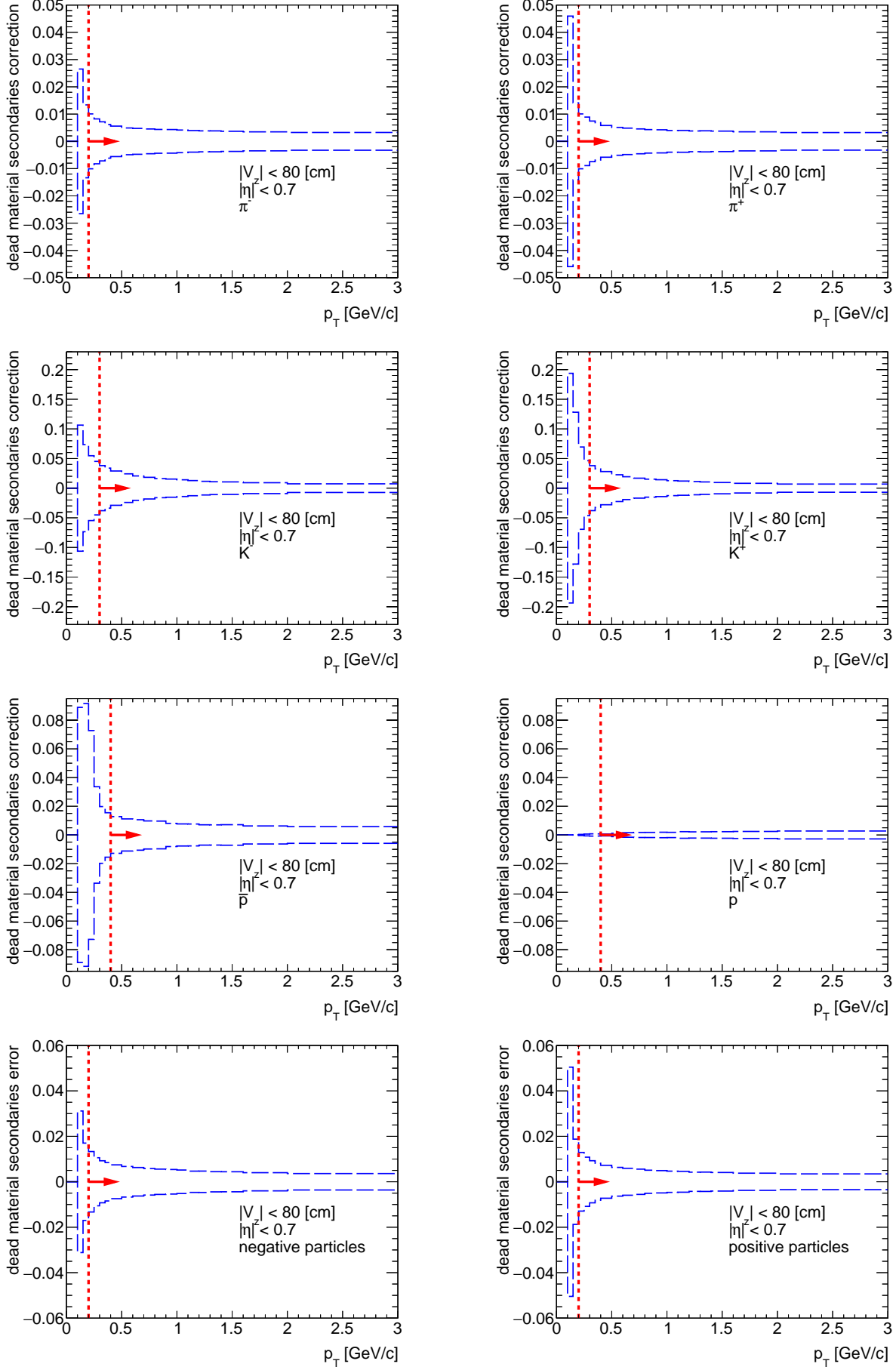


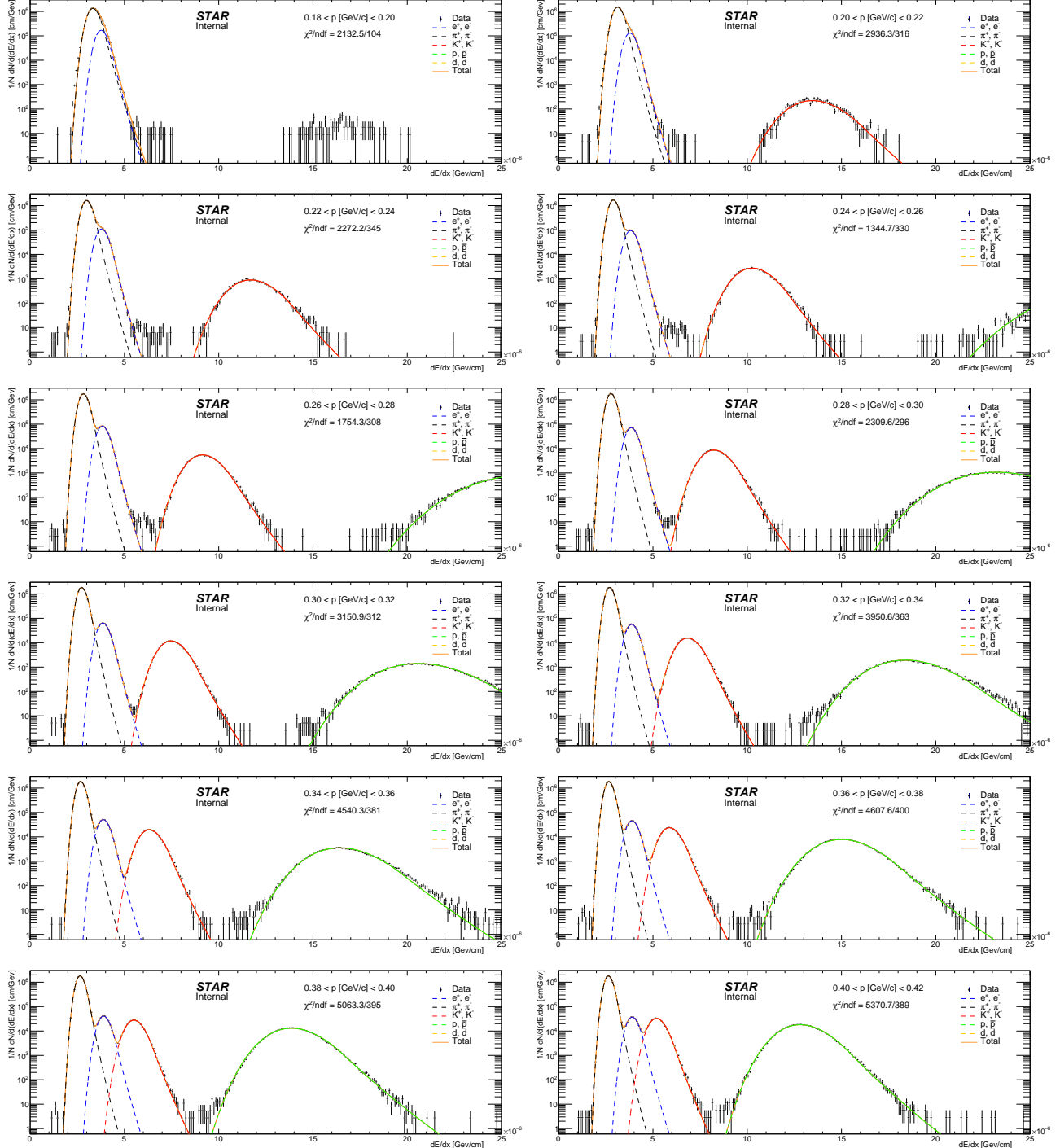
Figure E.16: The systematic uncertainty to the TPC track reconstruction efficiency due to amount of dead material in front of TPC using MC samples for SD. Each plot represents the systematic uncertainty as a function of true particle  $p_T$  ( $|\eta| < 0.7, |V_z| < 80 \text{ cm}$ ) for given particle species:  $\pi^-, \pi^+, K^-, K^+, \bar{p}$  and  $p$ . It was also calculated for negative and positive particles without identification.

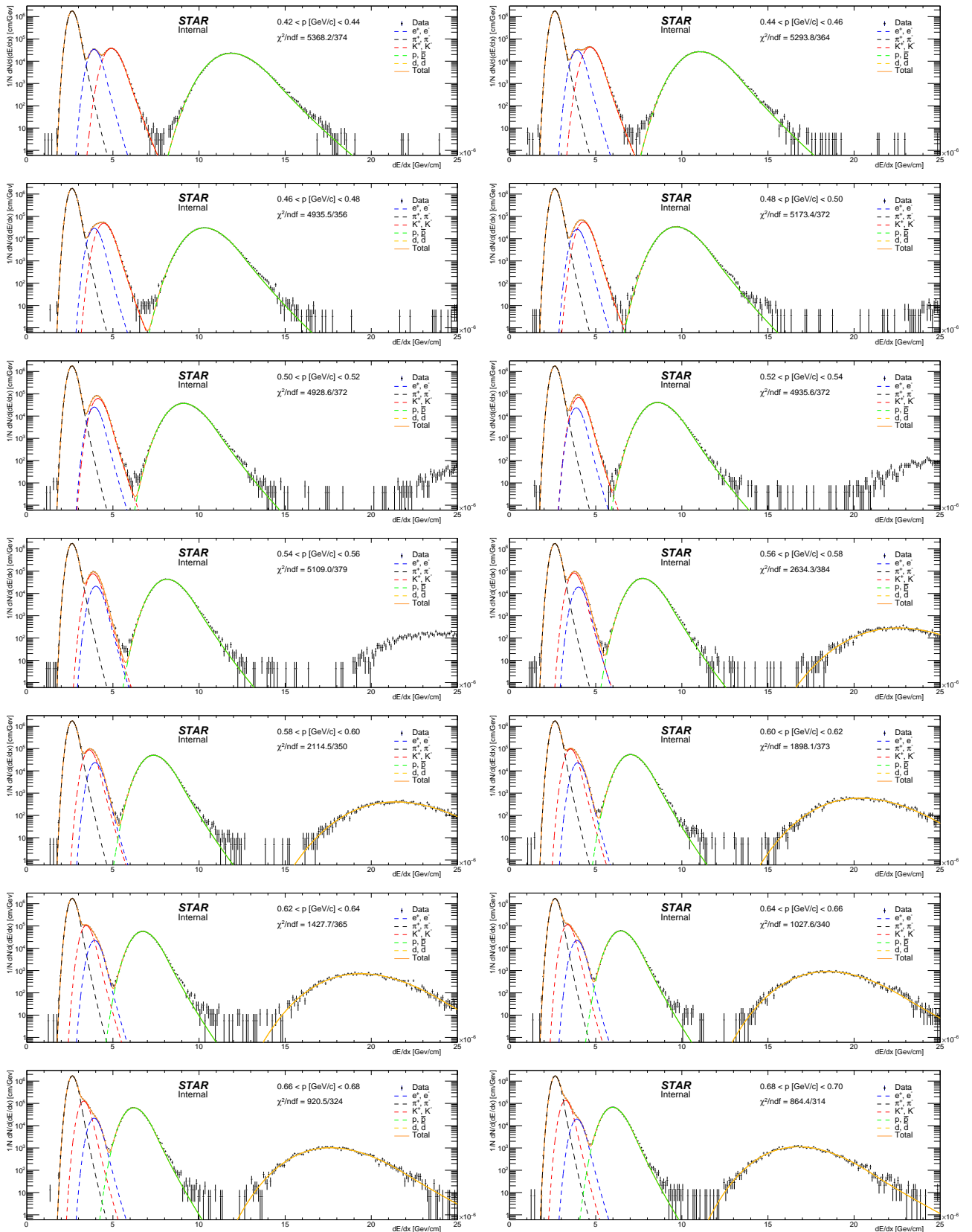


# Appendix F

## Fits to $dE/dx$ spectra, comparison of $dE/dx$ and $n_X^\sigma$ between data and MC

Figure F.1: Fits of sum of functions from Eq. (6.6) corresponding to different particle species to  $dE/dx$  spectra in the data in momentum bins.





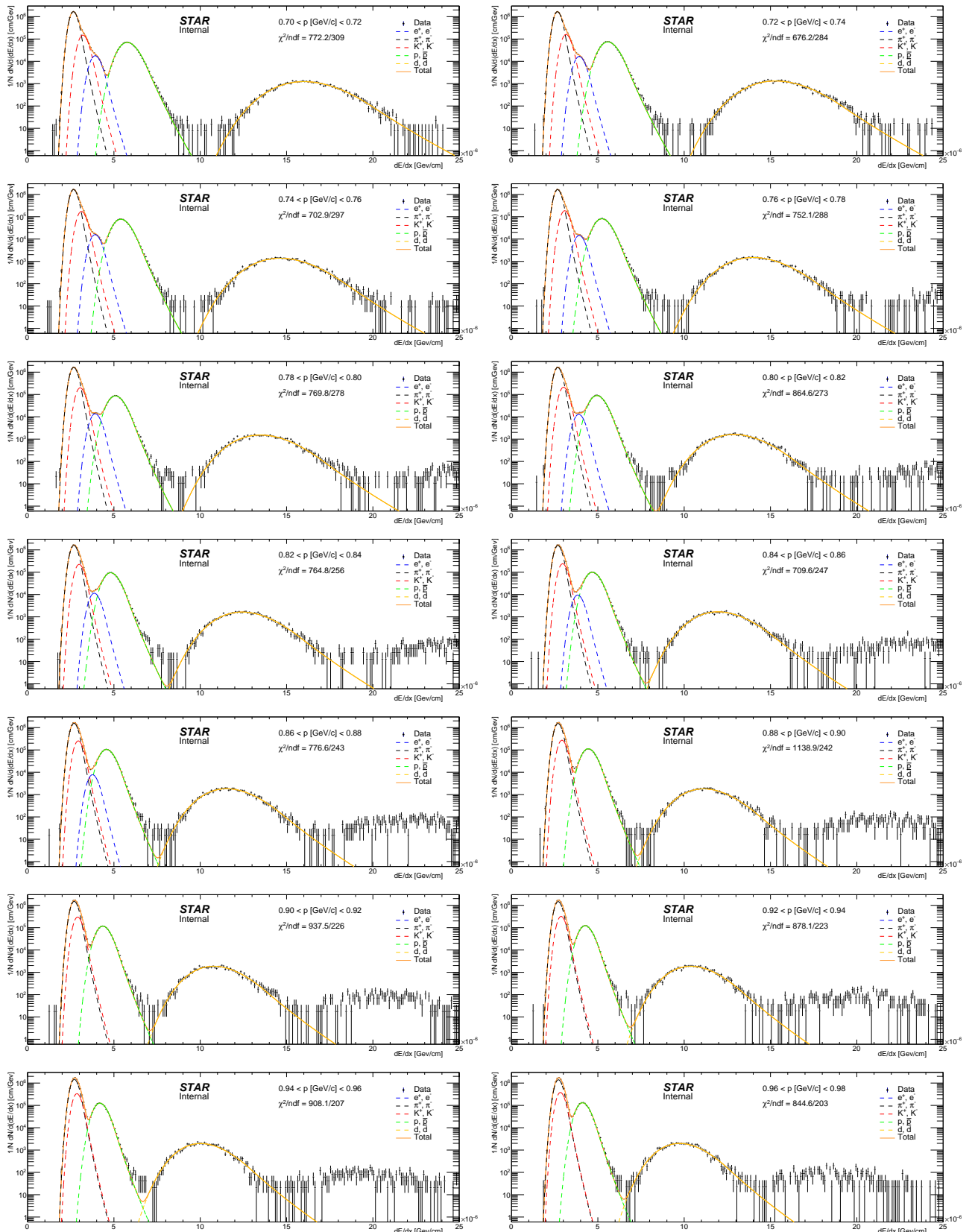
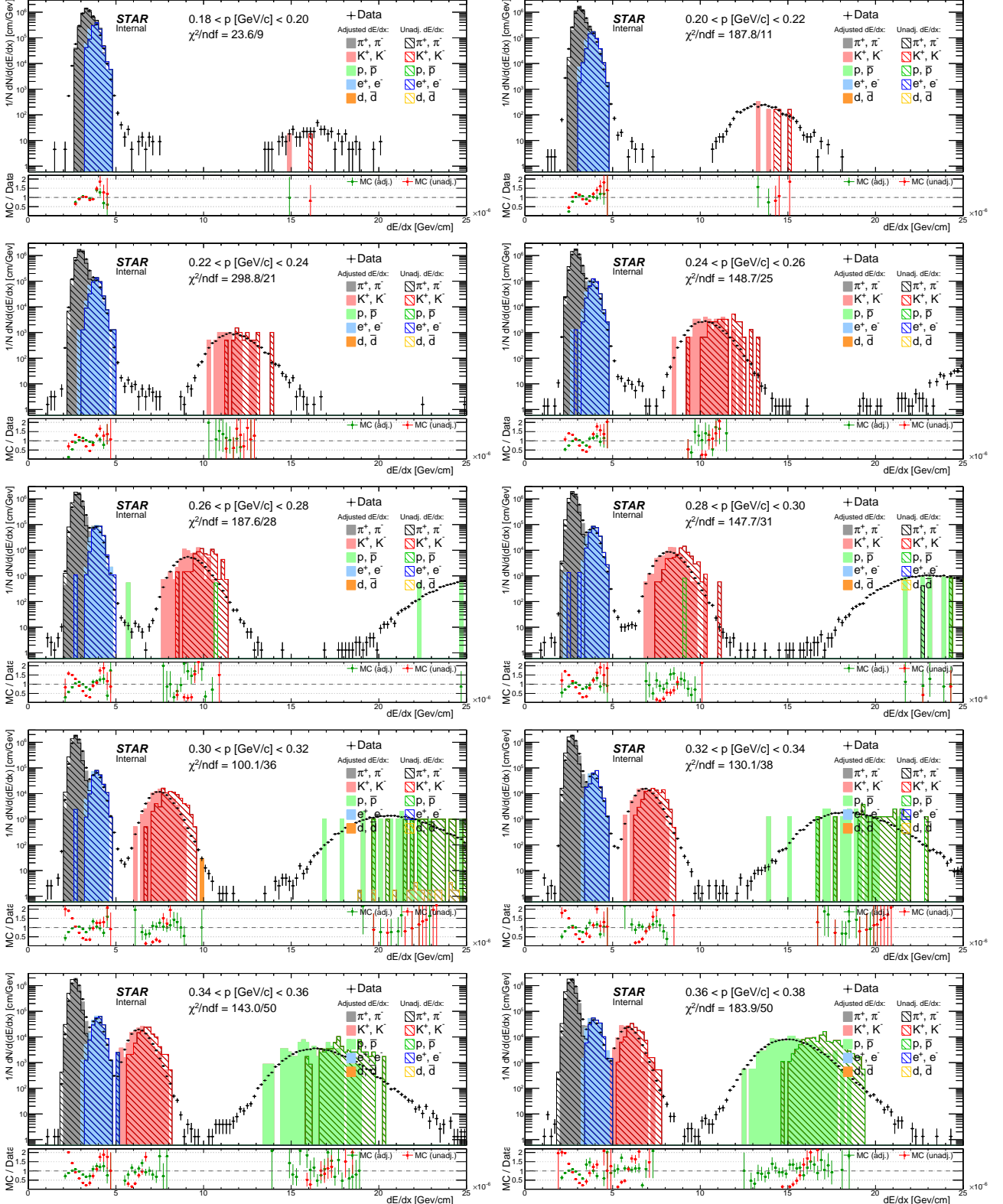
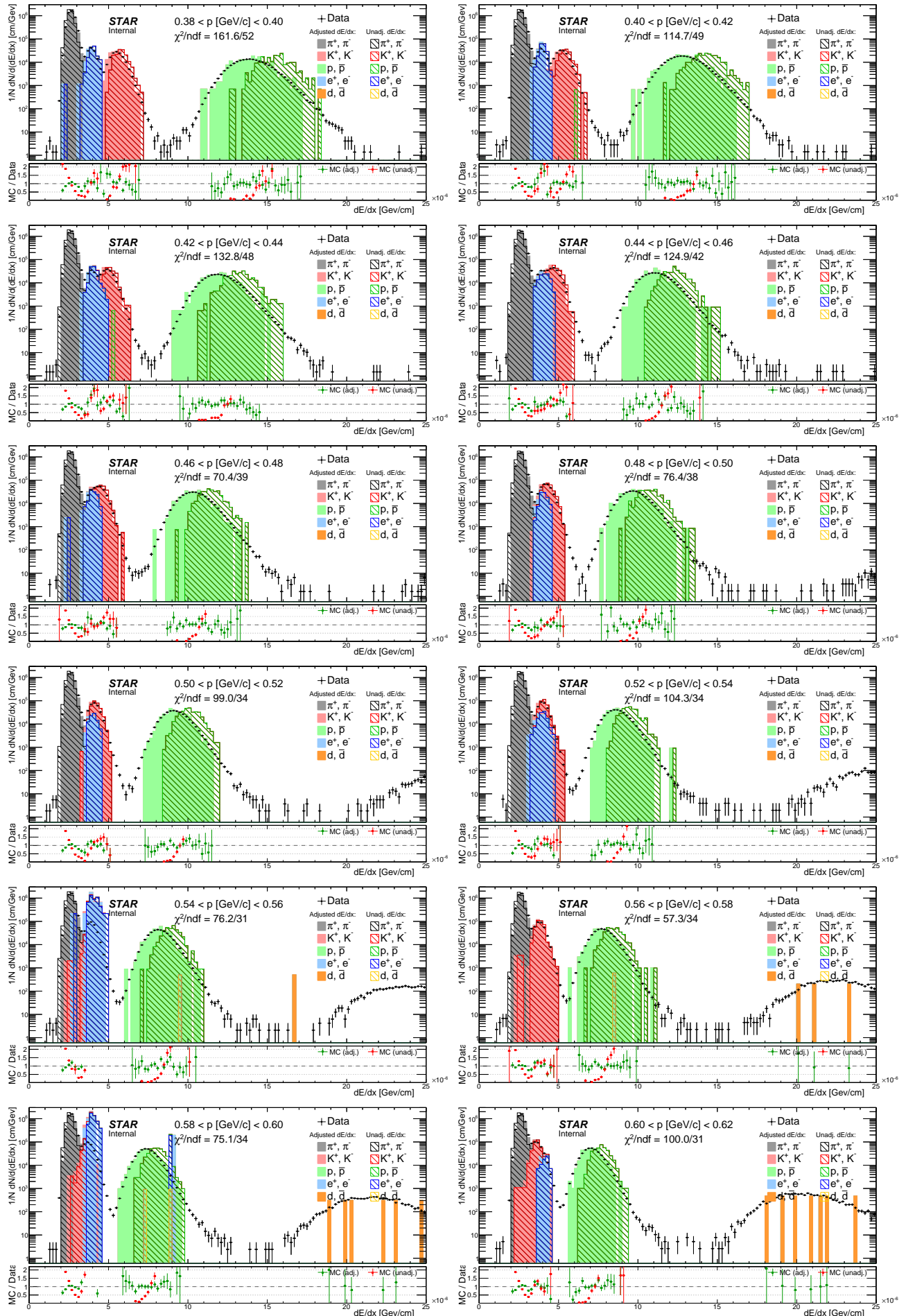
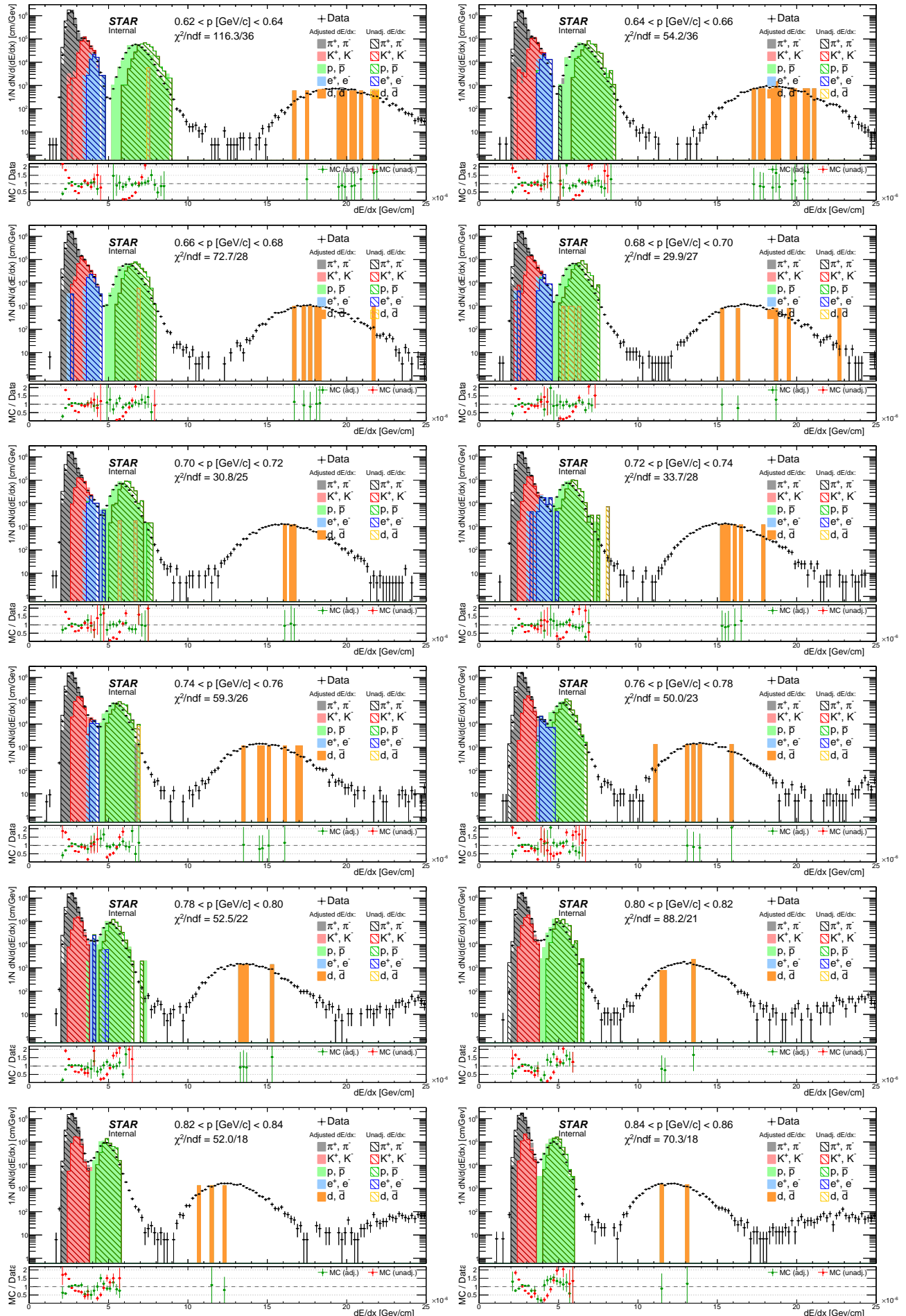


Figure F.2: Comparison of  $dE/dx$  spectrum between data and embedded MC (before and after  $dE/dx$  adjustment) in momentum bins.







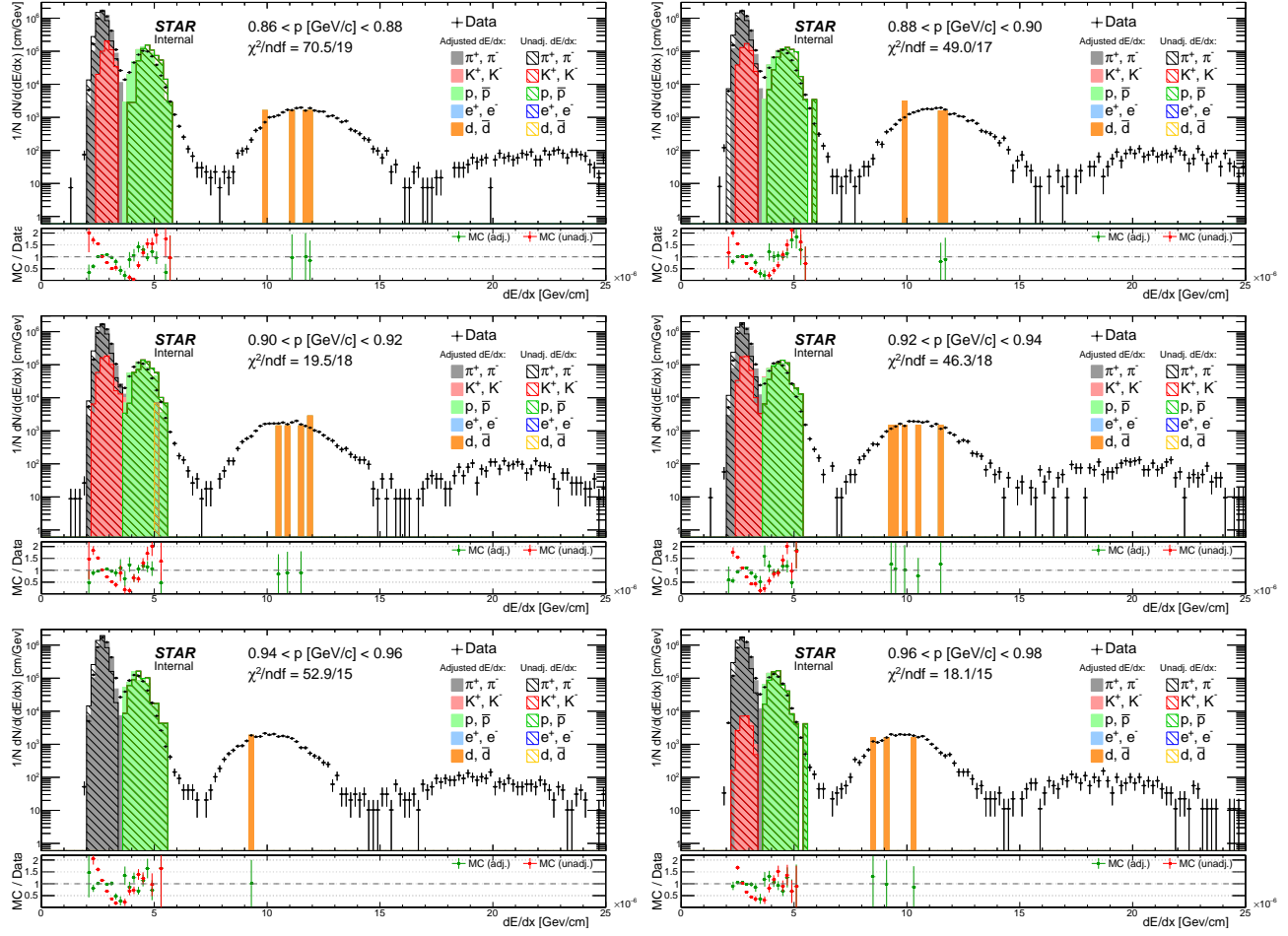
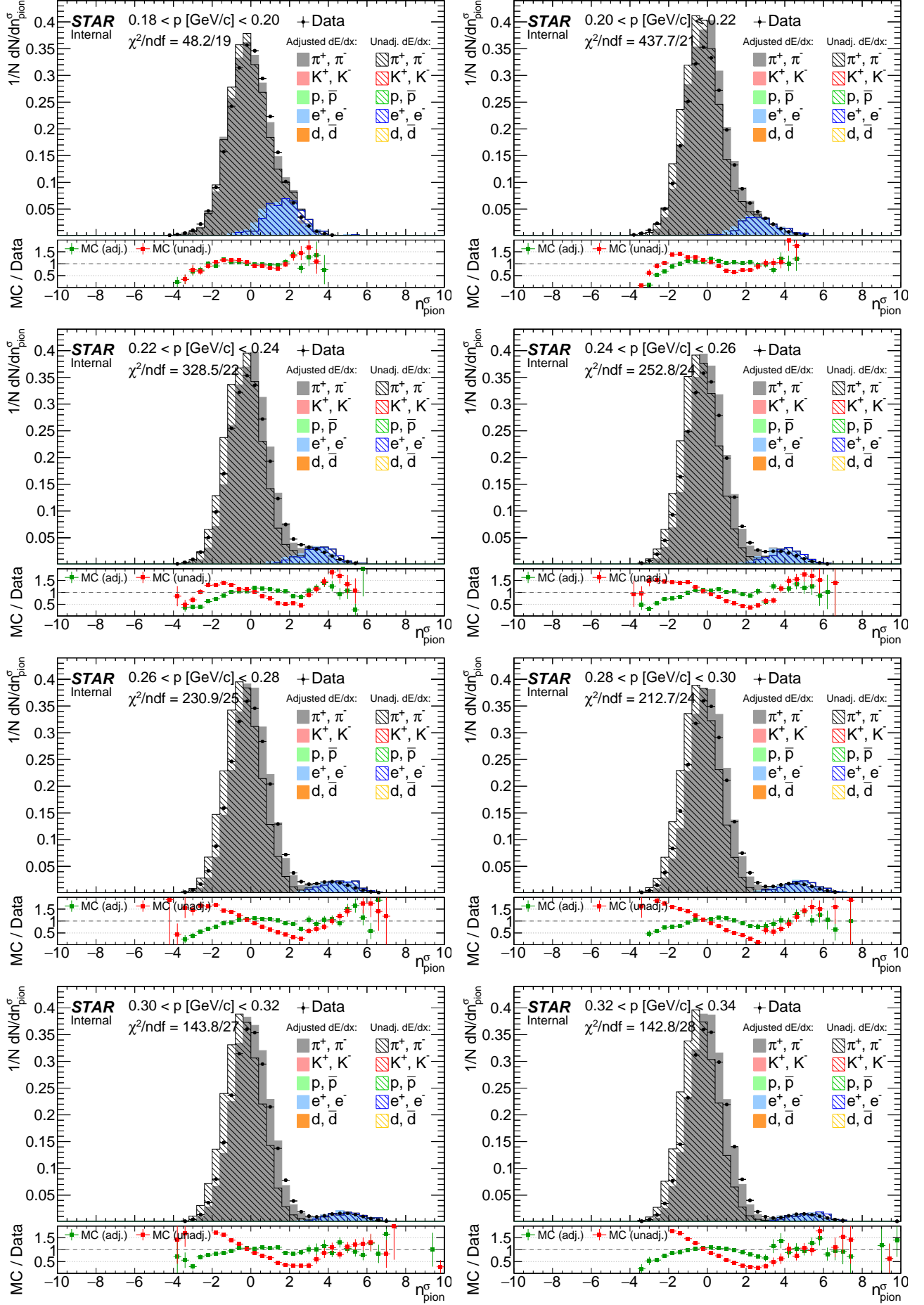
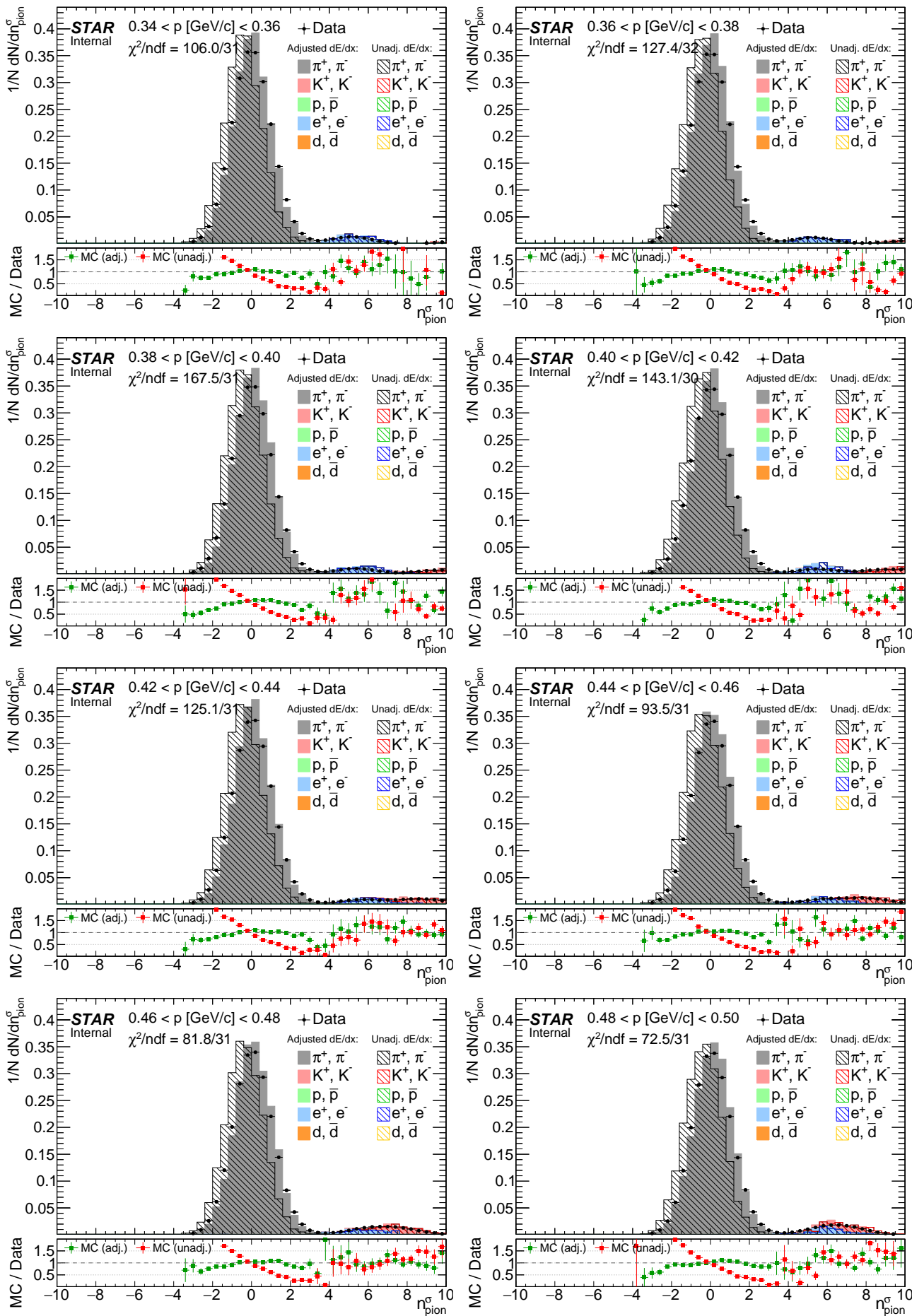
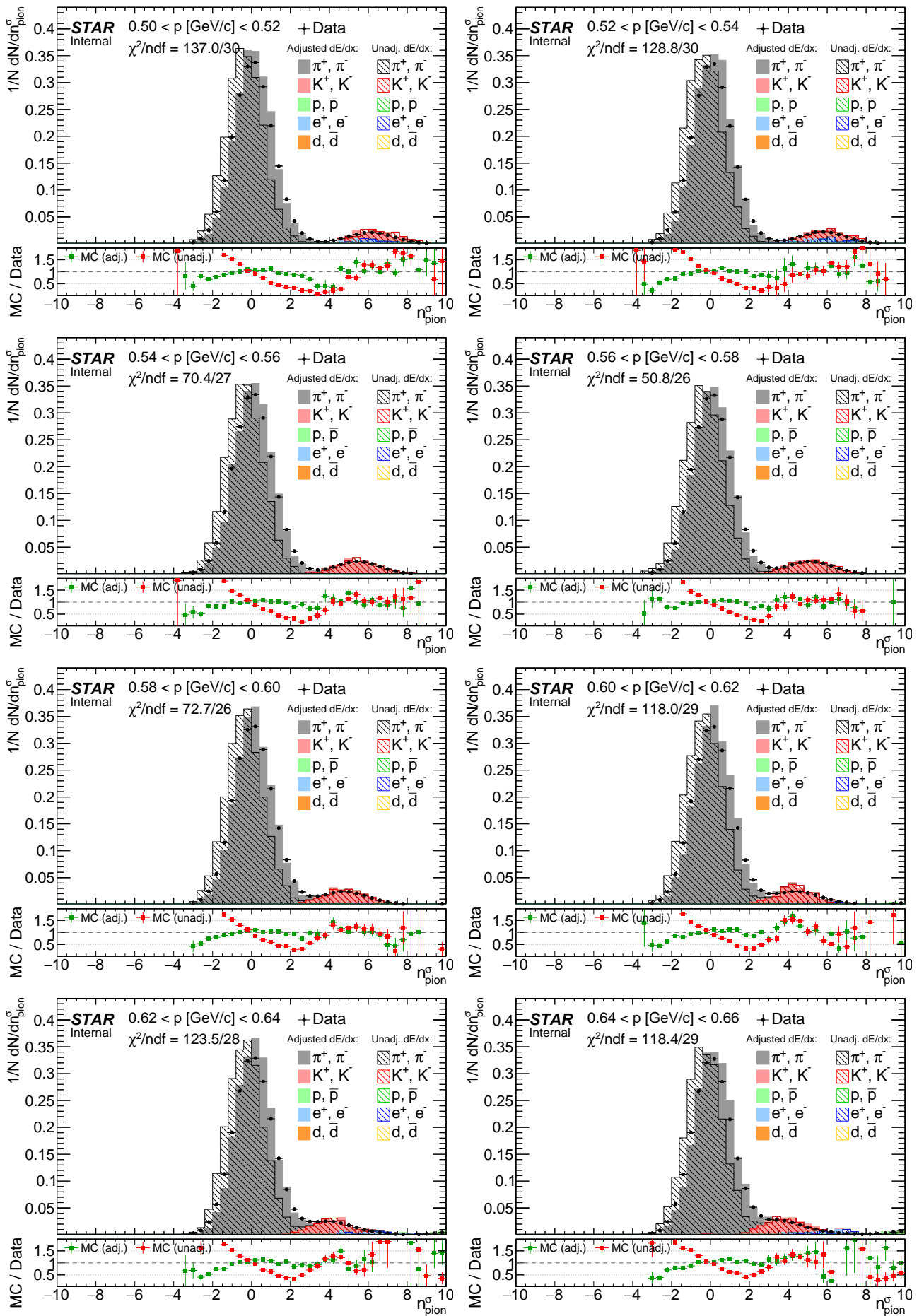
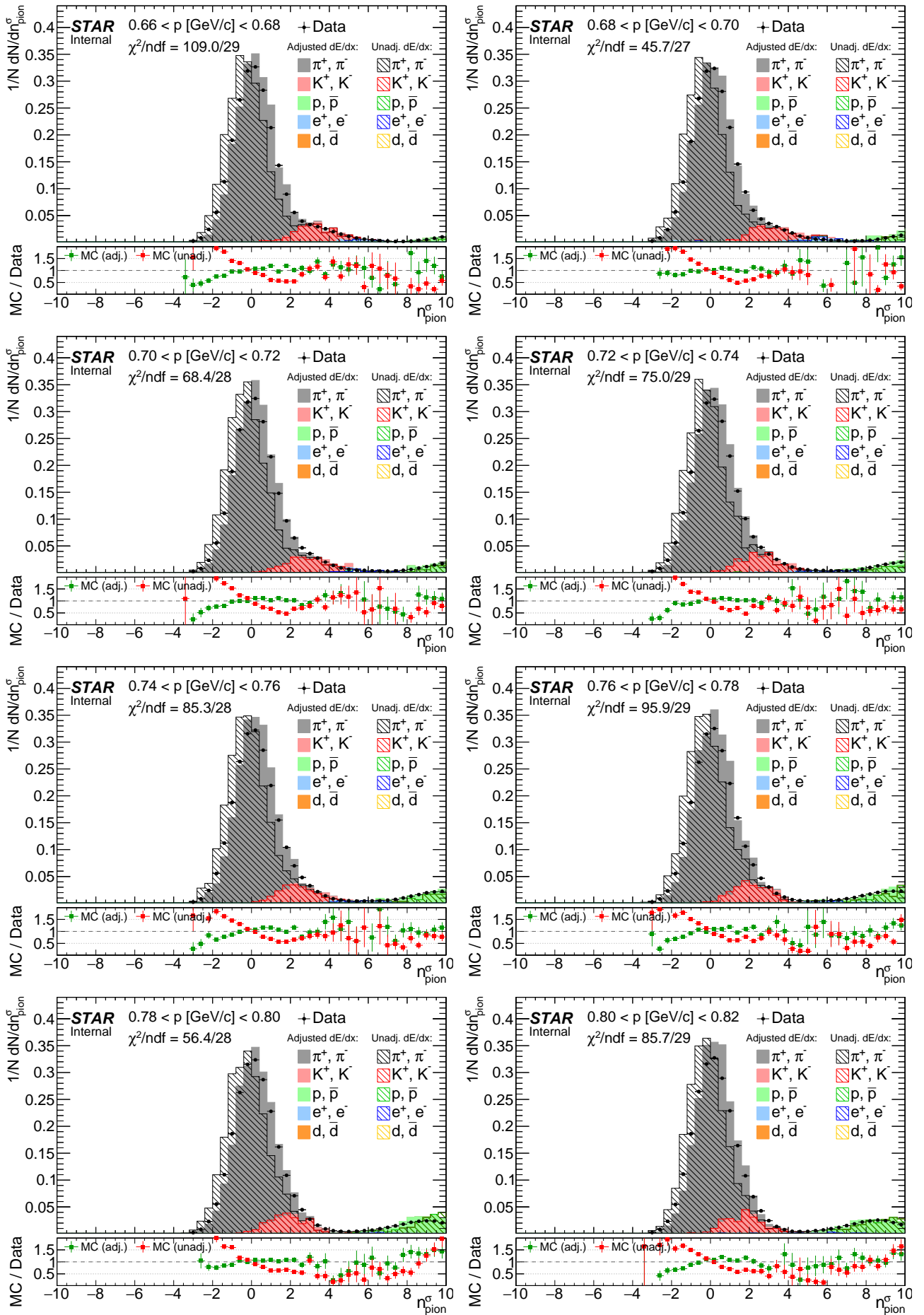


Figure F.3: Comparison of  $n_{\text{pion}}^{\sigma}$  distribution between data and embedded MC (before and after  $dE/dx$  adjustment) in momentum bins.









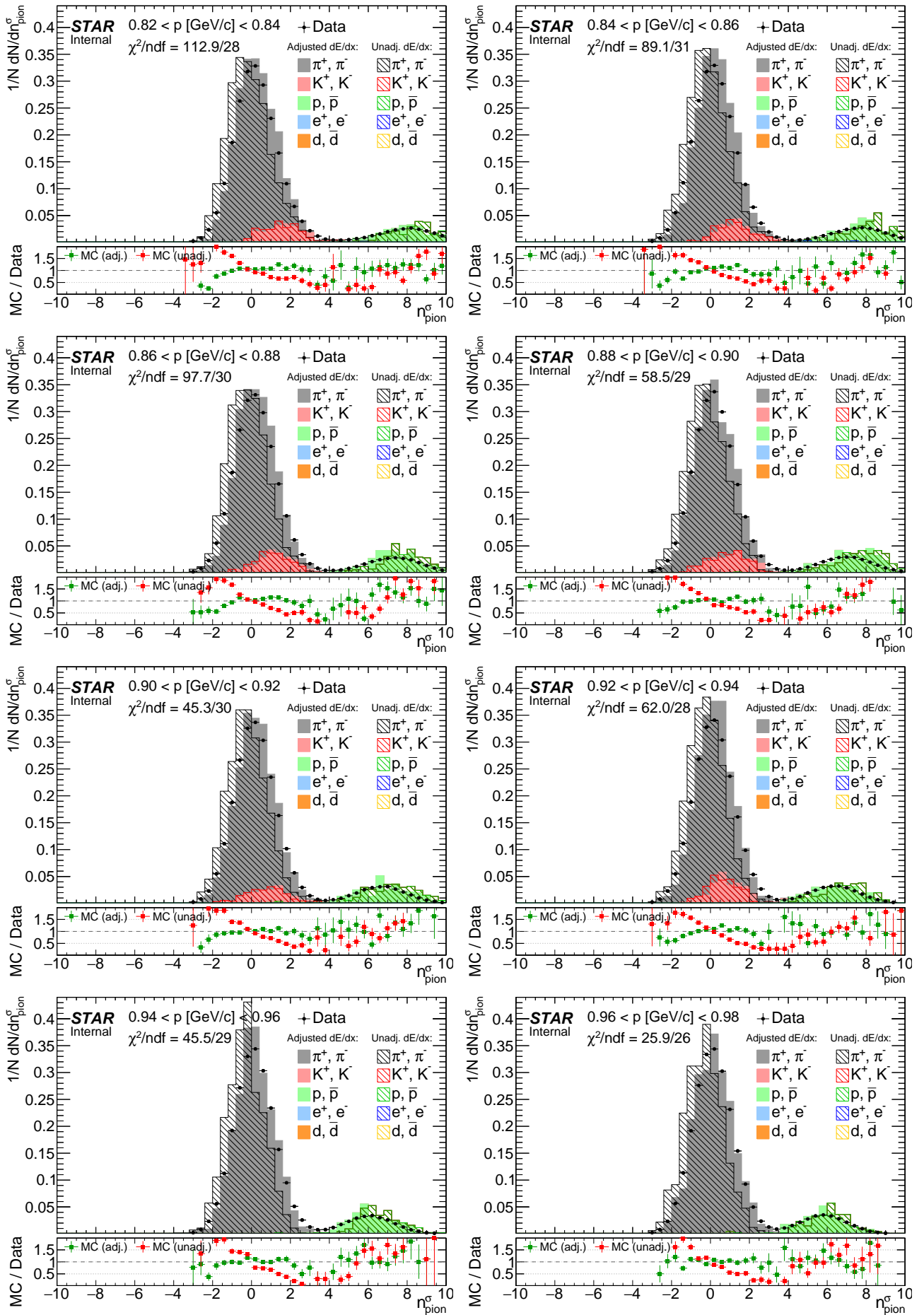
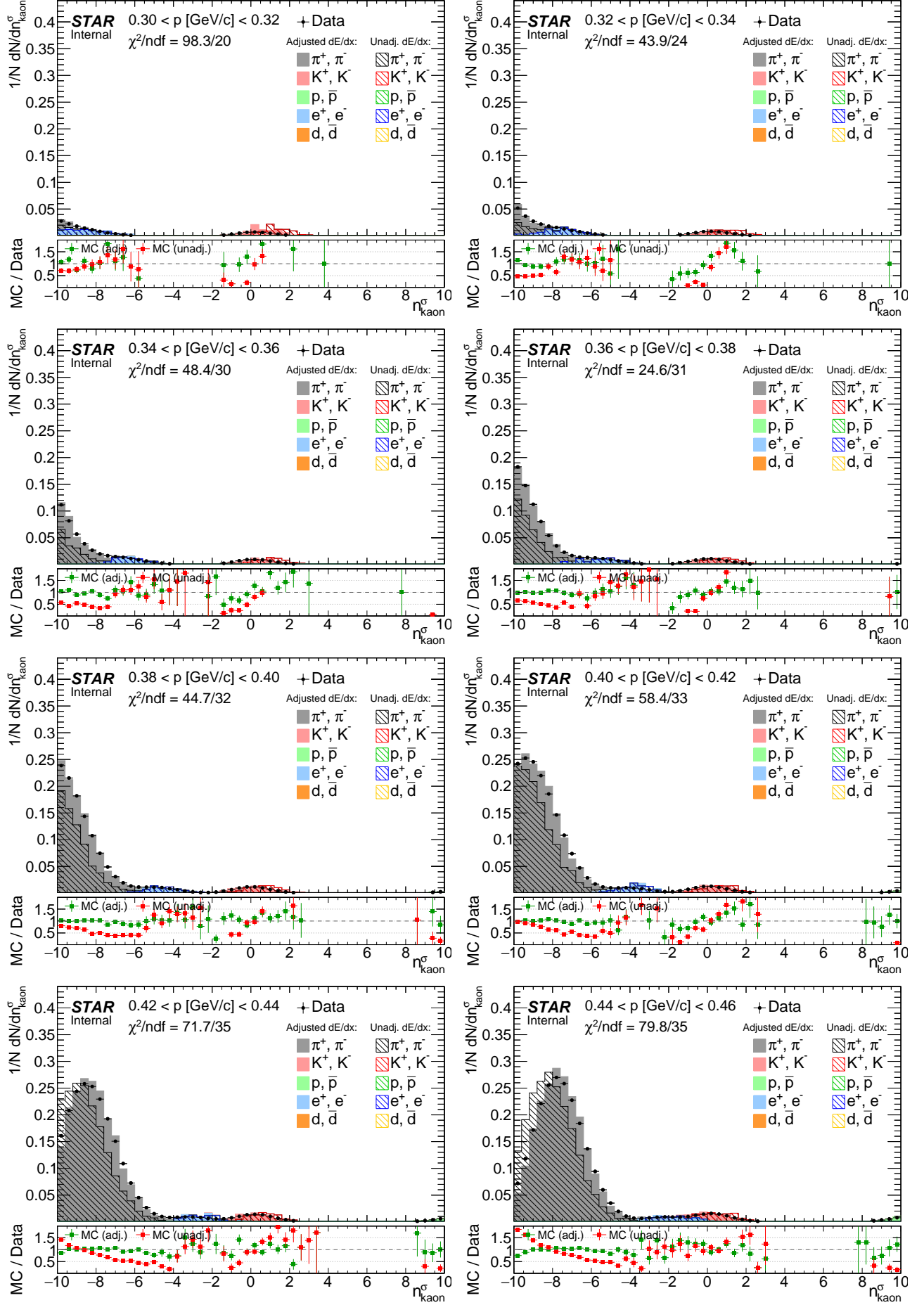
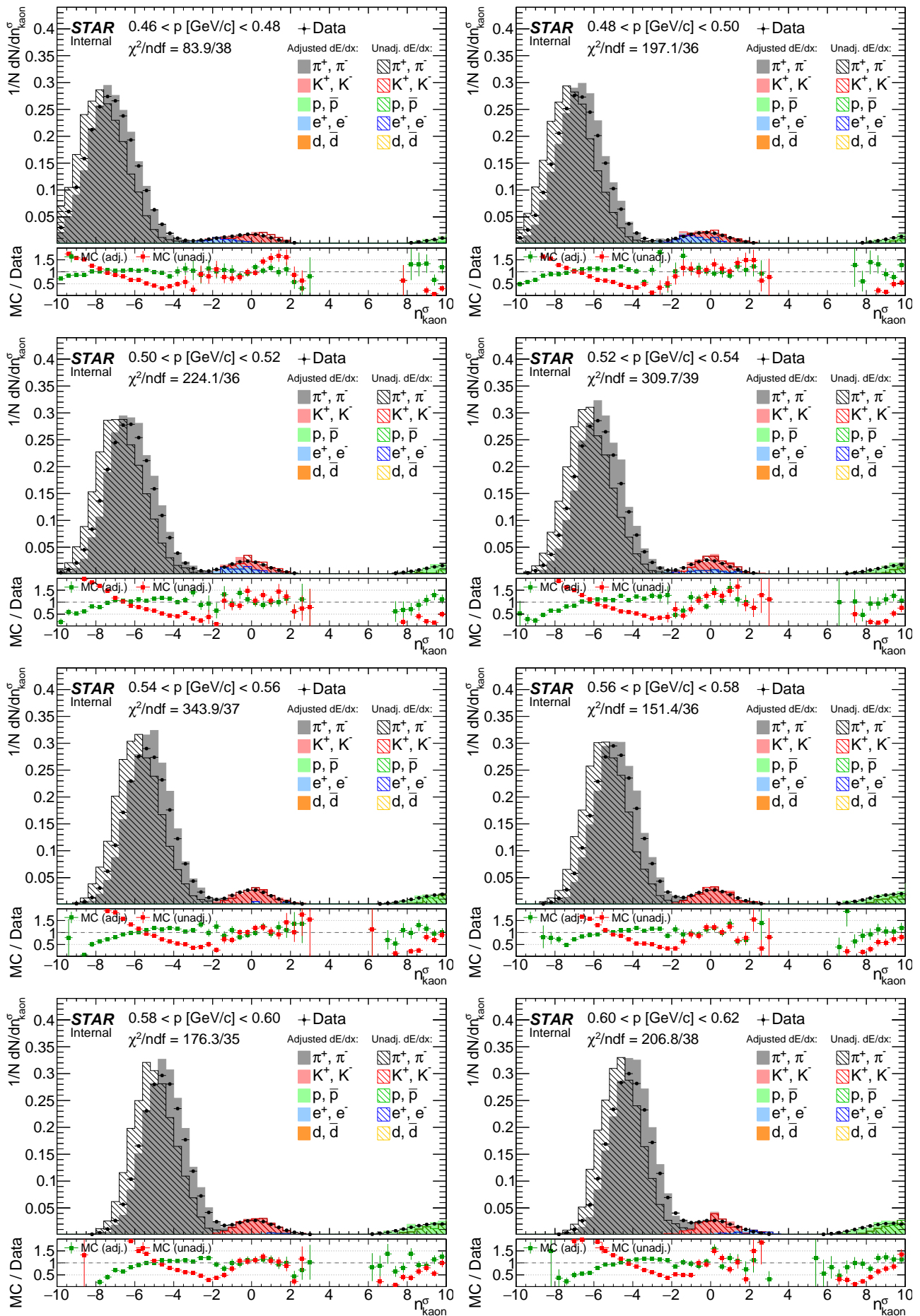
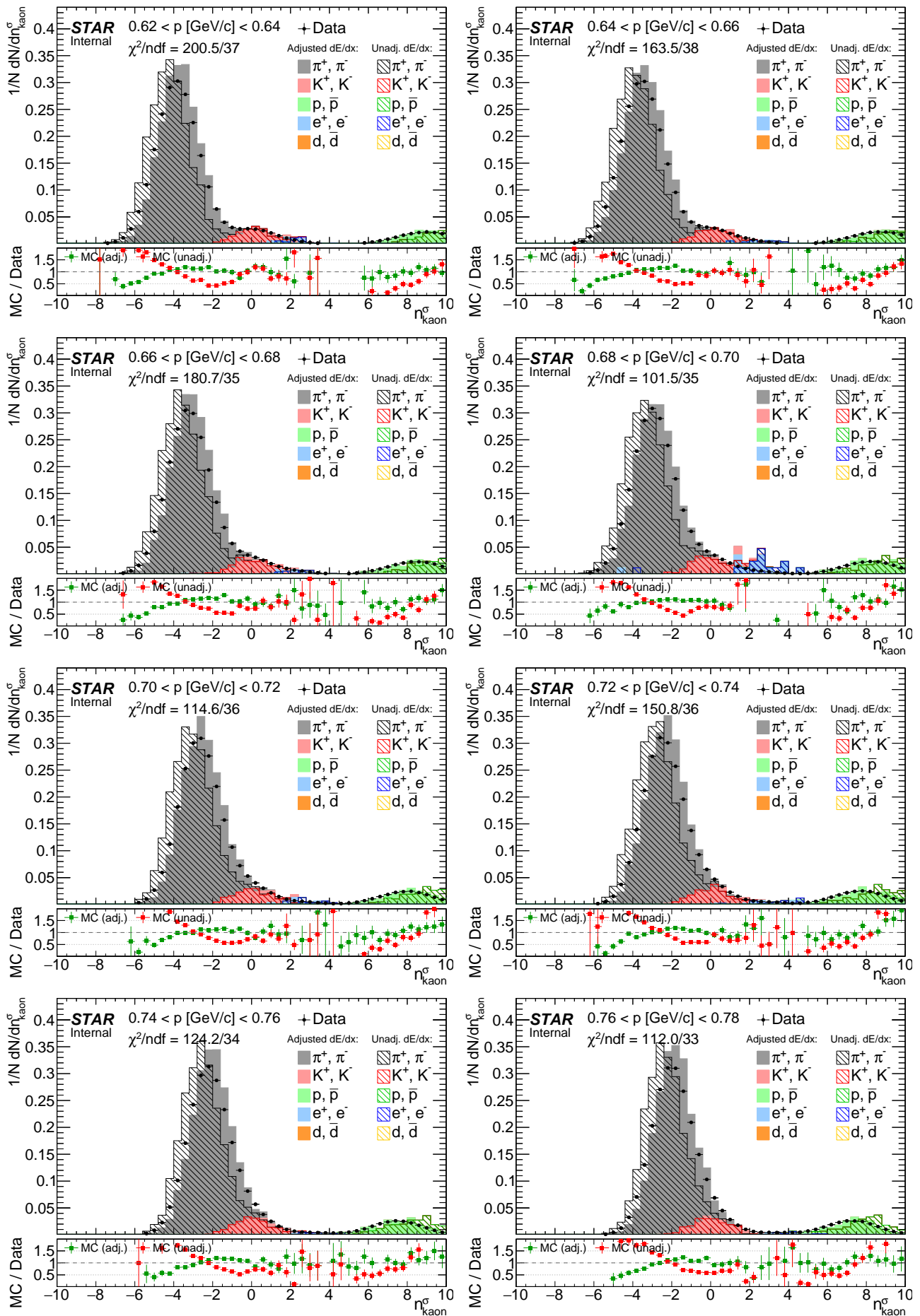
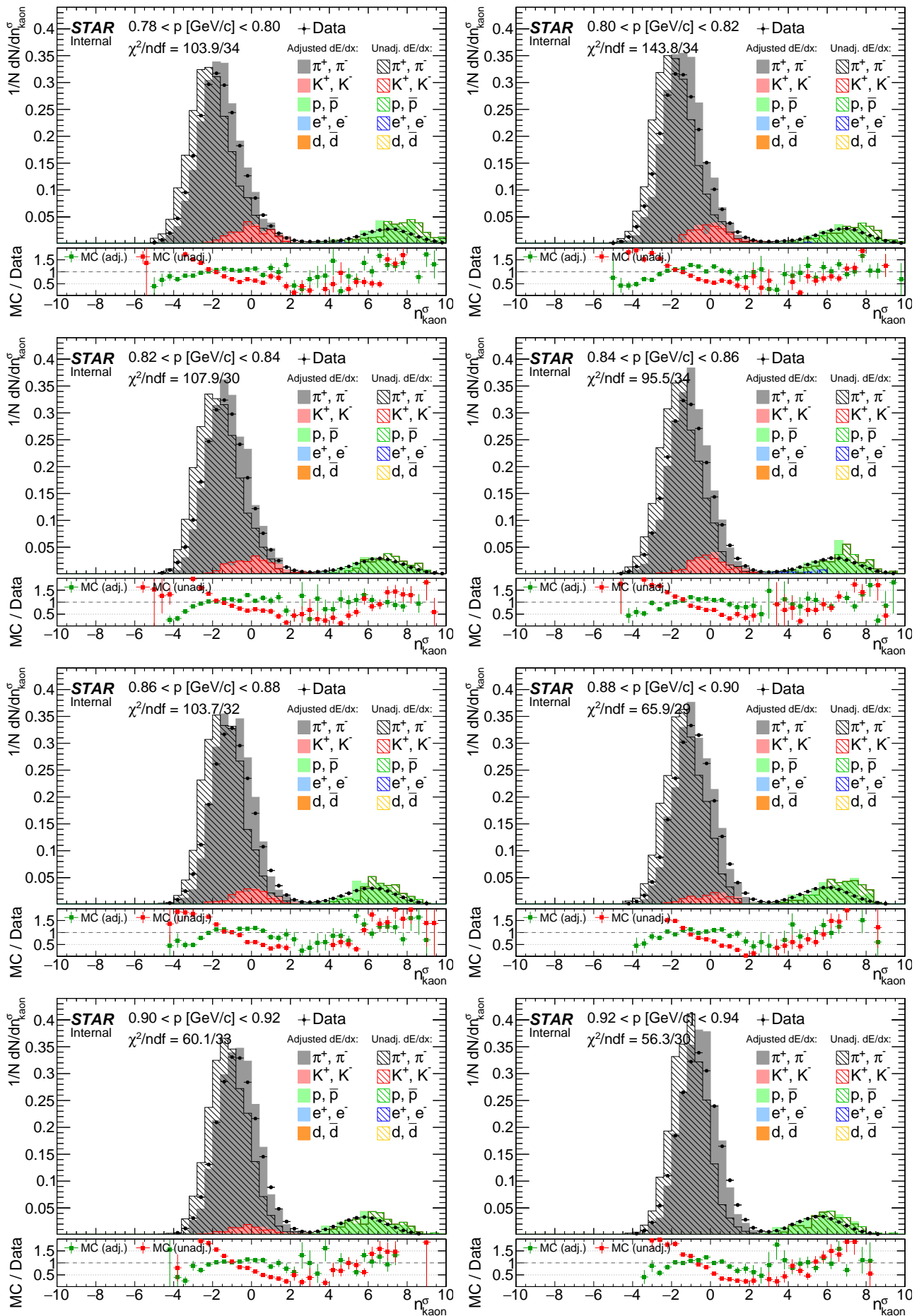


Figure F.4: Comparison of  $n_{\text{kaon}}^{\sigma}$  distribution between data and embedded MC (before and after  $dE/dx$  adjustment) in momentum bins.









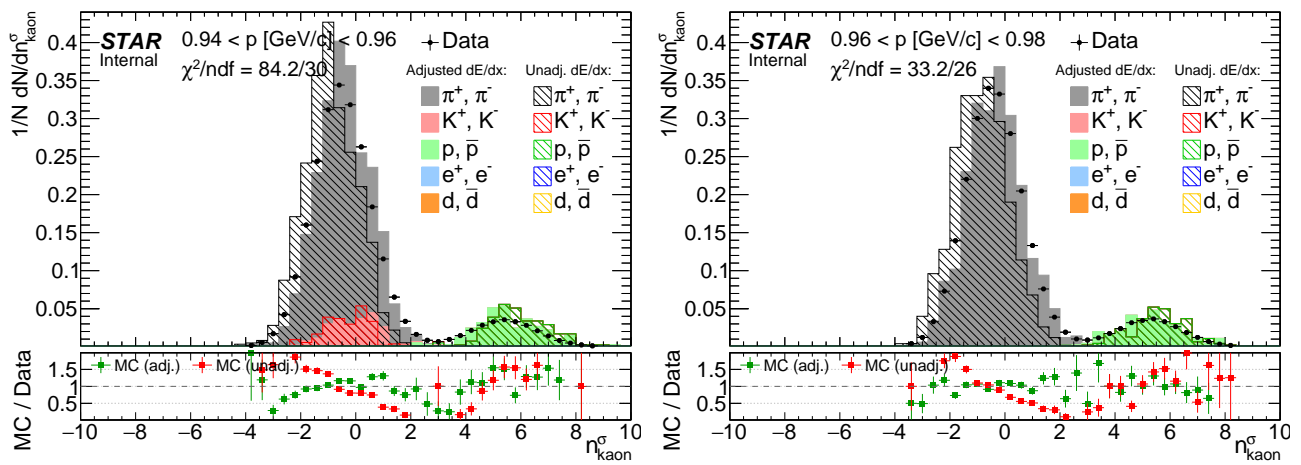
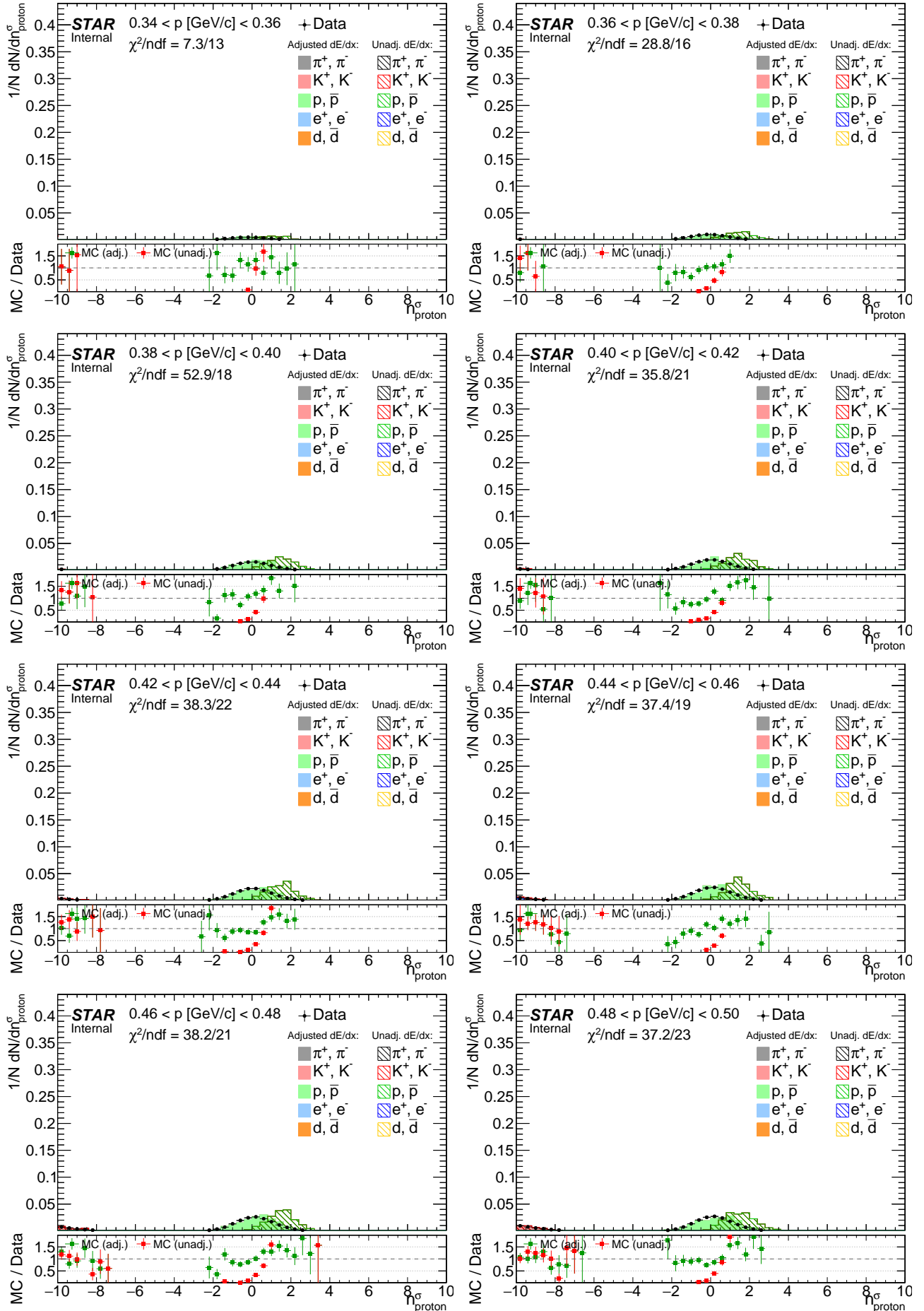
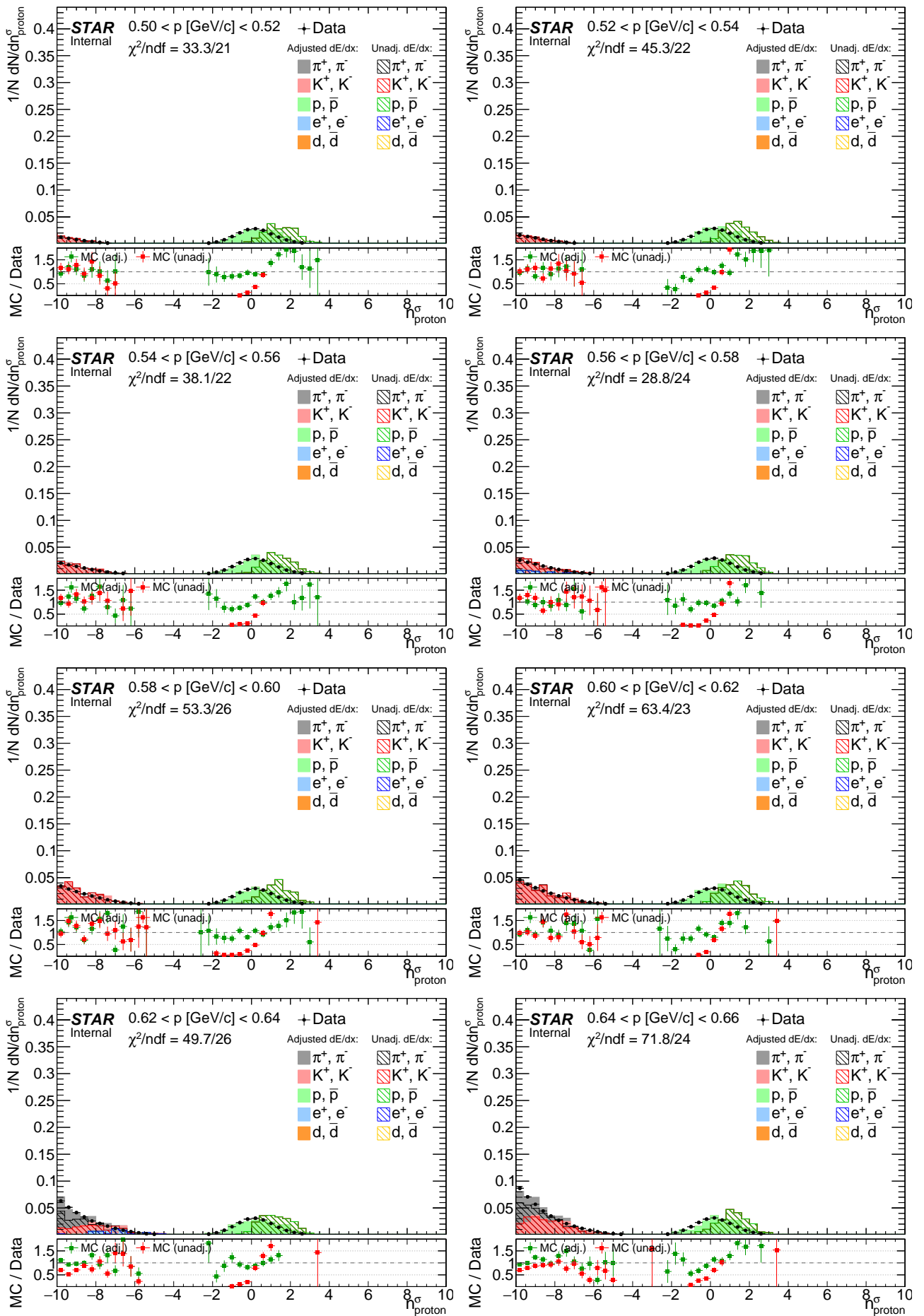
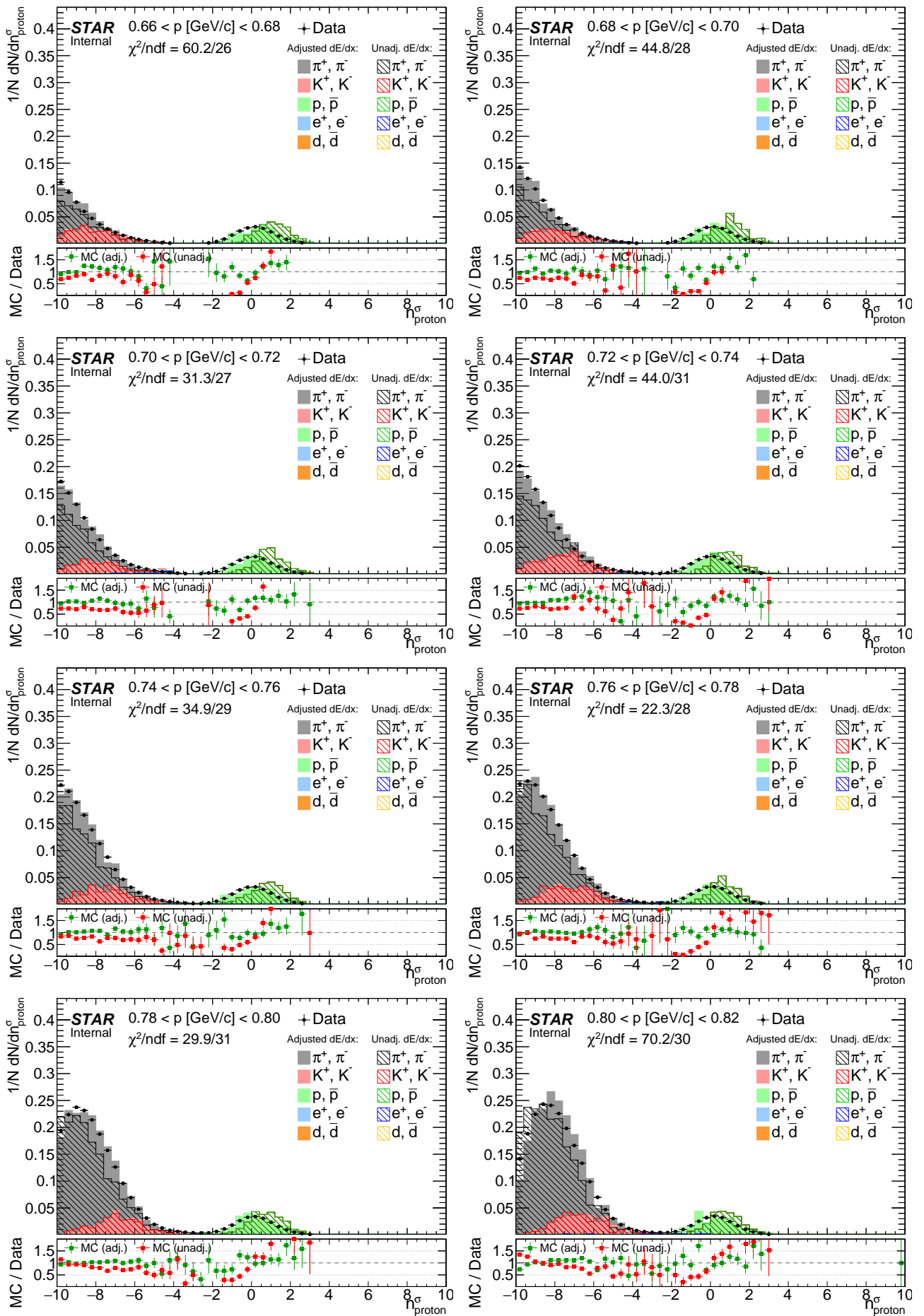
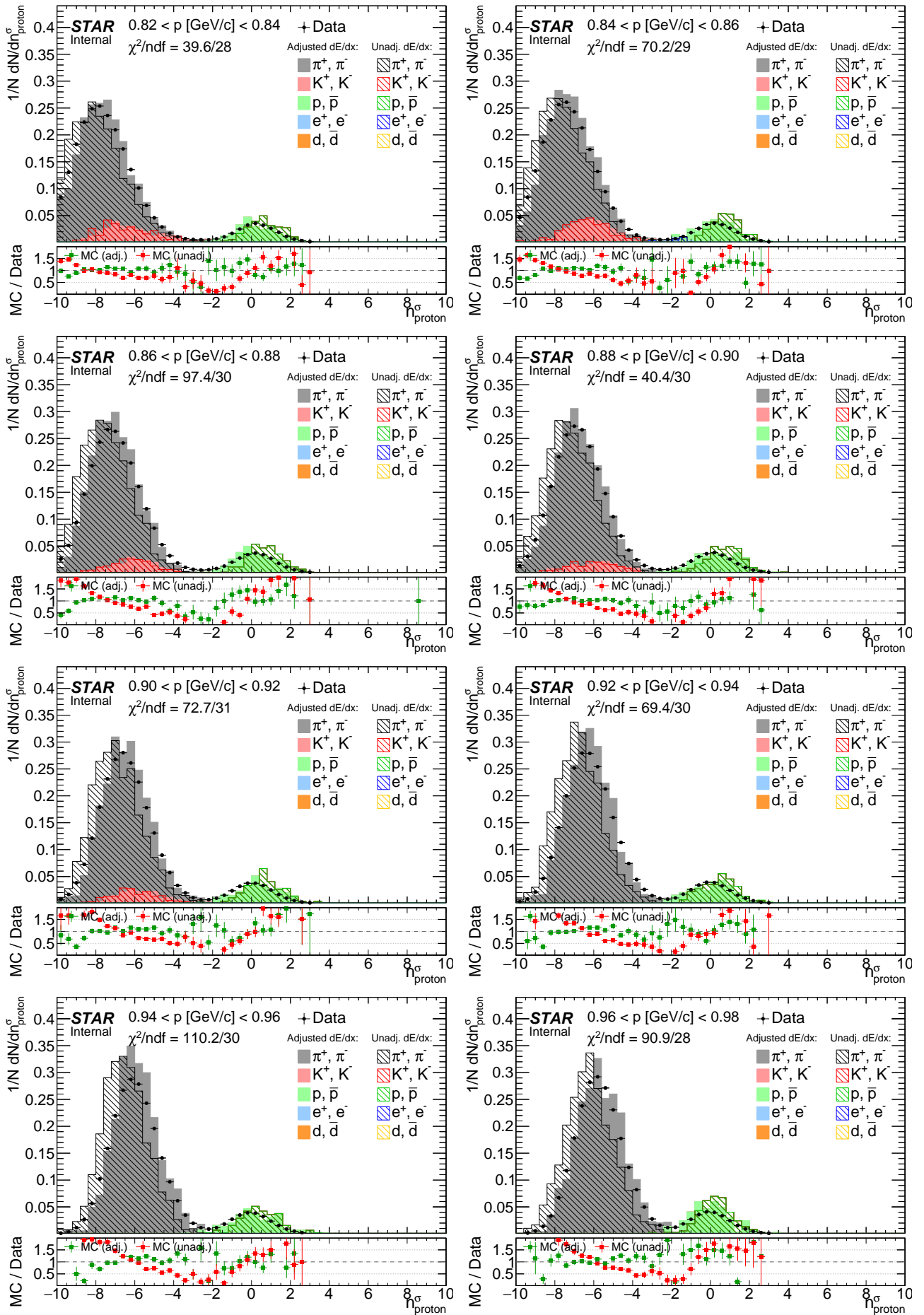


Figure F.5: Comparison of  $n_{\text{proton}}^{\sigma}$  distribution between data and embedded MC (before and after  $dE/dx$  adjustment) in momentum bins.





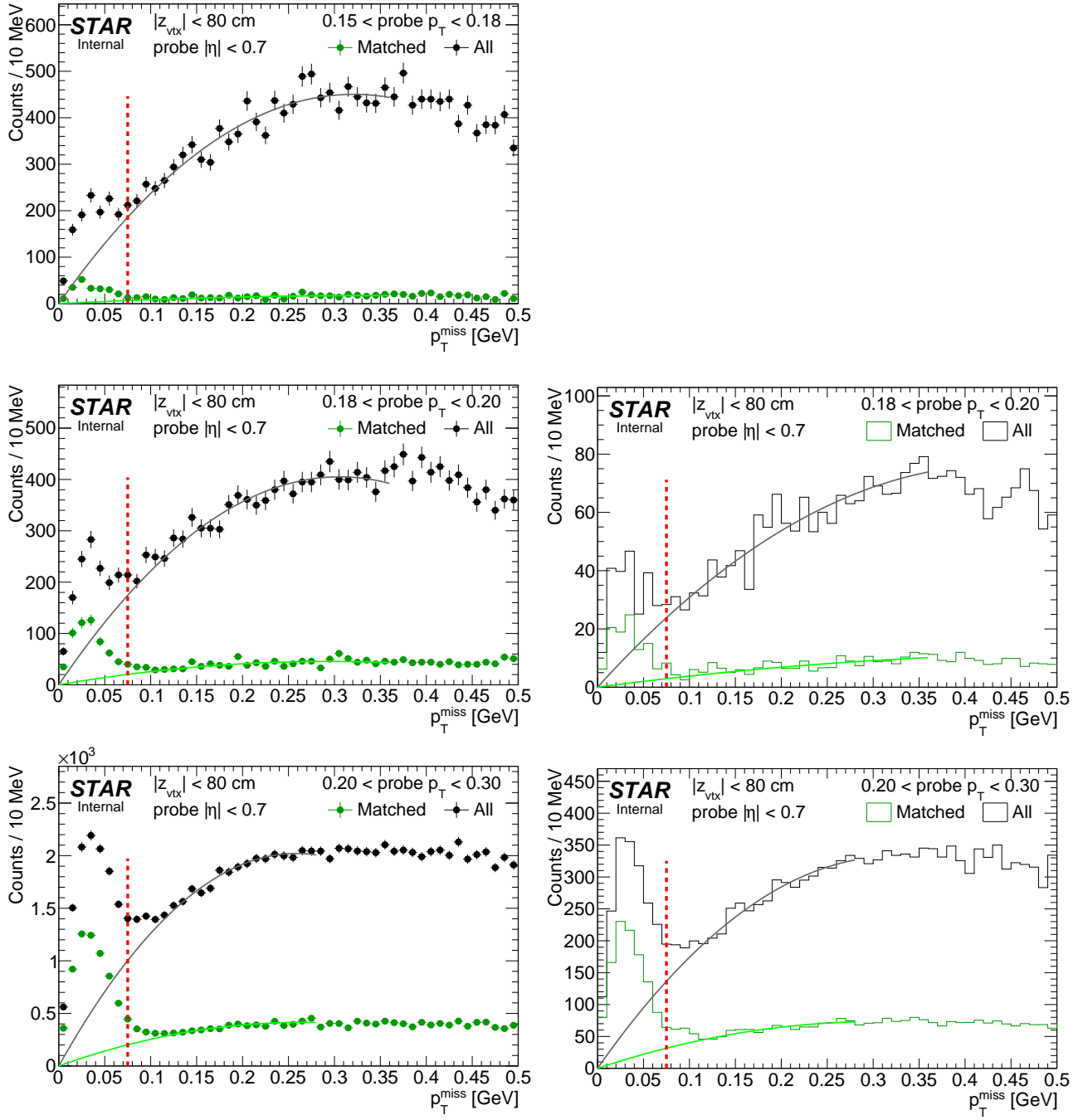




# Appendix G

## Tag&Probe fits for TOF hit reconstruction and matching efficiency

Figure G.1: lines and arrows indicate region accepted in analyses.



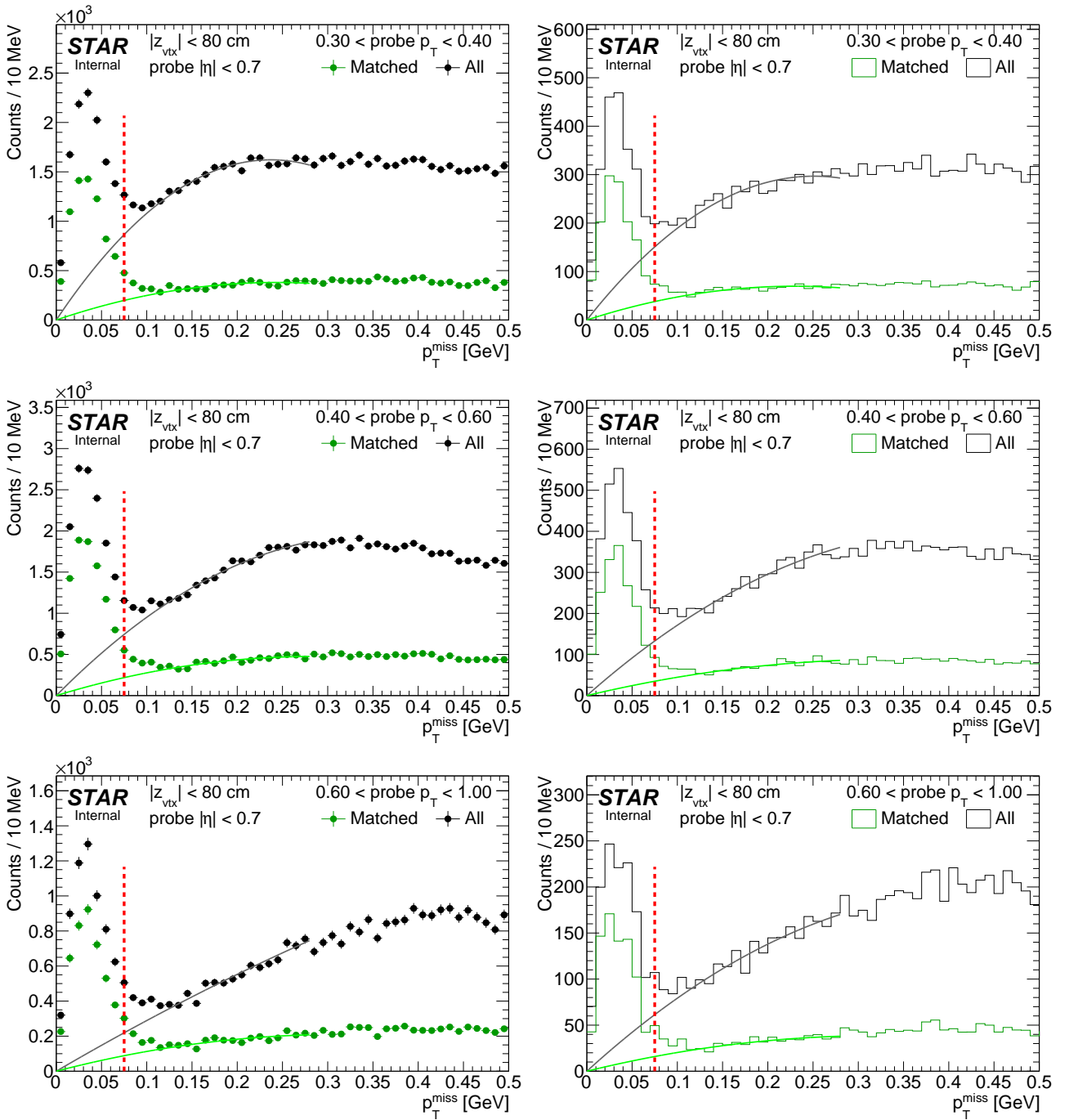
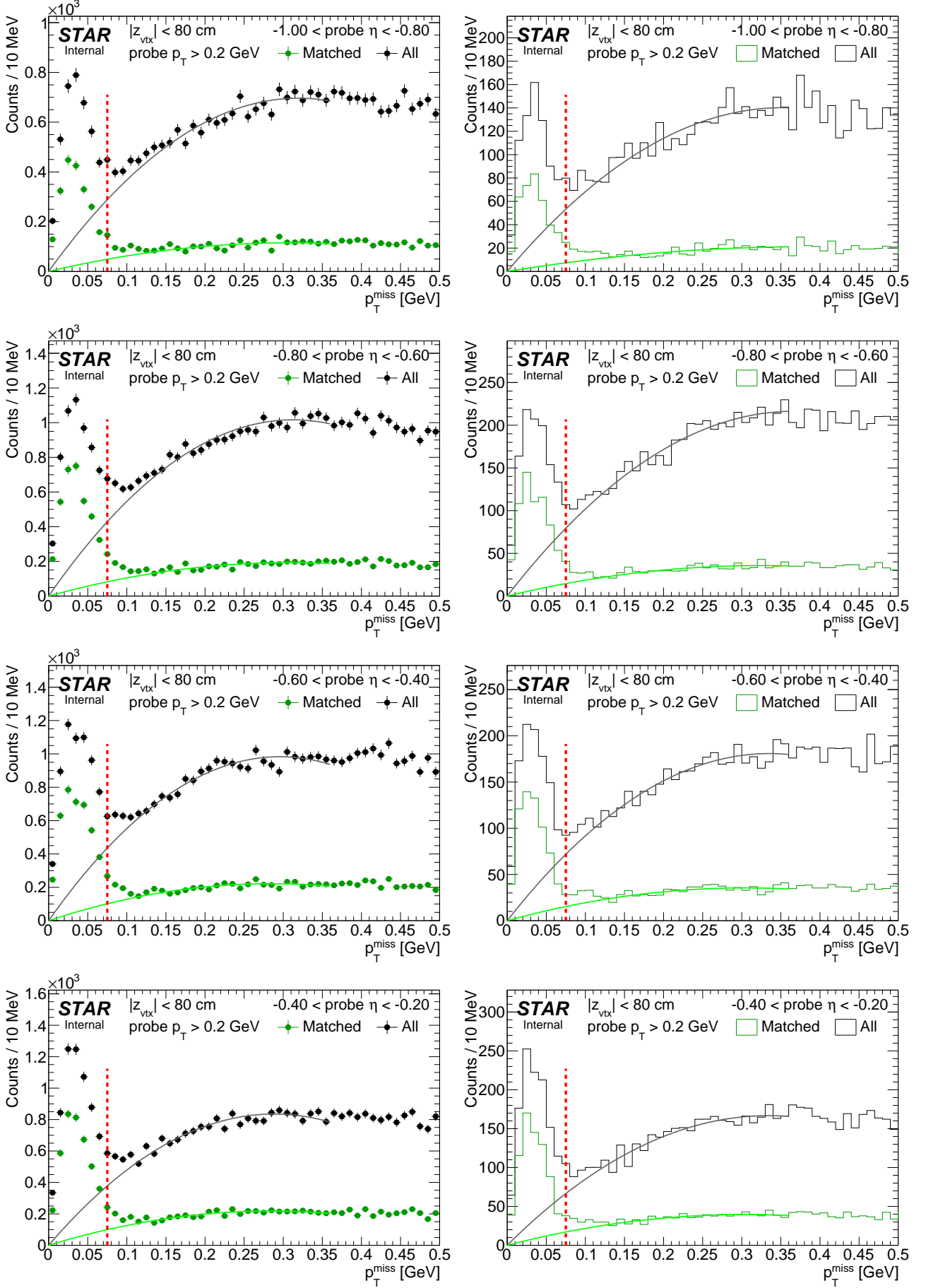
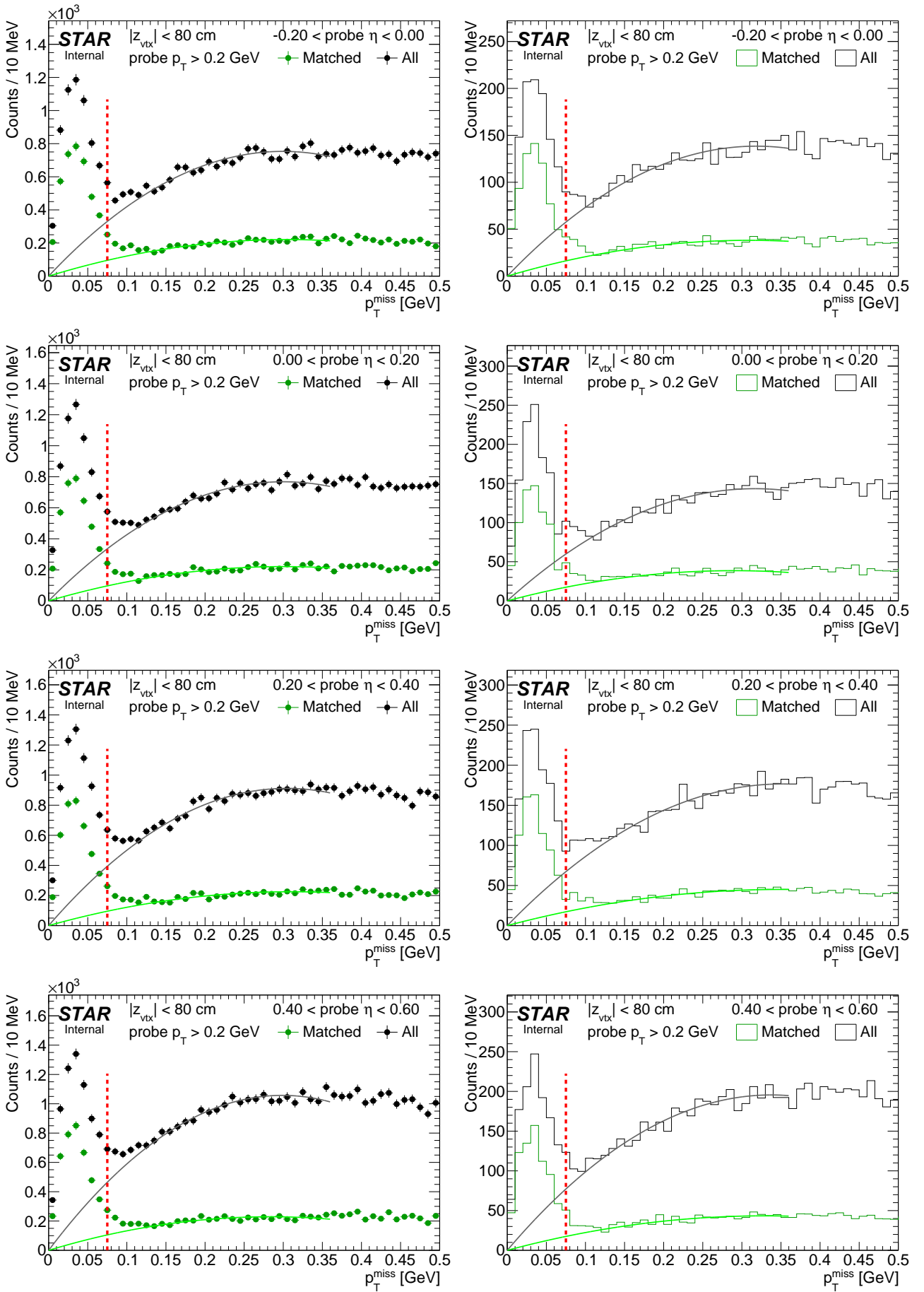
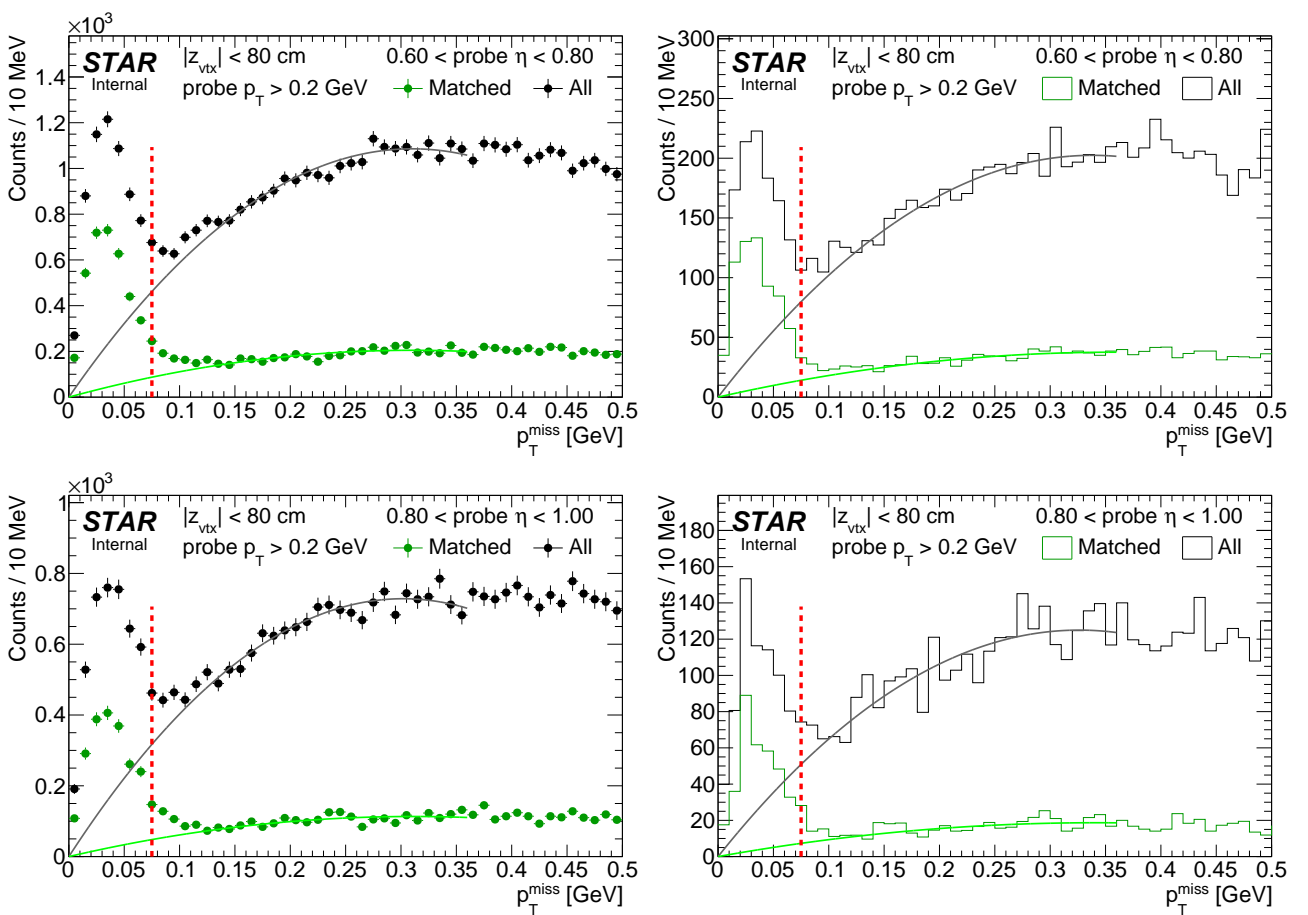


Figure G.2: TOF acceptance, reconstruction and matching efficiency of  $\pi^+$ . Each plot represents the TOF efficiency  $\epsilon_{\text{TOF}}$  ( $z$ -axis) as a func.







# List of Figures

1.1	Beam-detector distance of the Roman Pots in run 15.	4
3.1	Sample TPC acceptance and reconstruction efficiency of $\pi^-$ .	6
3.2	Sample plot of TOF acceptance, reconstruction and matching efficiency of $\pi^-$ .	7
4.1	Energy loss correction for $K^-$ as a function of reconstructed transverse momentum $p_T^{meas}$ .	8
5.1	Schematic representation (top view) of the Roman Pot Phase II* at STAR.	10
5.2	Side view of the Roman Pot Phase II* setup with an illustration of Roman Pot track point and track.	10
5.3	Correlation between the hit position of constituent track point in the first RP station and the local angle of track in elastic scattering events.	11
5.4	View of the Geant4 implementation of the Roman Pot Phase II* detector setup.	13
5.5	Roman Pot vessel (photo).	13
5.6	Silicon Strip Detector packages stored in the protective atmosphere (photo).	13
5.7	Geant4 implementations of the Roman Pot vessel and SSD package with trigger counter.	13
5.8	Sample hit map of track points of proton tracks in events selected as elastic scattering in the data (5.8a) and MC (5.8b) with the DX aperture "shadow" marked with black points. The DX aperture envelopes were fitted with circles (5.8c) which helped to establish the offsets of DX magnet positions in $x$ and $y$ with respect to the ideal (nominal) geometry, leading to nearly perfect agreement between the data and MC after introducing the offsets in Geant4 geometry (5.8d).	14
6.1	Sample fit to dE/dx spectrum in the data in single momentum bin.	17
6.2	Parameters of reconstructed track dE/dx as a function of reconstructed momentum for a few particle species.	17
6.3	Sample comparison of dE/dx spectrum between data and embedded MC in single momentum bin.	19
6.4	Sample comparison of $n_{\text{pion}}^\sigma$ , $n_{\text{kaon}}^\sigma$ and $n_{\text{proton}}^\sigma$ distribution between data and embedded MC in single momentum bin.	19
7.1	Sketch of helix modification procedure and $d_0$ calculation.	20
7.2	Example of comparison of $d_0$ histograms in the data and embedded MC in the procedure of TPC pointing resolution adjustment.	21
7.3	Example of $-\chi^2/\text{NDF}$ map in a parameter space in the procedure of TPC pointing resolution adjustment.	21
7.4	Best-fit parameters obtained in the procedure of the TPC track pointing resolution adjustment.	21
7.5	Comparison of distribution of pion $d_0$ and components of DCA vector in the data and embedded MC, before and after adjustment of TPC pointing resolution.	22
8.1	Comparison of primary track multiplicity, $p_T$ and $\eta$ distribution in zero-bias data and embedded MC (minimum-bias).	23
8.2	Comparison of $d_0^{(0,0)}$ distribution of global TPC tracks matched with TOF in zero-bias data and embedded MC (minimum-bias).	24
8.3	Multiplicity of tracks in reconstructed secondary vertices.	25
8.4	$\eta_{\text{vtx}}$ definition (sketch).	25
8.5	Comparison of raw $R_{\text{vtx}}^{\text{secondary}}$ and $z_{\text{vtx}}^{\text{secondary}}$ distribution in the data and embedded MC.	26
8.6	Comparison of DCA between all pairs of secondary track candidates selected for the secondary vertex reconstruction in the data and embedded MC.	26
8.7	Comparison of radial DCA of all primary tracks matched with TOF and passing quality criteria in events selected for secondary vertex analysis, between the data and embedded MC.	26

8.8	Comparison of background-subtracted $R_{\text{vtx}}^{\text{secondary}}$ and $z_{\text{vtx}}^{\text{secondary}}$ distribution in the data and embedded MC . . . . .	27
9.1	Number of events in embedded MC as a function of BBC_AND rate . . . . .	28
9.2	$\pi^\pm$ TPC track reconstruction efficiency as a function of $p_T$ ( $ \eta  < 0.7,  V_z  < 80$ cm) for embedded MC samples with $<\text{BBC\_AND}> = 700$ kHz and $<\text{BBC\_AND}> = 1400$ kHz . . . . .	28
9.3	The difference $\Delta\epsilon_{\text{TPC}} = \Delta\epsilon_{\text{TPC}}^{1400 \text{ kHz}} - 2 \cdot \Delta\epsilon_{\text{TPC}}^{700 \text{ kHz}}$ for $\pi^\pm$ as a function of $p_T$ and $\eta$ ( $ V_z  < 80$ cm)	29
9.4	The amount of lost $\pi^-$ due to the interaction with dead material in front of TPC as a function of $p_T$ , $\eta$ and $z$ -vertex in CD . . . . .	30
9.5	The systematic uncertainty to the TPC track reconstruction efficiency due to amount of dead material in front of TPC using MC samples for CD . . . . .	32
9.6	$\pi^\pm$ TOF matching efficiency as a function of $p_T$ ( $ \eta  < 0.7,  V_z  < 80$ cm) for embedded MC samples with $<\text{BBC\_AND}> = 700$ kHz and $<\text{BBC\_AND}> = 1400$ kHz . . . . .	33
9.7	The difference $\Delta\epsilon_{\text{TOF}} = \Delta\epsilon_{\text{TOF}}^{1400 \text{ kHz}} - 2 \cdot \Delta\epsilon_{\text{TOF}}^{700 \text{ kHz}}$ for $\pi^\pm$ as a function of $p_T$ and $\eta$ ( $ V_z  < 80$ cm)	33
9.8	Sketch of the tag&probe method . . . . .	34
9.9	Comparison of original and reconstructed TOF multiplicity at the trigger level . . . . .	34
9.10	Tag&Probe TOF efficiency from CEP data compared with the result from embedded CEP MC . . . . .	36
9.11	Tag&Probe TOF efficiency from CEP data compared with the result from embedded CEP MC (divided w.r.t. $\eta$ of the probe) . . . . .	37
A.1	TPC acceptance and reconstruction efficiency of $\pi^-$ . . . . .	39
A.2	TPC acceptance and reconstruction efficiency of $\pi^+$ . . . . .	41
A.3	TPC acceptance and reconstruction efficiency of $K^-$ . . . . .	43
A.4	TPC acceptance and reconstruction efficiency of $K^+$ . . . . .	45
A.5	TPC acceptance and reconstruction efficiency of $\bar{p}$ . . . . .	47
A.6	TPC acceptance and reconstruction efficiency of $p$ . . . . .	49
B.1	TOF acceptance, reconstruction and matching efficiency of $\pi^-$ . . . . .	52
B.2	TOF acceptance, reconstruction and matching efficiency of $\pi^+$ . . . . .	54
B.3	TOF acceptance, reconstruction and matching efficiency of $K^-$ . . . . .	56
B.4	TOF acceptance, reconstruction and matching efficiency of $K^+$ . . . . .	58
B.5	TOF acceptance, reconstruction and matching efficiency of $\bar{p}$ . . . . .	60
B.6	TOF acceptance, reconstruction and matching efficiency of $p$ . . . . .	62
C.1	Energy loss correction for $\pi^-$ as a function of reconstructed transverse momentum $p_T^{\text{meas}}$ . . . . .	64
C.2	Energy loss correction for $\pi^+$ as a function of reconstructed transverse momentum $p_T^{\text{meas}}$ . . . . .	66
C.3	Energy loss correction for $K^+$ as a function of reconstructed transverse momentum $p_T^{\text{meas}}$ . . . . .	67
C.4	Energy loss correction for $\bar{p}$ as a function of reconstructed transverse momentum $p_T^{\text{meas}}$ . . . . .	68
C.5	Energy loss correction for $p$ as a function of reconstructed transverse momentum $p_T^{\text{meas}}$ . . . . .	69
C.6	Energy loss correction for negative particles as a function of reconstructed transverse momentum $p_T^{\text{meas}}$ . . . . .	70
C.7	Energy loss correction for positive particles as a function of reconstructed transverse momentum $p_T^{\text{meas}}$ . . . . .	71
C.8	Energy loss correction for $\bar{p}$ as a function of reconstructed global track transverse momentum $p_T^{\text{meas}}$ . . . . .	72
C.9	Energy loss correction for $p$ as a function of reconstructed global track transverse momentum $p_T^{\text{meas}}$ . . . . .	74
D.1	Apertures . . . . .	77
E.1	The amount of lost $\pi^+$ due to the interaction with dead material in front of TPC as a function of $p_T$ , $\eta$ and $z$ -vertex in CD . . . . .	78
E.2	The amount of lost $K^-$ due to the interaction with dead material in front of TPC as a function of $p_T$ , $\eta$ and $z$ -vertex in CD . . . . .	80
E.3	The amount of lost $K^+$ due to the interaction with dead material in front of TPC as a function of $p_T$ , $\eta$ and $z$ -vertex in CD . . . . .	81
E.4	The amount of lost $\bar{p}$ due to the interaction with dead material in front of TPC as a function of $p_T$ , $\eta$ and $z$ -vertex in CD . . . . .	82
E.5	The amount of lost $p$ due to the interaction with dead material in front of TPC as a function of $p_T$ , $\eta$ and $z$ -vertex in CD . . . . .	83

E.6	The amount of lost negative particles due to the interaction with dead material in front of TPC as a function of $p_T$ , $\eta$ and $z$ -vertex in CD . . . . .	84
E.7	The amount of lost positive particles due to the interaction with dead material in front of TPC as a function of $p_T$ , $\eta$ and $z$ -vertex in CD . . . . .	85
E.8	The amount of lost $\pi^-$ due to the interaction with dead material in front of TPC as a function of $p_T$ , $\eta$ and $z$ -vertex in SD . . . . .	86
E.9	The amount of lost $\pi^+$ due to the interaction with dead material in front of TPC as a function of $p_T$ , $\eta$ and $z$ -vertex in SD . . . . .	87
E.10	The amount of lost $K^-$ due to the interaction with dead material in front of TPC as a function of $p_T$ , $\eta$ and $z$ -vertex in SD . . . . .	88
E.11	The amount of lost $K^+$ due to the interaction with dead material in front of TPC as a function of $p_T$ , $\eta$ and $z$ -vertex in SD . . . . .	89
E.12	The amount of lost $\bar{p}$ due to the interaction with dead material in front of TPC as a function of $p_T$ , $\eta$ and $z$ -vertex in SD . . . . .	90
E.13	The amount of lost $p$ due to the interaction with dead material in front of TPC as a function of $p_T$ , $\eta$ and $z$ -vertex in SD . . . . .	91
E.14	The amount of lost negative particles due to the interaction with dead material in front of TPC as a function of $p_T$ , $\eta$ and $z$ -vertex in SD . . . . .	92
E.15	The amount of lost positive particles due to the interaction with dead material in front of TPC as a function of $p_T$ , $\eta$ and $z$ -vertex in SD . . . . .	93
E.16	The systematic uncertainty to the TPC track reconstruction efficiency due to amount of dead material in front of TPC using MC samples for SD . . . . .	94
F.1	Fits to dE/dx spectra in the data. . . . .	95
F.2	Comparison of $dE/dx$ spectrum between data and embedded MC in momentum bins. . . . .	98
F.3	Comparison of $n_{\text{pion}}^\sigma$ distribution between data and embedded MC in momentum bins. . . . .	102
F.4	Comparison of $n_{\text{kaon}}^\sigma$ distribution between data and embedded MC in momentum bins. . . . .	107
F.5	Comparison of $n_{\text{proton}}^\sigma$ distribution between data and embedded MC in momentum bins. . . . .	112
G.1	TOF acceptance, reconstruction and matching efficiency of $\pi^+$ . . . . .	116
G.2	TOF acceptance, reconstruction and matching efficiency of $\pi^+$ . . . . .	118

## List of Tables

6.1	Parameters of functions from Fig. 6.2 describing reconstructed track dE/dx as a function of reconstructed momentum for a few particle species. . . . .	18
-----	--	----

# References

- [1]
- [2]
- [3] <https://online.star.bnl.gov/RunLogRun15/>.
- [4] <https://drupal.star.bnl.gov/STAR/system/files/survey.pdf>.
- [5] [https://drupal.star.bnl.gov/STAR/system/files/pawlik\\_alignment\\_28\\_Oct\\_2015.pdf](https://drupal.star.bnl.gov/STAR/system/files/pawlik_alignment_28_Oct_2015.pdf).
- [6] <https://www.star.bnl.gov/~pawlik/AutoIndex.php?dir=Geometry/pp2pp/>.
- [7] <https://online.star.bnl.gov/rp/pp200/>.
- [8] STAR Collaboration, L. Adamczyk *et al.*, “Single Spin Asymmetry  $A_N$  in Polarized Proton-Proton Elastic Scattering at  $\sqrt{s} = 200$  GeV,” *Phys.Lett.* **B719** (2013) 62–69, [arXiv:1206.1928 \[nucl-ex\]](https://arxiv.org/abs/1206.1928).
- [9] K. Yip and J. Lee, “Analysis Note for the Single Transverse-Spin Asymmetries ( $A_N$ ) in elastic p+p collisions at  $\sqrt{s} = 200$  GeV.” Unpublished, February, 2012.
- [10] R. Sikora, “Study of elastic proton-proton scattering with the STAR detector at RHIC,” Master’s thesis, AGH-UST, Cracow, 2014-06-20. <https://drupal.star.bnl.gov/STAR/theses/masters/rafalsikora>.
- [11] R. Sikora, “Momentum reconstruction with the Roman Pot Phase II\* subsystem.” [https://drupal.star.bnl.gov/STAR/system/files/MomentumReconstruction\\_1.pdf](https://drupal.star.bnl.gov/STAR/system/files/MomentumReconstruction_1.pdf), August, 2015.
- [12] R. Sikora, “Naming convention and layout of the Roman Pot Phase II\* subsystem in the STAR experiment.” [https://drupal.star.bnl.gov/STAR/system/files/RomanPotNomenclature\\_0.pdf](https://drupal.star.bnl.gov/STAR/system/files/RomanPotNomenclature_0.pdf), October, 2014.
- [13] R. Sikora, “Description of Roman Pot data structure in StEvent.” [https://drupal.star.bnl.gov/STAR/system/files/RomanPotsInStEvent\\_0.pdf](https://drupal.star.bnl.gov/STAR/system/files/RomanPotsInStEvent_0.pdf), November, 2015.
- [14] R. Sikora, “Track reconstruction algorithm update.” [https://drupal.star.bnl.gov/STAR/system/files/Rafal\\_pp2pp-UPC\\_21October2015.pdf](https://drupal.star.bnl.gov/STAR/system/files/Rafal_pp2pp-UPC_21October2015.pdf), October, 2015.
- [15] <https://drupal.star.bnl.gov/STAR/subsys/romanpot/software/stmurpsutil-roman-pot-data-analysis-utilities-afterburner>.
- [16] [https://drupal.star.bnl.gov/STAR/system/files/userfiles/265/TotalElastic200GeVAnalysisNote\(3\).pdf](https://drupal.star.bnl.gov/STAR/system/files/userfiles/265/TotalElastic200GeVAnalysisNote(3).pdf).
- [17] [https://drupal.star.bnl.gov/STAR/system/files/Rafal\\_AlignmentBiweekly\\_4March2016.pdf](https://drupal.star.bnl.gov/STAR/system/files/Rafal_AlignmentBiweekly_4March2016.pdf).
- [18] [https://www.star.bnl.gov/~pawlik/AutoIndex.php?dir=Geometry/pp2pp/README/&file=IP\\_and\\_MPT\\_positions.pdf](https://www.star.bnl.gov/~pawlik/AutoIndex.php?dir=Geometry/pp2pp/README/&file=IP_and_MPT_positions.pdf).
- [19] L. Fulek, “Geant4 simulation status.” [https://drupal.star.bnl.gov/STAR/system/files/fulek\\_January\\_20\\_2016.pdf](https://drupal.star.bnl.gov/STAR/system/files/fulek_January_20_2016.pdf), January, 2016.
- [20] R. Sikora, “Elastic proton-proton scattering in the STAR experiment at RHIC,” 2013. <https://misio.fis.agh.edu.pl/media/misiofiles/ff1d4d716fb2efde2d2e2e931070473b.pdf>.
- [21] L. Fulek, “Transport of particles through RHIC magnet lattice,” 2013. <https://misio.fis.agh.edu.pl/media/misiofiles/15450addc55712ecdb681873692cde5e.pdf>.

- [22] L. Fulek, “Study of proton-proton scattering with the diffractive dissociation of one of the protons in the STAR detector at RHIC collider,” Master’s thesis, AGH-UST, Cracow, 2014-06-18.  
<https://drupal.star.bnl.gov/STAR/theses/masters/rafalsikora>.
- [23] [https://drupal.star.bnl.gov/STAR/system/files/LFS\\_UPC\\_Geant4SimulationOfRomanPots\\_170October2016.pdf](https://drupal.star.bnl.gov/STAR/system/files/LFS_UPC_Geant4SimulationOfRomanPots_170October2016.pdf).
- [24] <https://www.star.bnl.gov/rt3/SelfService/Display.html?id=3272>.
- [25] S. Das, “A simple alternative to the Crystal Ball function,” arXiv:1603.08591 [hep-ex].
- [26] <https://www.star.bnl.gov/rt3/SelfService/Display.html?id=3332>.
- [27] [https://drupal.star.bnl.gov/STAR/system/files/LFSUPC\\_PWGMeeting\\_RafalSikora\\_23April2018.pdf](https://drupal.star.bnl.gov/STAR/system/files/LFSUPC_PWGMeeting_RafalSikora_23April2018.pdf).
- [28] <https://www.star.bnl.gov/HyperNews-star/protected/get/startof/2730.html>.